

A Multi-Modal Instrument Combining Optical Coherence Tomography and Microscopic Spectral Imaging for Cultural Heritage Applications

A thesis submitted in partial fulfilment of the requirements of the
Nottingham Trent University for the degree of Doctor of Philosophy

This research programme was carried out in
collaboration with the National Gallery, London

Patrick Saul Atkinson

27th February 2024

Copyright Notice

This work is the intellectual property of the author. You may copy up to 5% of this work for private study, or personal, non-commercial research. Any re-use of the information contained within this document should be fully referenced, quoting the author, title, university, degree level and pagination. Queries or requests for any other use, or if a more substantial copy is required, should be directed in the owner(s) of the Intellectual Property Rights.

Acknowledgement

I would like to massively thank the supervisory team of Prof Haida Liang, Dr Catherine Higgitt and Prof Lucas Goehring for support, insight and mentoring throughout my studies and providing me the opportunity to carry out this research. Additionally, I would like to thank Dr Sammy Cheung for the massive support in the development, construction and testing of the hybrid instrument and the collection of crucial data during field trips. I would also like to express my thanks to Dr Alex Hogg and Russell Metcalfe for technical support in the construction of the hybrid OCT and Spectral imaging instrument.

I would also like to thank the Scientific and Conservation Departments at the National Gallery, London, in particular Marta Melchiorre, David Peggie, Marika Spring and Jo Russell (Scientific); and Kristina Mandy, Jae Youn Chung, Lynne Harrison and Larry Keith (Conservation) for providing insight into the field of conservation and aid in during field trips.

I would also like to express my thanks to the current and previous ISAAC research group team members for the support and many constructive conversations during my studies. I would like to extend a massive thanks to Michael Macleod for aiding and supporting my studies.

I would like to thank all my Family and friends for all the support during this work.

Finally, I would like to express my gratitude to the AHRC collaborative doctoral partnership for funding this project.

Abstract

The potential of Optical Coherence Tomography (OCT) as a non-invasive tool for the monitoring of conservation treatments and investigation of sub-surface microstructures in artworks and historical objects is well recognised. This is thanks to its ability to provide micron scale three dimensional measurements of the stratigraphy of turbid and/or transparent multi-layered structures such as the varnish layers, glaze and paint layers seen in Old Master Paintings. However, it can be challenging to distinguish semi-transparent paint and glaze layers on paintings from layers of aged and degraded varnish due to similarities in their scattering properties within OCT images. This problem can limit the use of OCT as a tool to assist with the cleaning of degraded varnish from paintings.

This work demonstrates a method to extract the spectral characteristics from such translucent layers using spectral imaging to allow pigment identification and the means to distinguish glaze layers from varnish layers. To do so, segmentation of the layer structure is performed, and a Beer-Lambert relationship is used to extract extinction coefficient spectrum associated with the layer by fitting the layer thickness against reflectance per spectral channel. The segmentation of OCT is also demonstrated to be advantageous in the analysis and interpretation of layer stratigraphy; providing access to additional information such layer thickness and interface topography mapping, adaptive windowed enface projections, and refractive index corrected data sets.

Previous attempts combining spectroscopic techniques with OCT have suffered from alignment issues and vastly different system resolutions. Thus, to facilitate this combined approach, a multi-modal instrument was developed combining filtered illumination based spectral imaging in the visible to near infrared (VIS-NIR) with a spectral domain OCT centred in the shortwave infrared (SWIR) at 1350 nm. The system produces OCT volumetric data sets, with axial and transverse resolutions of approximately 3 μm (in varnish/paint) and 5.5 μm respectively, co-registered with reflectance spectral image cubes with lateral and spectral resolutions of 5.3 μm and 10 nm respectively.

Even without the extraction of the layer spectral features, co-registration of data sets is demonstrated to be beneficial in the interpretation of data from the complementary modalities.

The instrument was successfully employed on both mock-up paints and historical paintings from the National Gallery in London to address both conservation and art historical questions, demonstrating the potential for online assistance to conservation treatment and decision making. Additionally, the instrument shows promise for applications outside of the context of online conservation of historical paintings with its utilisation in the analysis of 19th and 20th century paintings, historical wall paintings, 16th - 18th century enamels, and archaeological objects such as the Herculaneum and Nash papyri's.

Contents

Chapter 1:	Introduction	1
1.1.	Surface Coatings for Historical Paintings	1
1.1.1.	Historical Paintings, Varnishes and Cleaning	1
1.2.	Methods of Painting Stratigraphy Characterisation and Monitoring Varnish Removal.....	3
1.1.2.	Sample Based Approach	4
1.1.3.	Non-Invasive Analysis	5
1.1.4.	Applications of OCT for Painting Conservation.....	5
1.1.5.	Outline of the PhD	7
Chapter 2:	Optical Coherence Tomography	8
2.1.	Optical Coherence Tomography	8
2.1.1.	Introduction to Optical Coherence Tomography	8
2.1.2.	Time Domain OCT	11
2.1.3.	Fourier Domain OCT	14
2.2.	Spectral Domain OCT	16
2.2.1.	Introduction	16
2.2.2.	Axial Resolution	17
2.2.3.	Optical Dependence of Axial Depth of Field and Lateral Resolution	17
2.2.4.	Dispersion Mismatch	18
2.2.5.	Sensitivity Roll-off and Aliasing	19
2.2.6.	Apodization and Spectral Shaping	20
2.2.7.	Speckle and Scattering	21
2.3.	Optical Coherence Tomography of Varnished Paintings	23
2.4.	Optical Coherence Tomography of NG5015 ‘A Vase of Wild Flowers’	25

2.4.1.	Painting Background	25
2.4.2.	The Varnish and Paint Layers	31
2.4.3.	The Sketching and Preparation Layers, and the Background Paint Layer...35	
2.4.4.	The Wooden Support	44
2.4.5.	Scanned Cleaning Test	47
2.4.6.	Conclusion	48
Chapter 3: A Technique for the Extraction of Spectral Features from a Layer through the Combination of Optical Coherence Tomography and Spectral Imaging		49
3.1.	Spectroscopy for Material Identification	49
3.1.1.	Introduction	49
3.1.2.	‘PRISMS’ Spectral Imaging	50
3.1.3.	Relationship between Absorption and Layer Thickness	53
3.2.	Segmentation of OCT stratigraphy	54
3.2.1.	Introduction	54
3.2.2.	OCT Volume Denoising	55
3.2.3.	Graph Based Segmentation	59
3.2.4.	Cases of Failed Segmentation	61
3.2.5.	Thickness Mapping	62
3.2.6.	Interface Depth Mapping and Refractive Index Corrections	66
3.3.	Data Alignment	70
3.3.1.	Collection of OCT Region of Interest	70
3.3.2.	Enface Reference Projection	71
3.3.3.	Alignment of the Two Modalities	75
3.4.	Extraction of Spectral Features	77
3.4.1.	Extraction of Spectral Features for a Prepared Samples	77
3.4.2.	Extraction of Spectral Features in Paintings	80
3.4.3.	Virtual Varnish Removal	82

3.4.4.	Conclusion	85
Chapter 4:	A Multi Modal Instrument for the Combined Collection of Spectral Imaging and Optical Coherence Tomography	86
4.1.	Introduction	86
4.2.	Design of a Multimodal Instrument	88
4.2.1.	Overview of Design	88
4.2.2.	Considerations in the Choice of Objective Lens.....	91
4.3.	Spectral Imaging Modality.....	93
4.3.1.	Collection of Spectral Imaging	93
4.3.2.	Filter Band Calibration.....	96
4.3.3.	Out of Band Illumination Components	97
4.3.4.	Laser Stability	100
4.3.5.	Illumination Power and Potential for Light Induced Damage	103
4.3.6.	Illumination and Imaging Field.....	105
4.3.7.	Microscopic Spectral Imaging of Standards and Samples.....	109
4.3.8.	Microscopic Spectral Imaging of Historical Paintings	113
4.4.	Optical Coherence Tomography	123
4.4.1.	OCT Design	123
4.4.2.	OCT Calibration.....	125
4.4.3.	A-scan Depth Profile Characterisation	128
4.4.4.	OCT Volume Characterisation.....	132
4.4.5.	Application of Hybrid OCT to Historical Painting	134
4.4.6.	Optimisation of OCT Design & Performance Summary	139
4.5.	Extraction of Layer Spectral Features with a Multimodal Instrument.....	143
4.5.1.	Data Alignment in the Hybrid System.....	143
4.5.2.	Extraction of Spectral Features within Prepared Samples	144
4.5.3.	Extraction of Spectral Features from Historical Paintings via the Hybrid Instrument	150

4.6. Conclusion	155
Chapter 5: Conclusion	158
References	161

Chapter 1: Introduction

1.1. Surface Coatings for Historical Paintings

1.1.1. Historical Paintings, Varnishes and Cleaning

The application of a final transparent varnish coating is a common feature of Old Masters paintings, particularly for works in an oil medium. Often such coatings provide benefits to the final piece in two-fold. Firstly, as an isolating layer, providing protection to the paintings surface from debris and degradation; and secondly, by providing saturation to the painting's colours and reducing variations in gloss.

The latter is accomplished by the reduction of surface roughness resulting from the levelling of the coating while in fluid. This surface roughness reduction in turn reduces the contribution of diffuse surface reflections to diffuse scattering of pigments within the volume of the paint layer [Figure(1.1.1.1)] [1–4] .

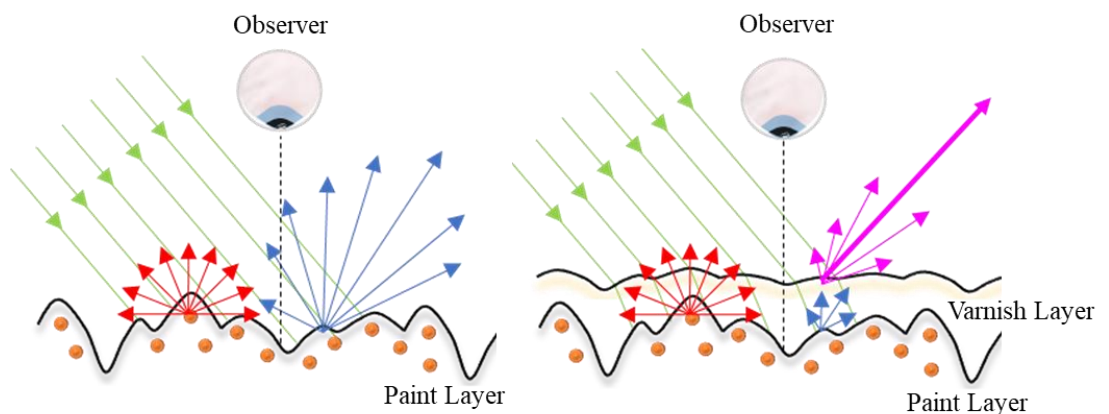


Figure 1.1.1.1. Diagram of the reflected light from an unvarnished and varnished painting. Here green rays correspond to the incident light, red the diffuse reflection from pigment particles, blue the reflected light from the interface between the air/varnish layer and the paint layer, pink the reflected light from the interface between the air and varnish layer.

Traditional painting varnishes are typically prepared using a natural plant resin (including pine, copal, dammar and mastic) [5,6] with early recipes often combining such resins with oil to form a solid coating through polymerisation. From the sixteenth century onwards 'spirit varnishes' became available in which the coating was produced by dissolving the resin within a volatile solvent such as alcohol or turpentine [7]. Once applied, the solvent would evaporate from the film leaving a hard resin coating. A variety of other materials including oil, or other resins were often added to achieve the desired properties in the resulting varnish.

However, natural resins, particularly when exposed as thin films such as in a varnish, tend to degrade over time becoming yellow and brittle or hazy, altering or visually obscuring the work [8]. Thus, to conserve the appearance originally intended by the artist and/or maintain an aesthetically appealing semblance, it is often necessary to remove and replace the surface varnish layer(s) [9]. Cleaning can also involve removal of overpaint or accumulations of surface dirt.

The removal of varnish and/or other surface layers is therefore a common procedure in the conservation of paintings but one that can potentially pose a significant risk. Varnish removal is generally undertaken using various solvents or solvent mixtures, either used as free solvent or as part of a gel formulation. However, due to chemical changes as a result of ageing, varnish layers can become more difficult to remove over time, requiring the use of more polar solvents for cleaning which can have a deleterious effect on the paint layers below. The paint layers themselves also alter over time, which can both render them more vulnerable during varnish removal and alter their appearance (they can become more translucent for example). In an ideal case, the cleaning procedure should result in the selective removal of these coatings without the disruption of proceeding layers which are integral to the work.

Varnish removal can be particularly challenging in cases where artist have applied glaze layers contiguous to the applied varnish coating. Glaze layers are semi-translucent paint layers that contain pigments with a refractive index that is closely matched with the binding medium. The semi translucent nature of these surface glaze layers can make them difficult to distinguish from a degraded varnish layer. Likewise, the degradation of the glaze layers themselves provide additional challenges, often resulting in the discolouration and/or alteration of the turbidity. In addition, the glaze layers are often quite vulnerable during solvent-based varnish removal as they are often relatively medium rich (compared to more opaque paint layers) or may include the addition of resins resulting in compositions and solubility behaviour similar to surface varnish layers. The pigments used within glaze layers also tend to exhibit poor drying behaviours when used alone (e.g. red and yellow lake pigments or ultramarine for example), leaving the layers vulnerable during cleaning procedures [10]. In turn, there are several examples of paintings where aggressive cleaning methods used in the past have led to damage or loss of the final surface glazes added by the artist, greatly altering the visual appearance of the paintings.

As the deterioration processes occurring within surface coatings and paint layers – and the interactions between such layers and the external environment – become better understood, it is becoming clear that interactions between layers may occur over time which may lead to the loss of the original clearly defined layer boundaries.[11] In some cases, it may therefore be desirable to control surface cleaning procedures carefully in order to only thin varnish layers rather than attempt to remove them entirely. This is often the approach adopted where there is evidence for the survival of original or very early varnish layers at the surface of a painting [5,6] .

1.2. Methods of Painting Stratigraphy Characterisation and Monitoring

Varnish Removal

Thus, to better inform and guide decision making in regard to cleaning and ensure that varnish removal is carried out in a manner which is controllable and alleviates the risk of damage, a full understanding of the nature and stratigraphy of the surface and underlying

paint layers is required alongside diagnostic methods that can support conservators to monitor cleaning procedures.

1.1.2. Sample Based Approach

One such approach utilised by conservators is the physical sampling of the painting stratigraphy from which the characterisation of the materials can be obtained through scientific analysis. Such sampling often comes in one of two forms: either through the removal of a small amount of material from the paintings surface/subsurface or through the collection of cross-sectional samples. This former approach is usually applied where there is interest in identifying the organic components of the binding medium of a particular paint layer or the composition of an individual surface coating. The analysis methods used for the identification of organic materials such as gas chromatography mass spectrometry (GC-MS) [12] are bulk analysis methods so care needs to be taken when sampling to only include the material from the layer of interest.

In the latter, small samples which preserve the layer structure are collected, mounted in a synthetic resin and polished to expose the sample cross-section for analysis [13,14]. This approach benefits from its ability to provide direct access to the entire stratigraphy, enabling the characterisation of the layer structure through microscopic imaging and spectral mapping methods [15] including optical microscopy (with visible or UV illumination), scanning electron microscopy with energy dispersive X-ray analysis (SEM-EDX), Fourier Transform infrared microscopy (external reflection or Attenuated Total Reflection (ATR)) [16], Raman spectroscopy, staining and immunological testing, spectral imaging microscopy [17], and a range of synchrotron-based methods (including SR- μ -FTIR, SR- μ -XRF), SR- μ -XANES and SR- μ -XRD) [18].

This sampling approach however has several disadvantages which should be addressed. Firstly, sampling is heavily localised to small regions of the painting and conservation practices often limit the locations of sampling to the peripheries of the painting subject or regions of damage. Thus, sampling may not produce a representative characterisation of

painting stratigraphy globally. Secondly, sampling is a destructive method and requires the removal of material to facilitate analysis. With this, the quantity of sampling is limited and thus the technique is not particularly suitable for in-situ monitoring during conservation treatment where multiple measurements may be required. Sample-based approaches usually also require sample preparation and/or analysis time and so are also not well suited to following a conservation treatment in real time [19].

1.1.3. Non-Invasive Analysis

Ideally then, non-invasive, and in-situ and/or real-time techniques should be available to extend the analysis of a painting beyond these limitations. Traditionally for in-situ monitoring of the varnish during cleaning, conservators assess the progress of varnish removal with detailed visual observation, stereomicroscopy or by observing the fluorescence of the aged varnish under ultraviolet illumination. More recently external reflection Fourier Transform Infrared (FTIR) spectroscopy has been used to detect residue varnish during cleaning [20,21].

1.1.4. Applications of OCT for Painting Conservation

A potentially useful diagnostic tool in the non-invasive analysis of painting stratigraphy is optical coherence tomography (OCT). OCT is a white light interferometry technique based on the Michelson interferometer which provides non-invasive three-dimensional surface and subsurface measurements of transparent and turbid microstructures. In relation to paintings, this yields micron scale volumetric measurements of the layer structure of all transparent and semi-transparent surface layers, over regions that are typically on the order of a couple of millimetres. Figure (1.1.4.1) shows an example region of OCT compared to a cross-sectional sample.

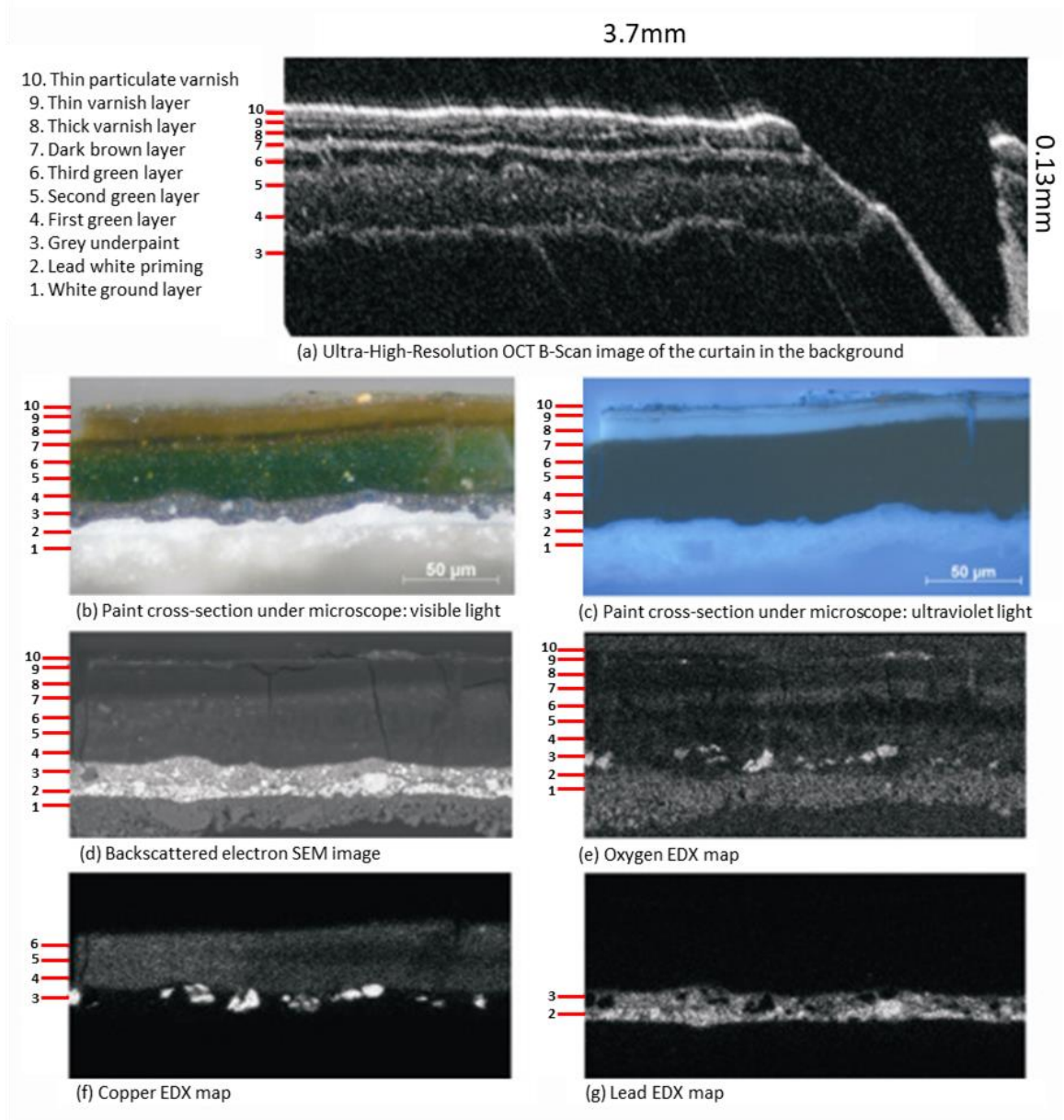


Figure 1.1.4.1. Comparison between OCT B-Scan cross-section (top) and data collected from a sample taken from a nearby position on the painting 'The Madonna and Child' (NG929), housed at the National Gallery, London [22]

The technique has been used within the field of heritage science over the past twenty years, with applications including: the investigation of painting, varnish, and glaze stratigraphy [23,24]; the extraction of paint layer scattering properties and underdrawings [25,26]; the profilometry of varnish and paint coatings [27]; and the in-situ study of degradation [28].

Of particular interest to this work is the monitoring of varnish cleaning and conservation treatments. The use of OCT as an online monitoring tool for varnish removal has been demonstrated in numerous instances with the use of solvent cleaning [23,24] and laser ablation [20,29,30]. Difficulties may arise when trying to distinguish glaze layers from varnish layers as both can be similarly turbid and have similar appearance in OCT images. In recent studies OCT has been combined with FTIR and laser induced fluorescence spectroscopy LIF to ascertain the chemical properties of the surface of a painting during cleaning treatment [20,21]. However, inefficiencies occur, when comparing the point based spectral analysis with OCT. The large spot size and the low penetration (restricted to the surface) of the spectral analysis techniques can also produce readings that may not be representative of the layer. A technique that distinguishes the glaze layers from varnish layers is therefore required to avoid overcleaning.

1.1.5. Outline of the PhD

The outline of this PhD is as follows:

Chapter 2- An introduction to the physics of OCT and the application of existing equipment (a bespoke ultra-high-resolution OCT) to a 19th Century oil painting housed at the National Gallery, London which presented a difficult conservation challenge due to the complex stratigraphy.

Chapter 3- Covers the automatic segmentation of layers from OCT volumetric datasets and the demonstration of a technique combining spectral imaging and OCT to extract the spectral characteristics of a layer.

Chapter 4- Covers the development of a hybrid instrument to collect co-registered OCT and microscopic spectral imaging and its application to both mock-up samples and historical paintings.

Chapter 2: Optical Coherence Tomography

2.1. Optical Coherence Tomography

2.1.1. *Introduction to Optical Coherence Tomography*

Since its showcase in the 1990s by Huang et al [31], the technique of optical coherence tomography (OCT) has seen wide applications, especially within in the medical field in which it is routinely applied to ophthalmology. The technique excels especially well in this case, owing to its ability to provide three-dimensional non-contact non-invasive micron-scale measurements of the layer stratigraphy for multi-layered semi-transparent/turbid objects, enabling the detailed examination of retinal structures.

The main basis of OCT is white light interferometry, often in the form of a Michelson interferometer seen in Figure (2.2.1.1), in which a polychromatic source is bifurcated via a beam splitter between two interferometer arms with one arm incident on the sample whilst the other acts as a reference where the beam is reflected from a simple reflector such as a mirror. The reflected beams from each arm can then be recombined within the beam splitter and the irradiance probed via a detector. When the optical path lengths of the two arms are closely matched, interference signals will be observed [32,33].

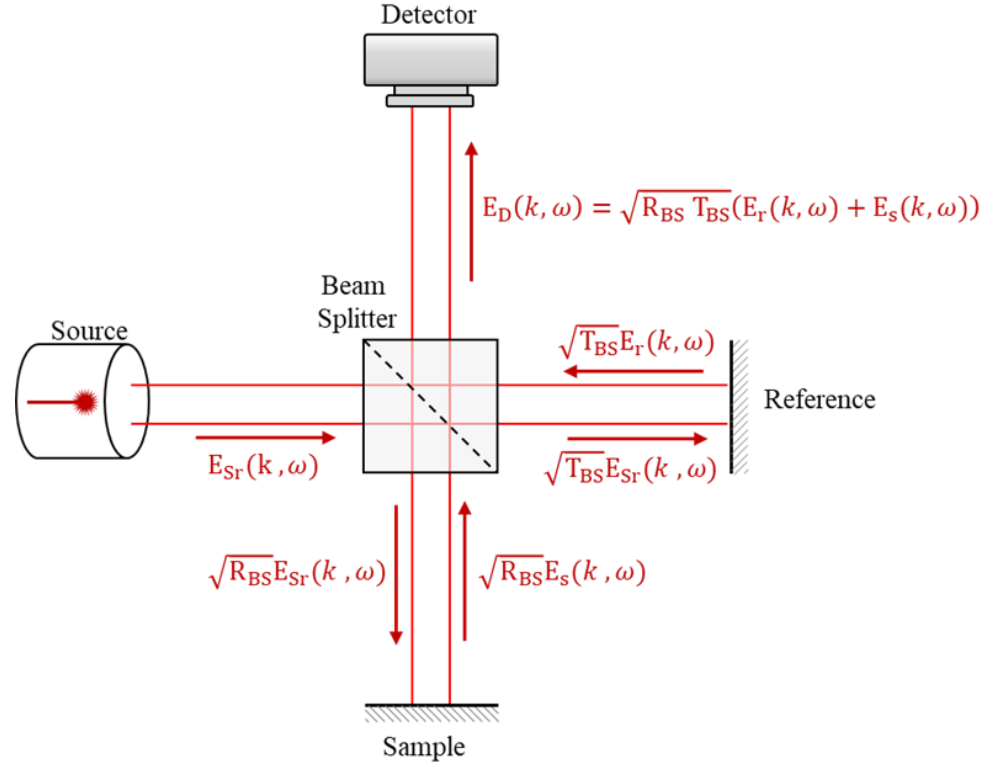


Figure 2.1.1.1. Schematic of a Michelson Interferometer E_s and E_r correspond to the portion of the electric field E_{Sr} reflected back from the reference and sample and reference respectively

The irradiance or intensity of light observed at the detector I_d over the collection time can be calculated through the time averaged square of the amplitude of the electric field (Equation 2.1.1.1). Considering that light can be represented in terms of the electric field as a polychromatic complex plane wave, the Equation 2.1.1.2 of the plane wave describing the laser source $E_{Sr}(k, \omega)$ can be given where k represents a propagation constant, in this case angular wave number given by $2\pi/\lambda$; angular frequency ω is given by $2\pi\nu$; $s(k, \omega)$ is the amplitude of the electric field and; z is the axial position l of the wave multiplied by the group refractive index $n_g(l, \omega_0)$ of the medium the wave is traveling through i.e. $z = n_g(\omega_0, l)l$.

$$I_d = \langle E_d E_d^* \rangle$$

$$E_{Sr}(k, \omega) = s(k, \omega)e^{i(kz - \omega t)}$$

Equation 2.1.1.2

Given that the transmission and reflection from the beam splitter are T_{BS} and R_{BS} , the incident irradiance on the detector can be given by Equation 2.1.1.3. Where $\gamma_{r,s}(z)$ is the complex degree of coherence as defined in Equation 2.1.1.4. E_R and E_S correspond to the Electric field components associated with signal from the reference and sample interferometer arms after recombination in the beam splitter.

$$I_d(k, z) = R_{BS}T_{BS}(I_s(k) + I_r(k) + 2\sqrt{I_r(k)I_s(k)}\Re[\gamma_{r,s}(k, z)])$$

Equation 2.1.1.3

$$\gamma_{r,s}(k, z) = \frac{\langle E_S^*(k, z)E_R(k, z) \rangle}{\sqrt{\langle |E_S(k, z)|^2 \rangle \langle |E_R(k, z)|^2 \rangle}} = \frac{\langle E_S^*(k, z)E_R(k, z) \rangle}{\sqrt{I_S(k, z)I_R(k, z)}}$$

Equation 2.1.1.4

Expanding Equation 2.1.1.2 to a situation in which the sample probed exhibits distinct layers and a number of interfaces positioned at material transitions, the electric field incident on the detector is given via Equation 2.1.1.5 where p is an interface from a set of interfaces P along the sample arm; R_p and R_r are the reflectivity of the sample interface p and reference (e.g. mirror) in the reference arm; z_p and z_r are the optical distance to sample interface p and the reference.

The irradiance incident on the detector will then be given by Equation 2.1.1.6. Here $\Delta z_{p,r}$ and $\Delta z_{p,q}$ are the optical path differences: between waves reflected from the reference interface and sample interface p ; and between sample interfaces p and q respectively [32,33].

$$E_D(k, \omega) = \sqrt{R_{BS} T_{BS}} S(\omega, k) \left(\sqrt{R_r} e^{i(2kz_r - \omega t)} + \sum_{p \in P} \sqrt{R_p} e^{i(2kz_p - \omega t)} \right)$$

Equation 2.1.1.5

$$\begin{aligned} I_D(k, z) = & R_{BS} T_{BS} S(k) \left(R_r + \sum_{p \in P} R_p \right) \\ & \dots + 2R_{BS} T_{BS} S(k) \sum_{p \in P} \sqrt{R_r R_p} \cos[2k\Delta z_{p,r}] \\ & \dots + R_{BS} T_{BS} S(k) \sum_{\substack{p, q \in P \\ p \neq q}} \sqrt{R_p R_q} \cos[2k\Delta z_{p,q}] \end{aligned}$$

Equation 2.1.1.6

2.1.2. Time Domain OCT

With Equation (2.1.1.6), it can be seen that a maximum in the irradiance at the detector is reached when the optical path difference $\Delta z_{p,r}$ is equal to zero. In a Time Domain OCT arrangement (TD OCT), this is taken advantage of by scanning the reference mirror along the optical axis and recording the irradiance change to obtain ranging of the interfaces. In such a set up a singular detector measures the irradiance with varying reference mirror positions. The irradiance measured by the detector will then be proportional to the integral of Equation (2.1.1.6) with respect to k . For a Gaussian source spectrum $S(k)$, defined in Equation (2.2.2.7), irradiance incident on a detector will be given via Equation (2.2.2.8). Here S_0 is defined as the integral of $S(k)$, k_0 is the central angular wavenumber of the spectrum and Δk expressed in relation to the full width half maximum bandwidth $\Delta\lambda$ and central wavelength of the source λ_0 as seen in Equation (2.1.1.9).

$$S(k) = \frac{1}{\Delta k \sqrt{\pi}} e^{-\left(\frac{k-k_0}{\Delta k}\right)^2}$$

Equation 2.1.2.7

$$I_D(z) = R_{BS} T_{BS} S_0 \left(R_r + \sum_{p \in P} R_p + \sum_{\substack{p, q \in P \\ p \neq q}} \sqrt{R_p R_q} e^{-(\Delta k \Delta z_{p,q})^2} \cos[2k \Delta z_{p,q}] \right) \\ \dots + R_{BS} T_{BS} S_0 \left(\sum_{p \in P} \sqrt{R_r R_p} e^{-(\Delta k \Delta z_{p,r})^2} \cos[2k \Delta z_{p,r}] \right)$$

Equation 2.1.2.8

$$\Delta k = \frac{\pi}{\sqrt{\ln[2]}} \frac{\Delta \lambda}{\lambda_0^2}$$

Equation 2.1.2.9

From these Equations, several observations can be surmised. Firstly, the component of the irradiance at the detector resulting from auto correlation between the sample interfaces is expected to be invariant for non-dynamic structures and thus will simply contribute as a D.C. component of irradiance. Secondly, that OCT does not measure a real interface position relative to the reference path Δl but instead optical path difference and thus must be corrected through the division of sample group refractive index as function of position into the sample $n_g(l, k_0)$. Finally, that the resolution of an OCT system is dependent on λ_0 , $\Delta \lambda$ and the refractive index of the probed material n_g . As n_g is fixed in accordance with the material being measured, the maximisation in resolution can be achieved through the minimisation of λ_0 and maximisation of, $\Delta \lambda$. For simplicity in this work the term depth will correspond to optical path difference dimension Δz . A simulation of such a profile can be seen in Figure (2.1.1.2.b). Here the interface position can be obtained via the fitting of an

envelope around the local maxima of the interference pattern with the envelope maximum providing the interface position [32,33].

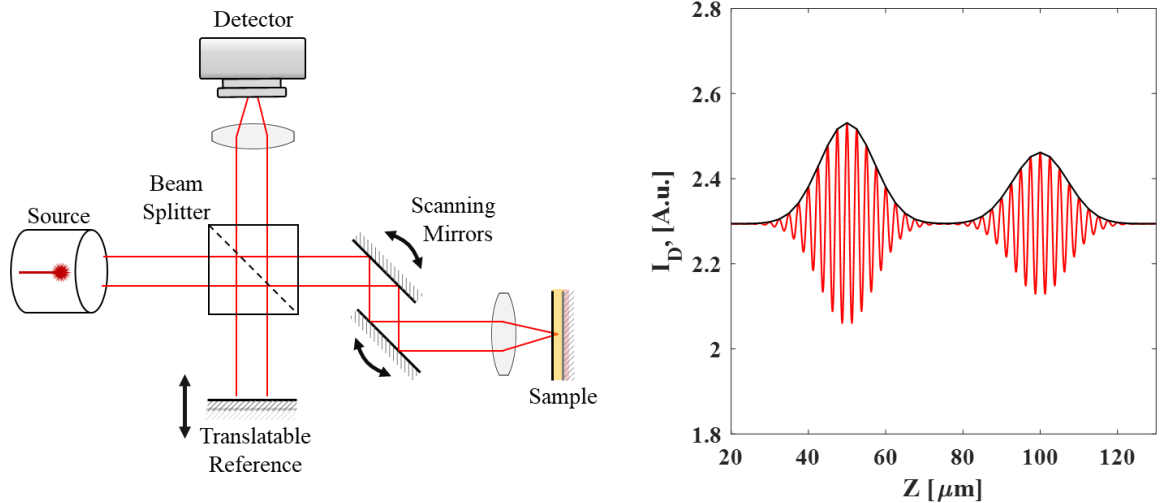


Figure 2.1.2.1. a) A schematic of a Time Domain (TD) OCT system. Here for a single transverse position the reference is scanned along the optical axis to produce an A-Scan depth profile of a sample. In this schematic, a pair of scanning mirrors enable the construction of volumetric datasets through raster scanning of the laser spot across the sample. b) A simulation of an A-scan depth profile with two interfaces i.e. one transparent layer (red) with a fitted local maxima envelope (black)

The above system entails a single depth profile often referred to as an A-Scan depth profile. For more practical implementations of the technique, lateral information is desirable as to provide two dimensional cross sections (referred to here as B-Scans) or three-dimensional volumes of a region.

Although not exclusively, this has often been accomplished through raster scanning the low coherence light source across a region to build volumetric data sets; a process that can severely limit data acquisition rates due to the requirement of scanning the reference path for each profile. Techniques exist which forgo the need for scanning in one (line scan OCT)

[34] or both (full field OCT) [35] lateral dimensions but these will not be the topic of discussion within this work.

2.1.3. Fourier Domain OCT

An alternative method for the collection of interface ranging is that of Fourier Domain OCT (FD OCT) where the reference arm pathlength is fixed. Interference fringes from the combined signals from the two arms can be recorded either as a function of the pathlength difference or as a function of wavelength, since the interference signal depends on the ratio between the optical pathlength difference and the wavelength. The ranging of the sample interfaces can be directly extracted from the Fourier transform of the irradiance with respect to angular wavenumber k . Doing so provides a new irradiance profile as a function of depth z , $\hat{I}_D(z)$. As seen in Equation (2.1.3.2).

$$\begin{aligned} \hat{I}_D(z) = \mathcal{F}_z[I_D(k, z)](k) &= \frac{R_{BS}T_{BS}}{2} H(z) \left(R_r + \sum_{n \in N} R_p \right) \\ &\dots + R_{BS}T_{BS} H(z) \otimes \sum_{p \in P} \sqrt{R_r R_p} \delta[z \pm 2\Delta z_{p,r}] \\ &\dots + \frac{R_{BS}T_{BS}}{2} H(z) \otimes \sum_{\substack{p, q \in P \\ p \neq q}} \sqrt{R_p R_q} \delta[z \pm 2\Delta z_{p,q}] \end{aligned}$$

Equation 2.1.3.2

Here the Fourier transform of the autocorrelation components of irradiance produce a function consisting of the axial point spread function (given by the Fourier transformed source spectrum) $H(z)$ convolved with a Dirac delta function $\delta[z]$ denoting axial position of the interfaces.

With closer inspection of Equation (2.1.3.2) several artifacts can be expected to manifest within a FD OCT depth profile. Firstly, the DC component of irradiance is exhibited as a new peak in the signal present at a zero-path length which changes shape in accordance with the axial point spread function.

Secondly as ranging is now reconstructed from the wavelength dependent interference rather than from scanning through depth positions, terms involving autocorrelation between sample interfaces will now manifest within the depth profile as additional peaks that do not change in depth with changing reference path length. These come in the form of additional interfaces positioned at a depth of $\Delta z_{n,m}$ and are referred to as autocorrelation artifacts.

Finally, with the loss of all phase terms excluding contributions of the path difference the Dirac function $\delta[z \pm 2\Delta z_{n,r}]$ of Equation (2.1.3.1) is seen to be symmetric around a path difference of zero. This is due to the symmetric nature of a Fourier transformed real function and thus positive path differences where $z_n > z_r$ and negative path differences where $z_n < z_r$ become indistinguishable. The outcome of this is that in cases where an interface of negative path length difference is present, the reconstructed interface will be mirrored in position around the zero depth position. This phenomenon will be referred to as a mirror artifact.

Such artifacts can become problematic in cases where they may overlap with real structures and thus may further limit the depth range over which the stratigraphy may be probed. Phase information can be reintroduced into FD OCT to enable full range collection of the stratigraphy. However such methods are not discussed in this work due to the additional instrumental requirements for implementation [32,33].

2.2. Spectral Domain OCT

2.2.1. Introduction

Fourier Domain OCT relies on the measurement of interference signal as a function of wavelength. This in general has been achieved in two ways: the direct measurement of the spectrum through the replacement of a single detector with a sufficiently precise spectrograph; or via the implementation of a spectrally tuneable laser source in which the laser wavelength is swept and collected by a single detector, such that discrete wavelengths may be collected temporally. Simplified schematics for the two implementations of the technique can be seen in Figure (2.2.1.1).

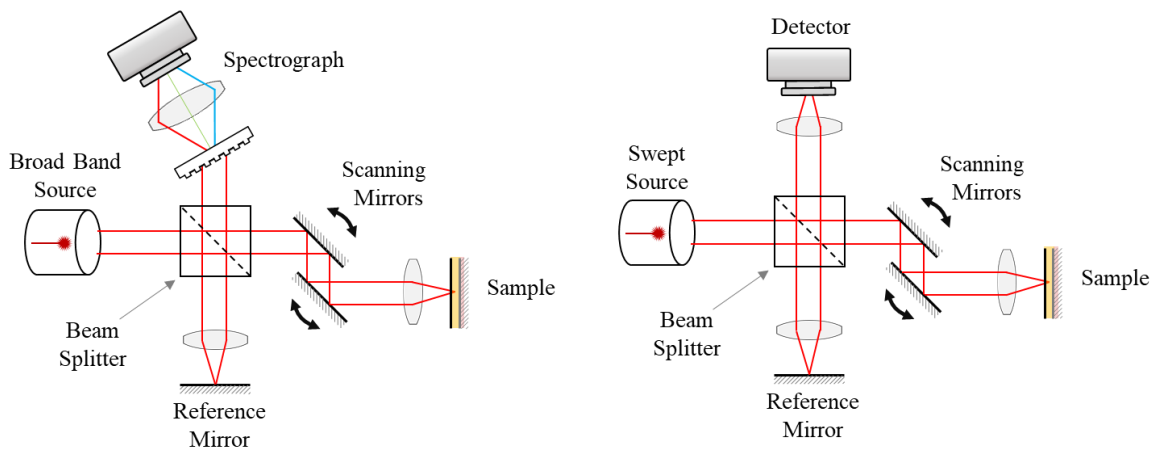


Figure 2.2.1.1. a) A Spectral Domain OCT schematic in which a spectrograph is used to collect the spectral response and b) A Swept Source OCT schematic in which the spectrum is collected by scanning through the spectral range of the illumination source with an instantaneous laser line of a very narrow bandwidth. The reference mirror is fixed in both cases. Here again a pair of scanning mirrors provides a volumetric dataset

The former technique known as spectral domain OCT (SD OCT) will be the focus of this work. With this, several practical considerations for the implementation of SD OCT should be explored.

2.2.2. Axial Resolution

Assuming a Gaussian spectral relationship, the theoretical maximum axial resolution for a smooth flat interface, defined by the FWHM of the axial point spread function, is given via the coherence length of the source seen in Equation 2.2.2.1. Here again it can be seen that an optimisation of the axial resolution is dependent on the nature of the spectral distribution where increasing the FWHM bandwidth and decreasing the central wavelength will both act to improve the axial resolution. Thus, for smooth interfaces with planes perpendicular to the optical axis, the axial resolution is seen to be decoupled from the lateral resolution and thus only dependent on the spectra [32,33].

$$\Delta l = \frac{2 \ln[2] \lambda_0^2}{n_g \pi \Delta \lambda}$$

Equation 2.2.2.1

As Equation 2.2.2.1. gives a resolution defined by the FWHM of the axial point spread function (PSF). It can also be surmised that the axial resolution will be improved with increasing refractive index of the material probed.

2.2.3. Optical Dependence of Axial Depth of Field and Lateral Resolution

With the resolution along the lateral directions being entirely dependent on the objective and the laser beam diameter incident on the objective, the lateral resolution can be estimated by the diffraction limited spot size. Equation (2.2.3.1) shows the lateral resolution as defined by the diameter of the airy disk given by the Rayleigh criterion. Here λ is the wavelength, d is the laser beam diameter incident on the objective and f is the focal length of the objective [36].

$$\Delta x, y = 1.22 \frac{\lambda_0 f}{d}$$

Equation 2.2.3.1

In addition to the lateral resolution, the depth of focus: the axial range over which a sample imaged with the objective lens can remain in focus, is also seen to be dependent on the objective lens. Here the depth of focus can be quantified by the confocal parameter as seen in Equation (2.2.3.2)

$$b = \frac{\pi(\Delta x, y)^2}{\lambda_0}$$

Equation 2.2.3.2

With this, the lateral resolution of the system is inversely proportional to the axial depth of field. As the objective lens is fixed within a typical Spectral Domain OCT, to preserve the interferometer path mismatch, the axial depth of field will act to limit the signal to noise over depth range, thus presenting an additional trade-off between lateral resolution and the maximum probing depth.

2.2.4. Dispersion Mismatch

The system discussed so far does not consider differences in the group velocity dispersion (GVD) between the interferometer arms. For a dispersive material the phase of light propagating through its bulk has a nonlinear relationship with wavelength. This nonlinearity will result in the variation of fringe frequency in the collected spectra as a function of angular wavenumber known as chirping [32,37]. If left unaccounted for, the dispersion mismatch between the interferometer arms will result in a dynamic range reduction for the detected interface, a broadening of the axial point spread function (degrading the axial resolution) and can introduce additional artifacts through mechanisms like peak splitting [38].

Compensation for dispersion is usually addressed instrumentally through the addition of additional glass to the sample or reference arm or through compensations in processing.

2.2.5. Sensitivity Roll-off and Aliasing

Alongside limitations in the axial field of view resulting from the choice of optics, fundamental limitations in sensitivity with depth are present in Fourier Domain OCT. As indicated in section 2.1.2, the relationship between the intensity incident on the detector and the angular wavenumber, enables the direct extraction of the A-Scan depth profile simply through Fourier Transform. For spectral domain OCT, this relationship is offered via a spectrograph in which the interferogram spectra is sampled discretely. In most applications, this is in the form of a non-linear step in angular wavenumber and thus interpolation is required before a discrete Fourier transform is performed to obtain an A-scan depth profile.

In accordance with Nyquist's theorem of sampling, the required sampling frequency of a signal must be at least twice that of the signals frequency else the resulting measurement will exhibit aliasing artifacts: artifacts which result from under sampling the signal frequency and losing the higher signal frequency components blurring the interference fringes.

In relation to optical coherence tomography the effects of this can be explained through Equation 2.1.1.6. Here it can be seen that the frequency of modulation in the spectra of the light incident on the spectrograph as a function of angular wavenumber is dependent on the cosine of the optical path length difference Δz leading to an increase in the signal modulation frequency with greater depth. For an interface placed at increasing depth positions, the frequency of modulation will begin to surpass the Nyquist limits for a given wavelength. With this, an increasing portion of the modulation in the spectrum will be made up of aliased signals. After Fourier transform, the reduction in the resolvable modulation will reduce the intensity of the interface [39].

Thus, as an interface is probed in increasing depth, a drop in the signal to noise ratio of the interface/ a roll off in the sensitivity is to be expected alongside a limit on the maximum probeable depth. The maximum probeable depth of a system can therefore be estimated at the Nyquist limit of the wavelength bins as seen in Equation 2.2.3.1. In this case λ_0 is the central wavelength and $\delta\lambda$ the size of the wavelength bin [33].

$$Z_{max}(\lambda) = \frac{\lambda_0^2}{4\delta\lambda}$$

Equation 2.2.5.1

This effect can be accentuated in the presence of cross talk between the sampled wavelengths where the spot size of the incident beam is greater than the pixel size of the spectrograph. Here the Nyquist frequency of the system is reduced as wavelength measurements bleed into neighbouring pixels, effectively reducing the spectral resolution. Such effects are to be expected to worsen in the presence of optical aberrations within the optical system of the spectrograph.

2.2.6. Apodization and Spectral Shaping

In Equation 2.1.2.1, it can be seen that an A-scan depth profile of a given interface will be obtained from the convolution of the interface position with the discrete Fourier transform of the sampled source spectrum. In general, for non-Gaussian spectral distributions, the discrete Fourier transform of the interferogram will result in prominent side lobes within the axial point spread function. Even for Gaussian spectral distributions, the discrete Fourier series of the sampled intensity may in turn produce prominent side lobes through spectral leakage [40]. For example, in the case where the Gaussian spectral distribution is truncated due to the finite detector length, the detected spectrum will now be described as a Gaussian distribution multiplied by a rectangular function. In accordance with convolution theorem, the Fourier transform of this signal will produce an axial point spread function that is

convolved with a sinc function (the Fourier transform of the rectangular function) and thus introduce sidelobes into the data.

A method of mitigating this is through apodization, in which the signal is multiplied by a tapered window function prior to Fourier transform, reducing the magnitude of side lobes precipitated into the axial points spread function [41]. Of the many windowed functions utilized in signal processing, the Hann window function seen in Equation 2.2.5.1 will be discussed for its application within the majority of this work. Here the window functions are defined over an arbitrary maximum and minimum angular wavenumber bounds k_{\max} and k_{\min} with $\#N$ equalling the number of samples within the bounding window. With the application of apodization, Δk will be reduced as a result of the multiplication of the spectral distribution $S(k)$ with the tapered window function. Thus apodization is seen to introduce a trade-off between the reduction of side lobe magnitude in the axial PSF and preservation of axial resolution.

$$w_{\text{Hann}}(k) \triangleq \begin{cases} \frac{1}{2} \left(1 - \cos \left[\frac{2\pi(k - k_{\min})}{\#N} \right] \right) & , \quad k_{\min} \leq k \leq k_{\max} \\ 0 & , \quad (k \leq k_{\min}) \vee (k \geq k_{\max}) \end{cases}$$

Equation 2.2.6.1

2.2.7. Speckle and Scattering

In a realistic scenario, the illumination incident on the sample used in the collection of an A-Scan depth profile is not an infinitesimal spot. With this spatial component, for an interface with surface roughness, the variation in the interface position will introduce variations in the returning wavefront and thus produce localised regions of mutual interference in the OCT volume. Likewise, this phenomenon can be produced within the materials bulk in the presence of scattering sites. Here the multiple scattering of light within the material will act to introduce random delays and thus produce variations in the returning wavefront resulting in an interference pattern (speckle) [42]. The manifestation of this within the OCT data is seen in Figure (2.2.7.2) with localised variations in the intensity across the paint region being the result of the speckle pattern.

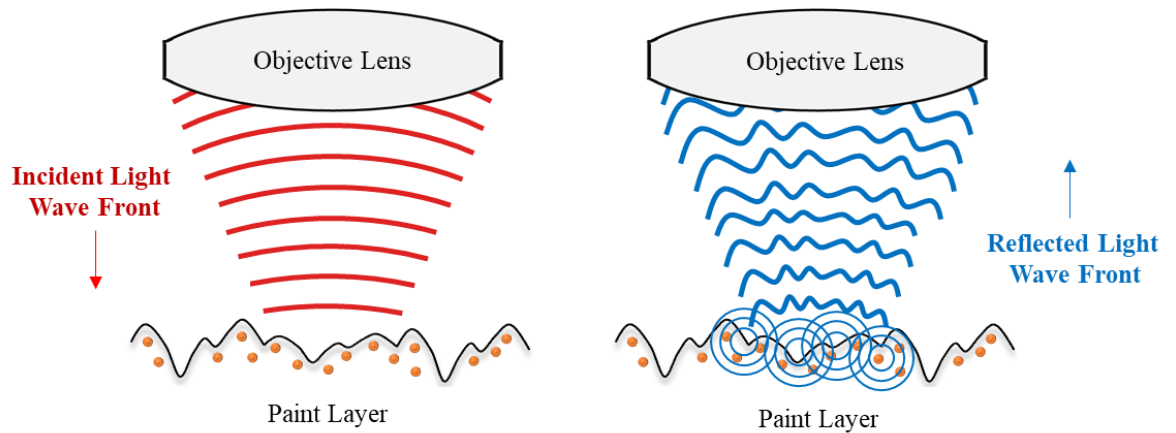


Figure 2.2.7.1. A diagram showing the wavefronts incident light (left) and reflected light from the sample (right). Changes in surface roughness, and multiple scattering

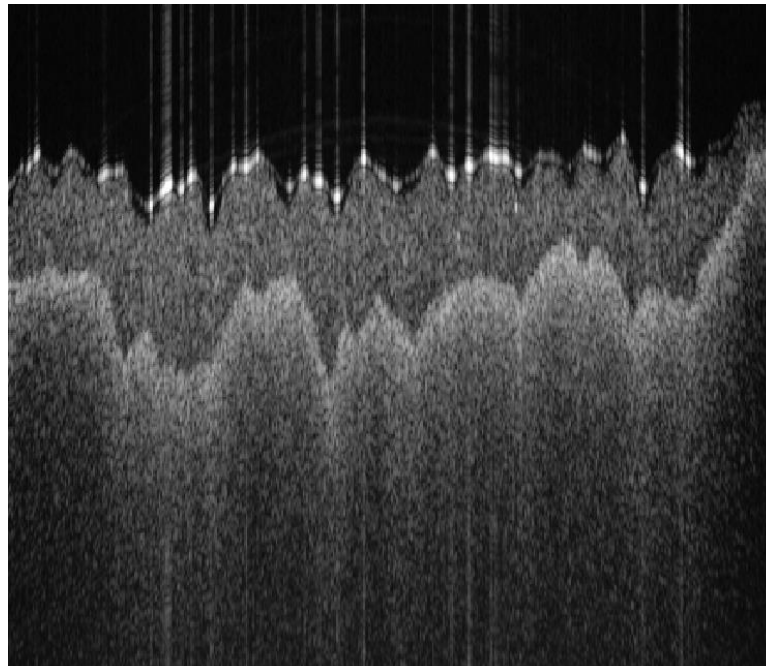


Figure 2.2.7.2. 100-scan averaged B-Scan for a sample of varnished Blue paint collected with the hybrid instrument of Chapter (4.4.6). A clear speckle pattern can be seen within the paint layers.

From Figure (2.2.7.3) another effect resulting from the multiple scattering of light is clearly visible. Here an artifact is present in which the paint layer appears to extend deeper in the B-Scan with a depreciating intensity. This is simply the result of the multiple scattering increasing path length experienced by the light before collection and is a common feature of heavily scattering layers such as those expected from paint [43].

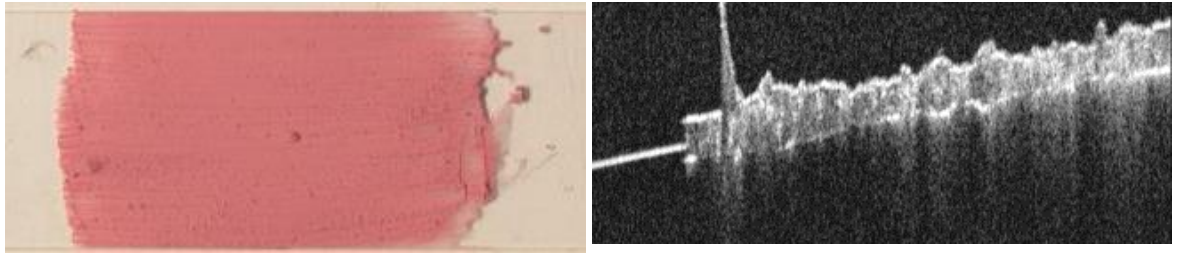


Figure 2.2.7.3. A colour image of a sample of madder lake in egg applied over glass (left) with the corresponding 930nm OCT B-Scan microscope slide showing evidence for multiple scattering [43].

2.3. Optical Coherence Tomography of Varnished Paintings

Within this and the following chapter, the instrument used for the collection of OCT data is that of an ultra-high-resolution spectral domain optical coherence tomography system developed for cultural heritage applications [22]. This optical coherence tomography system takes advantage of an NKT versa super continuum source for illumination with a Thorlabs FC632-50B-APC fibre coupler and single mode fibre tip acting as a Michelson interferometer and reference mirror respectively [Figure (2.3.1.1)].

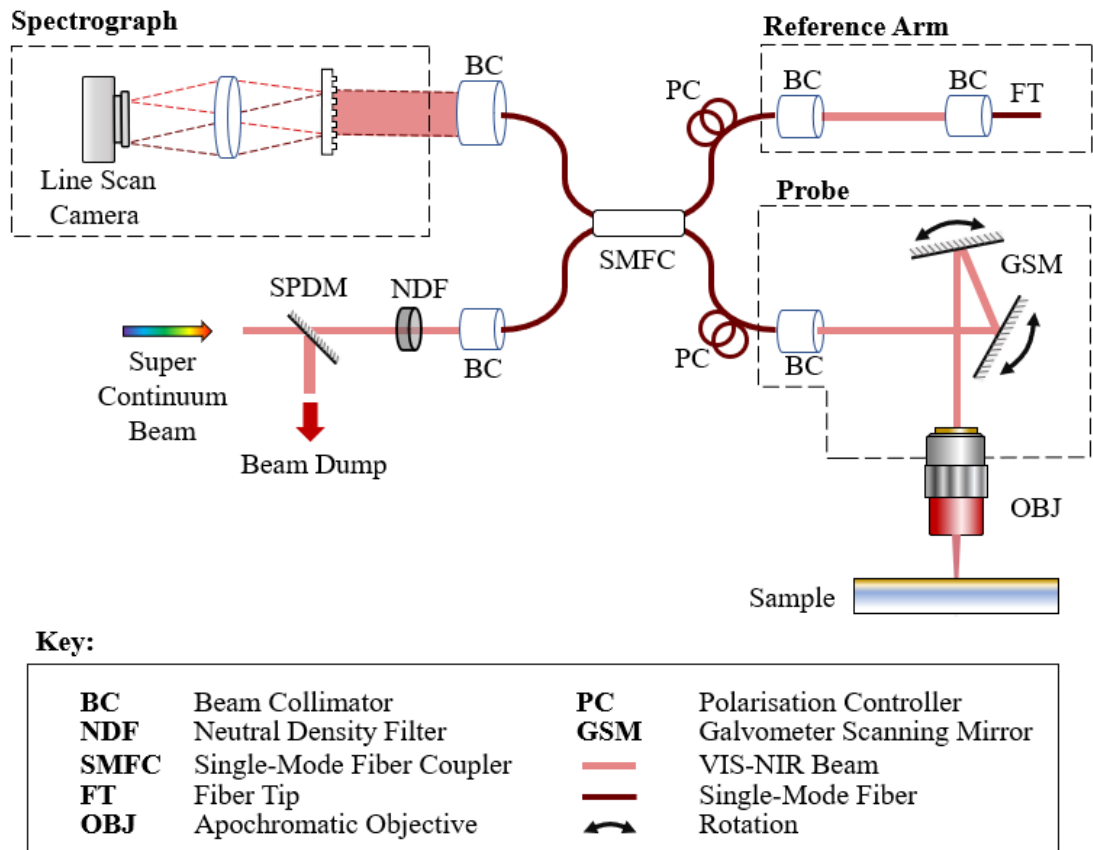


Figure 2.3.1.1. Schematic of the Ultra- High Resolution OCT system centred at 810nm

This produces a source spectral distribution centred at 810 nm with a ~ 200 nm FWHM incident on a spectrograph collecting wavelengths from 600nm to 1000nm [Figure (2.3.1.2.a)] allowing for an axial resolution of $2.2 \mu\text{m}$ in air to be obtained after apodization. The resulting axial point spread function can be seen in Figure (2.3.1.2.b). For this work, OCT volumes were collected at a lateral sampling resolution of $10 \mu\text{m}$.

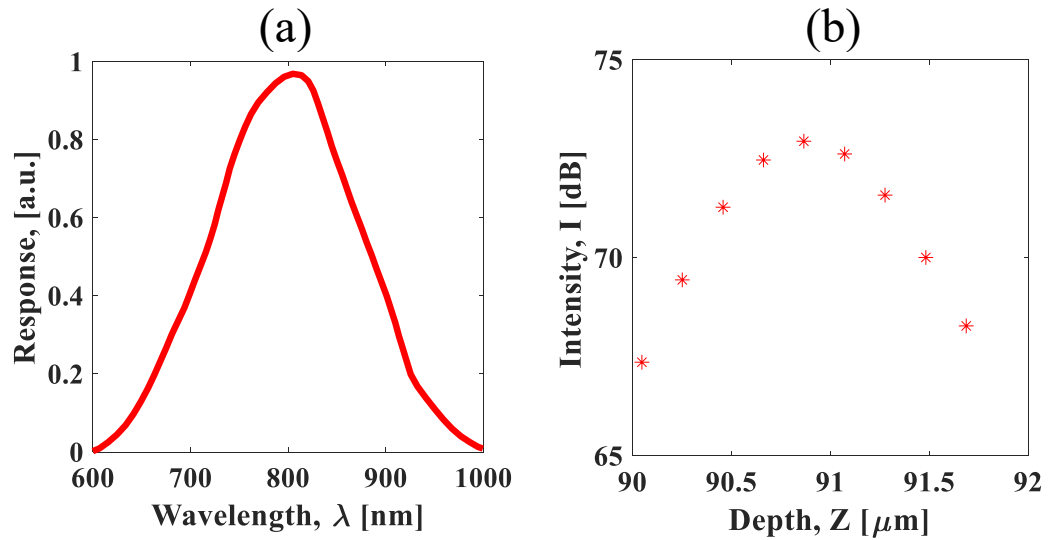


Figure 2.3.1.2. a) UHR OCT illumination spectrum b) UHR OCT axial profile of an air-glass interface

2.4. Optical Coherence Tomography of NG5015 ‘A Vase of Wild Flowers’

2.4.1. Painting Background

The following section demonstrates the application of optical coherence tomography for the analysis of the late 19th Century oil painting ‘A vase of Wild Flowers’ (NG5015) by Adolphe Monticelli housed within the collection of the National Gallery in London. The materials and techniques of this painting have been the subject of study in the previous work of Stoner and Morrison, 2012 [44] in which analysis was based on the examination of a number of micro-samples through the use of UV and visibly light imaging, GC-MS, ATR-FTIR and SEM-EDX. Here the analysis of ‘A Vase of Wild Flowers’ and the other works by Monticelli at the National Gallery reveal Monticelli’s idiosyncratic approach to painting and his choice of materials.

‘A Vase of Wild Flowers’ and most of the other works by Monticelli are painted on wooden panels repurposed from pieces of furniture. Analysis of the paintings suggested that some of the reused panels may have retained a surface coating applied to the wood when it was

furniture. In many areas of his paintings, Monticelli left the panel visible as a mid-tone (or only partially covered it with a semi-transparent red-brown paint), contrasting this with the thicker, more impastoed paint applied elsewhere, in bright, contrasting colours. Monticelli's desire to retain exposed wood meant that he did not apply a conventional, opaque ground layer to the panels before painting, but instead appears to have applied a transparent preparation layer (likely a partially pigmented pine resin varnish) to the panel to seal it and create the surface to receive paint. Over the preparation layer – in at least some areas of the painting – reddish-brown semi-transparent paint was applied to sketch in the composition or for shadows. This sketching layer contains more pigment than the preparation layer, but in this layer the medium again seems to contain some pine resin. Monticelli used Lefranc tube paints, often with a thick, impasto application. The tube paints had linseed or walnut oil binders, but Monticelli appears to have added some pine resin varnish to the tube paint in some cases.

Further analysis of NG5015 undertaken at the National Gallery in 2018 suggested that over the paint layers there were at least two varnish layers, with the lower layer more yellowed and containing dammar, mastic and larch resins, and the upper varnish containing both mastic and dammar as well as some drying oil and a significant proportion of pine resin. It is possible that the lowest varnish layer was the original varnish, potentially applied by Monticelli himself. The approximate stratigraphy of the painting is summarised in Table (2.4.1.1), presented in descending order of depth.

Strata	Description
i. Varnish Layers	Several discoloured varnish layers with the lowest of the layers (possibly original) being the most yellow and containing dammar, mastic and larch resins, and the upper varnish containing mastic, dammar, pine resin and containing drying oil.
ii. Paint Layers	Often applied with heavy impasto with a binder of heat-bodied linseed oil or walnut oil, with addition of pine resin in some cases.
iii. Sketching & Preparation Layer	Consisting of two semi-transparent layers: a reddish-brown paint layer marking out the composition (and areas of shadow) and a layer intended to seal the wooden substrate and produce a smooth flat working surface
Wooden Support	A mahogany wood support repurposed from its original use in furniture. As such the substrate may still retain its original preparative coating as a remnant of its previous use in furniture. For the Monticelli painting NG 5014 'Still Life: Fruit', the coating was identified as mainly consisting of beeswax.

Table 2.4.1.1

Over time, these varnish layers have become significantly discoloured and cloudy. These changes to the varnish layer had obscured the characteristic aspects of Monticelli's technique and thus the cleaning and revarnishing of the painting was desirable.

However, the resinous materials found in Monticelli's preparation and paint layers were found to be similar in solubility to the varnish coatings on the painting and thus sensitive to the traditional solvents used to reduce or remove varnish layers. Additionally, in many areas of the painting the varnish layers were seen in to be in direct contact with the sketching or preparation layers. In turn these factors made any attempt to remove the degraded varnish layers highly challenging. This was further complicated by a lack of understanding of the uniformity and presence of the strata described in Table (2.4.1.1) across the entire painting.

To provide some clarity on the paint stratigraphy across the entire panel, and the nature of the varnish layers across the painting, ultra-high-resolution OCT data sets were collected over several regions within the painting as marked on Figure (2.4.2.1) to complement the information available from the physical sampling undertaken by the National Gallery. The OCT was also used to assess the effectiveness of preliminary trials of methods for varnish removal and to help interpret some of the analysis of paint samples.

For this painting, larger volume regions were collected using the methodology described in Chapter (3.3.7), in which larger regions are constructed from concatenating multiple smaller volume scans. To produce continuous B-Scan regions, each constituent volume is aligned axially via the air-varnish interface position, and laterally by assuming constant lateral steps between scans. This is by no means an optimal method of mosaicking data sets, as it does not account for slight variations in the lateral and angular alignments between constituent volumes resulting from the presence of vibration. However, for the purposes of qualitative investigation of the layer structure over a larger region, such errors are negligible.

The broad stratigraphy of the painting described in Table (2.4.1.1) has been indicated within a B-Scan Cross section of OCT volume F as seen in Figure (2.4.1.2). Here the highlighted regions cover the areas associated with a given set of layers which are visible within the B-Scan, including artifacts resulting from multiple scattering. Areas which are unresolvable due to a lack of signal or those obscured by the above strata remain unmarked. Moving from right to left across the B-scan, there is an area of impasto paint of a flower, then an area where the panel can be seen through a semi-transparent red-brown layer and finally a thicker application of paint in the background (with drying cracks). This thicker background paint likely lies over the semi-transparent red-brown layer. For all future figures in this chapter, the coloured highlights will correspond to the same strata marked in Figure (2.4.1.2).

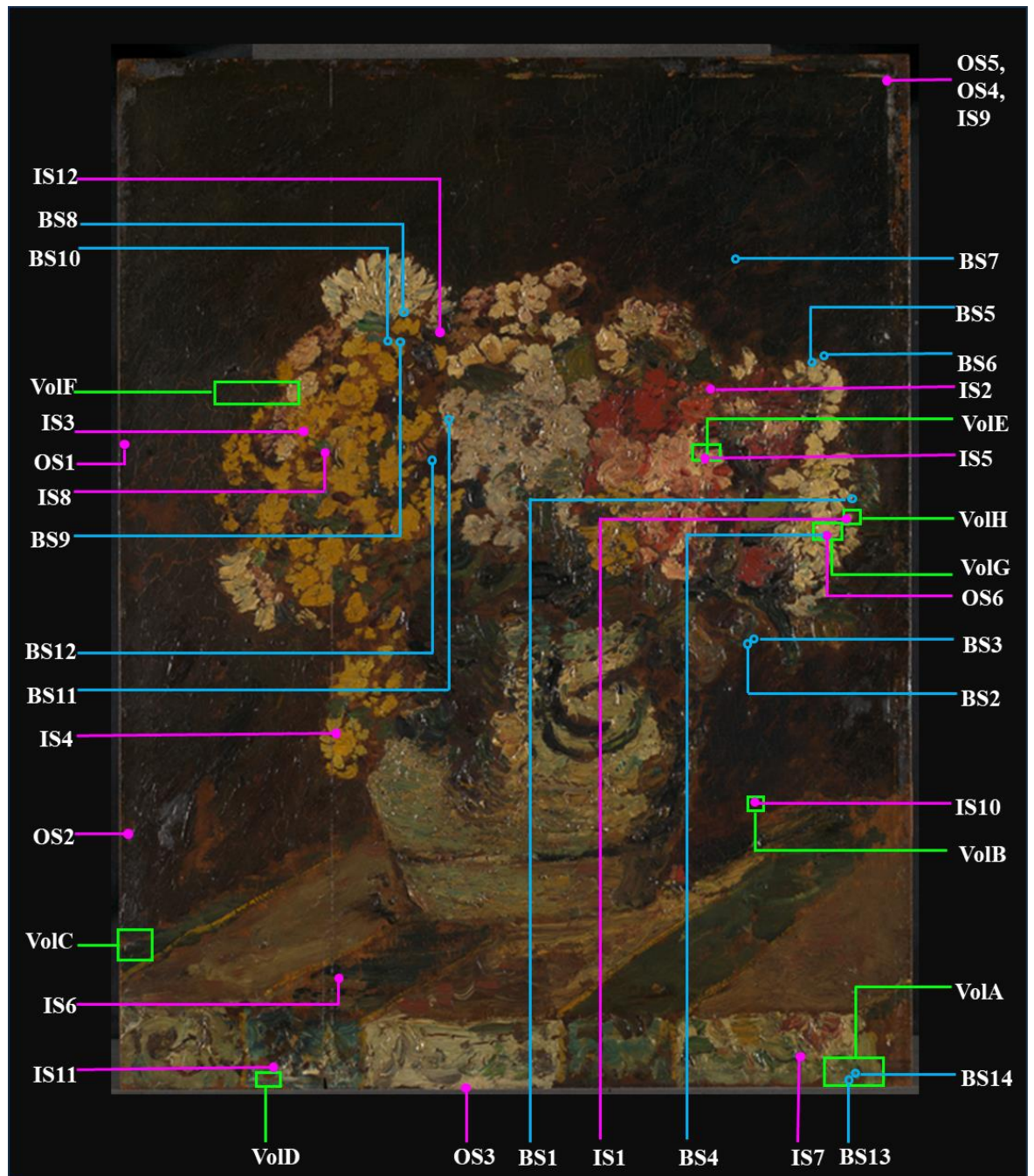


Figure 2.4.1.1. Approximate locations of data collection for physical sampling undertaken by the National Gallery (pink), OCT B-Scan Cross Sections (blue) and OCT Volumes (green) for NG5015 'A Vase of Wild Flowers' by Adolphe Monticelli © National Gallery London

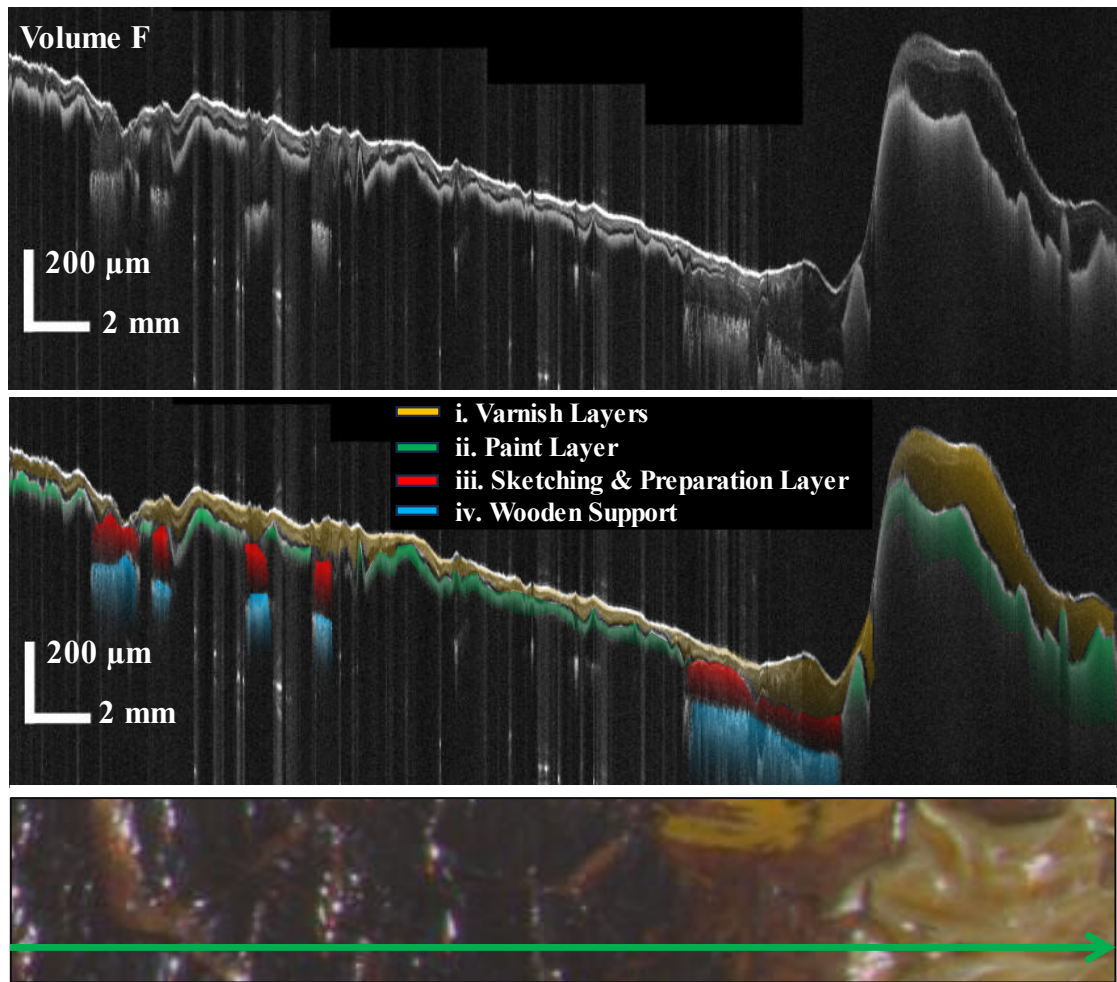


Figure 2.4.1.2. (Top) B-Scan cross section extracted from $20\text{mm} \times 5\text{mm}$ OCT volume *F* highlighted with the approximate strata of Table (2.4.1.1) (middle). The B-Scan region and direction is marked on a colour image by a green arrow (bottom)

2.4.2. *The Varnish and Paint Layers*

Across the painting, the stratigraphy of the applied varnish layers appears to be highly variable, with a lack of a clear continuity within the layer structure between scanned regions. Thus, to describe the varnish structure over the entire painting, several examples over differing locations will be discussed.

Over regions of heavy impasto such as those seen in Figure (2.4.2.1), the varnish layer structure can roughly be partitioned into two observable regions. The first and more superficial of the two regions is seen to consist of numerous thinly applied varnish layers. The number of layers within this region is unclear with the presence of additional scattering sites within the layers and inconsistencies in the interface intensity and small layer thickness, obscuring any consistency in the boundary throughout the plane. In extreme cases, this cumulates to reduce the region to the appearance of one to three semi-scattering layers.

Below this is that of a more transparent layer exhibiting within it sparsely distributed scattering sites. This layer is seen to be highly inhomogeneous in thickness over regions of heavy impasto, having pooled within the troughs to produce an optical thickness varying from 100s of microns in thickness to that of a thickness below the axial resolution of the OCT.

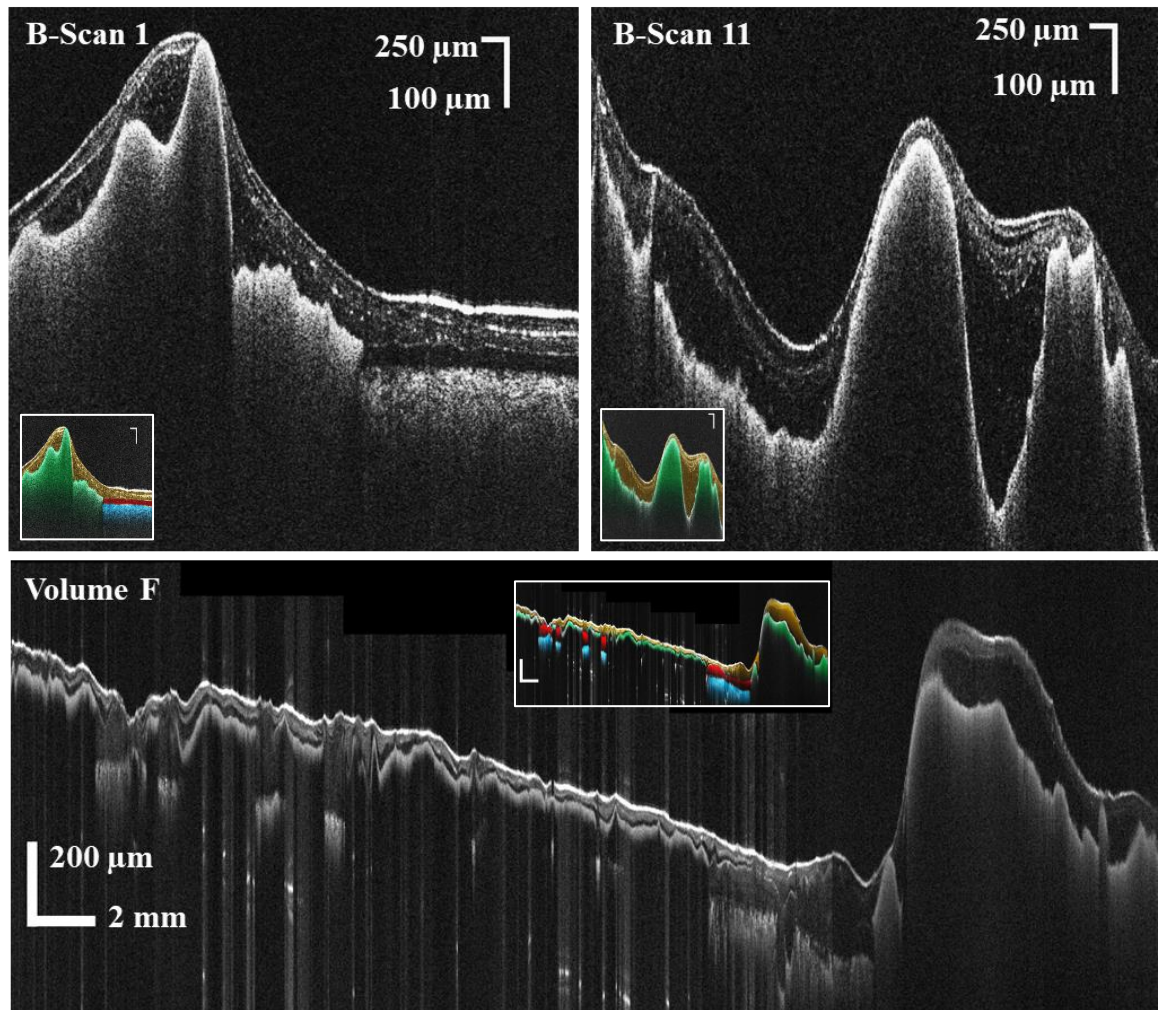


Figure 2.4.2.1. B-Scan cross sections from B-Scan 1 (Top Left), B-Scan 11 (Top Right) and Volume F (Bottom). Over the regions of heavy impasto, a thick varnish layer is visible filling the troughs of the corrugated paint surface.

This deepest varnish layer is also seen to greatly decrease in thickness over regions where the paint application is ‘smoother’ as seen in B-Scan 1 and B-Scan 11 of Figure (2.4.2.1). This is exemplified in B-Scan 10 [Figure (2.4.2.2)] in which the layer appears to be almost entirely absent with only local regions of reduced scattering indicating its presence.

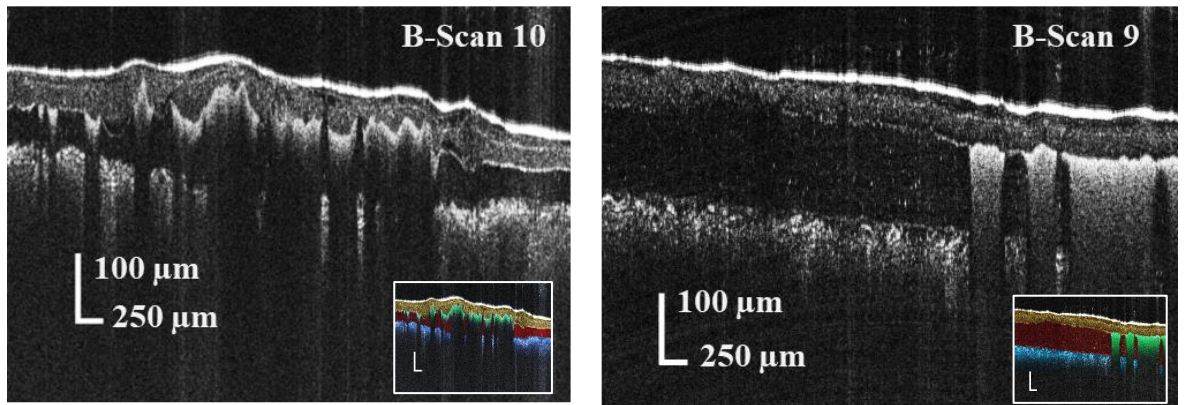


Figure 2.4.2.2. B-Scan cross sections from B-Scan 10 (Left) and B-Scan 9 (right).

Adding to the complexity of the stratigraphy, Figure (2.4.2.3) suggests that inhomogeneity in the layer thickness is exhibited by all the varnish layers applied. Here the totality of the varnish optical thickness is reduced to no greater than approximately 25μm.

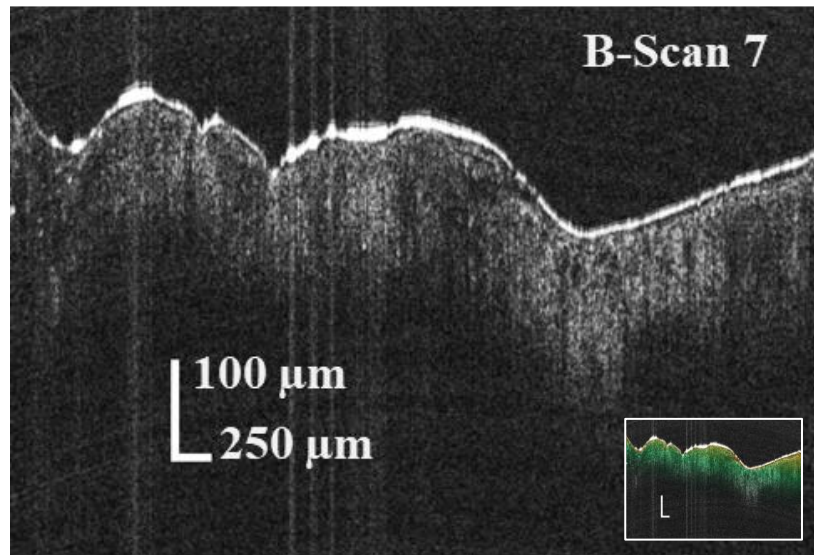


Figure 2.4.2.3. B-Scan cross section from B-Scan 7. Several thin varnish layers are applied over a semi-transparent scattering paint layer correlating to the reddish brown background region

To try to understand the composition of the varnish layers, attempts were made to sample the surface varnishes using a scalpel. The sample, OS6, was analysed at the National Gallery using Gas chromatography–mass spectrometry (GC–MS). This analysis suggested the layers were composed of a complex mixture of materials which included dammar, mastic, drying oil and a substantial quantity of pine resin. However, it was unclear whether these materials were associated with multiple different varnish applications or were combined, and indeed whether the sample contained all or only some of the surface varnish layers.

Cross referencing sample OS6 with the coincident OCT data sets of B-Scan 4 [Figure (2.4.2.4)] and Volume G indicates that the sample primarily consisted of the most superficial varnish layers and contained a much smaller proportion of the deeper varnish layer. The reduced varnish thickness in the centre of the area corresponds to the sample location with the underlying paint only being reached in a few areas. Thus, the sample contains little of the lowest, more yellowed varnish layer seen pooled in the areas of impasto. It therefore appears that the dammar, mastic and pine resins and drying oil are associated with the more superficial varnish layers, but detailed attribution of any particular material to a given layer however would come with some difficulties due the complexity of varnish stratigraphy.

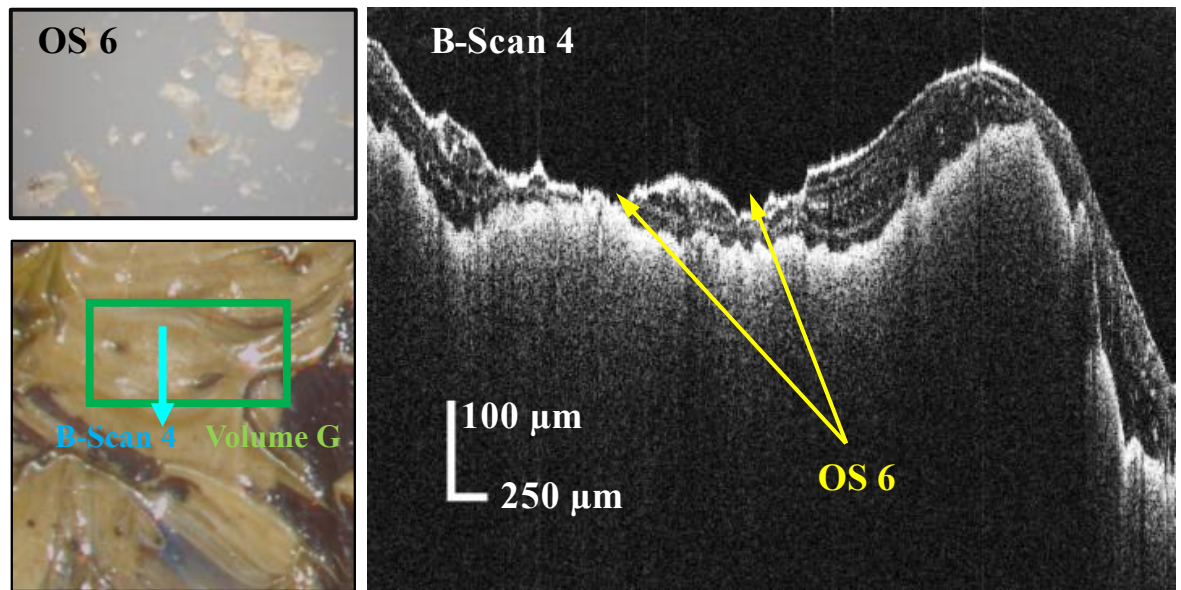


Figure 2.4.2.4. The region of sample OS 6, B-Scan 4 and 7.5 mm × 5 mm OCT Volume G (bottom left) alongside a microscopic colour image of the extracted varnish sample OS 6 (top left) and B-Scan 4 (right). B-Scan 4 covers a region of varnished white paint corresponding to a white petal on the painting. The sampled region corresponding to OS 6 is clearly visible in the B-Scan where material in the varnish layers appears to be missing.

2.4.3. The Sketching and Preparation Layers, and the Background Paint Layer

As noted above, the resinous materials found in Monticelli's preparation, sketching and paint layers were found to be similar in solubility to the varnish coatings on the painting, making any attempt to remove the degraded varnish layers challenging. This was a particular problem in the background areas of the piece where the varnish layers were in direct contact with the sketching or preparation layers on the wood or with the background paint layer. The preparation, sketching and background paint layers are also rather similar in appearance, making it hard to distinguish exactly what layers are present in each area and to establish the exact sequence of layers. It was therefore hoped that OCT could be used to help better understand and characterise the precise layer structure present in different regions of the background and thus inform decisions about potential conservation treatment approaches.

The data set OCT Volume B, for example, covers a region of background within which the sampled IS10 was collected. Figure (2.4.3.1) shows sample IS10 under both visible (top) and ultraviolet illumination (bottom). The stratigraphy visible in the sample has been labelled over a region of the sample (right).

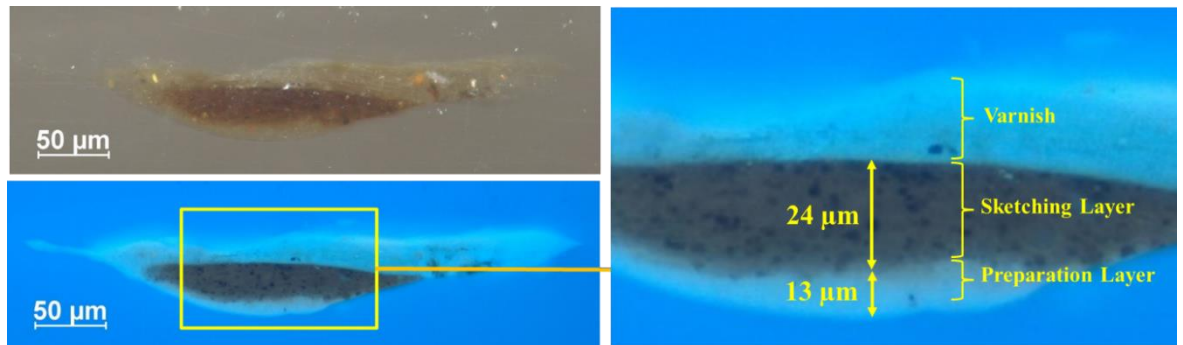


Figure 2.4.3.1. Sample IS10 under visible illumination (top left) and ultraviolet illumination (bottom left). The stratigraphy visible in the sample has been labelled over a region of the sample (right).

Within the OCT datasets, separating the preparation layer from the sketching is difficult due to the lack of a defined interface and relative transparency of the layers. While the sketching layer appears to contain marginally more pigment than the preparation layer, compositionally they are otherwise very similar [Figure (2.4.3.2)].

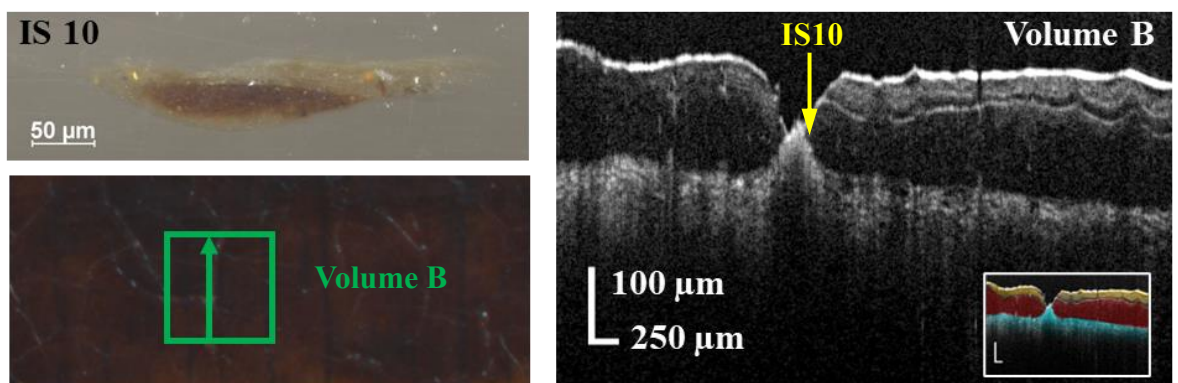


Figure 2.4.3.2. Sample IS10 under visible illumination (top left). Colour reconstruction from spectral imaging marked with $5\text{mm} \times 5\text{mm}$ OCT Volume B (bottom left) and a constituent B-Scan (right) showing the sampled region of IS10.

When looking at the concentration of scattering sites within the sketching/preparation layer, a small drop within the scattering intensity is present near to interface of the wood panel which would provide consistent layer thickness with the sketching and preparation layers seen in the sample IS10 [Figure (2.4.3.3)]. However, it is difficult to contribute this observation to an interface between the two layers, with any scattering present being so close to the noise floor.

The refractive index corrections to OCT data sets are discussed in Chapter (3.2.5). In this case refractive index for all material deeper than the air-varnish interface has been approximated at 1.5.

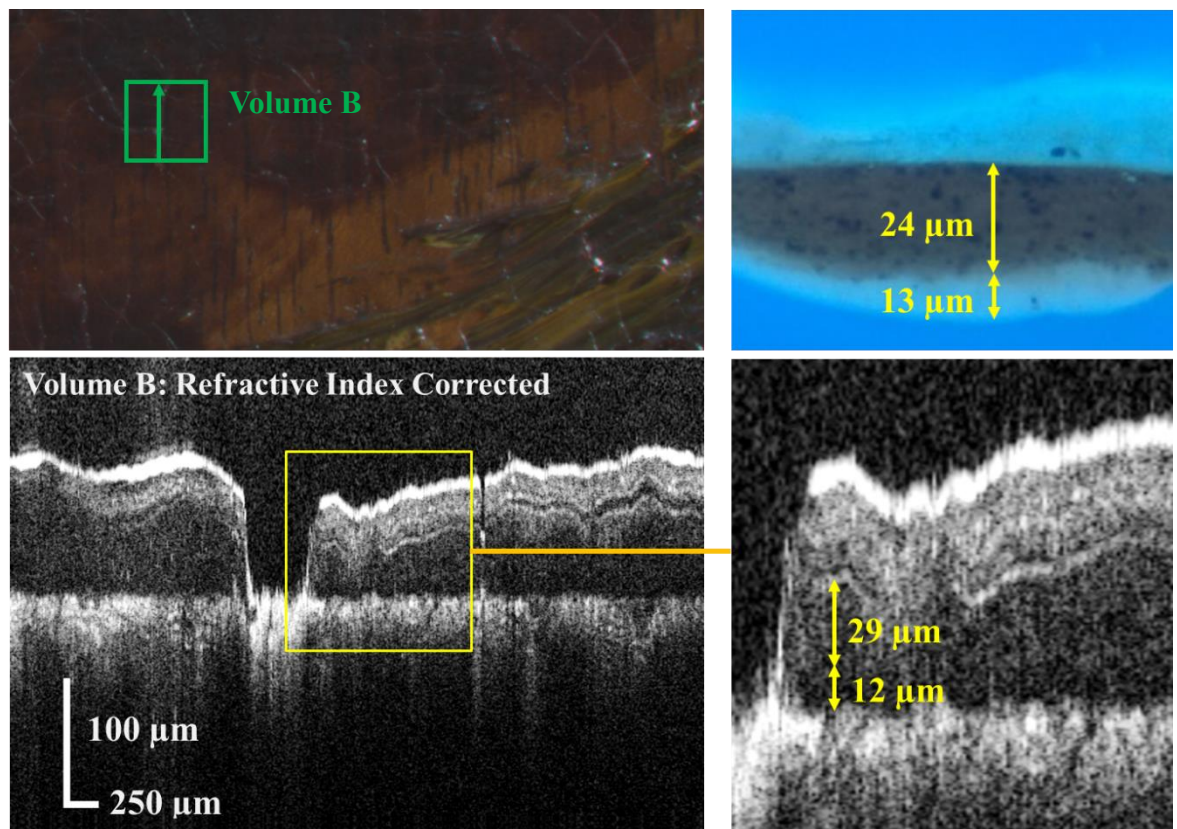


Figure 2.4.3.3. A colour reconstruction from PRISMS spectral imaging (top left) with OCT 5 mm × 5 mm Volume B marked alongside the position of the constituent B-Scan (bottom left). Comparisons between the thickness of the sketching and preparation layers within the ultraviolet image of sample IS10 (top right) and possible identification of the sketching and preparation layers in OCT Volume B (bottom right)

Figure (2.4.3.4) shows another example of a dataset collected in which the sketching and preparation layers were thought to be present, based on visual examination of the surface of the painting. Here a relatively transparent layer can be seen within the OCT data sets, directly over the wooden support, again with the presence of sparsely distributed scattering sites throughout the bulk. This may represent just the preparation layer or both the preparation and sketching layer. In this area, a non-uniform semi-transparent layer is visible within this B-Scan on the left, which may instead represent the glaze-like paint associated with the sketching layer or possibly a more highly pigmented background paint layer (of similar colour to the sketching layer). However, the lack of volumetric data sets for the region makes it difficult to establish whether the layer in question continues below the paint layer or is simply associated with the complex varnish strata. On the right the white paint layer associated with the flower petal can be seen.

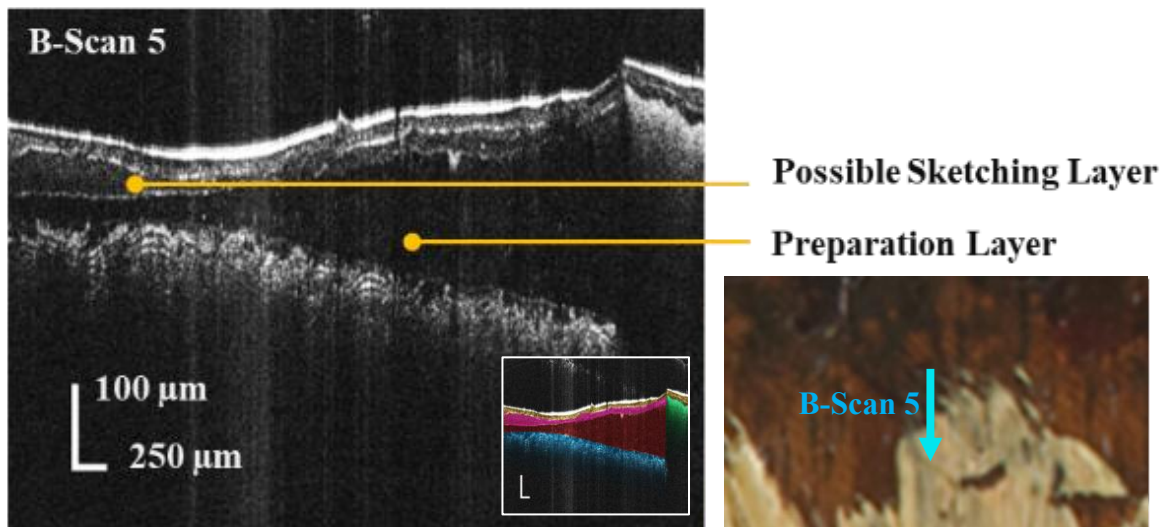


Figure 2.4.3.4. A colour reconstruction from PRISMS spectral imaging of a 15mm × 10mm region (right) with B-Scan 5 marked. B-Scan 5 (left) is expected to include the sketching layer. Here for the highlighted B-Scan, the pink region corresponds to a layer in which it is unclear if it is varnish or the sketching layer

Again, like the varnish strata, the thickness of the sketching/preparation is inhomogeneous across the painting, varying in most probed regions from the order of 10s of microns to 100s of microns [Figure (2.4.3.5)].

The extreme of this variation is visible in OCT Volume D, collected from an area of paint loss near the bottom left corner of the painting. In this area the presence of the varnish and/or preparation layers are almost entirely absent, leaving a thin transparent layer above the wooden support [Figure (2.4.3.6)].

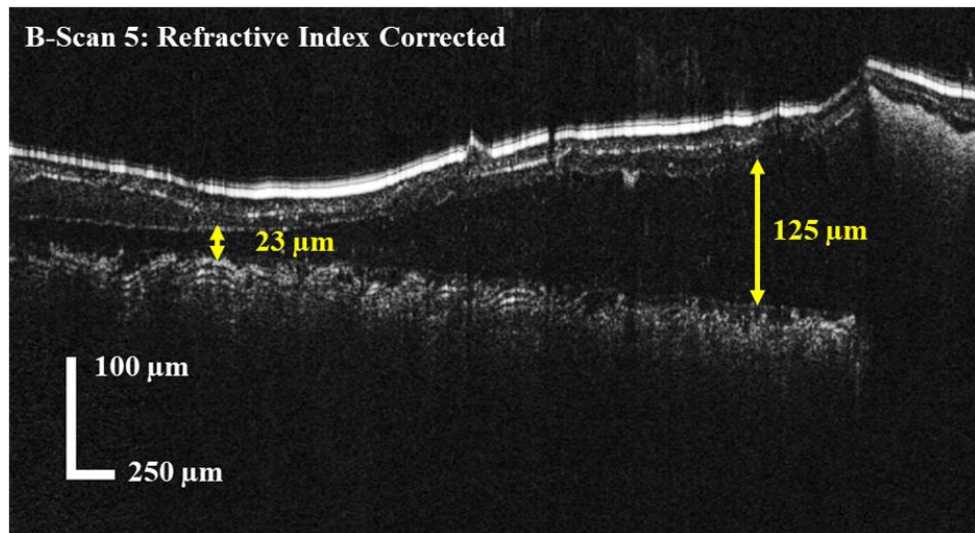


Figure 2.4.3.5. Refractive index corrected B-Scan 5

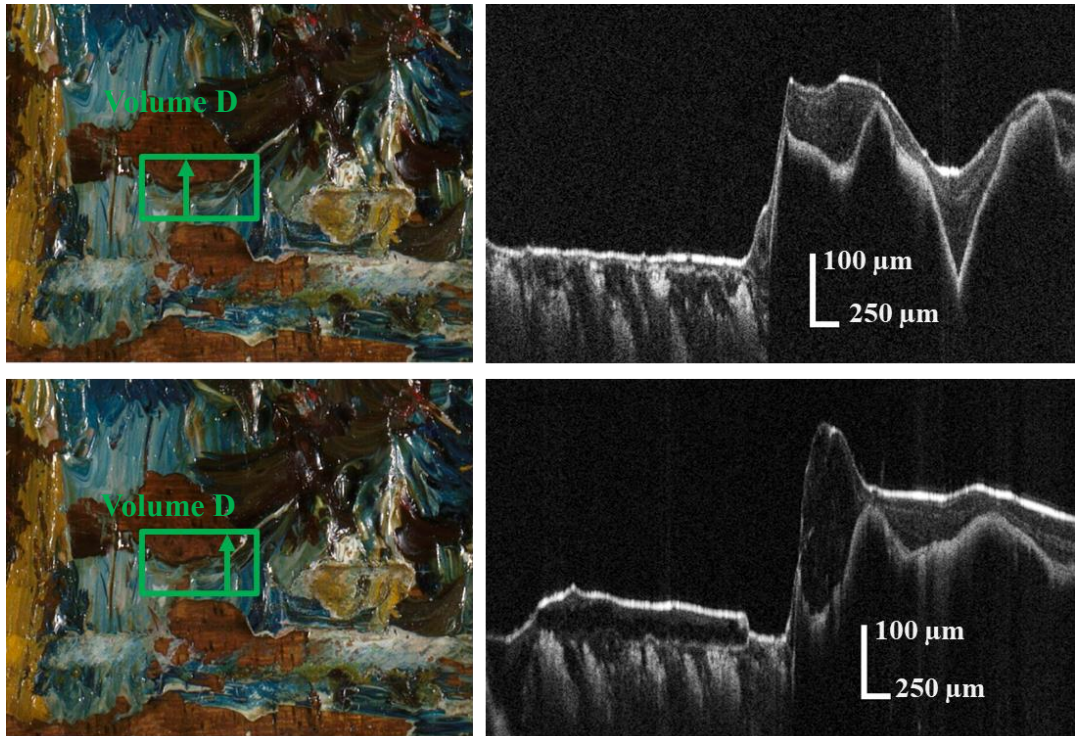


Figure 2.4.3.6. Colour images of the region © National Gallery London (left) with the 7.5 mm × 5mm region of OCT Volume D marked. Here the top left and bottom left images show the positions of the constituent B-Scans seen in the top right and bottom right respectively. Moving from left to right along the scans, both B-Scans show a region of exposed wood along side a region of impastoed paint. Over the region of exposed wood, the sketching/preparation layer is highly inhomogenous and it is unclear if it is present across the whole region

Figure (2.4.3.7) shows B-scan 6 corresponding to an area of the red-brown background paint above the flowers and where this paint layer thins to reveal the exposed wooden panel. Several varnish layers appear to be present in this area, but the interface between the red-brown background paint layer and the varnish layers is poorly resolved. This could indicate that the binding medium of the red paint and lowest varnish layer are of similar refractive index or that the varnish was applied before the background paint was fully dry, or perhaps more likely that the varnish and red paint layer have partially interacted. It is possible that the application of the varnish on top of the background paint may have slightly solubilised the background paint so that the layers then dried together. On the left of the B-scan cross section of B-scan 6 where the reddish background paint is thick, a significant increase in the layer scattering is observed, obscuring any deeper strata below. However, on the right-hand

side where the paint layer is thinner, the wood substrate and the transparent preparation layer (or possibly the sketching and preparation layers) can be seen below the background paint.

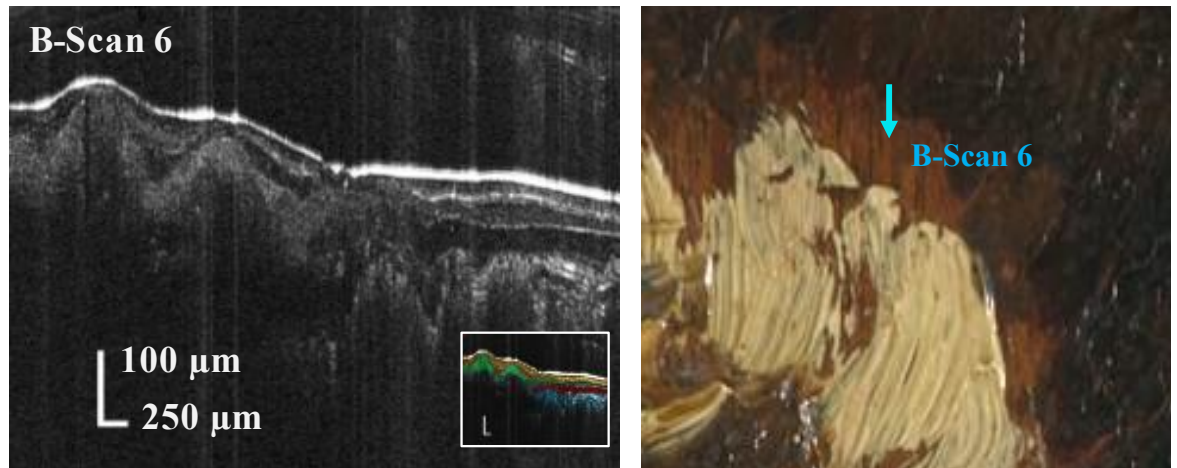


Figure 2.4.3.7. A colour reconstruction from PRISMS spectral imaging of a 32mm × 28mm region (right) marked with B-Scan 6 (left).

When comparing this data set to sample IS9, a sample taken from the background paint region in the top right-hand corner of the painting, yields a similar stratigraphy with the preparation layer, red glaze/paint region and varnish layers all visible [Figure (2.4.3.8)]. Likewise, IS9 is seen to corroborate the previous observations regarding the complexity of the layer structure with a clear inhomogeneity in the thickness of the layers and their presence throughout the sample.

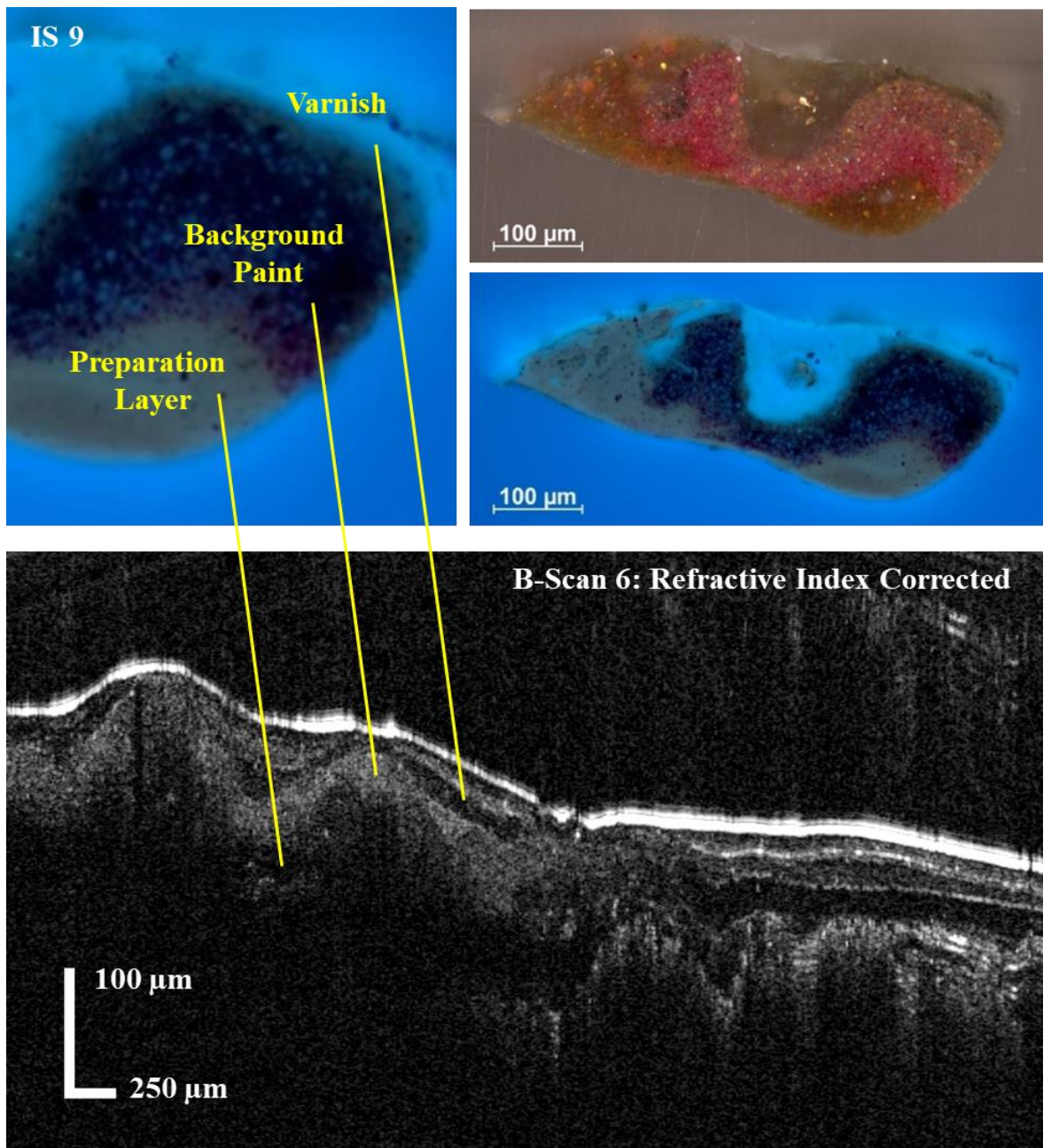


Figure 2.4.3.8. Sample IS9 collected from a region of background paint at the top right corner of the painting taken under visible illumination (top right) and UV illumination (middle right). The varnish layers, background paint and sketching/preparation layer has been marked on sample IS9 (top left) as well as on the refractive index corrected B-Scan 6 (bottom).

Similarly, Figure (2.4.3.9) shows two B-scans (B-Scan 7 and B-Scan 12) corresponding to other areas of the red-brown background paint. Again, these data sets correspond to regions where the background paint is quite thick and thus a significant increase in the layer scattering is observed, obscuring any deeper strata below. The interface between the red-brown background paint layer and the varnish layers is again poorly resolved as noted previously.

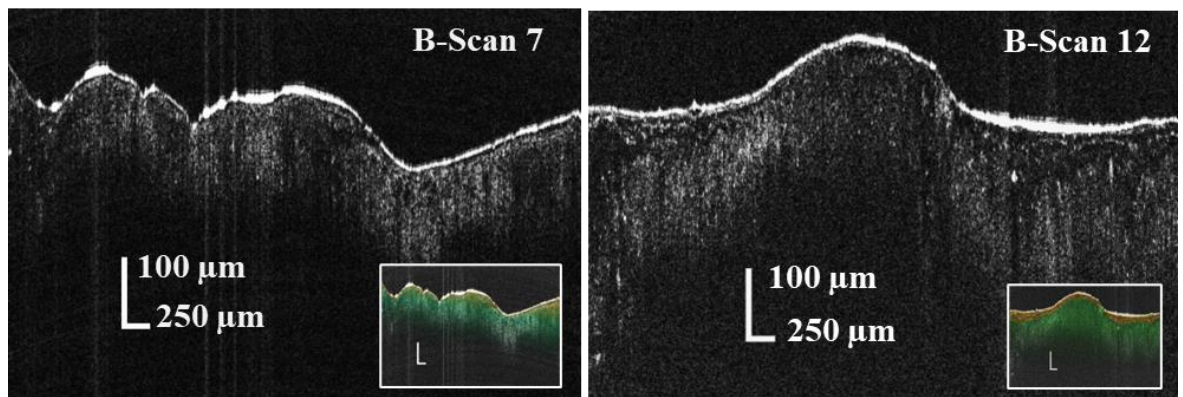


Figure 2.4.3.9. B-Scan 7 (left) and B-Scan 12 (right) corresponding to regions of background paint.

Finally of note is the presence of inhomogeneity in the thickness of the preparation and/or sketching layers as a result of cracking. Stonor et al attributed such crack formations as the product of drying defects during the creation of the artwork [44]. This is evident within the OCT Volume B seen in Figure (2.3.4.10) and discussed above, which shows the impregnation of all varnish layers into the cracked regions suggesting that the crack formations appeared at least at the time of varnish application. Interestingly, the varnish within the cracks of this region appears to be dominated in thickness by the top two varnish layers.

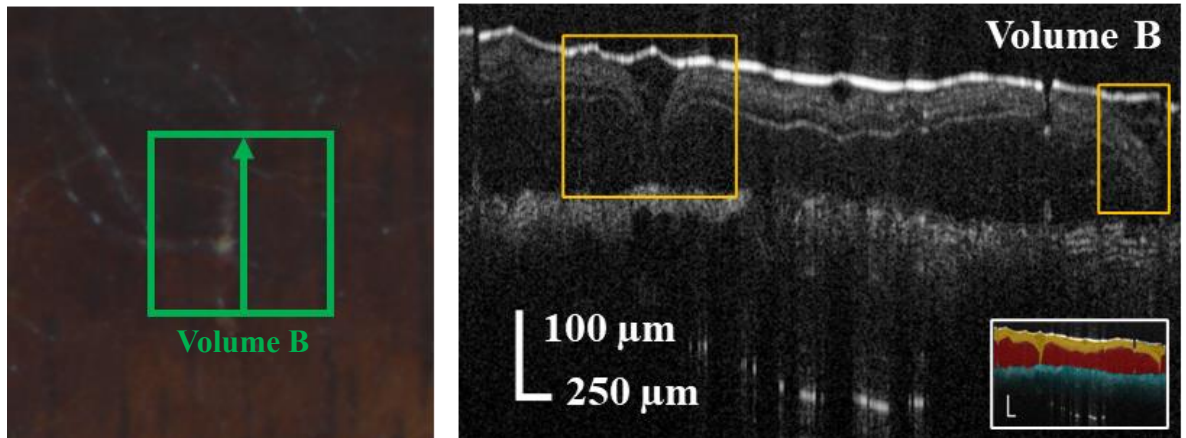


Figure 2.4.3.9 A colour reconstruction from PRISMS spectral imaging (left) with 5 mm × 5 mm OCT Volume B marked. A constituent B-Scan from OCT Volume B (right) shows the impregnation of varnish into the drying cracks of the sketching/preparation layer.

2.4.4. The Wooden Support

With Monticelli's propensity to produce his works on reclaimed furniture panels, investigation of the wooden support for evidence of remnants of coating layers associated with its previous use is of interest. Figure (2.4.4.1) displays a selection of B-Scan regions in which the wooden support is visible. OCT can be seen to unveil a complex grain pattern within the wooden support, in which large semi-transparent channels are visible as seen in B-Scan 2 and B-Scan 3. It is uncertain whether such structures can be attributed to the encroachment of resin layers into pores within the wood or are in fact a component of the wood structure. In B-Scan 3, the interfaces within the channel appear similar to what would be expected from the meniscus of a fluid layer settling within a crevice. With this, the presence of two resolvable interface within the channel could then provide evidence of a remnant coating layer on the wood panel.

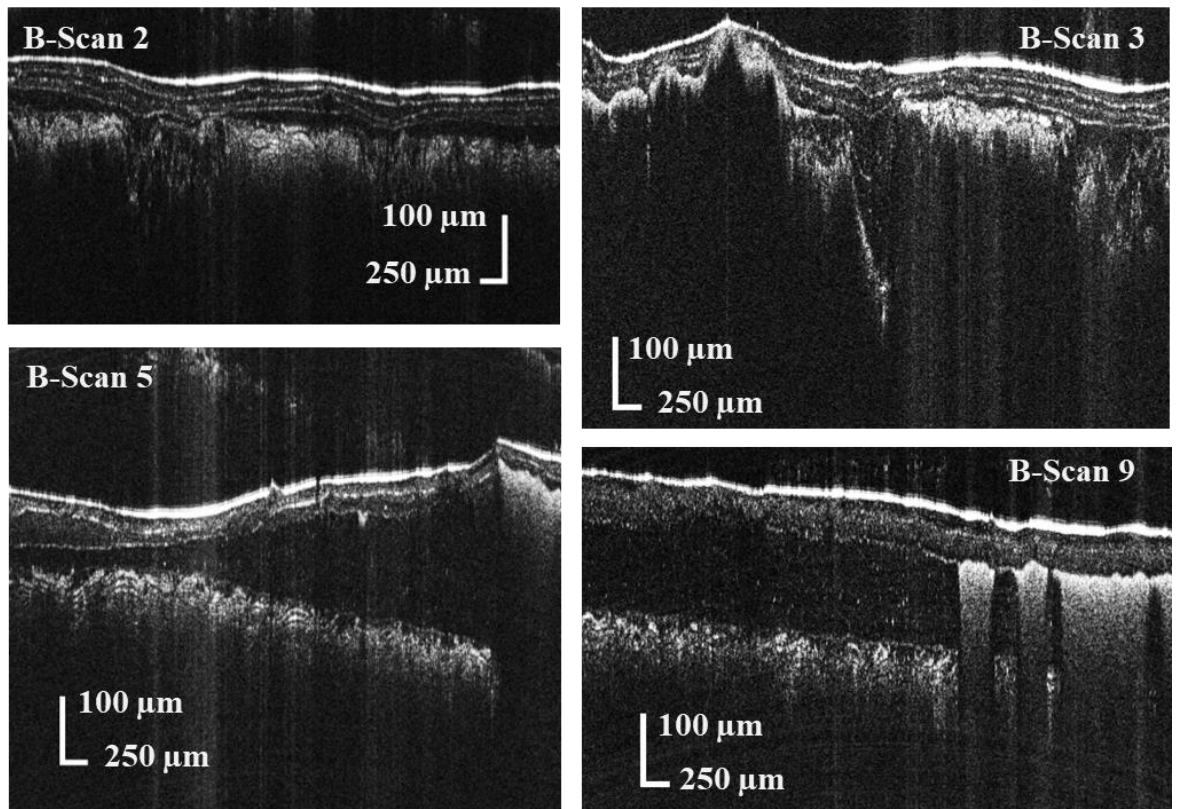


Figure 2.4.4.1 B-Scans corresponding to regions in which the wood is visible.

Alongside this, a thin transparent layer can be seen above the region of wood grain [Figure (2.4.4.2)]. Again, it is uncertain if this corresponds to a remnant coating or an extension of the wood.

Figure (2.4.4.3.a) and Figure (2.4.4.3.b) displays a cropped region of B-Scan 6 which more clearly shows the layer in question with respective A-Scan depth profile of the indicated region where the optical thickness of the layer is seen to be approximately 13μm.

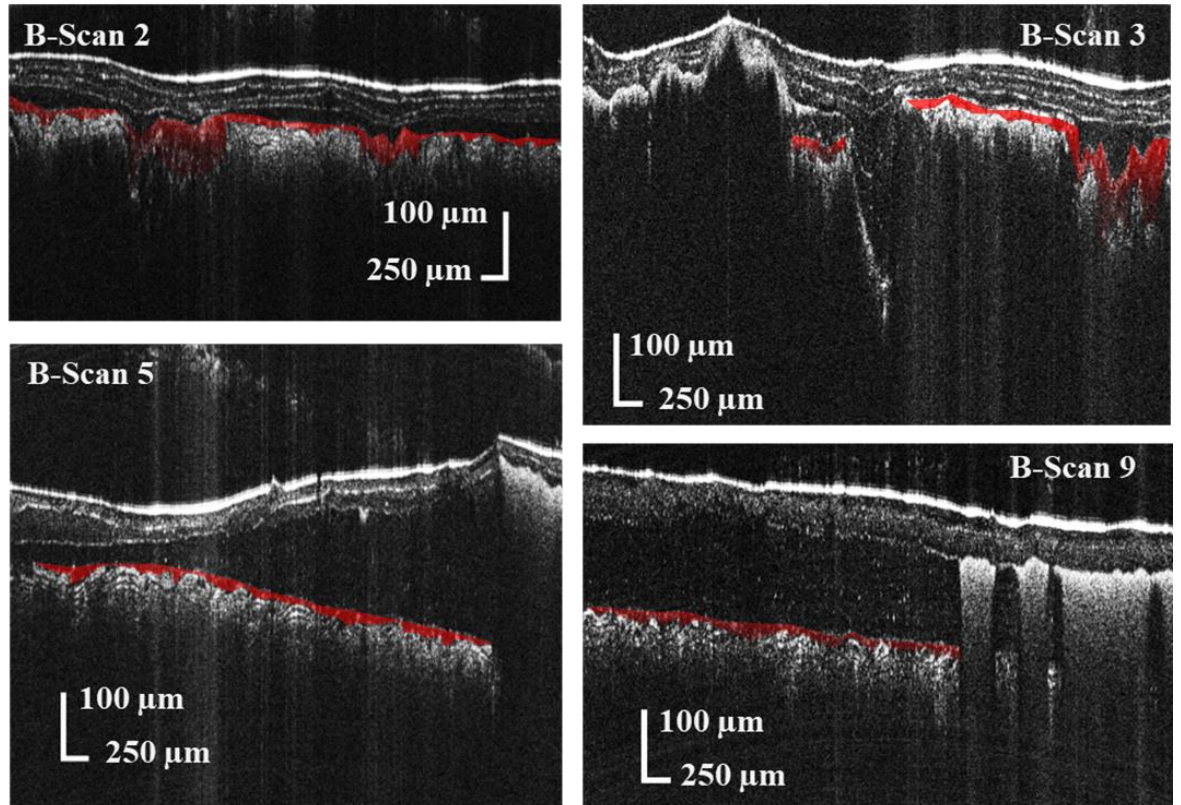


Figure 2.4.4.2 B-Scans corresponding to regions in which the wood is visible with a possible transparent layer has been marked in red

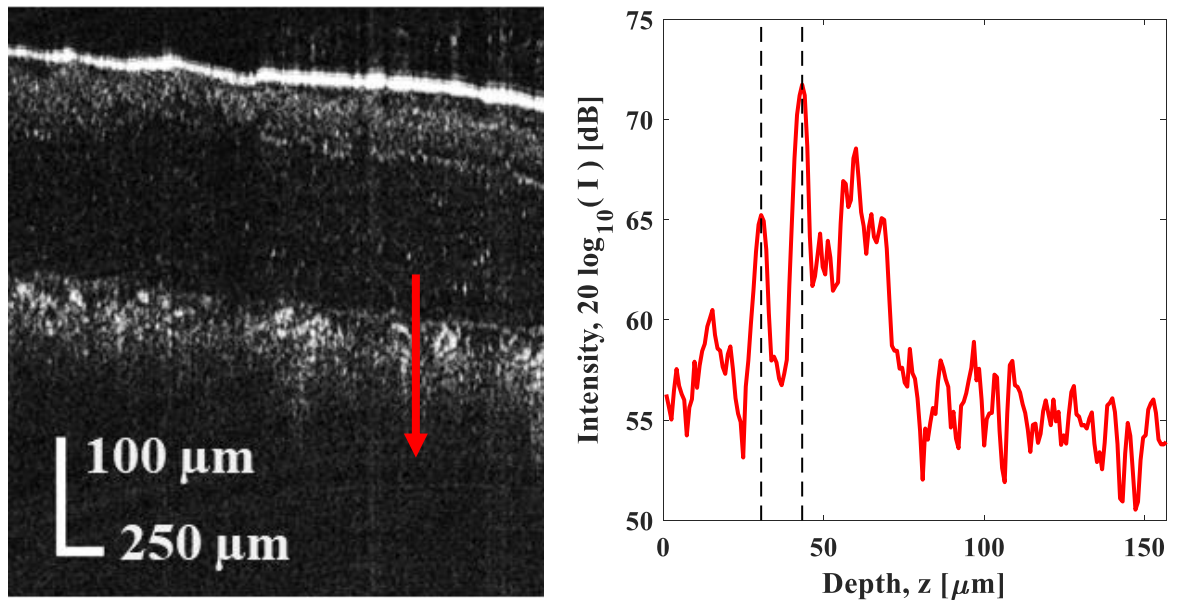


Figure 2.4.4.3 A Region of B-Scan 9 (left) with an A-Scan (right) plotted over the marked red arrow displaying as possible layer of approximately 13 μm thick.

2.4.5. Scanned Cleaning Test

To try and improve the appearance of the painting, some cleaning tests were undertaken at the National Gallery to determine whether the varnish layers could be safely thinned or removed. In an effort to avoid the use of free solvents and the potential risk of swelling paint layers, a solvent gel (benzyl alcohol in xanthan gum) was used to try and restrict the solvent action to the very surface of the painting and OCT was used to assess the effectiveness of the cleaning tests. The gel was applied to the surface, gently agitated to help the solvent action, and then cleared. Measurements of the region were then made after the clearance step. Figure (2.4.5.1) shows a B-scan across one of the cleaning test areas (the pale green tablecloth from the bottom right-hand corner of the painting). On the left of the scan is an area where the gel was not applied, and the varnish layers are intact. In the middle and right-hand side of the scan, the gel was applied with mixed results. The gel is seen to have resulted in uneven clearance of the varnish, leaving a disrupted surface. The gel also proved very difficult to work with in the areas of impasto: the tops of the areas of impasto could be cleaned (even if unevenly) but the varnish layers can still be clearly seen pooled in the areas between the peaks of the impasto.

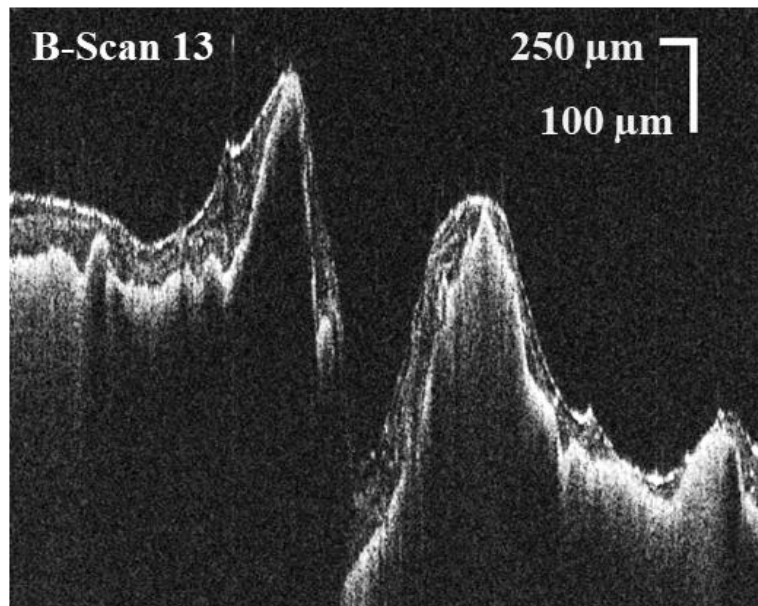


Figure 2.4.5.1. B-Scan corresponding to the gel cleaning test region. The gel resulted in uneven clearance of the varnish and left a disrupted surface as seen from the irregularity in the layer thickness.

Unfortunately, these gelled systems proved unworkable on this particular painting as the mechanical action needed to clear the gels and rinse the area further disrupted the surface of the painting. After further cleaning tests, it proved possible to clean the painting using free solvents, with the varnish layers being reduced rather than fully removed.

2.4.6. Conclusion

In order to better appreciate Adolphe Monticelli's 'A Vase of Wildflowers' and understand his influence on other artists including Vincent Van Gogh, the Conservation Department at the National Gallery were interested to understand whether it was possible to treat the painting and removed the discoloured and degraded surface coatings. Ultra-high-resolution OCT data sets collected over several areas of the painting, allowed for a much-improved understanding of the nature of the surface coatings and various semi-transparent layers present in the stratigraphy across the entire panel. Often varnish, resin-containing/ medium-rich paint and glaze layers on a painting can appear quite similar under ultraviolet light and in cross section, and OCT scanning helped to distinguish these transparent or translucent layers and how these varied across the painting.

As well as providing information about the paint stratigraphy entirely non-invasively, the OCT scanning also proved helpful where physical samples were taken for analysis. The OCT data clarified exactly which layer or layers were present within the physical samples, helping with interpretation of the resulting analytical data. OCT scanning also helped to inform decisions about how to approach the cleaning of the painting.

Although the OCT scanning provided extremely valuable new insights and allowed visualisation of the layer structure, it was still necessary to rely on physical samples to gain an understanding of the chemical composition of the different layers. In the next chapter, the combined use of OCT with spectral imaging to provide a non-invasive means by which to provide more detailed chemical information about the nature of different layers within a painting is presented.

Chapter 3: A Technique for the Extraction of Spectral Features from a Layer through the Combination of Optical Coherence Tomography and Spectral Imaging

3.1. Spectroscopy for Material Identification

3.1.1. Introduction

It is clear from the previous chapter, that OCT alone cannot provide a clear interpretation of the chemical composition of layer stratigraphy requiring cross referencing with physical sampling. The collection of physical samples however is not always possible and is often limited to the peripheries of the painting where the stratigraphy is not guaranteed to be representative of the region of interest.

This issue of interpretation becomes much more complex with the introduction of glazing layers within a painting. Semi-transparent and/or sparsely pigmented layers can in many cases appear very similar to degraded varnish [Figure (3.1.1.1)].

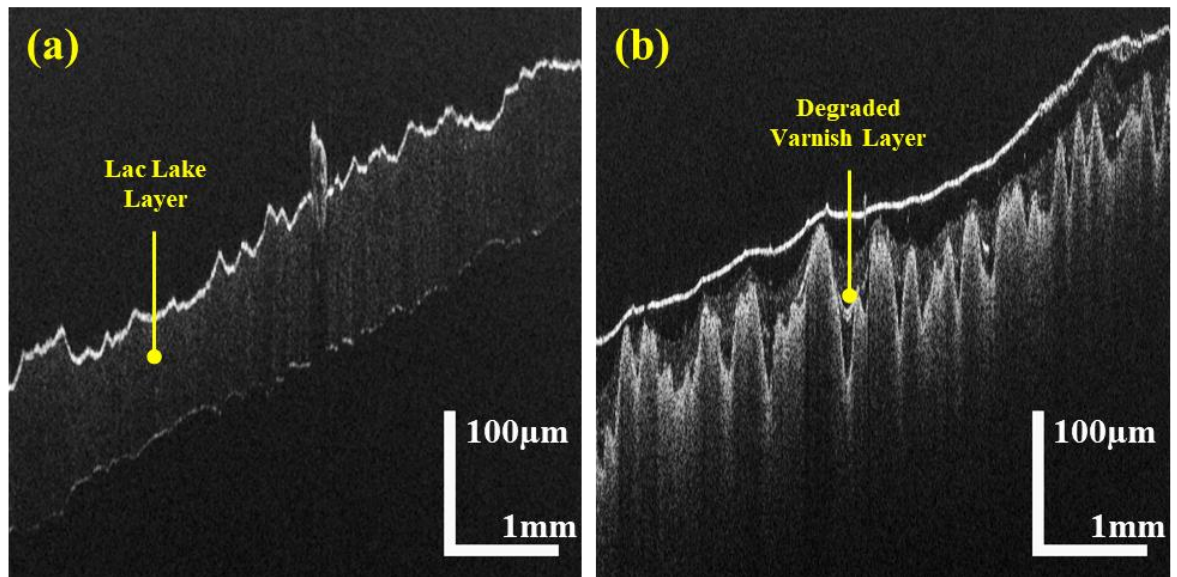


Figure 3.1.1.1 Ultra high-resolution OCT cross sections, averaged over 10 B-Scans with an image width of 5mm and image height of 400 μ m: (a) Red Lac Glaze in linseed oil applied to a glass slide, (b) Several degraded varnish layers seem on a mockup painting. Note that the second varnish layer exhibits similar scattering properties to the Lac lake layer in an OCT B-Scan.

To aid with this issue, ideally the collection of material information is required alongside the layer structure. Reflectance Spectroscopy has been a widely applied technique within the field of heritage science for material differentiation and identification [45–48].

3.1.2. 'PRISMS' Spectral Imaging

Within this chapter, spectral imaging is obtained via a mobile remote spectral imaging system PRISMS designed for applications in heritage science [49,50]. The system consists of a 14-bit Jenoptik ProgRes MFcool CCD camera, Finger Lakes instrumentation high speed ten band motorised filter wheel and Schneider Componon-S 5.6/150 lens which is axially translatable to enable focussing. The filter wheel is set to hold 10 40nm FWHM band pass filters, ranging from 400nm to 850nm in steps of 50nm enabling sequential collection of the entire lateral field of view for each spectral band to build a spectral image cube. By mounting PRISMS onto a motorised alt-azimuth mount, automatic collection over an entire painting can be achieved.

A schematic of the system set up can be seen in Figure (3.1.2.1). Here the collection of spectral imaging is carried out at 2m from the target painting to produce a 1360 by 1024 pixel ($\sim 105\text{mm}$ by $\sim 80\text{mm}$) spectral image with a lateral sampling resolution of approximately $70\mu\text{m}$. Illumination is provided by two 150 W tungsten- light sources positioned 1m away from and at a 45° angle to the plane of the image.

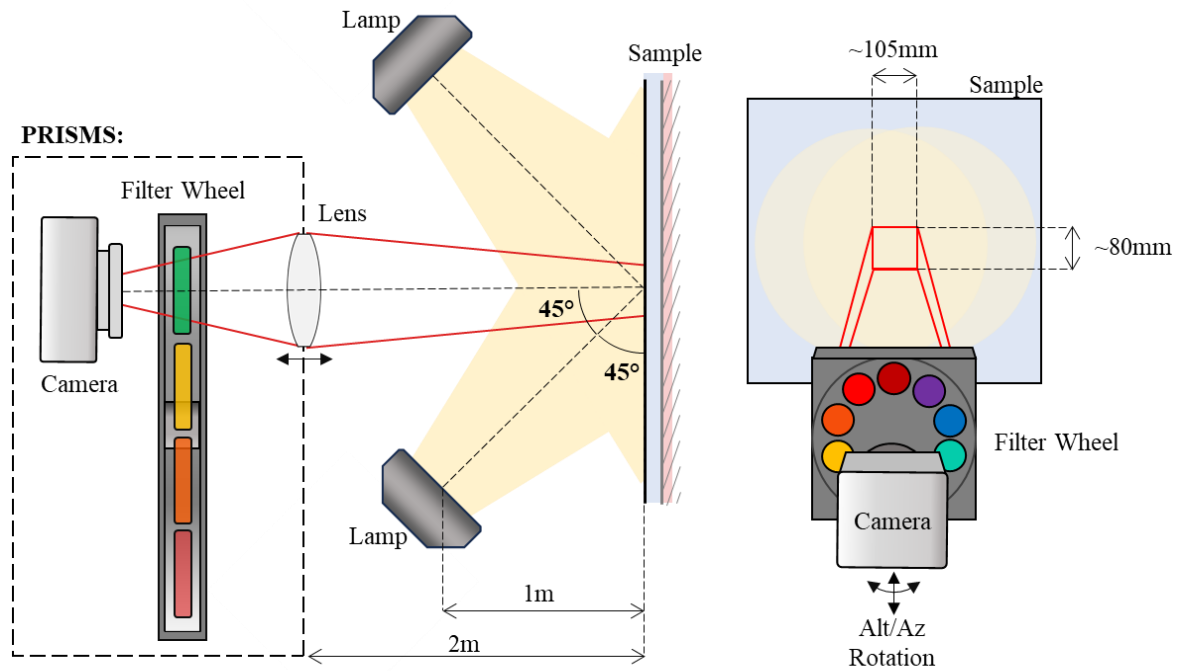


Figure 3.1.2.1 Diagram of the experimental setup for the collection of spectral images from historical paintings using the 'PRISMS' spectral imaging system.

The reflectance $R(x, y, \lambda)$ as a function of the pixel position in the image x, y and wavelength λ can be calculated from Equation 3.1.2.1 with the assumption that spectral irradiance of the illumination source is constant. Where $I_S(x, y, \lambda)$ corresponds to the counts of the sample, $D_S(x, y, \lambda)$ the dark counts at integration times $t_S(\lambda)$ for the sample and $f(x, y, \lambda)$ the flat fielding correction which corrects for spatial inhomogeneity in the illumination. Additionally, as the white standard may not encompass the entire image $I_W(m, n, \lambda)$ corresponds to the counts for pixel positions m, n in the region of the image relating to the white standard $A(m, n)$, $D_W(m, n, \lambda)$ the dark counts at the white standards

integration time $t_w(\lambda)$ and $\#A$ equalling the number of pixels enclosed within said region. $c_w(\lambda)$ corresponds to a correction factor to account for the spectrum of the white standard. For this work, the reflectance measurements are solely present as a ratio, scaled between zero and one. A reflectance of one represents a perfect reflector where 100% of the light is reflected from the sample for collection. The opposite can be said for a reflectance of zero where the incident illumination is fully attenuated by the sample or reflected away from collection.

$$R(x, y, \lambda) = \frac{I_S(x, y, \lambda) - D_S(x, y, \lambda)}{\frac{1}{\#A} \sum_{m,n \in A} I_W(m, n, \lambda) - D_W(m, n, \lambda)} \frac{t_w(\lambda)}{t_s(\lambda)} f(x, y, \lambda) c_w(\lambda)$$

Equation 3.1.2.1

Within this relation, the white standard calibration of known reflectance, in this case a spectralon 99% reflectance, enables the radiometric calibration of the collected signal. Thus, parity in the spectral irradiance of the illumination between measurements is required. To ensure this, three factors are considered. Firstly, the illumination source is allowed to stabilise for a period of 30 minutes before data collection, enabling the filaments to reach an equilibrium temperature and thus produce a constant spectral irradiance. Secondly to ensure parity between the incident irradiance on the white standard and painting, the white standard is positioned at the axial plane of the painting. Finally, to account for inhomogeneity in the illumination laterally across the painting, a flat white matt target is imaged at the locations of data collection. By multiplying the reflectance spectra by the normalised flat field images $f(x, y, \lambda)$ a correction for the lateral variation in illumination can be obtained.

For the construction of RGB colour images from the reflectance data the CIE D65, 1931 standard illuminant with a 2 degree standard observer is used here [51].

3.1.3. Relationship between Absorption and Layer Thickness

Assuming that the reflectance $R_g(\lambda)$ of the underpaint for a region can be treated as an infinitely thick layer such that light from any deeper layers cannot contribute to the collected reflectance, Beers-Lambert's law of attenuation can be applied to characterise the contributions of a given layer. Equation 3.1.3.1. gives the relationship for a single semi-transparent layer of uniform composition applied over the ground layer. Here $R(x, y, \lambda)$ and $R_g(x, y, \lambda)$ are the reflectance of the total system and ground layer respectively; $\mu_{ab}(\lambda)$ and $\mu_{sc}(\lambda)$ the absorption and scattering coefficients of the semi-transparent layer and $\tau(x, y)$ the thickness of the semi-transparent layer.

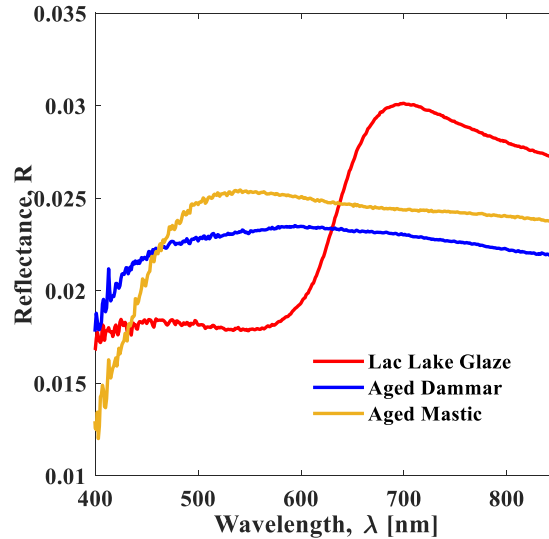


Figure 3.1.3.1. Reflectance Spectra of some typical aged varnish and glaze layers over a black background. If the black is assumed to be 100% absorbing, the reflectance given should be entirely dominated by scattering within the layer. As the reflectance from such scattering is low in magnitude (below 3% in these cases), the effects of scattering are considered negligible.

$$R(x, y, \lambda) = R_g(x, y, \lambda)e^{-2[\mu_{ab}(\lambda)+\mu_{sc}(\lambda)]\tau(x,y)} = R_g(x, y, \lambda)e^{-2\epsilon(\lambda)\tau(x,y)}$$

Equation 3.1.3.1

With this, the absorption and scattering coefficients, can be combined to produce the extinction coefficient $\epsilon(\lambda)$, characterising the total attenuation of light by the layer at a given thickness. Here we only deal with transparent layers such as varnish and glaze, which means scattering is minimal [Figure (3.1.3.1)]. As OCT can directly provide the layer structure over a given region and can demonstrate the layer of interest and ground layer are both of uniform composition, the extinction coefficient of the layer can be extracted through a linear relationship [Equation (3.1.3.2)] provided there is sufficient variation in the layer thickness [52–54].

$$\ln[R(x, y, \lambda)] = -2\epsilon(\lambda)T(x, y) + \ln[R_g(\lambda)]$$

Equation 3.1.3.2

For highly scattering layers, as it is often the case, the above equation breaks down, but such layers will be excluded for analysis by examining OCT B-Scan cross section for how intense the scattering is.

3.2. Segmentation of OCT stratigraphy

3.2.1. Introduction

Given the above dependency on the extinction of a given layer on the layer thickness, the automated extraction of a global thickness map is desirable and thus image segmentation of the layer structure within an OCT volume is required.

In the simplest approaches to OCT segmentation, layers are extracted through the calculations of the local maxima within a region of interest under the assumption that a given layer interface will correspond to a peak in the A-scan depth profile [27]. Such a method,

however, struggles with more complex structures. With the extracted interface depth at a given lateral position lacking any dependency on its neighbouring positions, continuity within the extracted layer structure can be lost.

The segmentation of layer structures within OCT data sets is however a well-established and rich field of study, with algorithms primarily targeted toward ophthalmology [55–57]. This work applies a common and simple approach to volumetric OCT segmentation based on the minimisation of energy within a weighted graph [58] with workflow seen in Figure (3.2.1.1)

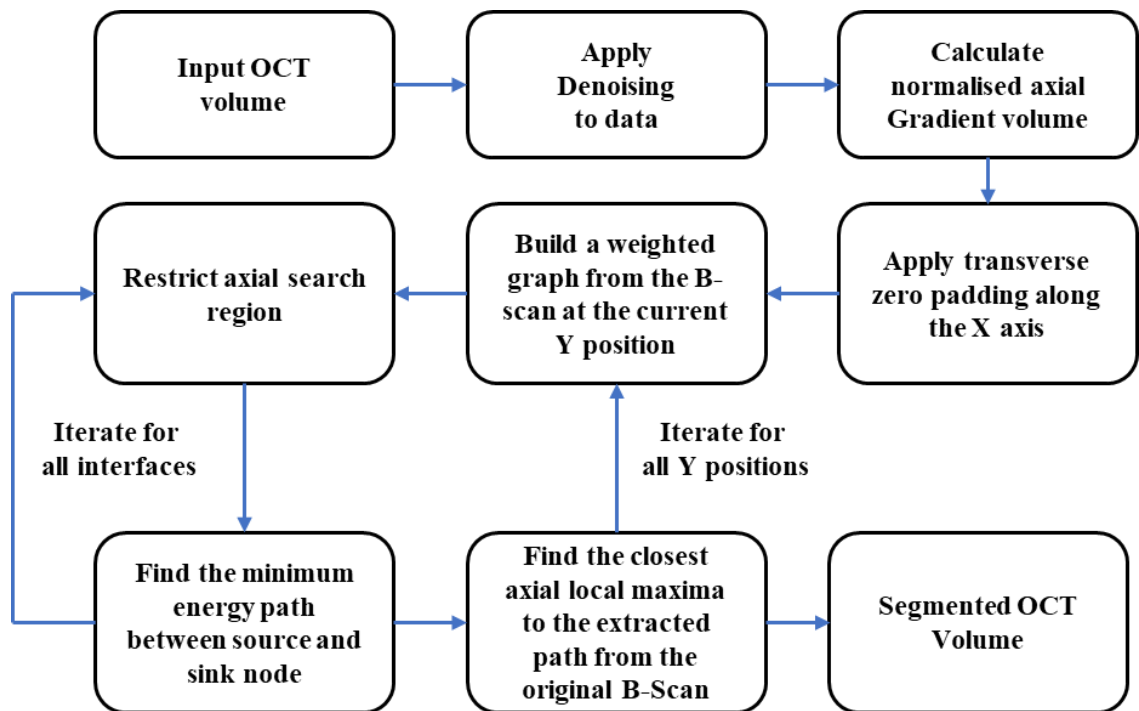


Figure 3.2.1.1. Workflow for the segmentation process for an OCT volumetric cube

3.2.2. OCT Volume Denoising

With this implementation of segmentation, edges are extracted from the gradient image of the volumetric cube. With this method, the derivative of the pixel intensities in relation to its neighbours are calculated. This has the implication of greatly magnifying high frequency

variation and thus magnifying speckle and noise variations. This in practice results in a minimisation in the interface contrast and thus often results in significant errors within an extracted interface.

Ideally, denoising would be obtained during data collection through the time averaging of multiple A-scans to reduce contributions of excess noise. In practice, however this may not be achievable due to the limitation on collection time when dealing with large collections or the introduction of interface smearing when vibration is present.

For this work two techniques have been applied depending on the scenario, the first being the application of a simple median filter to the data set with an arbitrary kernel size. This had the major advantage of being a time efficient method of reducing speckle and background noise, however, it often came at a greater expense in reductions in resolution when addressing cases of high speckle noise when scattering layers are present.

To improved denoising in situations of increased speckle, TNode filtering [59], a probabilistic based nonlocal mean filtering [60] where speckle statistics are used with a non-local means filter designed for use on OCT volumetric data, is applied. The probability of two given regions within the volume (patches) being the same underlying object, but with different realisations of noise, is used to inform a weighted mean. This method again is limited in its ability to preserve the fine details but performs much better at preserving edges than the median filter.

For this work, the kernel sizes of the applied filters were chosen entirely based on the preservation of axial resolution and the minimisation of processing time and as such likely do not provide optimal results for denoising. Figure (3.3.3.1) shows a comparison between an unfiltered B-Scan, median filtered B-Scan with a 3 by 3 by 3 kernel and TNode filtered B-Scan with a 3 x 3 x 3 search patch and 7 x 7 x 3 similarity patch.

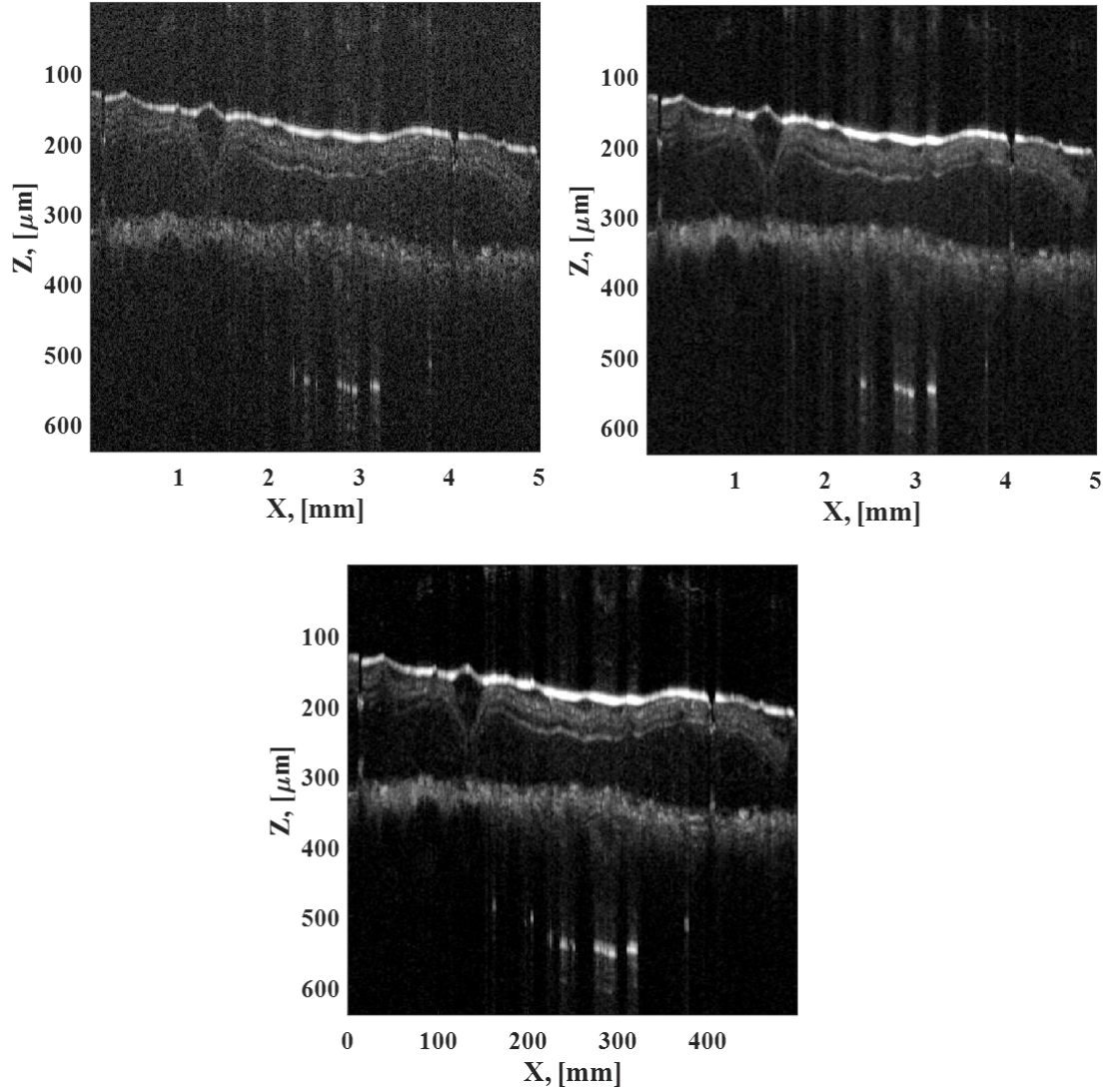


Figure 3.2.2.1. a) A constituent B-Scan from OCT Volume B of NG5015 alongside b) a median filtered B-Scan with a 3 by 3 by 3 kernel and TNode filtered B-Scan with a 3 by 3 by 3 search patch and 7 by 7 by 3 similarity patch.

The filtered data cube is not only useful in segmentation but can be applied to obtain a rudimentary denoising in the OCT data sets $I_{DN}(z, x, y)$. To do so, high frequency information from the original volume can be reintroduced into the data sets with an arbitrary weighting α through Equation 3.2.2.1. when the datasets are in decibel space. Here $I_F(z, x, y)$ corresponds to the intensity in decibels of filtered OCT data sets and $I(z, x, y)$ corresponds to the original intensity values of the OCT data sets.

$$I_{DN}(z, x, y) = I_F(z, x, y) + \alpha[I(z, x, y) - I_F(z, x, y)]$$

Equation 3.2.2.1

Figure (3.2.2.2) displays a raw B-Scan alongside a 100-scan time averaged B-Scan and denoised B-Scan for a test sample with a transparent blue paint and varnish collected via the hybrid OCT discussed in Chapter (4.4.6). Here an increase in signal to noise is visible in the time averaged data set [Figure (3.2.2.2.b)], but intensity variation in the layer from speckle remains unaddressed. The image denoising in Figure (3.2.2.2.c) via the TNode method is seen to reduce the weighting of speckle within the layer.

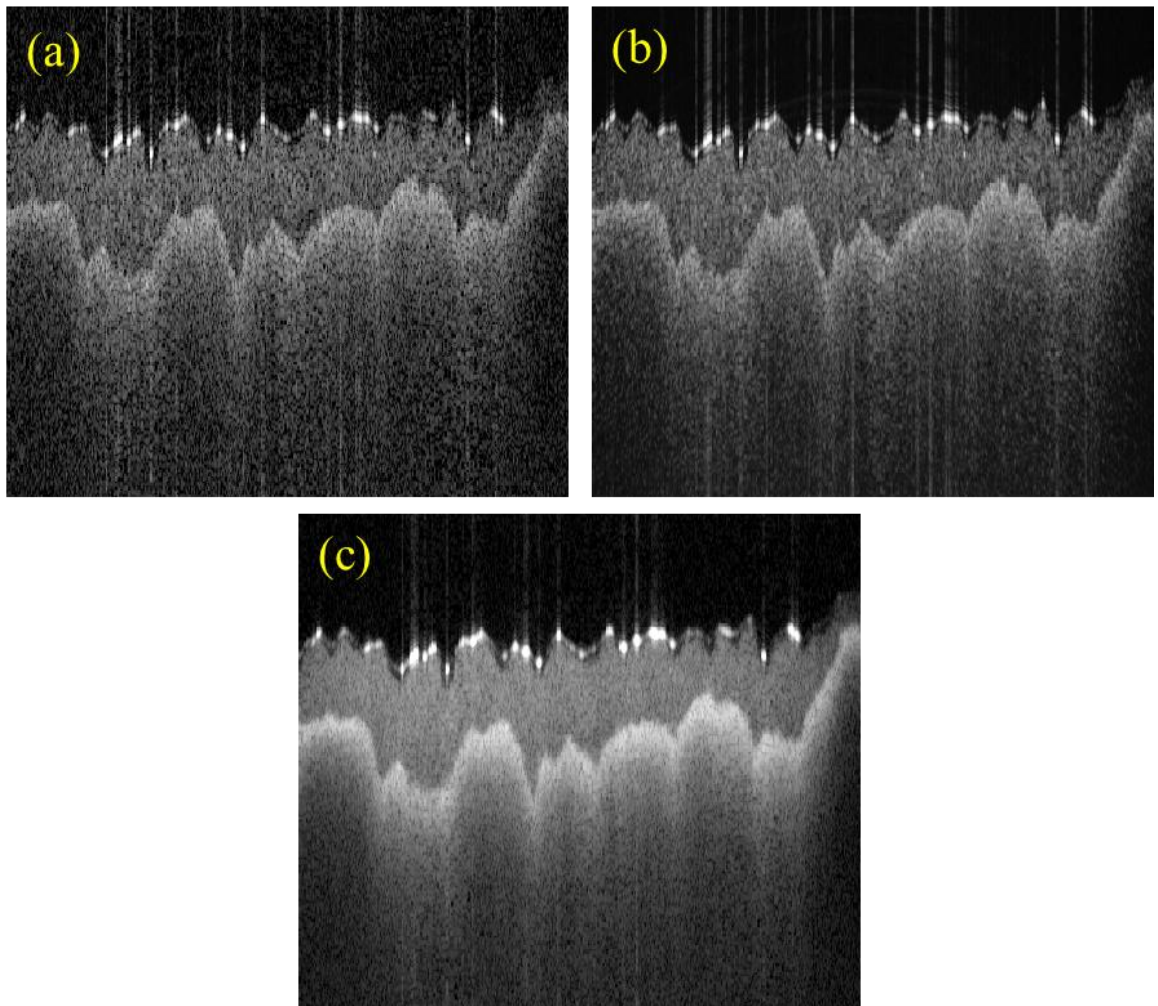


Figure 3.2.2.2. a) A single B-Scan b) a 100-scan averaged B-Scan and c) denoised B-Scan for a sample of varnished Blue paint collected with the hybrid instrument of Chapter (4.4.6)

3.2.3. Graph Based Segmentation

The edge detection in this work is based on a Sobel operation in which volumetric gradient image cube are obtained through the discrete convolution of the denoised data cube with a three-dimensional Sobel kernel $K(i, j, k)$ seen in Equation 3.2.3.1. Here (i, j, k) correspond to the z, x and y directions of OCT volume. The kernel restricts gradient contributions to only involve adjacent axial pixels to avoid lateral gradient components associated with changes in the background floor.

$$K(i, j, k) = \begin{cases} \begin{bmatrix} 0 & 0 & 0 \\ 0 & 0 & 0 \\ 0 & 0 & 0 \end{bmatrix}, & k = 1 \\ \begin{bmatrix} 0 & 1 & 0 \\ 0 & 0 & 0 \\ 0 & -1 & 0 \end{bmatrix}, & k = 2 \\ \begin{bmatrix} 0 & 0 & 0 \\ 0 & 0 & 0 \\ 0 & 0 & 0 \end{bmatrix}, & k = 3 \end{cases}$$

Equation 3.2.3.1

The normalised gradient image cube is obtained via Equation (3.2.3.2). Here for the image convolution edge conditions, the data cube is simply padded with the adjacent pixel values and cropped post convolution to return the gradient image to the original dimensions.

$$G_z(z, x, y) = \frac{K(i, j, k) * I_F(z, x, y)}{\max[K(i, j, k) * I_F(z, x, y)] - \min[K(i, j, k) * I_F(z, x, y)]}$$

Equation 3.2.3.2

The gradient cube $G_z(z, x, y)$ is then extended along the x direction with a single element zero padding at the beginning and end of the cube. At a given y position in the gradient cube, a weighted graph $g(N, E)$ is derived with nodes $n \in N$ positioned at all x and z pixel locations. Edges (i, j) with weights $w(i, j)$ are then derived between all spatially adjacent

nodes i and j as seen in Figure (3.2.3.2). In this case nodes are labelled such that the node $n = z_n + \#Z(x_n - 1)$ and thus $N = \{n: 1 \leq n \leq \#Z\#X\}$ where $\#Z$ and $\#X$ are the number of pixels in their respective dimensions. Weightings can be obtained via Equation 3.2.3.3.

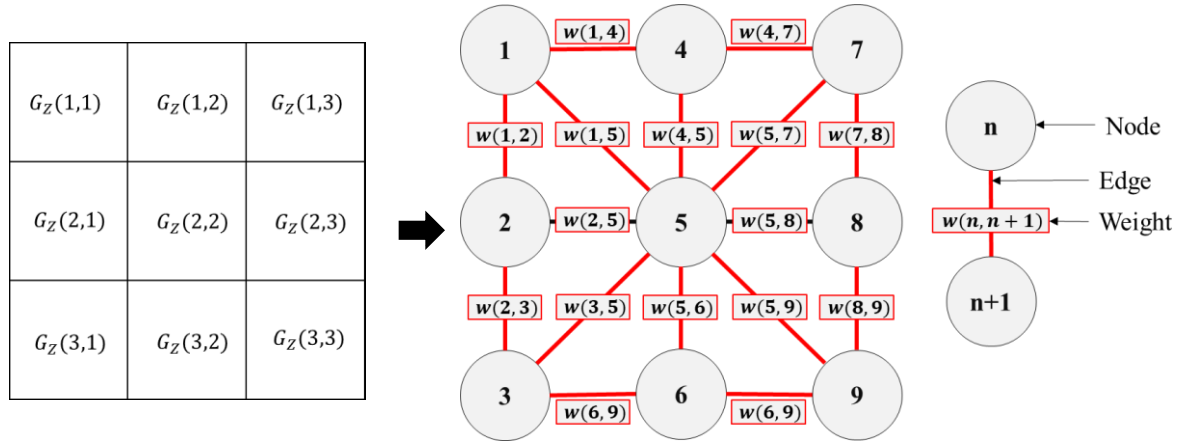


Figure 3.2.3.1. A diagram of the conversion from a gradient image to a weighted graph in which pixels correspond to nodes with weighted edges connecting them.

$$w(i, j) = \begin{cases} 2 - (G_z(z_i, x_i) + G_z(z_j, x_j)) + 10^{-5}, & (1 < x_i < \#X) \\ 10^{-5}, & ((x_i \vee x_j) = (1 \vee \#X)) \end{cases}$$

Equation 3.2.3.3

With this edge weightings become minimised when the gradient values of the respective nodes are both large and thus a local minimisation in the edge weightings is expected to be visible along an interface edge. With this the minimum energy path across the Gradient B-scan can then be calculated between the source node $n = 1$ (corresponding to the top left pixel of padded Gradient image) and destination node $n = \#Z\#X$ (corresponding to the bottom right pixel of padded Gradient image) through a Dijkstra's shortest path algorithm [61] in order to find an approximate interface position.

Here weightings are set to an arbitrary minimum weight for edges connecting to the nodes of padded pixels. This enables low energy movement along the axial plane to and from the source and destination nodes, reducing bias in the path minimisation due to the axial

positions of the source and destination nodes. The process can be iterated for multiple interfaces by removing edges relating to the calculated path from the graph and restricting the search region and then repeating the process for every y position to build a set of 2 dimensional surfaces relating to the interface positions for each interface.

As the extracted surface should correspond to axial maxima positions within the denoised gradient image, the position of the interface is expected to be offset from the true interface. This is simply addressed by finding the closest axial local maxima position within the original OCT volume to the extracted surface for each lateral position.

3.2.4. Cases of Failed Segmentation

The above implementation of stratigraphy segmentation works well for layer structures with well-defined uniform interfaces which do not display extreme variations in depth e.g. in regions without cracking or heavy impasto. Erroneous segmentation results are likely to be present in the following situations.

In cases of corrugated interfaces with larger variations in depth, two key issues become present. Firstly, variations in interface depth throughout the B-scan will result in a greater number of graph edges associated with that interface. This increase in edges can become problematic when the total weighting of the interface path becomes greater than that of an alternative route. In such cases the shortest path algorithm will extract an erroneous segmentation for such a region.

This issue is greatly compounded for situations involving specularly reflective corrugated interfaces. Here when the plane of the interface is orientated away from the optical axis, a large component of the incident light will reflect away from collection, resulting in the reduction of interface intensity and thus an increase in the total weighting of the interface path.

For this work, situations involving these issues have been excluded or in cases where such regions are of particular interest, segmentation has been achieved through the flattening of data sets via an interpolated surface based on manually selected interface positions before the extraction of interfaces via the graph-based minimisation method. However, this is a non-ideal solution of addressing such issues due to the time intensity of manual selecting points over the entire span of the OCT region.

Solutions to this interface corrugation issue have been suggested such as in Callewaert et al [62,63]. Here correct interface positions are extracted through upshifting the initial segmentation and increasing the depth position of a given lateral position until its intensity is within an arbitrary range from a mean intensity of the initial segmentation. However, this method works on the basis of the initial segmentation being mostly correct and that the interface intensity remains relatively homogeneous across the lateral plane.

3.2.5. Thickness Mapping

With the segmentation and extraction of interface locations throughout the volume, the layer thickness of a layer $\tau_i(x, y)$ can simply be extracted via the difference in the axial positions of adjacent interfaces normalised by the layer group refractive index [Equation 3.2.5.1]. Here $Z_{i,i+1}(x, y)$, $Z_{i-1,i}(x, y)$ and n_{g_i} correspond to the top interface, bottom interface, and the group refractive index of the layer i . As the layer refractive index is unknown, a typical group refractive index of 1.5 is applied within this work [64,65]. This was deemed suitable for this work as glazing layers are expected to contain pigments with a refractive index that closely matches the binding medium and/or expected to be sparsely pigmented.

$$\tau_i(x, y) = \frac{(Z_{i,i+1}(x, y) - Z_{i-1,i}(x, y))}{n_{g_i}}$$

Equation 3.2.5.1

The segmentation procedure was applied to the volumetric data from two of the scanned areas, volumes G and B, from Adolphe Monticelli's, 'A vase of Wild Flowers' (NG5015), the painting from the National Gallery described in section 2.2.4.2.

In Figure (3.2.5.1), the extraction of the entire varnish thickness, over a region of Volume G collected from the surface of the white paint depicting a flower. Volume G covers an area where attempts were made to sample the surface varnishes using a scalpel for use in gas chromatography-mass spectrometry (GC-MS) analysis.

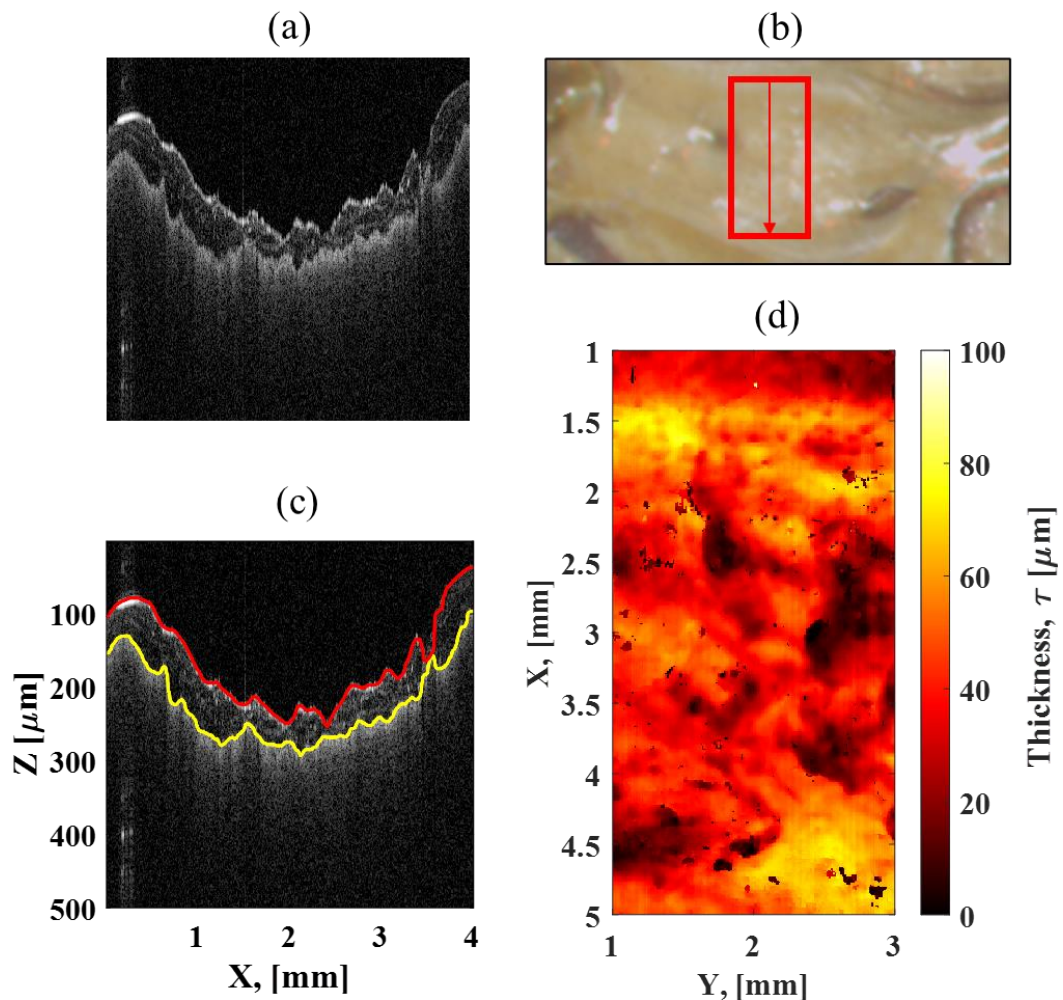


Figure 3.2.5.1. a) A B-Scan of OCT Volume G from NG5015. b) A colour reconstruction from PRISMS spectral imaging with the region of the extracted varnish thickness map marked. c) The segmented B-Scan extracting the combined varnish layers. d) The extracted thickness map for the combined varnish layers for OCT Volume G.

The segmentation provides a measurement of the inhomogeneity in the varnish layer resulting from the manual sampling of the varnish, showing a variation in the layer thickness of $\sim 100\mu\text{m}$. The reduced varnish thickness in the centre of the area can be seen, corresponding to the sample location. From this thickness map it can clearly be seen that the sampling has disrupted the surface varnish and partially removed the more superficial varnish applications, but the underlying paint has only been reached in a few areas (corresponding to locations where the varnish thickness is zero) meaning that the sample analysed by GC-MS analysis only includes a limited amount of material from the lowest varnish layer as discussed in Chapter 2.

With Volume B, a key area of interest is the impregnation of the varnish layers into the preparation/sketching layers. Thus, the segmentation here has been performed such that the total varnish thickness and the combined thickness of the sketching and preparation layers have been extracted [Figure (3.2.5.2)]. From Figure (3.2.5.2.d), the segmentation of the varnish seeping into the crack is seen to have not been completely successful with an underestimate of the varnish thickness and overestimate of the preparation/sketching layer thickness in the region. This is simply due to the low SNR of interfaces within the region with the extreme interface angle of the varnish within the crack relative to the optical axis, the similar refractive indices of the varnish and preparation/sketching layers, and attenuation in the layer from absorption and scattering all acting to reduce the interface signal. The thickness maps of Figure (3.2.5.2.e) and Figure (3.2.5.2.f) do however provide a qualitative view of the thickness variation in the varnish layers; and combined thickness of the sketching and preparation layers respectively and clearly demonstrate the varnish layers infilling the crack pattern.

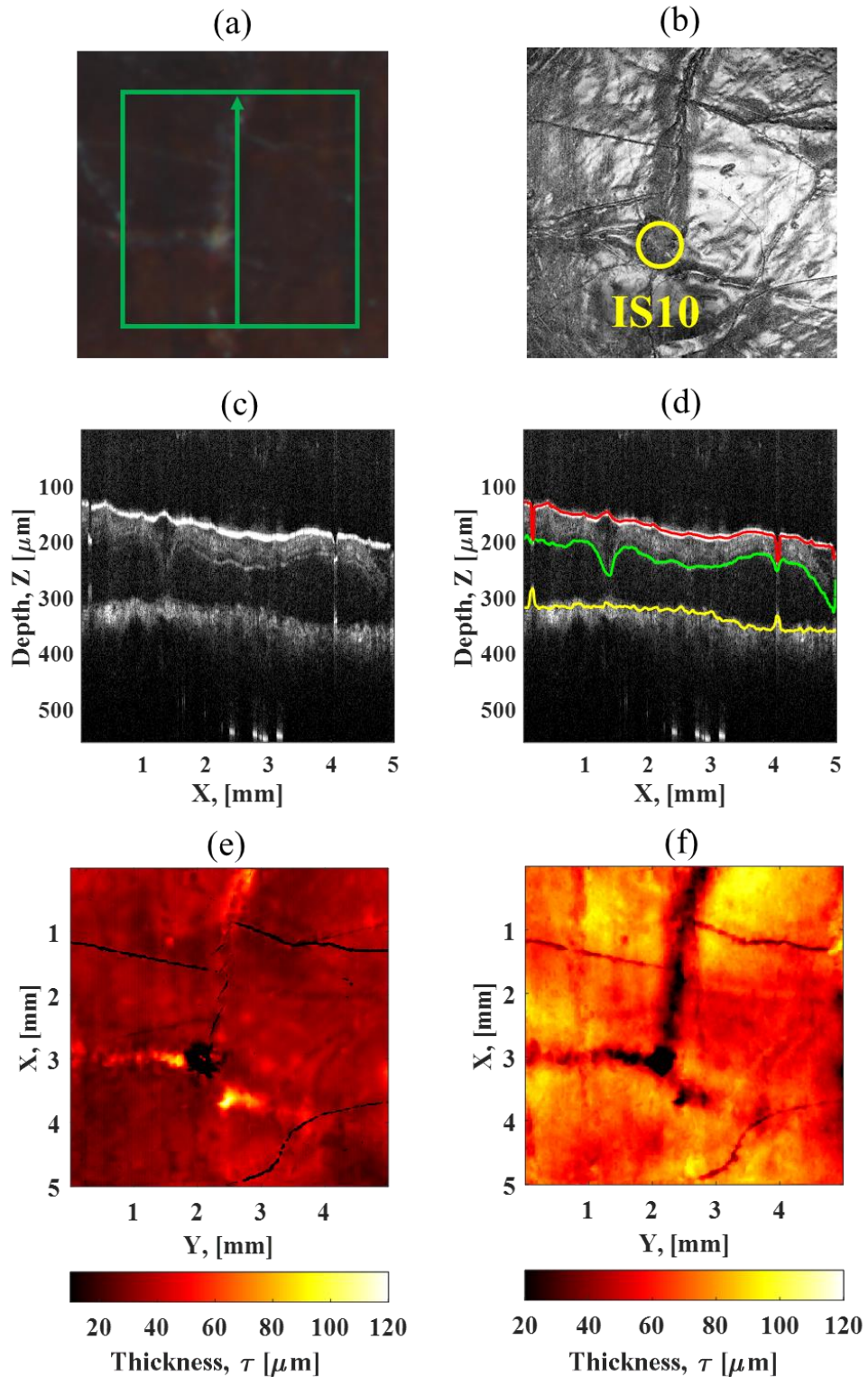


Figure 3.2.5.2. a) Colour reconstruction from the PRISMS spectral imaging for OCT Volume B of NG5015 alongside b) the enface max projection with IS10 marked. c) A B-Scan from the OCT with d) segmented varnish layers (green-red), sketching/preparation layers (green-yellow) and wood (yellow). e) The thickness map of the combined varnish layers and f) sketching/preparation layers.

Here the thickness variation appears to be consistent with that seen in sample IS10 (Figure (3.3.6.3)). The sample site (IS10) is also clearly visible in both thickness maps, and the dimensions of the sample can be seen to be approximately 400 μm in diameter.

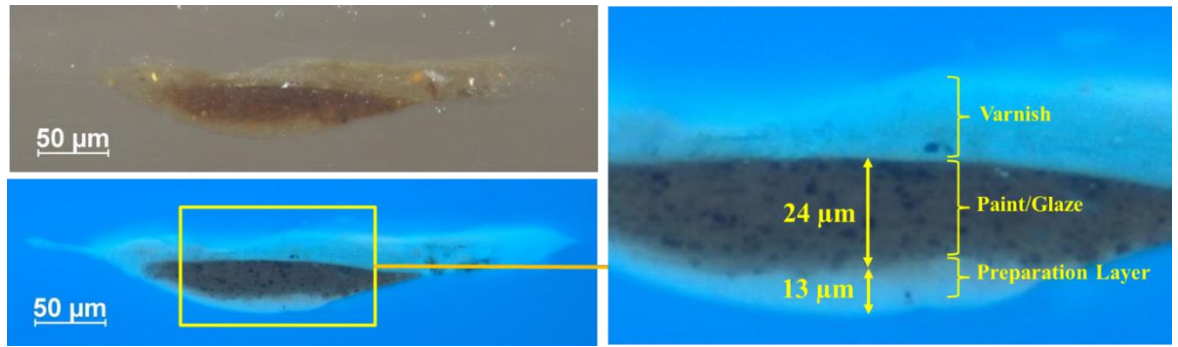


Figure 3.2.5.3. Sample IS10 under visible illumination (top left) and ultraviolet illumination (bottom left). The stratigraphy visible in the sample has been labelled over a region of the sample (right).

3.2.6. Interface Depth Mapping and Refractive Index Corrections

With the extraction of the thickness map of the layer, the depth of the interface position can be corrected for the contribution of refractive index via Equation (3.2.6.1). Here $L_{N,N+1}$ is the corrected depth for an interface between layers N and layer $N + 1$, $z_{0,1}$ is the interface between the air and first layer and $\tau_i(x, y)$ again is the thickness of layer i which has been corrected for a refractive index of approximated at 1.5 for all paint and varnish layers.

$$L_{N,N+1}(x, y) = z_{0,1}(x, y) + \sum_{i=1}^N \tau_i(x, y)$$

Equation 3.2.6.1

Figure (3.2.6.1.a) and Figure (3.2.6.1.b) show the depth maps and refractive index corrected depth maps respectively for the interfaces corresponding to the air-varnish interface, varnish-sketching/preparation interface and the sketching/preparation-wood interface in OCT Volume B discussed in Chapter (2.4.3) and Chapter (3.2.5). Here the contributions to the interface positions from the layer thickness of the varnish-preparation layer interface and preparation layer-wood interface can be seen to be reduced, especially around the cracked regions where a reduction in layer thickness is seen to reduce the depth of the interface position in the uncorrected maps.

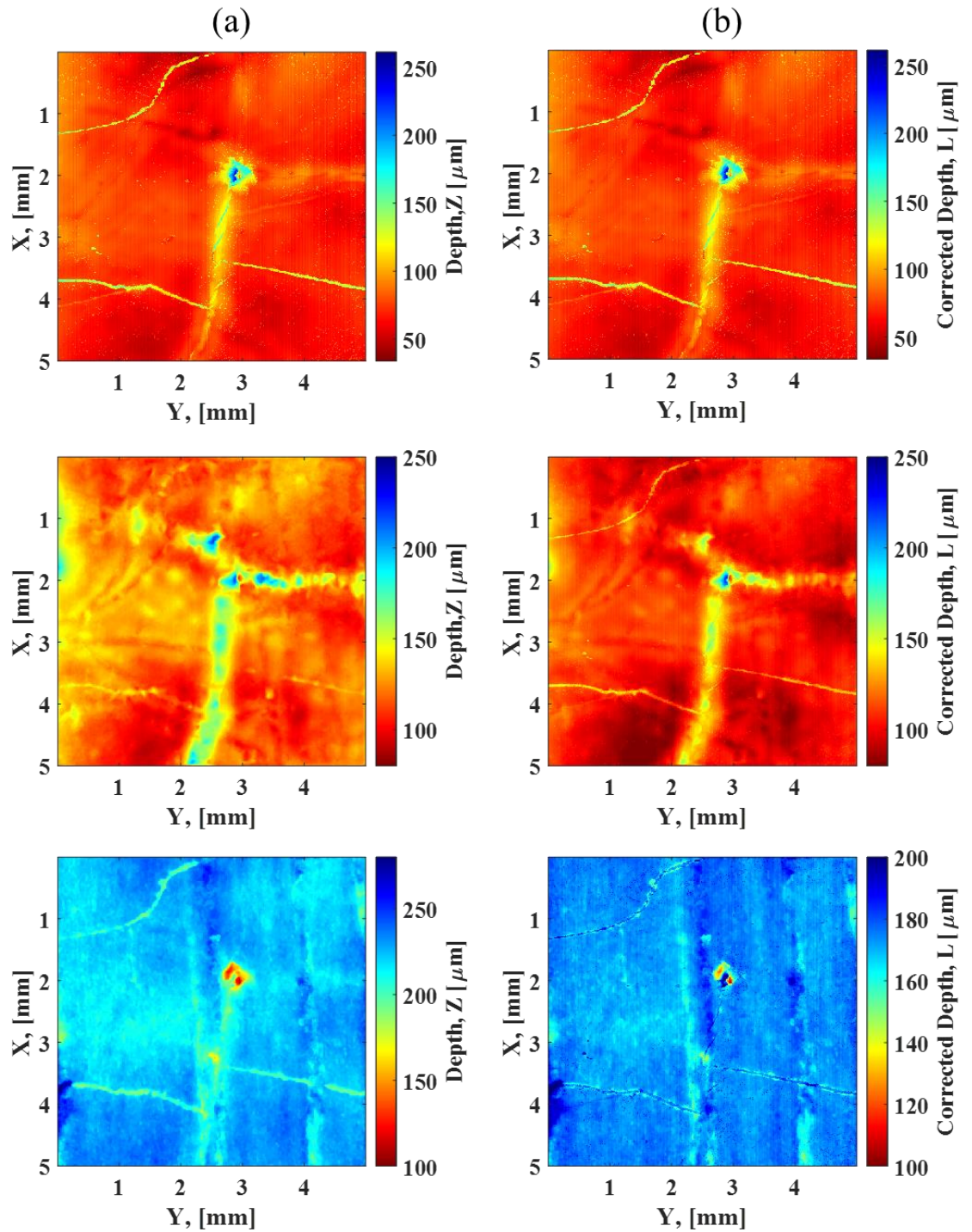


Figure 3.2.6.1. a) The depth map of the air-varnish interface, varnish-sketching/preparation layer interface and sketching/preparation layer-wood interface along side b) the refractive index corrected depth maps.

The correction of refractive index can likewise be expanded to the entire OCT volume. This proves particularly useful in qualitative analysis of OCT data sets with particularly complex stratigraphy such as those seen in NG 5015 in Chapter 2. Here for a given lateral position, the set of axial pixels corresponding to a layer can be segmented and linearly rescaled by the refractive index at each lateral position. Figure (3.2.6.2) shows a B-Scan from OCT Volume B, before and after refractive index corrections. The effects of the correction are most prominent around the region of material loss corresponding to sample IS10. Again, in the uncorrected B-Scan, the preparation layer-wood interface can be seen to dramatically reduce in depth position around the sampled region as the total layer thickness decreases. This contrasts with the corrected B-Scan where the preparation layer-wood interface can be seen to be relatively flat with the exception of the region directly corresponding to the removed material.

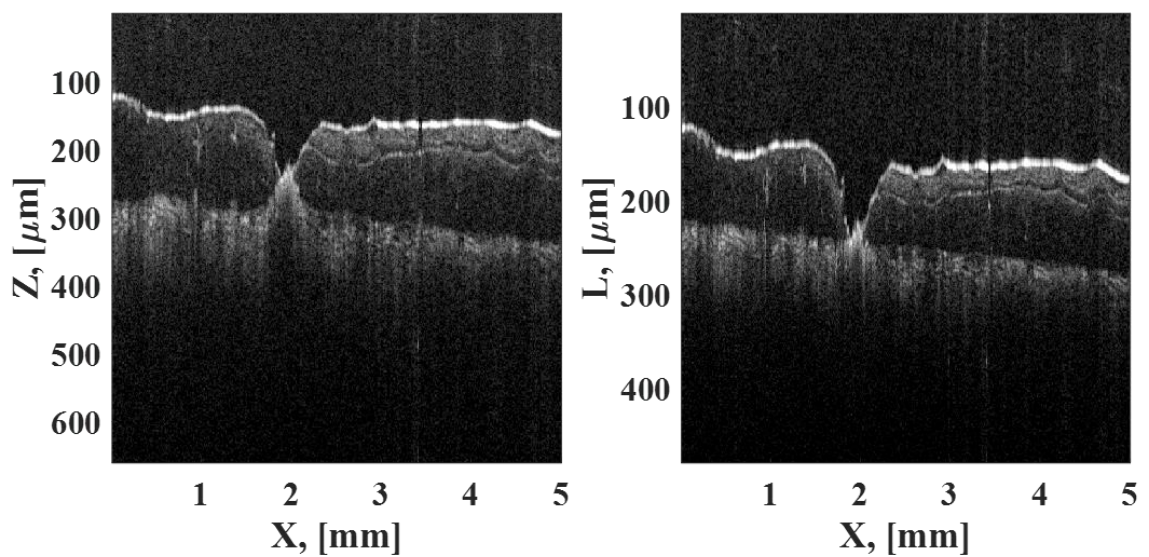


Figure 3.2.6.2. A B-Scan from OCT Volume B of NG5015 (left). The depth position of the wood interface is seen to reduce where the varnish a paint layer have been removed to produce sample IS10 (centre of the scan). With refractive index correction applied to the B-Scan (right), the distortion in the interface position resulting from the material refractive index has been corrected to provide better reflect the true stratigraphy of the region.

It should be noted that the above examples of refractive index correction are only valid given the assumption that the path of incident light rays are perpendicular to the layer interfaces.

A more rigorous approach would consider the path of light rays through the sample in accordance with Snell's law at a known refractive index [66]. The angle of incident light is expected to be small for most cases and any error in the corrected layer position is expected to be dominated by the differences in the estimation of the refractive index in comparison to the ground truth.

3.3. Data Alignment

3.3.1. Collection of OCT Region of Interest

To extract the respective spectral features of a layer, the two modalities must first be aligned to produce a one-to-one relationship. With this however, comes some considerable difficulty. For one, the comparative lateral resolutions and field of views of the two modalities used are both near to an order of magnitude in difference, leading to difficulties in locating and accurately marking common spatial features for the alignment and limiting the number of data points for the extraction of the trend. Thus, there is a requirement for the collection of a larger OCT region.

To do so without major modification of the system, the OCT probe is mounted on a set of three linear micrometre stages positioned perpendicular to each other. Here lateral travel is controlled via a Thorlabs NST150/M providing 150 mm of travel with a step error of approximately $\pm 2\mu\text{m}$ under load. Axial displacement of the probe for focussing is provided by a Melles Griot 17DRV114 motorised stepper with 50mm of travel. To avoid potential sources of vibration, reduce collection time and ensure that the datasets remain within the axial focal plane, the region of interest is partitioned into several 5mm-by-5mm OCT volumes with a 0.8mm overlap between cubes. The motorised stages are then used to move the probe to the central position of each cube and the lateral displacement during collection is controlled entirely by galvanometer scanning as before. After segmentation of the constituent cubes, the greater region of interest can then be stitched together to build a continuous thickness map of the entire region [63].

3.3.2. Enface Reference Projection

When aligning modalities, extracted thickness maps alone may not suffice in providing distinct and recognisable common features with spectral imaging. This presents the need for the extraction of additional information from the OCT volumes, in this case from the intensity of a A-scan depth profile.

A common method of achieving this is in the form of enface image projections of the OCT volume [25,67,68]. In the simplest applications of this, the maximum or mean of an axial region of interest can be extracted to produce a lateral intensity image as given by Equation 3.3.2.1. and Equation 3.3.2.2 respectively. Here A is a set of axial positions relating to an arbitrary axial region of interest with #A referring to the number of z pixels within the region of interest [Figure (3.3.2.1.b)].

$$I_{\max}(x, y) = \max_{z \in A} (I(z, x, y))$$

Equation 3.3.2.1

$$\bar{I}(x, y) = \frac{1}{\#A} \sum_{z \in A} I(z, x, y)$$

Equation 3.3.2.2

Figure (3.3.2.1) displays an example of a maximum and mean projection of a region from NG5015, covered in the previous chapter. Here the region of interest is chosen to minimise the inclusion of the background within the projection. Such an example can demonstrate several observations from the projection techniques.

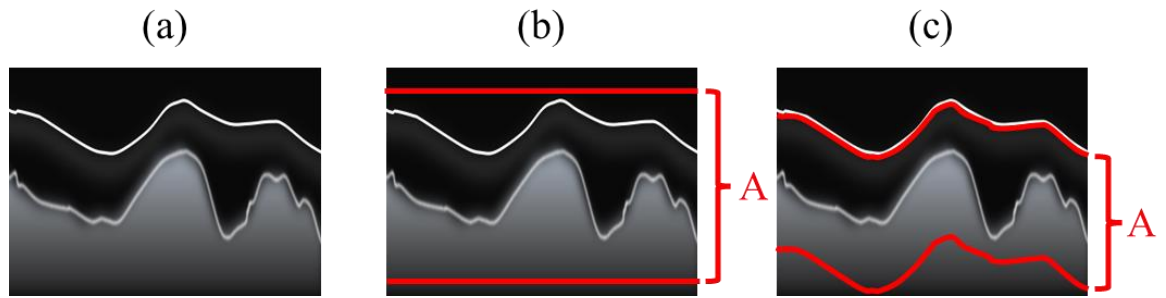


Figure 3.3.2.1. a) A diagram of an OCT B-Scan with b) the region of interest marked for enface projection and c) the adaptive region of interest based on segmentation for the adaptive window enface projection

Firstly, with the exclusion of the DC contributions within an OCT volume, it can be speculated that from most varnished oil paintings, the maximum projection should correspond to reflections from the air-varnish interface as that interface is expected to have the greatest reflectivity in comparison to interstitial layers. This is due to the larger refractive index mismatch between the materials and higher percentage of the illumination intensity reflected. It should be caveated, however that such an observation is dependent on a) the lack of high reflectivity interstitial interfaces such as those expected from metallic leaf; and b) if specular reflections from the air-varnish interface are not collected due to reflections away from the probe at regions of high topography.

Secondly, as the mean projection, is an average of the axial intensity profile of the volume, it should be expected to correspond similarly to a regular image collected with the same geometry (0° illumination, 0° collection) and illumination. Again, this should be caveated as, for situations in which large axial variations are present in the stratigraphy, an increase in the inclusions of the noise floor within the average, may lead to considerable reductions in signal to noise. With the 0° illumination, 0° collection geometry, specular reflection from interfaces, may dominate and skew the calculated mean depending on the region of interest, especially components related to the air-varnish interface or reflective metallic foils. This is in comparison to the expected dominance of diffuse reflection from scattering sites within spectral images due to the 45° illumination position relative to collection.

For this application, as feature similarity is paramount for alignment of the modalities, it is often more apt to extract a mean projection for feature alignment. However as stated, this can be heavily weighted towards the interface components or the noise floor depending on the stratigraphy. To adjust for this, an adaptive region of interest is applied based on the extracted interfaces from segmentation [63]. With this, an average of an arbitrary window can be extracted below a given interface, to produce a more targeted average projection, reducing the contribution of background. Here the region of interest A can be defined by Equation (3.3.2.3) where n is a set of z pixels in the region, $z_{i-1,i}$ is the interface axial position preceding layer i , σ is the standard deviation of the axial points spread function and b is an arbitrary region span [Figure (3.3.2.1.c)]. The ceiling function applied in the term $\lceil 3\sigma \rceil$ is included to simply produce an integer value to relate to an actual pixel position, for the ultra-high-resolution OCT applied here, this corresponds to around $6\mu\text{m}$ in polymer. For this work, projections for the alignment are produced relative to the air-varnish/ air-paint interface or relative to the varnish-paint/air-paint interface with a span of 200 pixels ($\sim 107\mu\text{m}$ in polymer) chosen for b . Figure (3.3.2.2.c) shows the adaptive window enface mean projection for the previous example based on segmentation results from of the varnish-paint/ varnish-wood interfaces.

$$A = \{n \in \mathbb{N}: z_{i,i+1} + \lceil 3\sigma \rceil \leq n \leq z_{i,i+1} + \lceil 3\sigma \rceil + b\}$$

Equation 3.3.2.3

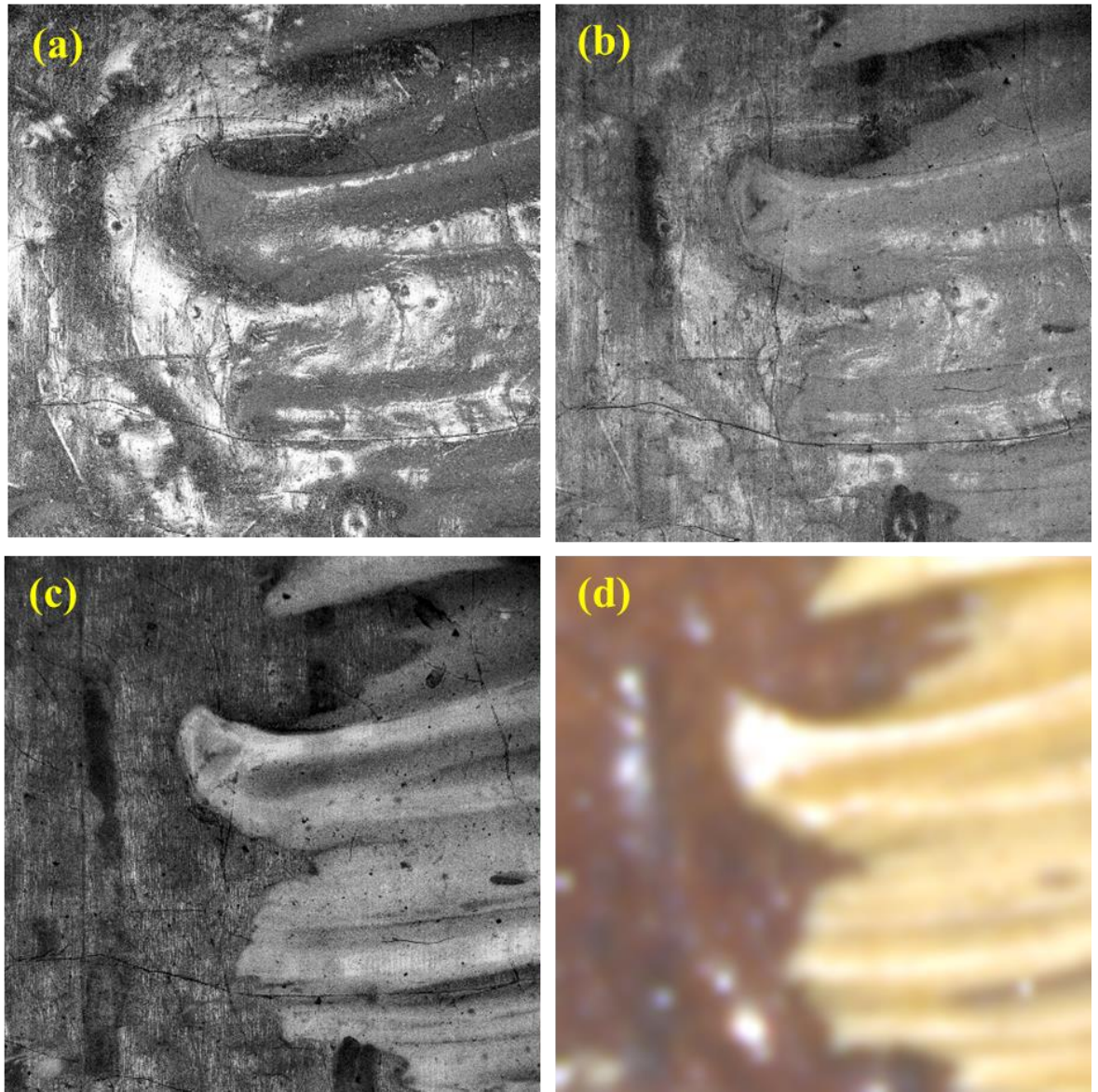


Figure 3.3.2.2 a) The enface max projection and b) enface mean projections of OCT Volume H from NG5015. c) The adaptive window enface mean projection based on the mean of 200 pixels below the varnish-wood and wood-varnish interfaces. d) The colour reconstruction of the region from PRISMS spectral imaging.

3.3.3. *Alignment of the Two Modalities*

With the creation of an enface reference projection image for the OCT region, the alignment of the two modalities can be carried out. For simplicity in implementation, alignment is achieved through the manual selection of points around common features within the spectral image and reference enface projection. A more robust and time efficient automated solution for such alignment would be ideal, but the optimal implementation of such a technique for the extraction of common features from different modalities, collected under different conditions and with markedly differing resolutions is beyond the scope of this work.

With extraction of enough common features, an affine transformation can be applied to the thickness map, producing a one-to-one relationship between reflectance and layer thickness. The transformation here is applied to the thickness map in this case as it has been collected at a much greater resolution and thus can be easily down sampled. The opposite is avoided so as to reduce the introduction of artifacts from interpolation. An example of an aligned dataset can be seen in Figure (3.3.3.1) for a sample of copper resinate glaze applied over an opaque yellow paint layer from an experimental reconstruction panel prepared at the National Gallery (described in Chapter (3.4.1)).

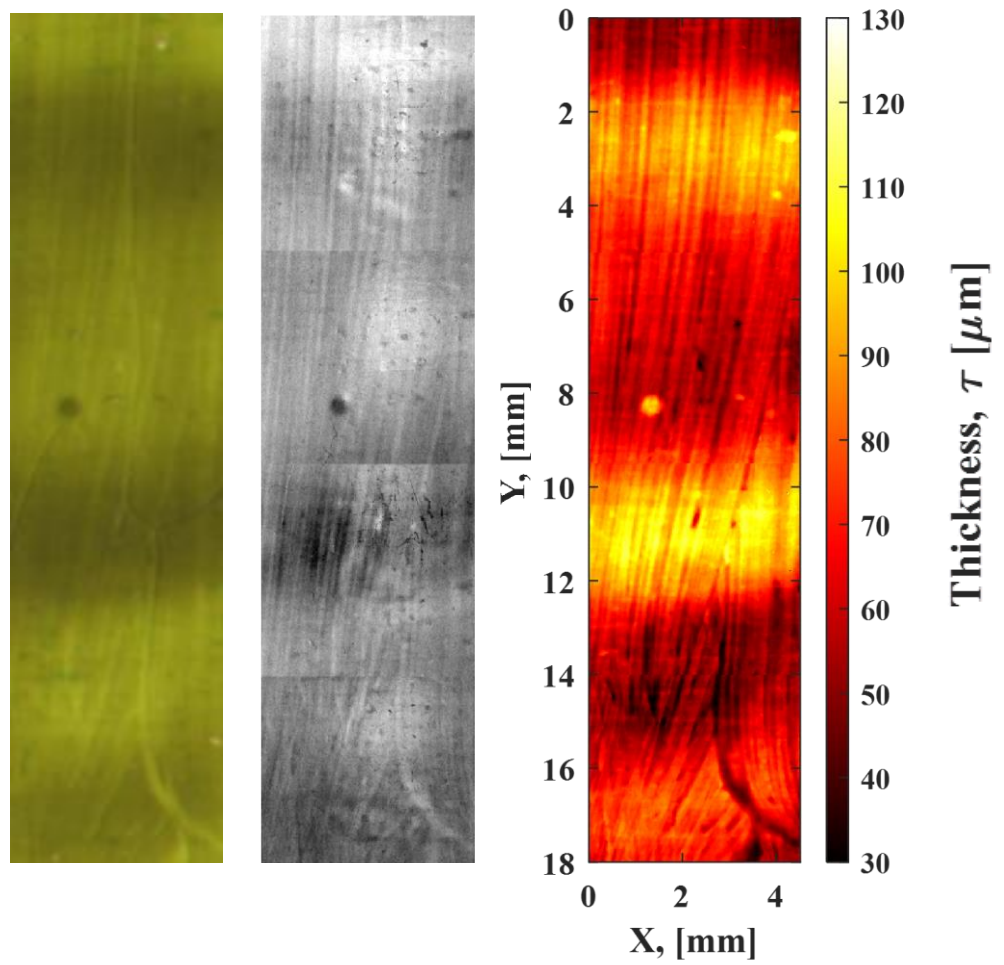


Figure 3.3.3.1. Colour reconstruction from PRISMS spectral imaging (left) with the aligned adaptive window enface mean projection (middle) and layer thickness map (right) for a layer of copper resinate glaze over yellow paint. Here the adaptive window enface projection is based on the air-glaze interface

3.4. Extraction of Spectral Features

3.4.1. Extraction of Spectral Features for a Prepared Samples

With the alignment of the thickness and reflectance results, when applying the Beer-Lambert law of Equation (3.1.3.2), an expected linear trend should be obtainable with the layer thickness against the log of reflectance at a given wavelength. To test this, the technique was applied to an experimental reconstruction panel prepared at the National Gallery in 1985, consisting of a green copper resinate glaze layer (now slightly discoloured) applied over four opaque underpaints (white, pale yellow, mid-green and yellow ochre in colour) as described in Table (3.4.1.1) and shown in Figure (3.4.1.1). The copper resinate in this case was prepared at the National Gallery from copper carbonate and abietic acid (the major resin acid found in pine resin) and was spread as a liquid with no additional binding medium added.

Number	Under Paint Colour	Under Paint
i	White	Titanium White + Acrylic binder
ii	Yellow	Primrose Cadmium Yellow + Acrylic binder
iii	Green	Primrose Cadmium Yellow +Viridian+ Acrylic binder
iv	Ochre	Yellow Ochre + Acrylic binder

Table 3.4.1.1

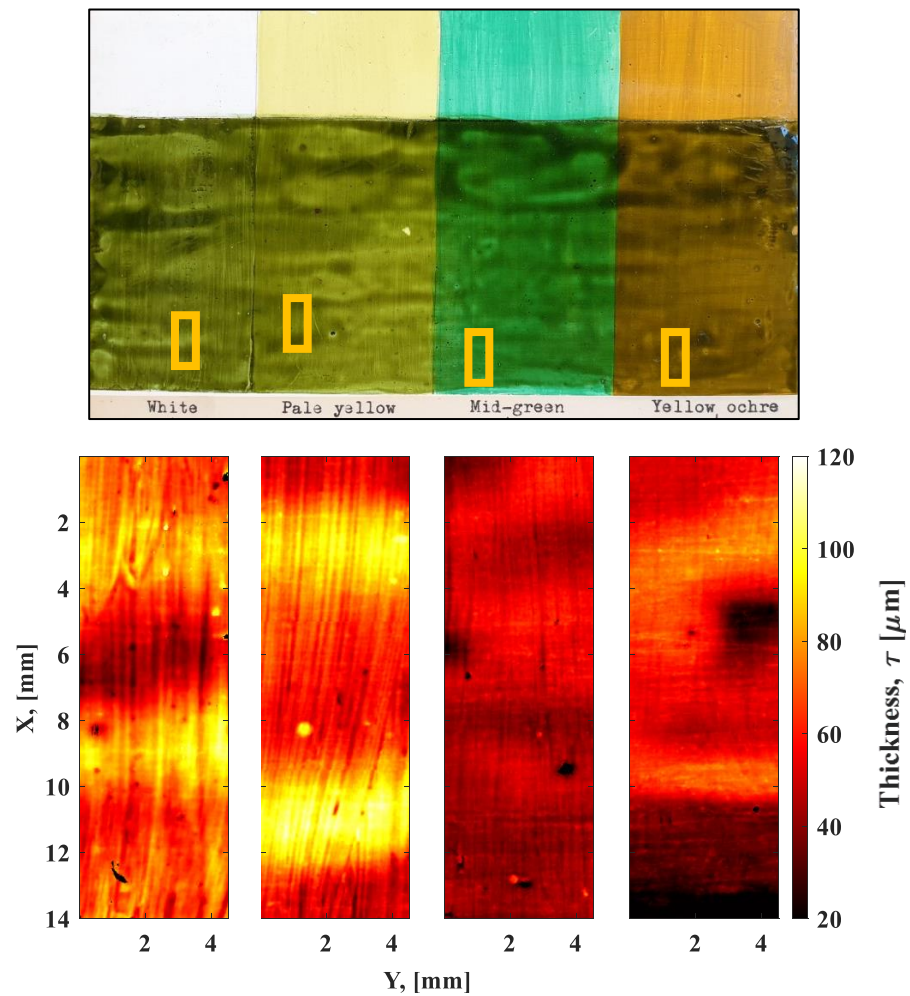


Figure 3.4.1.1. A colour image of the sample of a layer of copper resinate over various paint layers (top) with their respective layer thickness maps (bottom) marked

The associated relationship between thickness and the log of reflectance can be seen in Figure (3.4.1.2) as a function of the PRISMS spectral imaging band central wavelength for copper resinate over the white paint. From this extracted relationship a number of things become apparent. For this mock-up sample it is clear that the Beer's law relationship is justified, producing a linear relationship with thickness. It is however clear that the high absorption in the layer and lower illumination intensity towards the ultra-violet have resulted in a reduced photon count which significantly reduces the signal to noise limiting the accuracy of the extinction calculation. With the logarithmic transformation to the reflectance data, noise variation also becomes non-linear, introducing bias into the fitting.

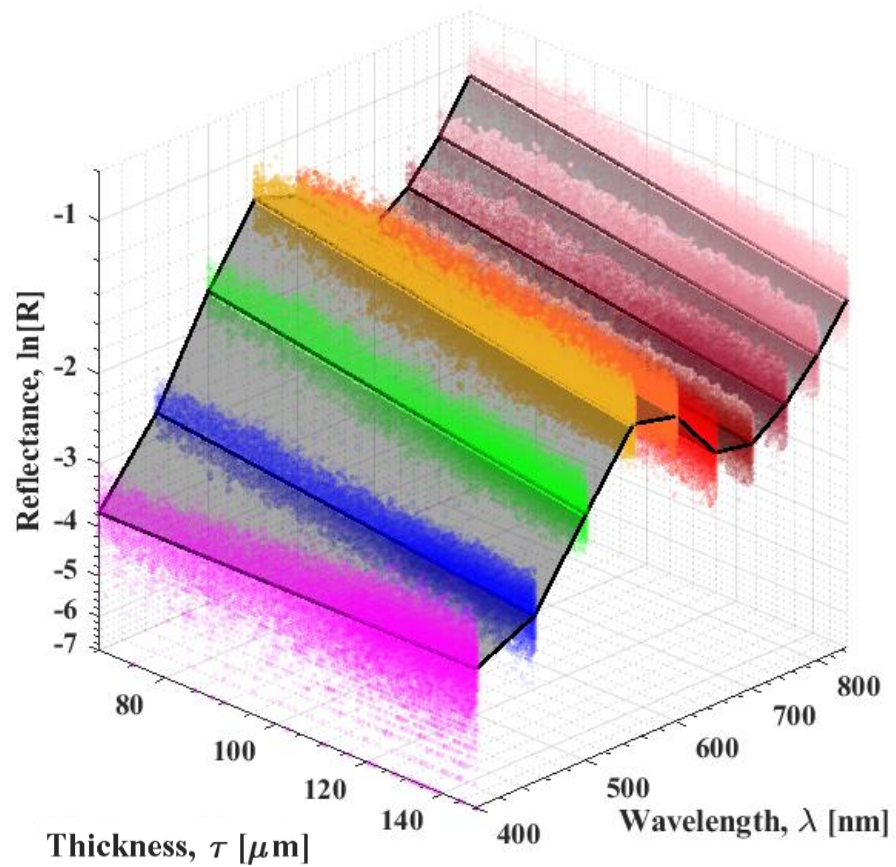


Figure 3.4.1.2. The log of reflectance as a function of layer thickness and wavelength for PRISMS spectral imaging cube for a layer of copper resinate over the white paint. A linear trend is visible for the relationship between the log of reflectance and layer thickness.

From this relationship it is then possible to extract the extinction coefficient as a function of wavelength $\epsilon(\lambda)$, for the copper resinate layer over each of the different colours of underpaint pigment as illustrated in figure (3.4.1.3). Here the 400 nm band has been excluded from the plotting as a result of the low signal to noise producing an erroneous extinction result. With this, the extracted copper resinate spectra over the different paints produced an absorption feature at 700nm consistent with the absorption feature in the reflectance of the copper resinate over white and with the expected absorption feature of 695nm described in Aceto et al., 2014 for copper resinate [69].

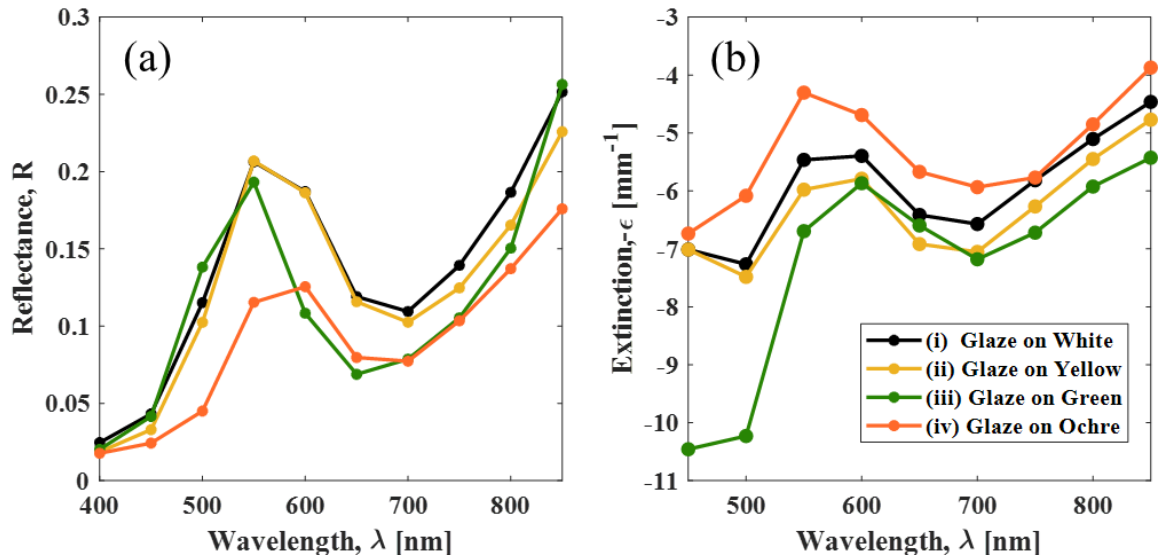


Figure 3.4.1.3 a) The reflectance and b) the extracted extinction coefficients of a copper resinate layer over (i) white, (ii) yellow, (iii) green and (iv) yellow ochre. The extraction of extinction coefficients produces a consistent absorption feature for the glaze layer

3.4.2. Extraction of Spectral Features in Paintings

To demonstrate the possibility of extracting spectral features of layers of interest from real paintings, data acquired from an area of red lake glaze over vermilion from a sixteenth century copy of a painting by Raphael in the National Gallery collection was used. PRISMS data was collected in 2018 from the region of the painting and was combined with existing OCT data acquired in 2013 using the UHR OCT (810 nm) [22] in order to extract the extinction coefficient as a function of wavelength of the red lake glaze layer on the Virgin's dress. The extinction spectrum seen in Figure (3.4.2.1.c) is that expected from a red glaze layer.

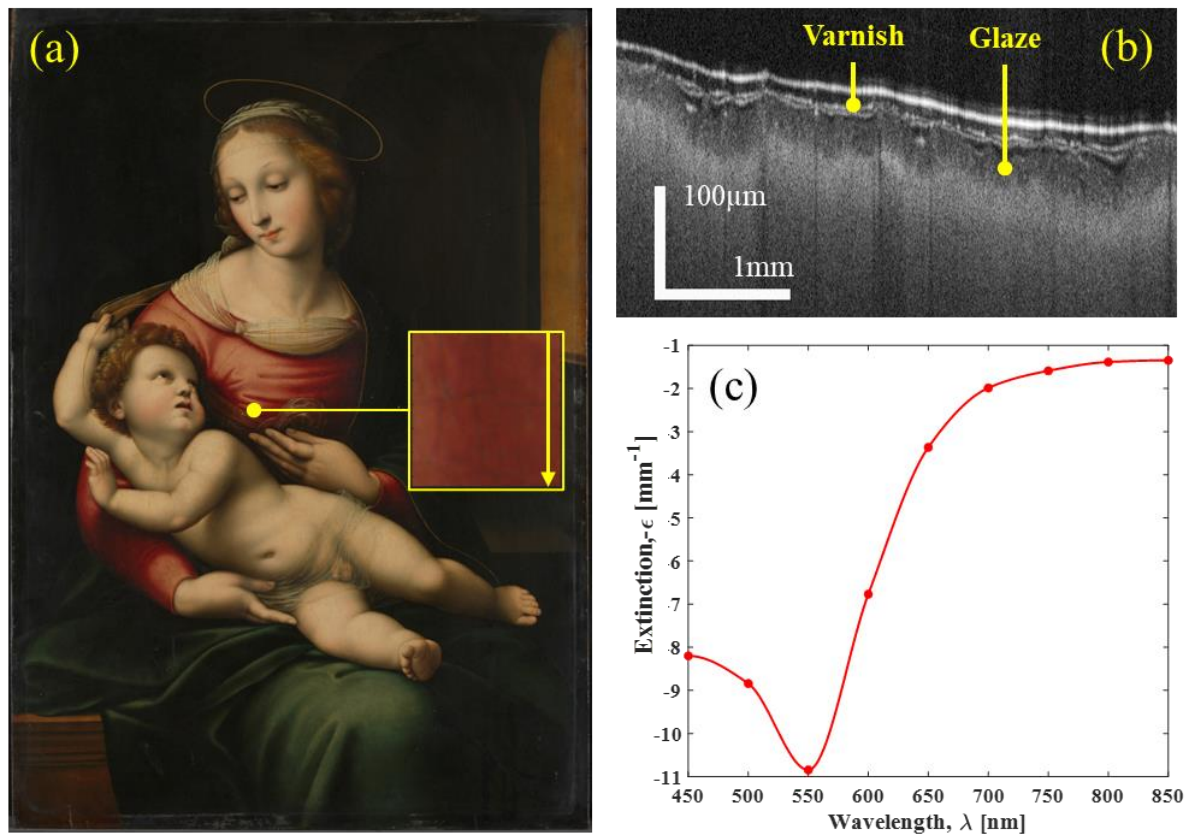


Figure 3.4.2.1. a) After Raphael, *The Madonna and Child* (NG929), probably before 1600 © National Gallery London with a colour reconstruction of the OCT volume region from PRISMS for a region of red glaze. b) A B-Scan with the glaze and varnish layers marked. c) the extracted extinction coefficient of the red glaze.

3.4.3. *Virtual Varnish Removal*

Another prospective application of this technique outside of material identification, is that of virtual varnish removal or virtual restoration in which the colour contributions from the degraded varnish can be corrected digitally to more closely estimate the original appearance [70–77]. The use of this technique may provide some benefits to current methods of virtual restoration as the global thickness mapping provides the ability to account for local variations in the total attenuation resulting from thickness variations. Again, in cases where the Beer-Lambert law hold true, the thickness map can be used directly as a corrective mask for the reflectance data again by reapplying Beer’s relation in Equation 3.2.3.1 to calculate the predicted value of the ground reflectance $R_g(x, y, \lambda)$. This can then be used to calculate a virtually corrected image in RGB space via the transform discussed in 3.2.2.

Applying virtual cleaning to the case of a yellowed varnish applied over a mock-up painting in Figure (3.4.3.1) yields the corrected colour reconstruction seen in Figure (3.4.3.2). Here the contribution of the varnish region is seen to be mostly removed with some residual contributions present. Such effects are likely a result of a) the incomplete segmentation of all layers, with the failure of the segmentation algorithm to extract the lowest most layer and b) the possible contribution of scattering and interfacial reflections to reflectance producing an under estimation in the extracted extinction. In any case with further refinement of the technique to include such factors, the technique proves promising for the application of virtual cleaning.

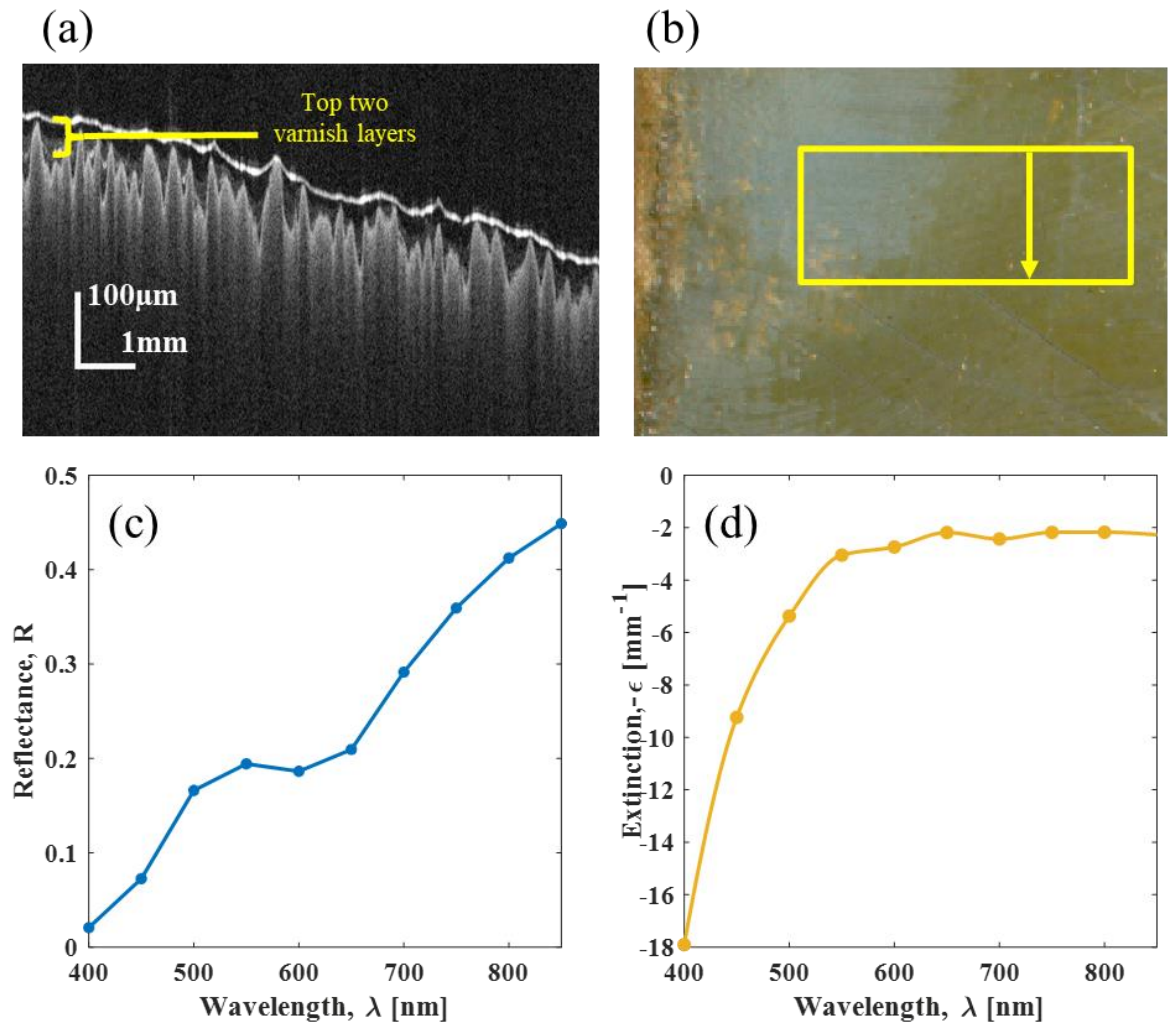


Figure 3.4.3.1. a) a constituent B-Scan from the OCT volume taken over a region of a mock-up painting in which three varnish layers are seen above a blue paint layer. Colour reconstruction from the PRISMS spectral imaging of a region of degraded varnish over blue paint beside a cleaning test with the OCT volume region marked. c) The average spectrum of the varnish layers over the blue paint. d) The extracted extinction coefficient of the top two varnish layers



Figure 3.4.3.2. a) A mock-up painting supporting several layers of degraded varnish. b) Colour reconstruction from the PRISMS spectral imaging of a 15mm × 34mm (Height × Width) region of degraded varnish over blue paint beside a cleaning test b) The thickness map of the top 2 varnish layers superimposed on the colour reconstruction. c) The colour reconstruction from PRISMS after the virtual cleaning of the top varnish layers.

3.4.4. Conclusion

The chapter demonstrates, the application of the Beer-Lambert law in extracting the extinction coefficients of a superficial varnish or glaze layer through the extraction of the layer thickness from OCT volumetric data sets and comparison with the reflectance spectra from spectral imaging. The technique was able to successfully identify the absorption features of a copper resinate sample and red lake layer within a historical painting. With the extraction of the extinction spectrum and layer thickness maps, the technique has been applied in the virtual cleaning of degraded varnish from a section of a mock-up painting.

To extract the layer thickness, the automated segmentation of material interfaces within the OCT volumetric data cube has been carried out through image denoising and a graph-based technique. Image denoising is shown to successfully reduce speckle and noise contributions at the expense of axial and lateral resolution. The graph-based segmentation technique was seen to perform poorly in cases of corrugated interfaces with large variations in depth over small lateral distances. Further work in the refinement of the segmentation is therefore required.

The segmentation of interfaces from the OCT volumetric cube also provides the opportunity for the manipulation of data sets in several ways. Firstly, the segmentation of layer boundaries in the data set enable the extraction and refractive index correction of depth mapping allowing for topographic measurements of the region. Likewise, with knowledge of the layer boundaries, approximate refractive index corrections can be attempted to remove distortion in the volumetric data sets and allow for clearer interpretation of the layer structure. Finally, segmentation of the interface position can be used to better limit the region of interest for the extraction of enface projections, increasing signal to noise and excluding specular interface contributions.

Chapter 4: A Multi Modal Instrument for the Combined Collection of Spectral Imaging and Optical Coherence Tomography

4.1. Introduction

As discussed in the previous chapter, the need for greater parity between the collection regions of spectral imaging and OCT data sets is desirable if the layer extinction is to be extracted via the relationship between reflectance and layer thickness. In this chapter the development of a multimodal instrument for the collection of coincident optical coherence tomography depth profiles and reflectance spectra measurements will be discussed.

The direct collection of spectral characteristics from OCT signal can be achieved by spectroscopic OCT [78]. Here such techniques partition the interference spectra, either instrumentally, such as by filtering the illumination into separated bands or during processing via a spectrally moving windowed function applied to the interference spectrum to produce a cluster of spectrally separated A-scan depth profiles at a given spatial position. This often becomes a trade-off between spectral and spatial resolution of the system, with the greater spectral resolution producing low axial resolution after conversion into to depth space [79] though the more sophisticated methods manages to preserve both high spectral and spatial resolution through bootstrapping [80]. Issues also arise in two major areas when applying this technique.

Firstly, instrumental limitations come into play when practically implementing such a technique. As OCT requires a high spectral resolution to resolve modulation with increased depth, the spectral bandwidth collected by the spectrograph will often be limited to a smaller band due to physical limitations of the detector dimensions and spectrograph optics. Thus, to collect a range suitable for the characterisation of pigments in the visible spectral range, would produce additional complexity to the system and limit the depth of penetration of the OCT as most pigments are opaque in the visible range. Secondly, limitations in the signal to

noise of reflectance spectra obtained via OCT will arise from the coherent nature of the light source required due to the introduction of randomly generated stationary speckle patterns within the stratigraphy.

An alternative approach to this would simply be through the combination of OCT with differing modalities within the same probe to obtain spatial alignment. A plethora of literature is available for this method where the combination of OCT with microscopy, Raman spectroscopy [81–88] and fluorescence imaging techniques [89–97] have been accomplished. Of particular interest to this work, are the examples of hybrid OCT and spectral imaging systems.

Within the work of Guay-Lord et al, co-registered OCT and spectral imaging was achieved through the use of a double clad fiber coupler [98]. Here the core and internal cladding of the fiber allows light propagation in single and multimode respectively which can be bifurcated between two ports. By collecting spectra through the multimodal port under an external broad band illumination source via a spectrometer and collecting OCT through the single mode port, the two modalities can be collected from the same region. The lateral dimensions of both data sets can then be built through raster scanning. This offers the advantage of providing one to one alignment between the two modalities while allowing for flexibility in spectrometer specifications. A major limitation of this technique, however, is that of the comparatively long collection times associated with the single point measurements of reflectance. For the study in question reflectance is collected at approximately 8ms per lateral pixel. Thus, for real applications if collection of spectra within a region is to be expediated, lateral resolution must be sacrificed, or a more sensitive detector is required.

Attenu et al addressed such issues with collection time for single point collection in double clad fibers through the use of frequency domain multiplexing of filtered laser illumination to produce multi spectral images at OCT acquisition rates [99]. Here several discrete laser bands are coupled into the single mode core of the double clad coupler for use as a filtered spectral imaging illumination source with collection of the reflectance spectra handled by a

photo detector at the multimode port. Delineation of the wavelength bands is achieved through the modulation of each laser band at distinct frequencies with spectral contributions to the collected signal being reconstructed through Fourier analysis. This method, however, is severely limited in the attainable spectral resolution from the laser illumination source and suffers greatly from specular reflectance due to the $0^\circ/0^\circ$ illumination/collection geometry.

A more common approach, to obtaining co-register OCT and other modalities, is simply through the use of a dichroic or flip mirror to bifurcate or redirect the light between modalities. Such an implementation is seen within the work of Dontu et al., Savastru et al. and Göb et al, which simply use a dichroic mirror positioned before the objective [100–102] in which light is split between the OCT probe and a spectral camera.

4.2. Design of a Multimodal Instrument

4.2.1. Overview of Design

The design chosen and developed for the combination of OCT and spectral imaging is seen in Figure (4.2.1.1). This design takes advantage of the large bandwidth of super continuum light sources to combine a filtered illumination based spectral imaging with a SD OCT.

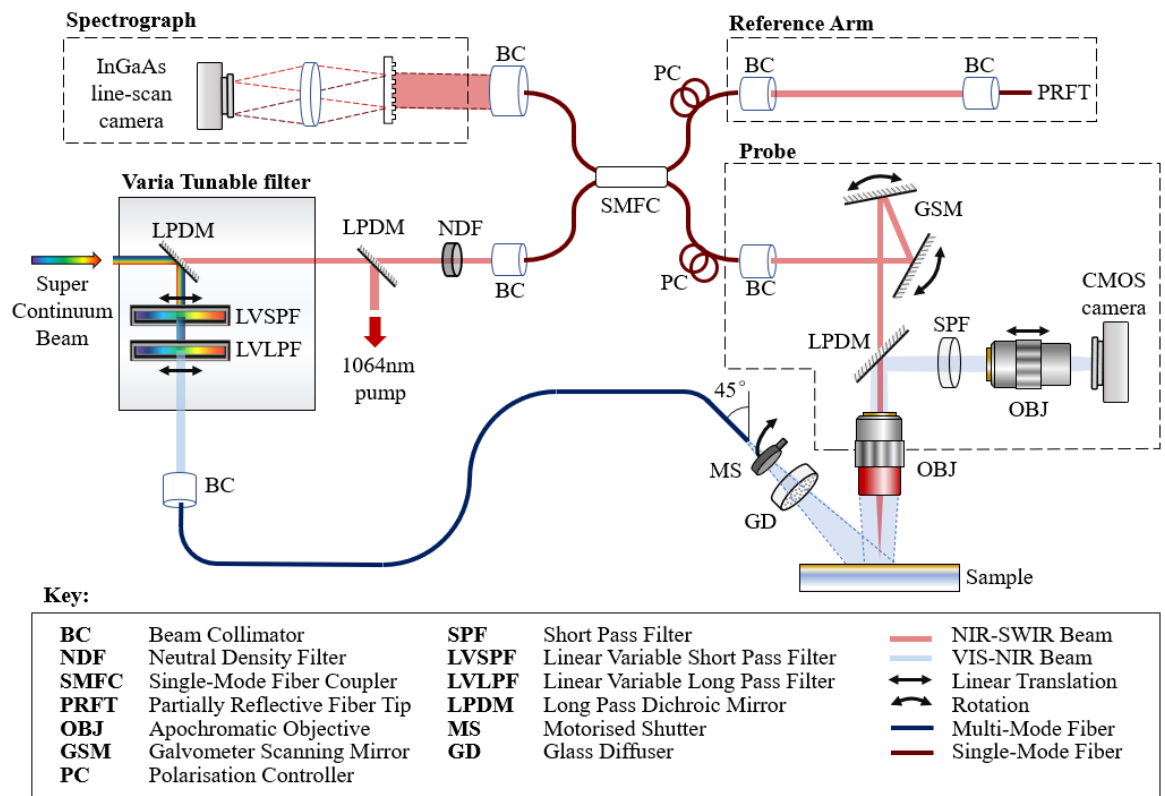


Fig. 4.2.1.1 Schematic showing the Hybrid optical coherence tomography and spectral imaging system using an NKT super continuum light source and varia tuneable filter. The spectral domain 1250nm optical coherence tomography system uses the long wavelength output of the NKT super continuum light source with a 1145 lp.mm^{-1} grating and 1024-pixel linear InGaAs array. Spectral imaging relies on the filtered visible output of the NKT super continuum source from the NKT Varia tuneable filter allowing for band with a minimum bandwidth of 10nm, with central wavelengths from 415nm to 845nm with collection via a 1280 by 1024 CCD.

Here a commercial NKT Photonics SUPER K EXTREME EXU-6 supercontinuum laser source, is utilised to provide illumination for both modalities. Such a source produces a single mode beam with a broad wavelength range spanning from approximately 390nm to 2350nm. Figure (4.2.1.2) shows the spectral shape associated with the supercontinuum light source. When coupled with an NKT photonics VARIA tuneable filter, illumination for both modalities can be segregated into two channels via an internal dichroic long pass filter: The NIR-SWIR portion, of wavelengths above $\sim 850\text{nm}$, is transmitted for use as a broadband spatially coherent OCT light source, while the residual VIS-NIR component is reflected

towards a pair of translatable linearly variable short and long pass filters, providing a tuneable spectral band for use as the spectral imaging illumination.

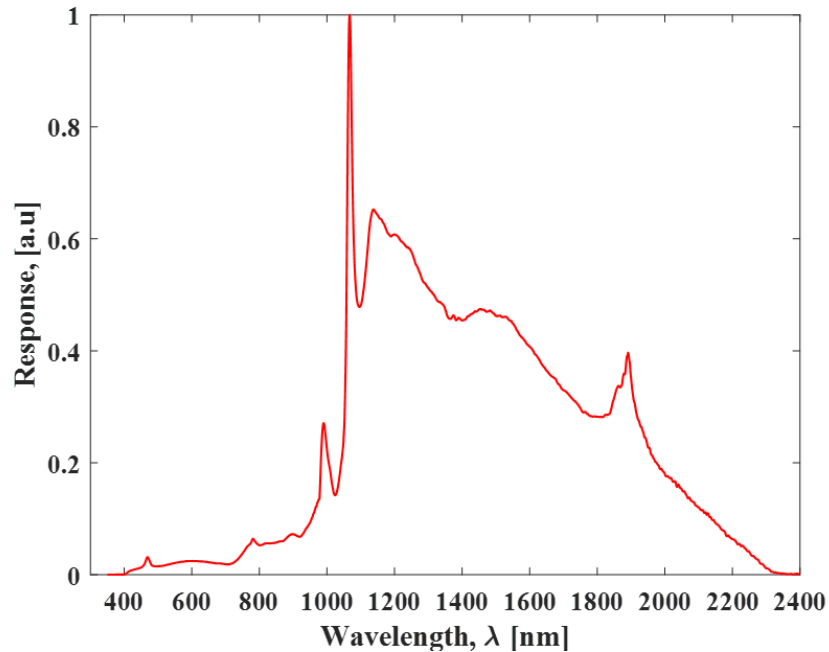


Fig. 4.2.1.2. The Normalised Spectral shape of the NKT Photonics SUPER K EXTREME EXU-6 supercontinuum laser at maximum power as measured with a Spectral Evolution SR-3500 fibre optics spectrometer.

In segregating the wavelength span of illumination for the two modalities, collection of data can be done via the same objective lens in a hybrid probe, ensuring spatial coincidence between the measurements.

The probe in question resembles that of the UHR SD OCT discussed in chapter 2. Here the sample arm of the OCT interferometer is coupled into the probe via a reflective collimator to produce a collimated beam. This is then steered, via a pair of galvanometer scanning mirror, over the objective lens which in turn focuses the beam onto the target sample and collects associated signal from the sample for recombination in the interferometer. By raster scanning this beam over the objective exit pupil, OCT depth profiles scan be collected over the target region of interest to build a three-dimensional volume.

To enable the collection of VIS-NIR spectral imaging, the filtered VIS-NIR output of the VARIA is used to illuminate the target region externally. A dichroic long pass filter (cut-on wavelength of 950nm) placed behind the objective lens, then allows bifurcation of light associated with the two modalities; transmitting and reflecting light associated with OCT and spectral imaging, respectively. With such a configuration, spectral images can simply be constructed by sequentially stepping the central wavelength of the spectral band and collecting the signal of sample with a 2D detector, with very little modification to the operation of the spectral domain OCT system. As such, this design benefits from its simplicity, enabling the instrument development and implementation to be carried out within the confines of this work while maintaining portability; enabling the system to be transported on site to objects of interest.

This filter-based design has several advantages. Firstly, its simplicity enables the OCT to be largely unchanged from a typical system. Secondly, the filter-based design enables the collection of all wavelength bands with the optimal photon counts via a generic monochrome camera while reducing the illumination power incident on a sample. Although the spectral resolution of the system is not on par with that obtainable via a spectrograph, the 10nm step demonstrated here, is sufficient for the identification of most common pigments associated with historical paintings.

4.2.2. Considerations in the Choice of Objective Lens

As the proposed design requires the collection of both spectral imaging and optical coherence tomography through a shared objective lens, several constraints in the choice of optics become present. This is especially so here, given that design requires good optical transmission and minimal aberration for a large bandwidth (~400nm to ~1350nm). In addition to this, the balancing of numerical aperture choice for the optimisation of axial depth of field at a 5 μ m lateral resolution; and the preservation of telecentricity to reduce variations in the sampled lateral plane as a function of depth are preferable for use in this application of OCT. With such constraints, lens choice is typically limited.

For this system, a Mitutoyo plano-apochromatic infinity corrected objective (MY5X-822), with a 40mm focal length, was found to perform suitably for this task. This exhibits an adequate optical transmission over the desired wavelength ranges for both modalities, with a minimum of 50% transmission between the ranges of 400nm and 1600nm.

Estimates for the lateral resolutions of both modalities were collated through the imaging of a 1951 USAF resolution test chart placed at the systems focus, producing close parity in the resolution. Here the OCT and spectral imaging modalities were able to resolve Ronchi rulings of 101.6 lp.mm^{-1} and 90.5 lp.mm^{-1} , respectively. In this case, the lateral resolution of the spectral imaging modality is likely limited primarily by the CMOS sensor pixel size of $5.3 \mu\text{m}$. The characterisation of chromatic focal shift for spectral imaging shows the visibility of a 16 lp.mm^{-1} Ronchi rulings in Figure (4.2.2.1). Here the system has been set such that the system is roughly focussed at the 645nm band (the central band captured) with the choice of spectral band discussed in Chapter (4.3).

The use of a long working distance objective additionally provided the benefits of providing sufficient clearance between the probe and sample such that the external VIS-NIR illumination incident on the sample would not face occlusion.

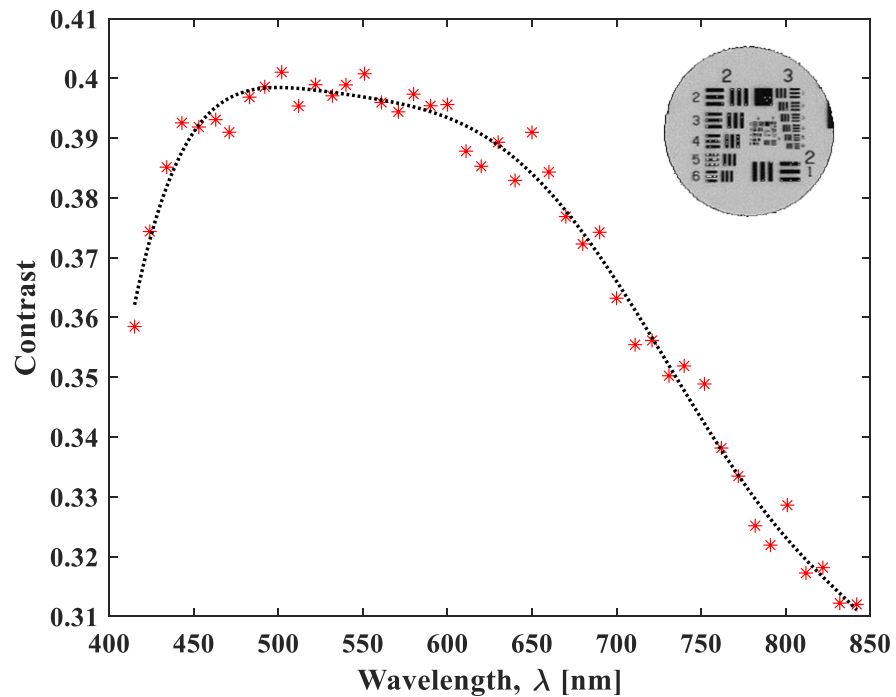


Figure.4.2.2.1. Contrast measurements (red stars) over a Ronchi ruling of 16 lp.mm^{-1} from a 1951 USAF resolution test chart with polynomial fitting (black dashed line). Here spectral images were collected with a bandwidth of 10 nm when the system focussed at a wavelength of 640 nm .

4.3. Spectral Imaging Modality

4.3.1. Collection of Spectral Imaging

As previously stated, spectral imaging within this instrument is based on the collection of the sample reflectance under filtered illumination bands provided by the VIS-NIR output of the varia tuneable filter. The NKT VARIA tuneable filter provides a tuneable spectral band, confined within a region spanning from 390 nm to 850 nm , and with an allowed bandwidth spanning from 10 nm to 100 nm . For this study, 44 spectral bands were collected to build a spectral image, with 10 nm bandwidth and with central wavelengths stepped in 10 nm intervals from 415 nm to 845 nm . This provides data sets with the maximum achievable spectral resolution for the device, while minimising collection times. Here illumination is

provided externally, to the sample via the coupling of the VIS-NIR output via a multimodal patch fibre to an illumination arm affixed to the hybrid probe. Illumination and collection are conducted at 45° and 0° relative to the normal of the plane of sample surface respectively for the reduction of the contribution of specular reflections to the reflectance spectra. Within the illumination arm, the output beam from the fibre is allowed to freely diverge through a motorised shutter before entering a 120 grit N-BK7 glass diffuser to produce a uniform diffuse illumination field over the target region of interest.

After the signal is collected and split from the OCT beam via the objective lens and long pass dichroic mirror respectively, it is refocussed via a Mitutoyo MY5X-802 plan apo microscope objective onto a 2D 1024 by 1280 pixel 10bit CMOS sensor (UI-3240CP-NIR-GL Rev.2 camera) for collection. The associated optical transmission of the probe, quantum efficiency of the camera and radiance of the illumination bands can be seen in Figure (4.3.1.1). With this, the integration time is adjusted such that the maximum intensity is 20% below saturation.

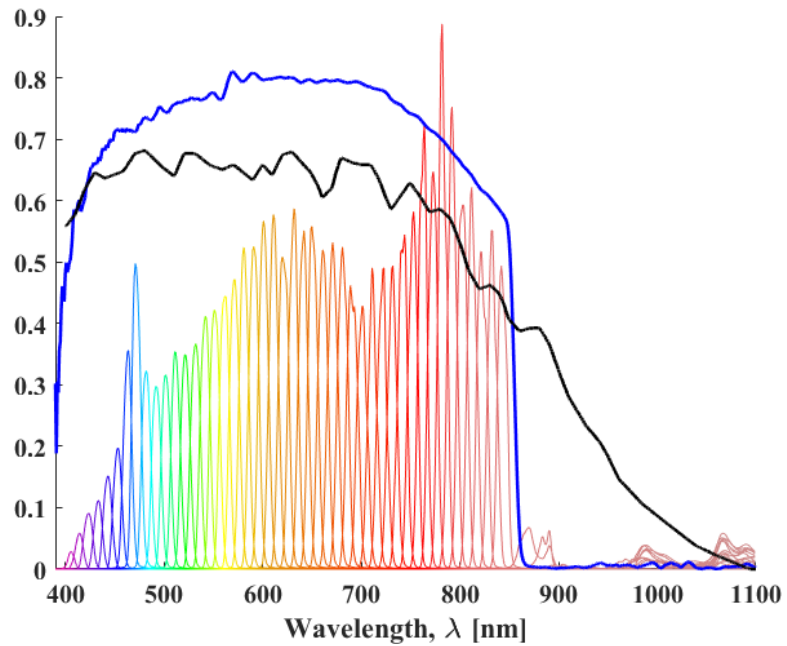


Figure 4.3.1.1. The Quantum efficiency of the monochrome 1280 by 1024 CCD camera (black), total transmission of the spectral imaging optical system with the inclusion of a short pass filter with an 850nm cut-off wavelength (blue) and the radiance of filtered NKT supercontinuum illumination for 10nm bands from 405nm to 845nm (coloured line).

As it is expected that the calibration standard to completely fill the imaging field in the case of the hybrid system, the instrumental flat field correction may be obtained directly from the white calibration counts $I_W(x, y, \lambda)$. Thus Equation (3.1.2.1) can be simplified to produce Equation (4.3.1.1). This will only be true in cases where deviations in intensity across the imaging field, outside of those resulting from instrumental flat field, are negligible. In this application, a British ceramics research 88% reflective white standard was deemed sufficiently smooth and uniform to provide such a case.

$$R(x, y, \lambda) = \frac{t_W(\lambda)[I_S(x, y, \lambda) - D_S(x, y, \lambda)]}{t_S(\lambda)[I_W(x, y, \lambda) - D_W(x, y, \lambda)]} c_w(\lambda)$$

Equation 4.3.1.1

Here $I_S(x, y, \lambda)$ again corresponds to the counts of the sample, $D_S(x, y, \lambda)$ the dark counts at integration times $t_S(\lambda)$ for the sample, $I_W(x, y, \lambda)$ corresponds to the counts for imaging of the white calibration standard at the same focal plane and $D_W(x, y, \lambda)$ the dark counts at the white standards integration time $t_W(\lambda)$. $c_w(\lambda)$ corresponds to a correction factor to account for the spectrum of the white standard. Again, here reflectance is presented as a ratio, scaled between zero and one with one indicating a perfect reflector.

4.3.2. Filter Band Calibration

From Figure (4.3.2.1), it can clearly be seen that the spectral shape of the illumination bands deviates from that of the filter window due to the spectral shape of the super continuum source. Mischaracterisation of the spectral band would result in shifts in the wavelength positions of reflectance spectra features and thus a calibration is required.

To do so, each spectral band was fit to a Gaussian distribution in order to extract an accurate measurement of the central wavelength λ_0 and full width half maximum $\Delta\lambda$. Figure (4.3.2.1) shows the Gaussian full width half maximum bandwidth, and deviation of the bands central wavelength from the varia filter central wavelength providing an accurate characterisation of the band's wavelength position.

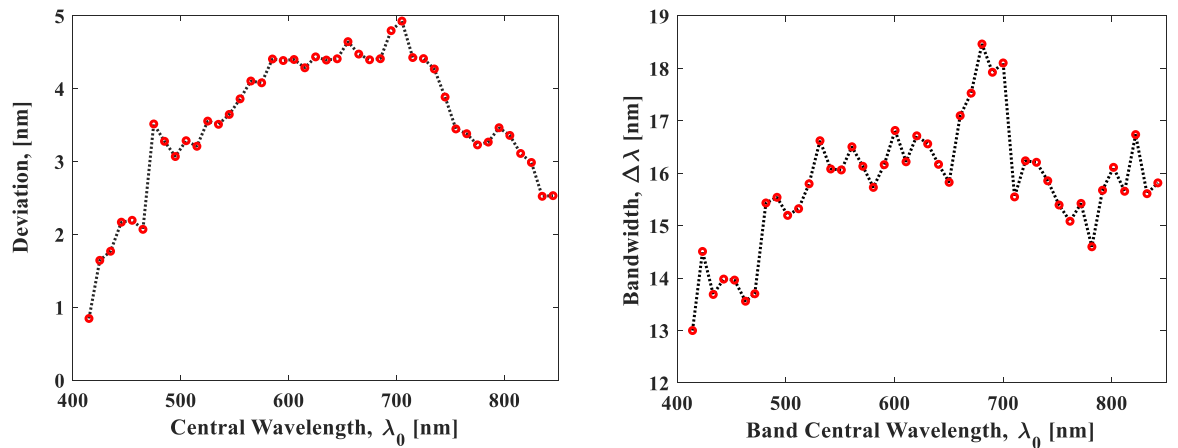


Figure 4.3.2.1. a) the deviation of the illumination band central wavelength from the band pass central wavelength. b) the fullwidth half maximum bandwidth of the filter band given by $2\sqrt{2} \ln[2]$ where σ corresponds to the standard deviation of the Gaussian fit.

4.3.3. Out of Band Illumination Components

It can also be seen from Figure (4.3.2.1), that there exists the presence of out of band spectral components within the illumination bands for wavelengths within the sensitivity range of the CMOS detector. This presents a particular issue as the presence of out of band components in the spectrum may heavily skew the resultant reflectance spectra especially when reflectance is particularly low at a given wavelength band in comparison with the out of band wavelength region. Figure (4.3.3.1) shows a map of the radiance of 10nm illumination bands ranging from 405nm to 845nm incident on a spectralon 99% reflectance white standard as measured with a Spectral Evolution SR-3500 fibre optics spectrometer. It can be seen from the heat map that there exists a significant response within the IR region of the spectrum which significantly grows when the central wavelength of the illumination band is lowered. Thus, to reduce the significance of out of band illumination components, a short pass absorption filter with cut-off wavelength of 850nm is included within the probe, placed between the long pass dichroic mirror and refocussing lens.

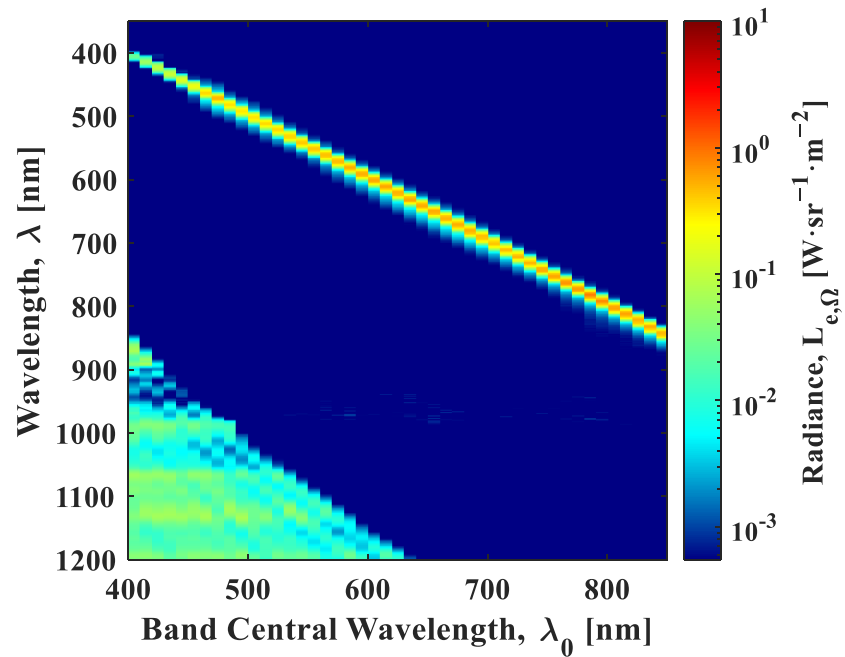


Figure 4.3.3.1. Radiance spectra measurements of the spectral imaging illumination bands as a function of wavelength and the band central wavelength. Significant out of band components of the illumination which are within the detection range of the CMOS camera can be seen for bands below 560nm central wavelength

The relationship between the intensity output of the detector I_c and the reflected signal from a perfectly reflective target sample can be seen in Equation (4.3.3.1) where $T(\lambda)$ is the optical transmission through the probe, $\eta(\lambda)$ is the quantum efficiency of the detector, $I(\lambda, t)$ is the irradiance of the illumination and t corresponds to the time.

$$I_c \propto \iint T(\lambda)\eta(\lambda)I(\lambda, t) d\lambda dt$$

Equation 4.3.3.1

To quantify the contribution of out of band components to the detected signal for a given band, the ratio of contributions from the out of band irradiance components $I_{\text{OOB}}(\lambda, t)$ to the total irradiance can be quantified via Equation (4.3.3.2). Here $I_{\text{OOB}}(\lambda, t)$ is given by the total intensity detected subtracted by the in-band contributions.

$$\frac{I_{\text{OOB}}(t)}{I_c(t)} = \frac{I_c(t) - I_B(t)}{I_c(t)} = \frac{\int_0^\infty T(\lambda)\eta(\lambda)I(\lambda, t)d\lambda - I_B(t)}{\int_0^\infty T(\lambda)\eta(\lambda)I(\lambda, t)d\lambda}$$

Equation 4.3.3.2

$$I_B(t) \propto \int_{\lambda_0 - \sqrt{2 \ln(2)}\sigma}^{\lambda_0 + \sqrt{2 \ln(2)}\sigma} T(\lambda)\eta(\lambda)I(\lambda, t)d\lambda$$

Equation 4.3.3.3

Here the contribution of the intensity from filter band is integrated between the wavelength limits of \pm the fullwidth half maximum from the central wavelength of the illumination band [Equation (4.3.3.2)]. The extracted ratio as a function of the filter band central wavelength is given in Figure (4.3.3.2.a) with and without the additional of the short pass filter.

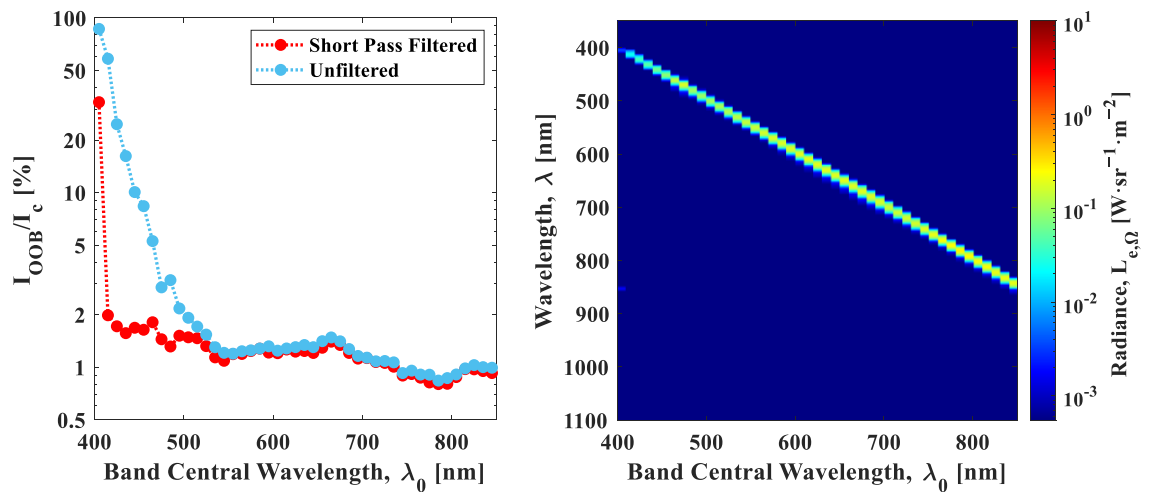


Figure 4.3.3.2. a) The ratio of the expected in band signal to out of band signal as a function of wavelength with (red) and without (blue) the inclusion of short pass filtering. b) Radiance spectra measurements of the spectral imaging illumination bands as a function of wavelength and the band central wavelength with the inclusion of the short pass filtering. The out of band components can be seen to be significantly reduced with exception to the 405nm band.

Significant out of band irradiance contributions are making up the majority of the total irradiance between the 405nm and 415nm band. Introducing the short pass filter limits such contributions to below 2% of the total irradiance over the whole wavelength range of 405-845nm.

4.3.4. Laser Stability

For spectral imaging to be correctly extracted, the spectral irradiance of the incident illumination during data collection of the target sample and white calibration standard must have parity, else such variations will be precipitated into the reflectance calculations. To assess the stability of the supercontinuum source, the visible portion of the source was monitored for a period of two hours from initiating emission, again via a Spectral Evolution SR-3500 fibre optics spectrometer when a constant current is applied to the source [Figure (4.3.4.1)]. To reduce collection time and the beam intensity for measurement, the

supercontinuum laser source was coupled into an NKT VIS/IR Split instead of the VARIA tuneable filter to measure the visible portion.

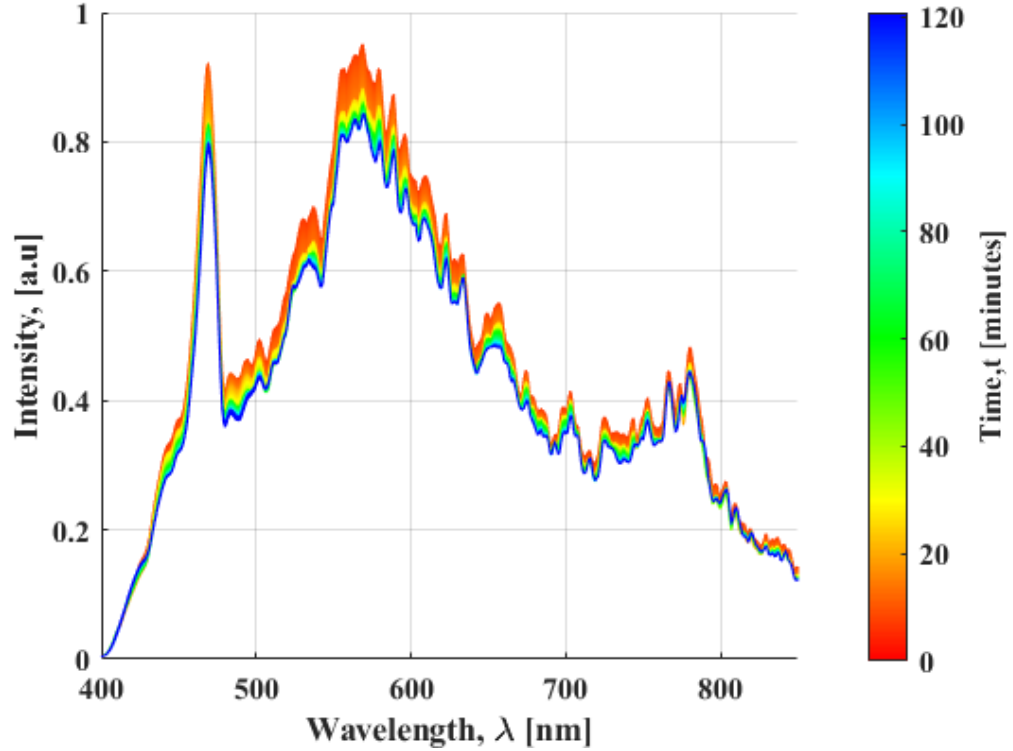


Figure 4.3.4.1. Intensity measurements of the source in the visible range of the super continuum spectrum as a function of time.

If stability has been reached by time t_s , the percentage deviation $D(\lambda, t)$ in intensity from the final stable intensity can be calculated from Equation (4.3.4.1), where $I(\lambda, t)$ is the intensity as a function of wavelength λ and time t ; $\bar{I}(\lambda)$ is the mean intensity once stability has been reached as a function of λ and; $\#N$ is the number of measurements from t_s i.e. $N = \{n \in t: n \geq t_s\}$.

$$D(\lambda, t) = 10^2 \frac{I(\lambda, t) - \bar{I}(\lambda)}{\bar{I}(\lambda)} = 10^2 \left(\#N \frac{I(\lambda, t)}{\sum_{n \in N} I(\lambda, t)} - 1 \right)$$

Equation 4.3.4.1

With the assumption that stability in intensity is reached before the last 20 minutes such that $t_s = 100$ minutes, Figure (4.3.4.2) provides the percentage deviation in intensity over measuring period.

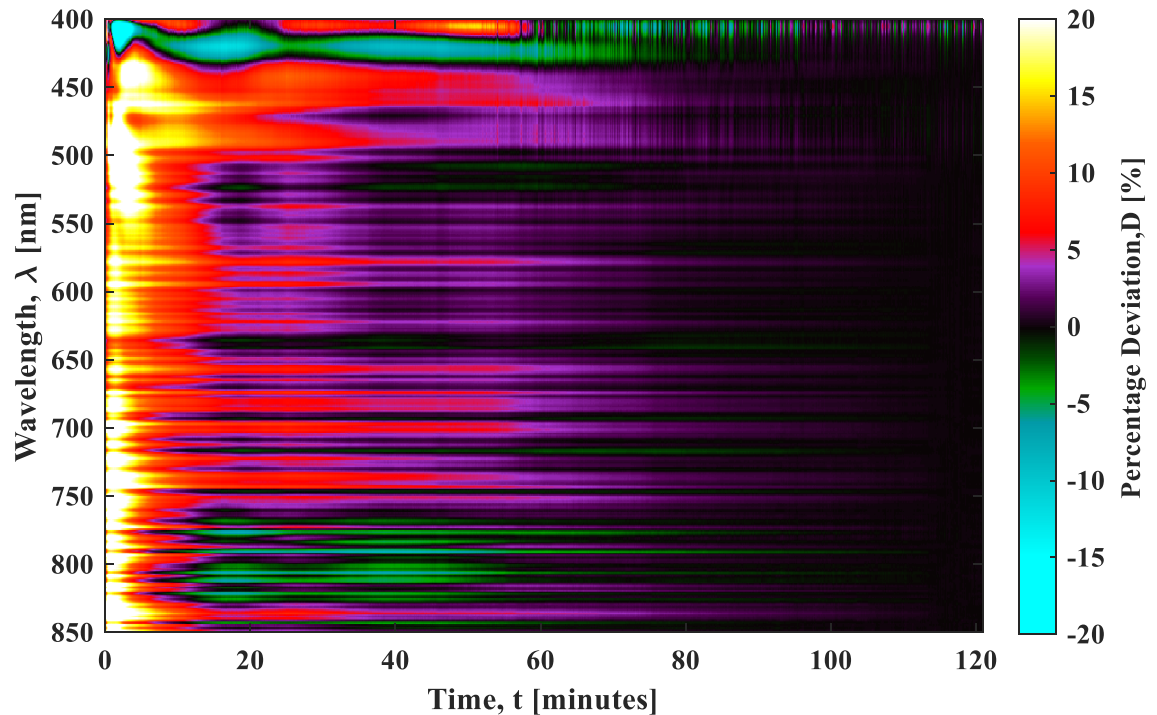


Figure 4.3.4.2. The percentage deviation in the intensity of the super continuum source from equilibrium as a function of wavelength and time from initiating emission.

It should be noted that as a result of low intensity in the measurements below 420nm, noise is seen to dominate the percentage deviation at approximately $\pm 5\%$. For wavelengths above 420nm the intensity can be seen to stabilise to approximately $\pm 3\%$ deviation from stability which would manifest into a maximum deviation in the calculated reflectance of 6%. For the purposes of this work, this was considered reasonable for demonstrating the instrument capabilities but could prove problematic due to the presence of artifical spectral features resulting from illumination differences between images of the target sample and white calibration standard. This could be alleviated by dynamically adjusting the power output to compensate for deviations in laser stability or by monitoring the power output of the spectral band in order to calibrate for such power changes.

4.3.5. Illumination Power and Potential for Light Induced Damage

The spectral irradiance of the resulting diffuse illumination incident on a flat plane at the objective's focus can be seen in Figure (4.3.4.1). To ensure that this does not present any major avenues of damage, the likelihood of photochemical or thermally induced damages were explored. Here in separate experiments, a blue wool 1 test standard and liquid crystal thermometer were exposed to the illumination of each filter band consecutively for a period of 2 minutes, providing an extreme scenario well above the exposure period for the collection of reflectance spectra. The liquid crystal thermometer was deemed to be analogous to the worst-case scenario i.e., in illuminating black paint. The resulting temperature rise throughout the period of exposure was measured with a 2°C precision to produce a temperature increase below 2°C with an ambient room temperature of 20°C and thus deemed to be within an acceptable limit.

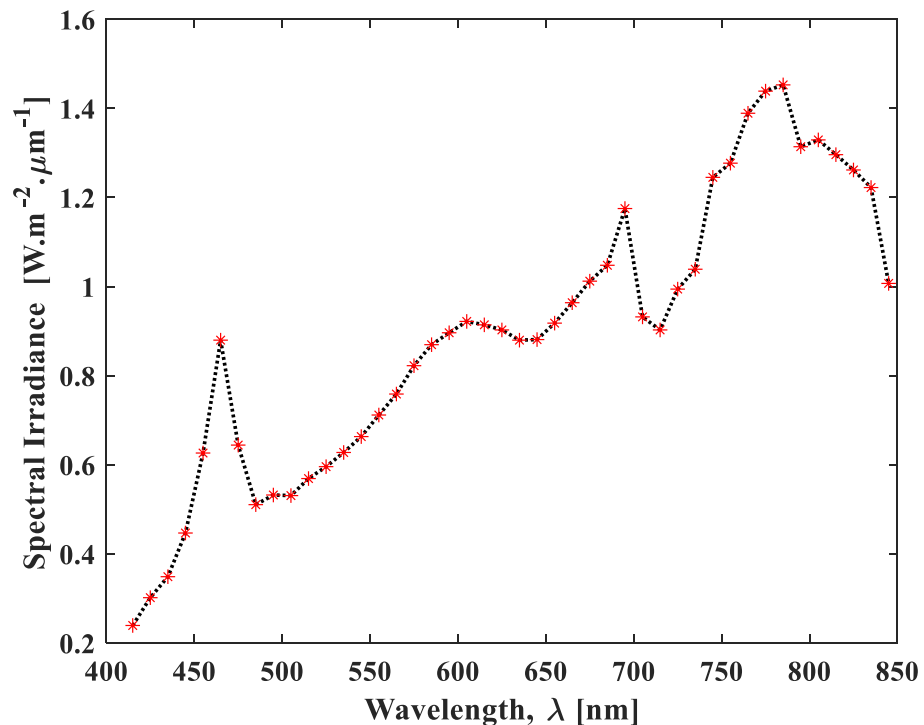


Figure.4.3.1.1. The Spectral Irradiance of the of the filtered NKT supercontinuum illumination for 10nm bands from 405nm to 845nm incident of the sample at focus.

In the case of photochemically induced damage, the effects of exposure were characterised through the change in reflectance ΔR as given in Equation (4.3.4.1). Here the reflectance of an ISO blue wool 1 standard [103,104] was measured prior to and after the exposure period.

$$\Delta R(\lambda, t) = 10^2(R_0(\lambda) - R(\lambda, t))$$

Equation 4.3.5.1

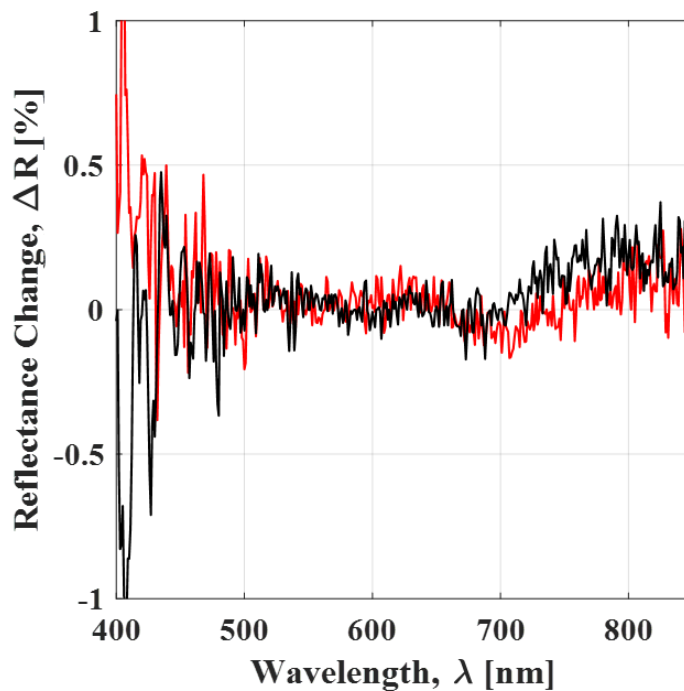


Figure 4.3.5.1. Reflectance deviation for a blue wool 1 standard after irradiation with the spectral imaging illumination (red) for 2 minutes per spectral band and without the spectral imaging illumination (black) over the same period. Here an additional tungsten source is used to illuminate the sample and enable the collection of spectra.

The produced result as shown in Figure (4.3.4.1) shows a negligible reflectance change for the blue wool 1 sample. This is with the exception of measurements above 700nm. Such reflectance variations, however, can easily be attributed to the stability of the tungsten illumination and spectrometer system used to probe reflectance, as such variations are visible with and without the supercontinuum illumination present. This in turn suggests that any

photochemical induced damage to an object will likely be negligible over a more typical collection duration.

4.3.6. *Illumination and Imaging Field*

In an ideal scenario for applications of spectral imaging, a uniform illumination field is required. This is to reduce variation in signal to noise across the image plane and avoid flat fielding artifacts resulting from the projection of a structured light source onto surfaces with varied topography.

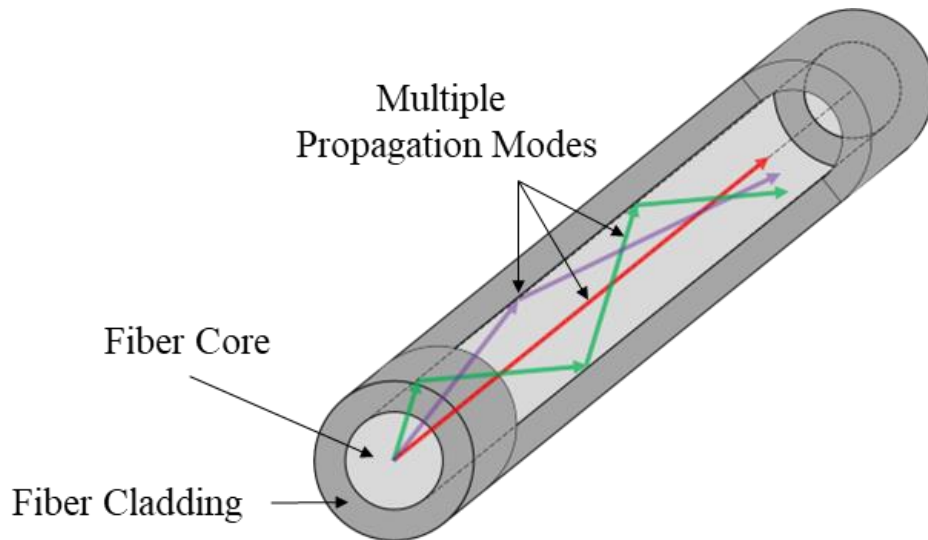


Figure 4.3.6.1. Diagram of propagation modes traveling through an multi-mode optical fiber

In this application, a multimodal fibre has been utilised for its larger core size and throughput over a large wavelength range to guide the VIS-NIR beam to the illumination arm. However, for sufficiently coherent light sources, a larger core size enables the creation of strong speckle structures across the beam profile. This is a result of an increase in the number of allowed propagation modes which follow differing optical paths and travel at phase velocities along the fibre which cumulate to produce interference between modes[105].

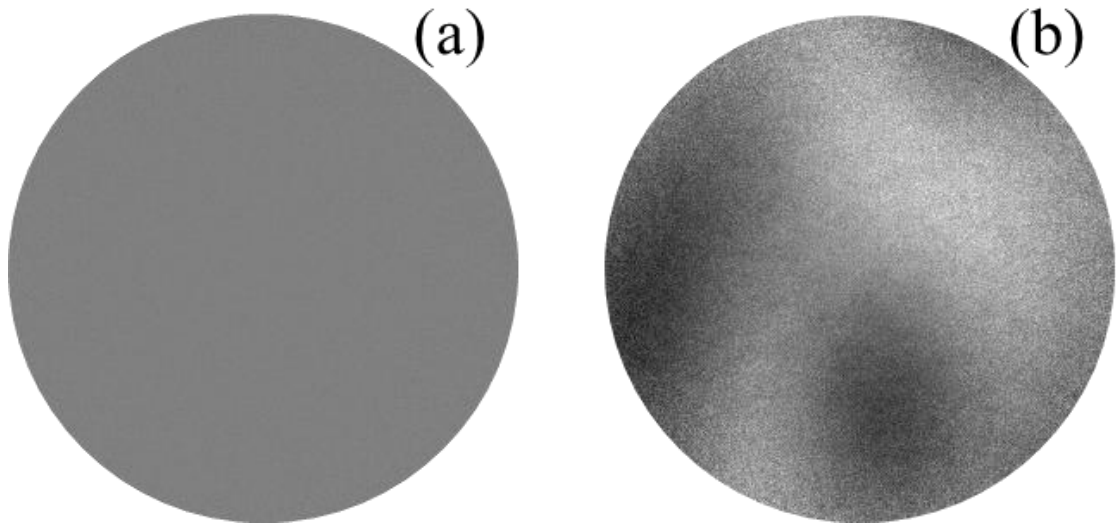


Figure 4.3.6.2. The intensity deviation from median of a white standard imaged under the 665nm illumination band a) with and b) without the inclusion of the diffuser. Both images have been flat field corrected to account for the vignette contributions to the intensity profile

To remedy this, the illuminating beam is allowed to diverge freely from the fibre output before it reaches a 25.4 mm diameter 120 grit N-BK7 glass diffuser which is placed so that the incoming beam fully fills the diffusing area. The effects of the diffuser's inclusion can be seen in Figure (4.3.6.2) in which the presence of speckle patterns within the imaging region is dramatically reduced. Here the imaging field has been corrected for any vignetting resulting from the collection optics.

Alongside, the illumination field, the collection optics are also seen to contribute to flat fielding artifacts along the imaging plane. As previously stated, the current system takes advantage of two Plano apochromatic microscope objectives: a Mitutoyo MY5X-822 VIS-SWIR objective lens for collection of both modalities with a Mitutoyo MY5X-802 for refocussing the collimated signal onto the CMOS array for collection. For diffuse broad band illumination incident on a CERAM (British Ceramics research Association) 88% reflective white standard, the intensity profiles collected across the centre of the image can be seen in Figure (4.3.6.3).

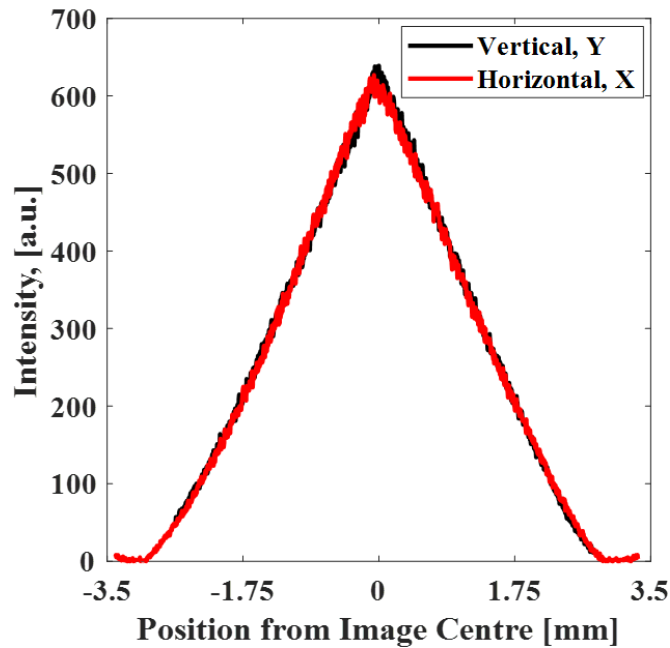


Figure.4.3.6.3. The Intensity profile along the vertical and horizontal imaging plane for a single image taken of a British ceramics research 88% reflective white standard illuminated by a tungsten light source. Here the pixel position of the data along horizontal plane has been displaced so that both profiles coincide.

Here the collected image does not fully cover the CMOS detector, producing an imaging circle in which the intensity reduces dramatically radially from the image centre. This reduction is typical of vignetting, where marginal rays from the periphery of the image are obstructed by an element or aperture within the optical system [106]. As vignetting is systematic for all datasets, the radial reduction in the reflectance can simply be addressed through the flat field correction. However, vignetting will induce a radial reduction in the signal to noise of the system.

The signal to noise in the reflectance image will be a function of the division of the sample image by white standard image and thus noise in the white standard image will precipitate multiplicatively into the reflectance measurements.

To reduce noise that may be precipitated into the reflectance calculations, a median filter with a 10 by 10 kernel is applied to the white standard image. Although the application of the median filter, does result in an increase to signal to noise across the reflectance image, its application will also result in deviations in the reflectance due to the smoothing of the flat field correction.

To quantify the deviations in the flatfield due to median filtering, a 100-scan averaged image of a Ceram (British Ceramics research Association) standard under broadband tungsten illumination was collected and median filtered. The percentage difference $D(r)$ as a function of radius from the image centre could then be calculated between the median filtered $I_{Wfilt}(r, \theta)$ and unfiltered white standard $I_W(r, \theta)$ as seen in Equation (4.3.6.1). To avoid interpolation between pixels when converting to polar co-ordinates, the mean percentage deviation is only calculated over the cardinal directions.

$$D(r) = \frac{10^2}{\#N} \sum_{\theta \in N} \left(1 - \frac{I_{Wfilt}(r, \theta)}{I_W(r, \theta)} \right), \quad N = \left\{ \theta: \frac{4\theta}{\pi} \in \mathbb{N} \wedge \frac{1}{4}\pi \leq \theta \leq 2\pi \right\}$$

Equation 4.3.6.1

The resultant percentage difference can be seen in Figure (4.3.6.4) in which the difference towards the peripheries of the image is seen to increase dramatically. As an arbitrary cutoff, reflectance values are ignored for deviations from the flat field above 0.1%, which is associated with an image intensity of 15% of the maximum intensity in the white standard image. The resulting spectral image therefore spans an imaging circle of approximately 5mm diameter.

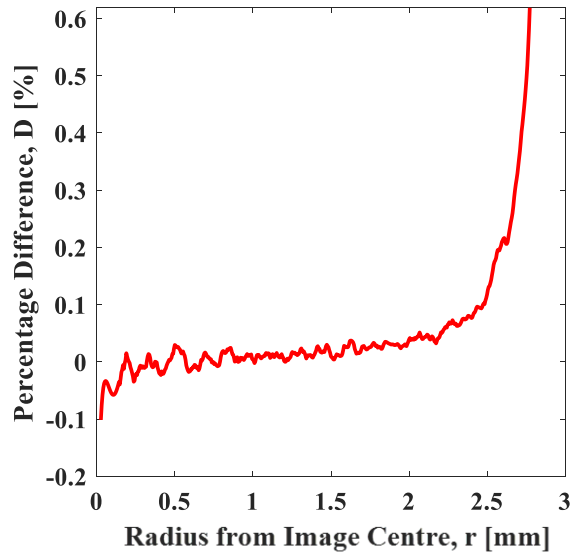


Figure 4.3.6.4. The percentage difference in intensity of the median filtered white standard image from the unfiltered image as a function of radius for a British ceramics research 88% reflective white standard under tungsten illumination.

4.3.7. Microscopic Spectral Imaging of Standards and Samples

The reflectance spectra collected from a mini-Macbeth chart is shown in Figure (4.3.7.1) alongside a colour reconstruction of imaged region and reference spectrum as measured with an ASD inc. LabSpec 4 FORS spectrometer illuminating and collecting at 45° relative to the sample surface. From this we can see close parity between the spectra collected from the hybrid system and a reference spectrum. The slight deviation from the expected spectra as seen in the Macbeth pigments in Figure (4.3.7.1) is most likely to be due to the difference in the illumination and collection geometry between the systems which results in different specular components.

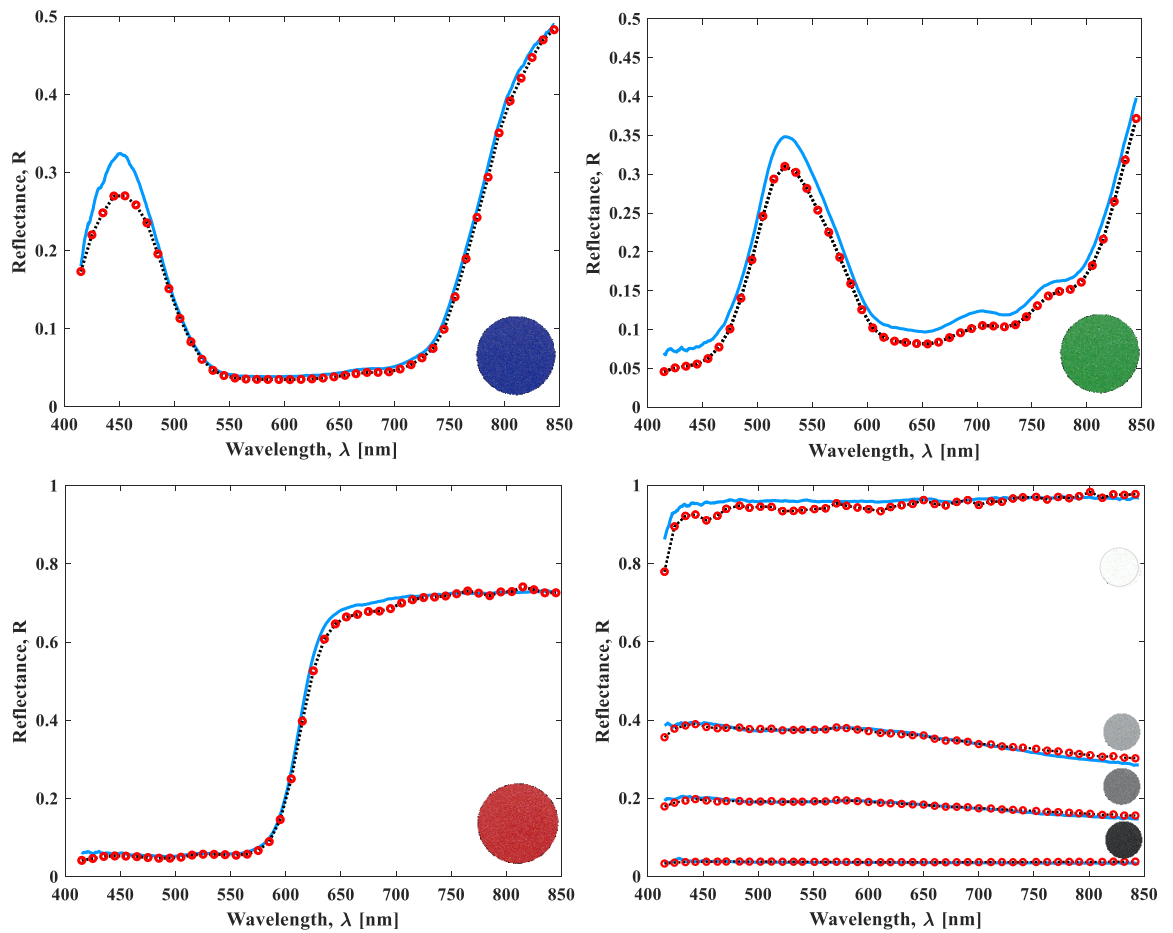


Figure 4.3.7.1. Reflectance Spectra of a mini-Macbeth colour chart measured with ASD inc. LabSpec 4 FORS under tungsten illumination (blue line) and hybrid spectral imaging system (red circles).

The application of the system to some more relevant samples to historical paintings can be seen in Figure (4.3.7.2.a). In this case three samples of madder lake pigments in oil prepared in the National Gallery following different historical methods [Table (4.3.7.1)] [107]. Such madder lake pigments have characteristic absorption features peaking at 510–515 and 540–545 nm which enable them to be distinguished from scale insect-based dyes [69].

Identifier	Absorption Feature Local Minima
MD4a	504nm & 536nm
MD6ai	505nm & 536nm
MD6aii	512nm & 544nm

Table 4.3.7.1

The collected spectra for each sample appear to deviate from that of the reference spectra collected via FORS at the National Gallery, especially toward the infrared where the reflectance appears to remain relatively constant in comparison to the reference. This could be attributed to differences in the region of collection where differences in paint composition and/or paint thickness may be present. A magnification of the identified absorption features can be seen in Figure (4.3.7.2.b). Here it can be seen that despite the comparatively larger spectral sampling step of the hybrid system, the madder absorption features appear to be visible for the MD4a and MD6ai samples but with a relatively low peak prominence it is difficult to confirm their presence with any confidence in the case of MD6aii. The identification of such features could in theory be improved through a more targeted choice of central wavelength illumination band in cases where such features are to be expected.

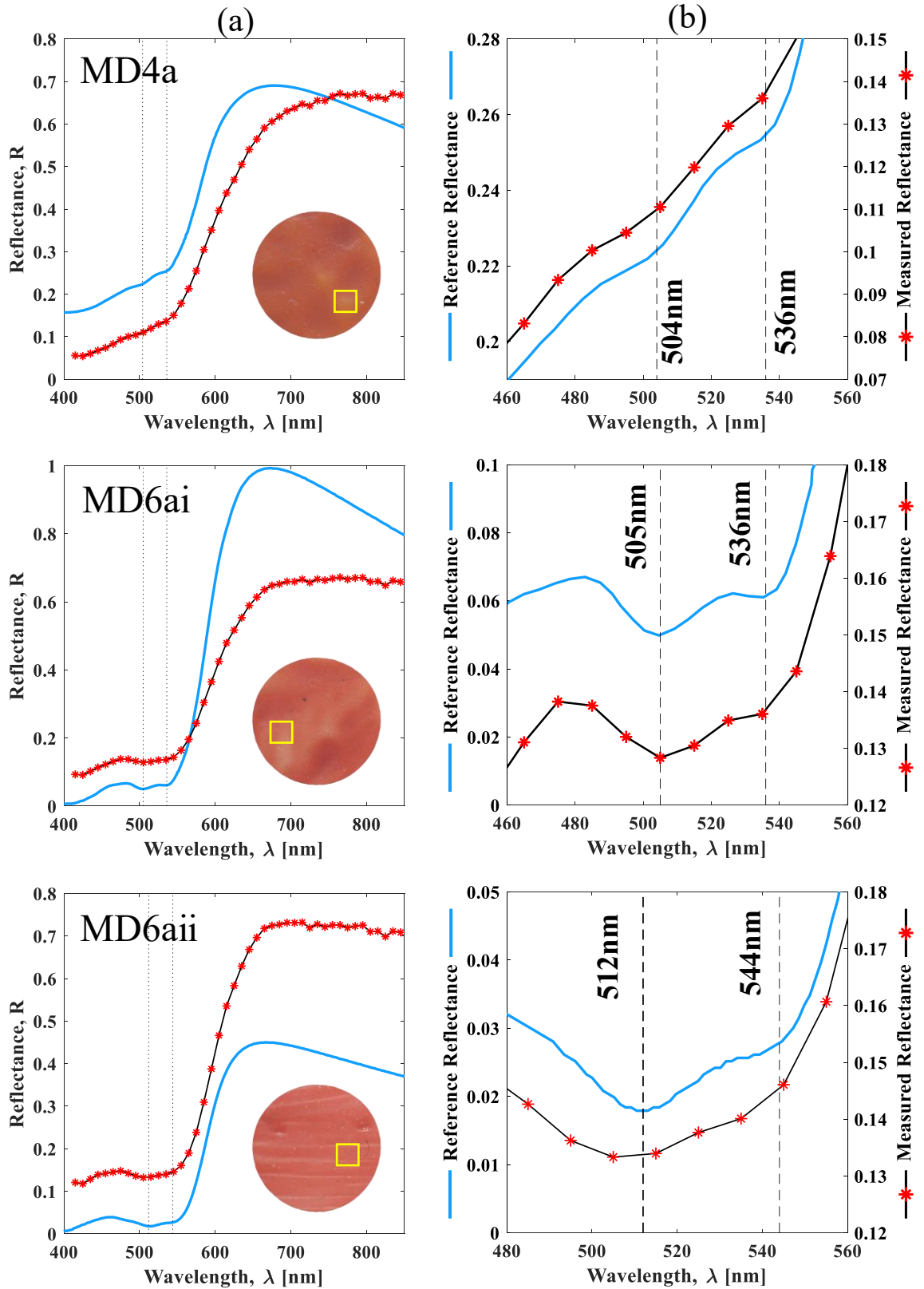


Figure 4.3.7.2. a) The average spectrum of a region of the hybrid spectral imaging cube (red & black) against FORS spectral measurements (blue) for three madder lake pigments in oil data collection regions marked on a colour reconstruction.. b) A zoom in on the characteristic absorption features.

4.3.8. Microscopic Spectral Imaging of Historical Paintings

Within this section, the Hybrid System has been applied for the collection of spectral imaging data from the 15th CE tempera painting NG6580 ‘The Triumph of David’ by Francesco Pesellino housed at The National Gallery, London. Figure (4.2.8.1) displays one of the data collection areas of this painting. Here spectral imaging has been applied for the identification of microscopic pigment particles within several areas of the painting. In this region, it is likely that the binding medium has degraded and discoloured over time, and in many areas the gesso ground layer below the paint is visible.

Dataset s8, collected over a region of semi-transparent blue paint layer can be seen in Figure (4.3.8.2). Here the blue paint region can be seen to consist of resolvable intensely coloured blue particles within a greyish white pigment matrix (likely consisting of accessory minerals associated with the blue pigments) from the colour reconstruction of the spectral imaging data cubes in Figure (4.3.8.2.b). Here the binding medium has likely deteriorated and discoloured over time to produce a brownish layer, and in areas the gesso ground layer below the paint can be seen (yellowish paint region). The inhomogeneity visible in the paint layer at this scale, necessitates more localised analysis of the region. Here five regions of interest, as seen in Table (4.3.8.1), have been collected for discussion with the mean spectrum of each region seen in Figure (4.3.8.2.c) and Figure (4.3.8.2.d).

Region	Region Width × Height [μm]	Descriptor
1	37 × 58	Light Blue Pigment Particle
2	37 × 37	Dark Blue Pigment Particle
3	37 × 37	Blue-Grey Region
4	53 × 58	Grey Region
5	74 × 69	Brown Binding Media Region:

Table 4.3.8.1

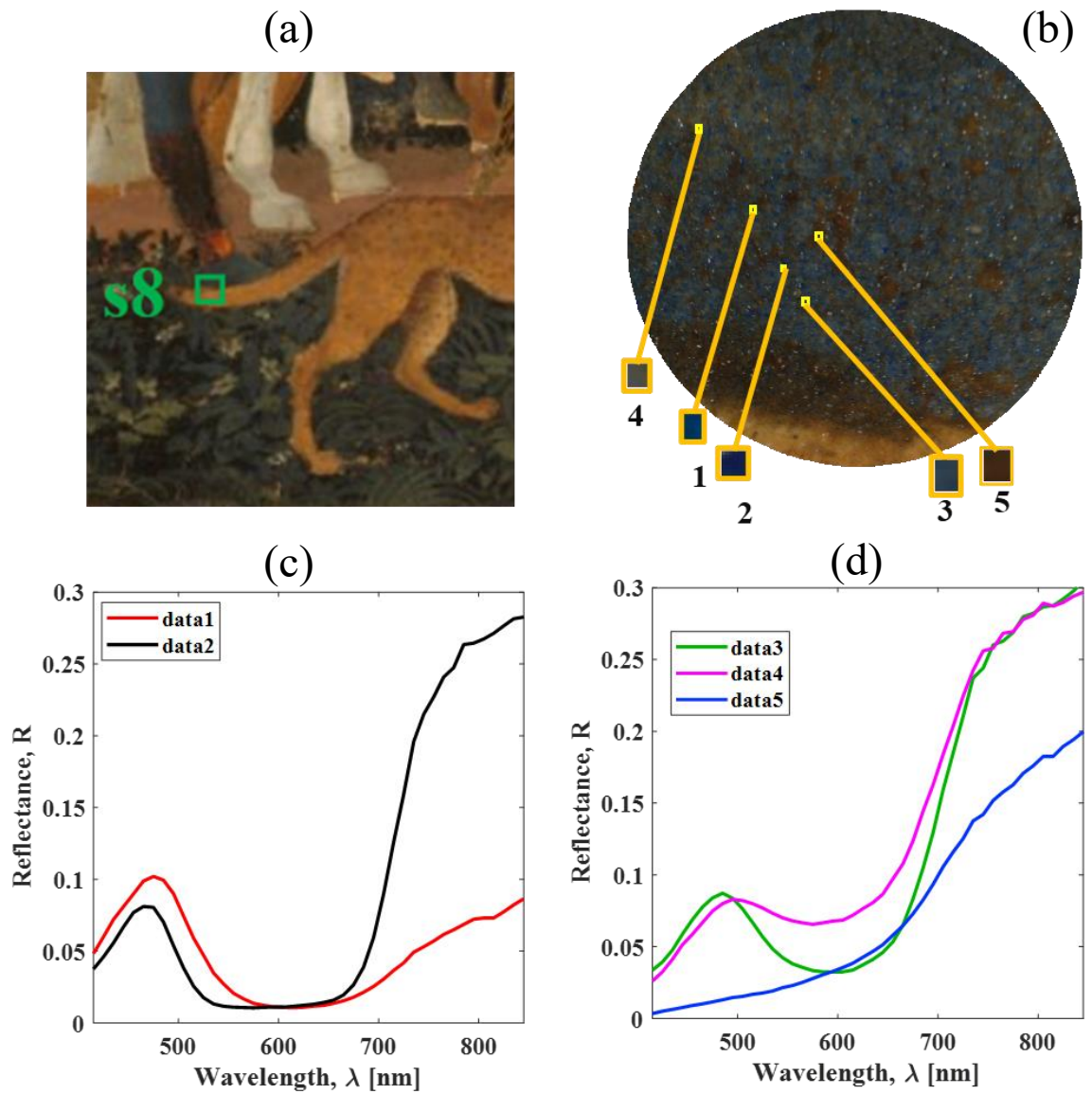


Figure 4.3.8.1. a) A section of NG6580 'The Triumph of David' by Francesco Pesellino © National Gallery London with the region of data set s8 marked. b) Colour reconstruction of regions s8 from the collected spectral image. c) average spectra of blue particles in regions 1 and 2. d) average spectra of regions 3 to 5.

Comparing extracted spectra for resolvable pigment particles in regions 1 and 2 to reference spectra in tempera binder, the pigment particles can be seen to correspond to azurite and ultramarine spectrums respectively as seen in Figure (4.3.8.3). With this however, deviations

are visible in the increased reflectance towards the infra-red spectrum. Possibilities for this deviation could be attributed to contributions to the reflectance from the brown binder and gesso of region 5 and/or contributions from the deviations in the incident illumination for the sample and white standard due to poor laser stability.

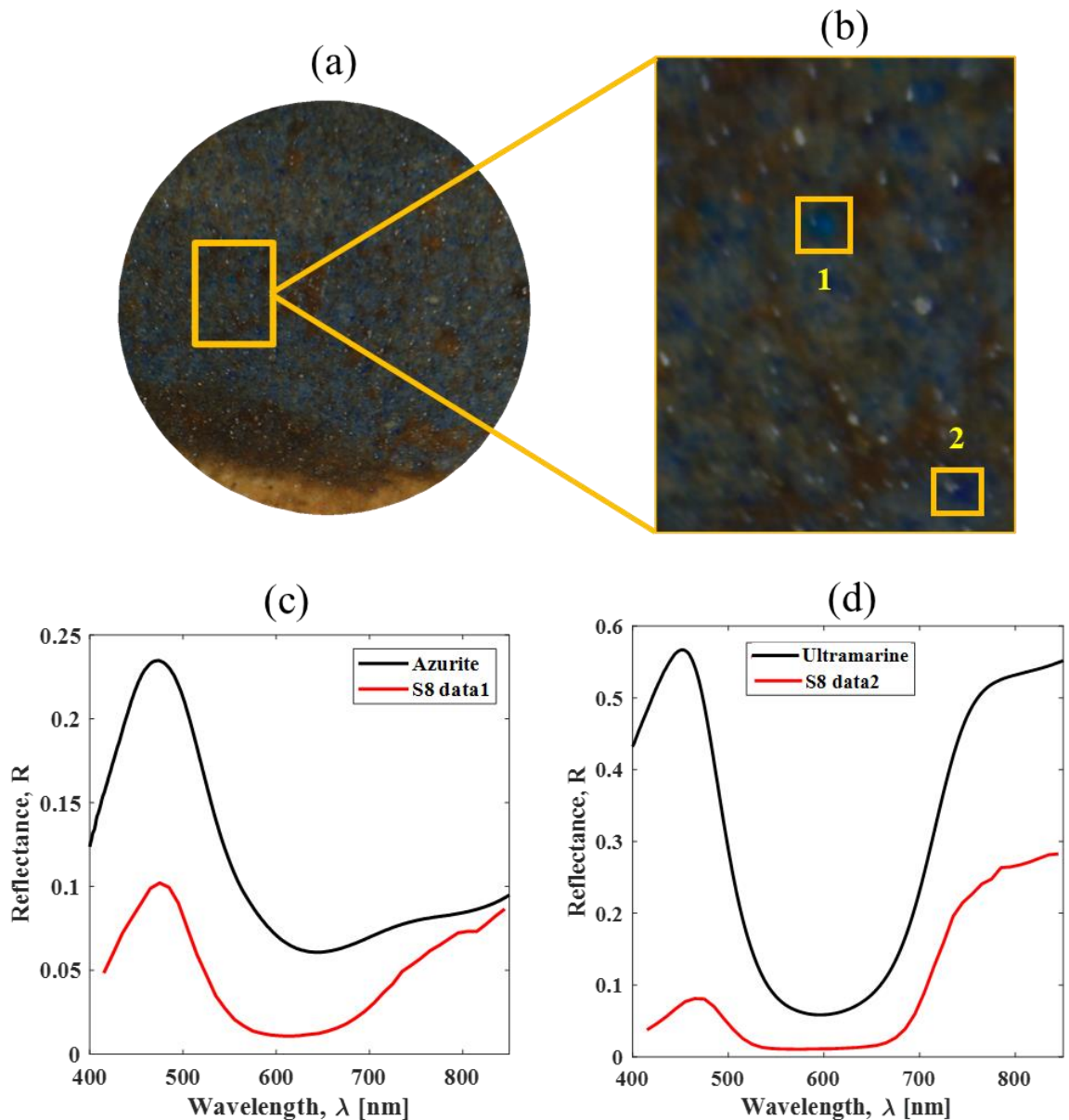


Figure 4.3.8.2. a) Colour reconstruction of data set s8 from the collected spectral image. b) zoom in showing the blue particles in regions 1 and 2. c) Average spectra of regions 1 (red) and reference spectra of azurite in tempera (black). d) Average spectra of regions 2 (red) and reference spectra of ultramarine in tempera (black).

The observation of azurite and ultramarine within this paint layer was previously suspected from the visual appearance of the pigment particles under photomicrography collected by The National Gallery [Figure (4.3.8.3)]. The application of microscopic spectral imaging has therefore provided conclusive evidence for this conjecture through its ability to provide reflectance measurements of particles.

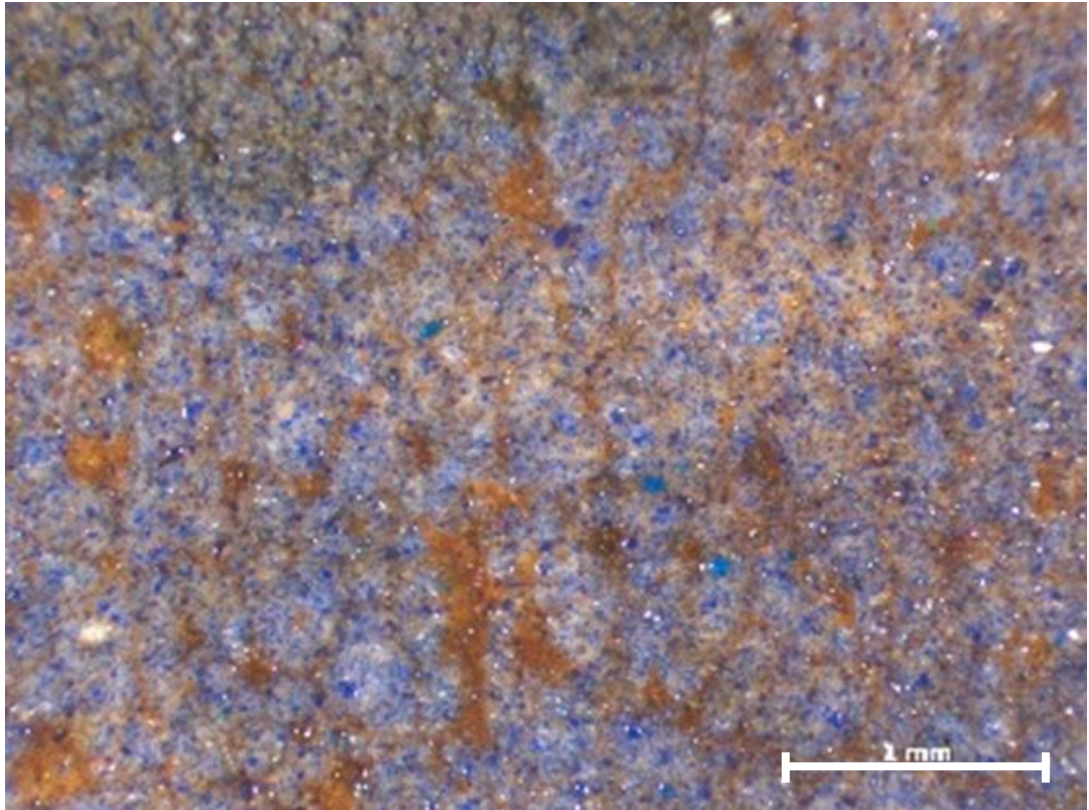


Figure 4.3.8.3. Photomicrography over a similar region to data set s8 showing the the azurite and ultramarine within the brown binding media © National Gallery London

It should be noted that for the microscopic spectral imaging demonstrated here, data sets were not focused optimally and thus, spectral images appear blurred with a reduced resolution. Figure (4.3.8.4) shows the colour reconstruction for a region taken from the late 19th CE painting ‘Girl with upturned Nose’ by James Ensor housed at the Royal Museum of Fine Arts, Antwerp. With the collection of data at a more optimal focussing of the system, particles of down to 16 μ m diameter are resolvable

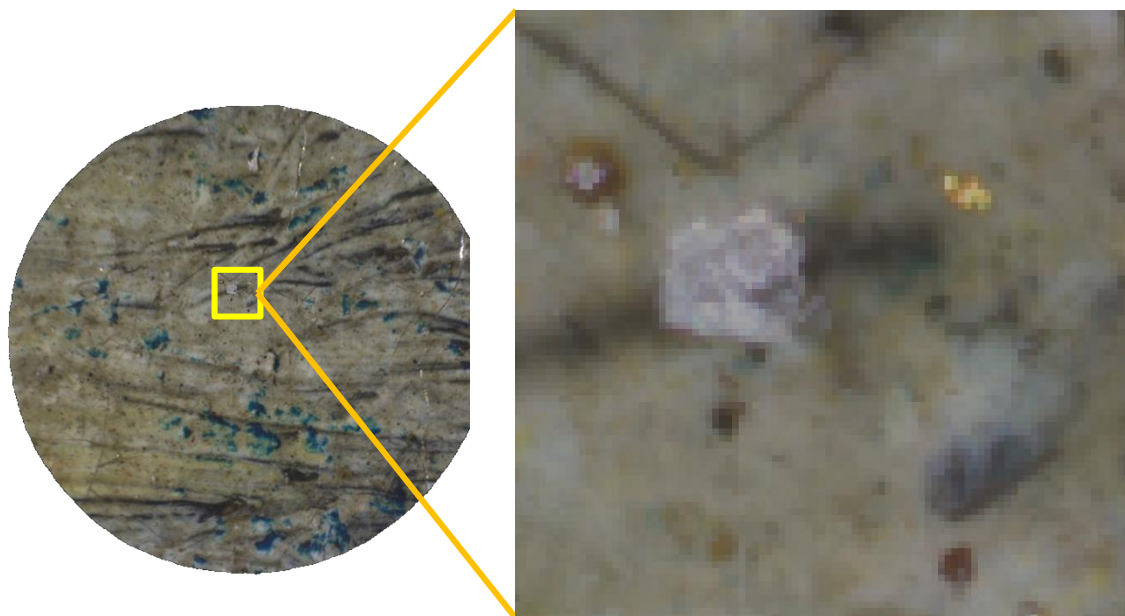


Figure 4.3.8.4. Colour reconstruction of a spectral image collected within the white bow in the painting 'Girl with upturned Nose' by James Ensor. The zoom in of the region (right) covers a region of roughly 0.5mm width by 0.5mm height.

Reflectance spectra were also collected from dark layers applied over the gold leaf in a number of areas of the painting NG6580. In analysis carried out by the National Gallery, macro x-ray fluorescence scanning (MA-XRF) indicated that such layers contain copper and thus were most likely to be that of a green paint/glaze which has degraded and discoloured over time.

Elsewhere within the landscape of the painting where copper is detected by XRF scanning and the paint still appears green, SWIR reflectance measurements of the region confirm that a copper-based green mineral pigment was used which contains some copper carbonate. A sample from an equivalent area confirms the use of a copper-based green mineral pigment containing copper carbonate and copper sulphate. The matrix has slightly darkened, suggesting some reaction with the binding medium, but the pigment particles still appear green.

It was therefore of interest to understand whether the dark coloured copper-containing layers applied over the metal leaf originally contained the same green mineral pigment seen in the landscape or a different copper-containing material. With the higher resolution of the hybrid instrument, it was hoped that it might be possible to extract spectra from any residual green particles as well as the surrounding matrix. Data set s16 was collected from the paint/glaze over the gold trappings of the brown horse on the left side of the painting.

The paint in question appears as a dark reddish-brown matrix with localised regions of green pigmentation [Figure (4.3.8.5)]. Again, the mean spectra within several regions [Table (4.3.8.2)] are shown and provide localised microscopic reflectance measurements from the data set as seen in Figure (4.3.8.5.c) and Figure (4.3.8.5.d).

Region	Region Width × Height [µm]	Description
1	196 × 217	Yellow-white ground layer
2	228 × 201	Gold leaf
3	69 × 132	Reddish-coloured region of the paint /glaze
4	69 × 69	Greenish-coloured region of the paint/glaze
5	37 × 207	Brownish-coloured part of the paint/glaze

Table 4.3.8.2

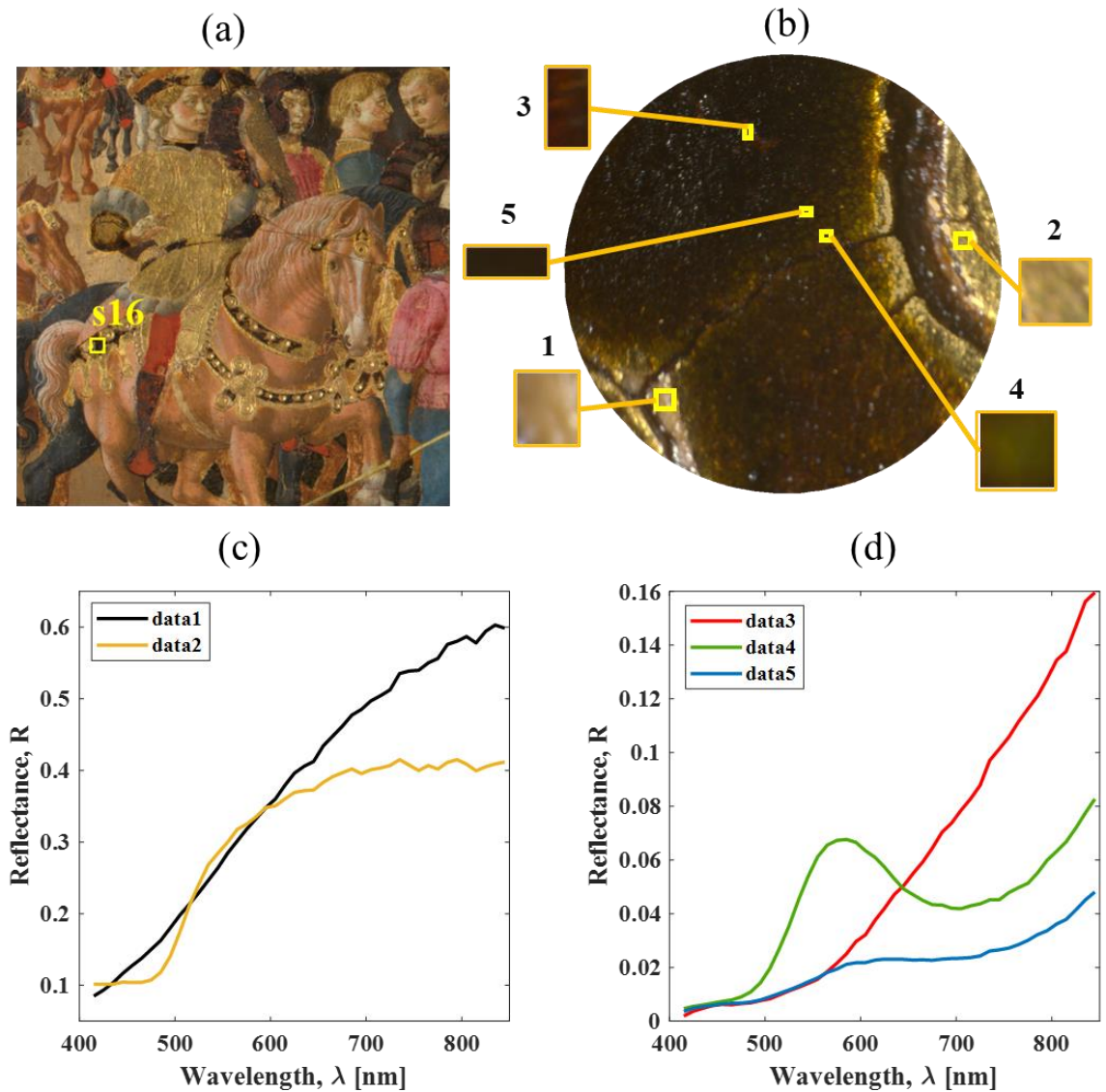


Figure 4.3.8.5. a) A section of NG6580 'The Triumph of David' by Francesco Pesellino © National Gallery London with the region of data set s16 marked. b) Colour reconstruction of regions s16 from the collected spectral image. c) average spectra of regions 1 and 2 corresponding to the ground layer (black) and gold (yellow). d) average spectra of regions 3 to 5 corresponding to glaze on gold

As expected for region 1, no clear spectral features from the ground layer are detectable within the measured wavelength region. Region 2 can be seen to be consistent with the reflectance spectra of gold leaf reported in Aceto et al., 2014 [69], producing an inflection point at approximately 510nm [Figure 4.3.8.6)].

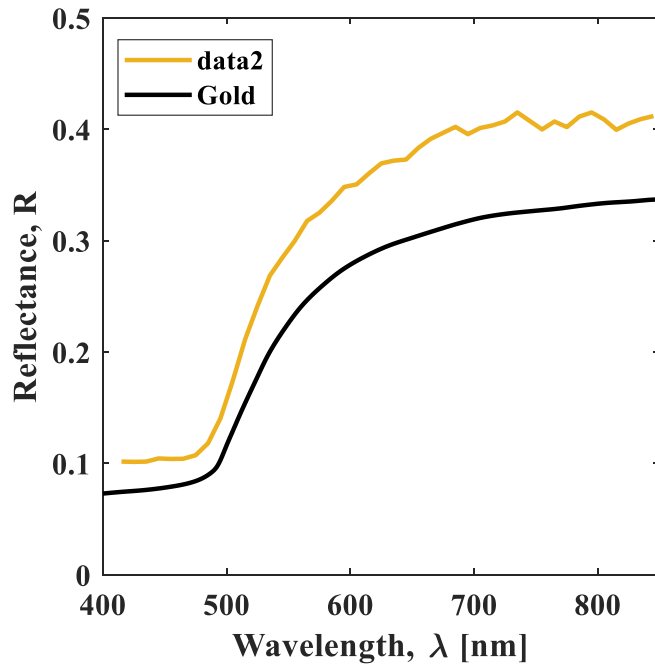


Figure 4.3.8.6. The mean reflectance spectra of region 2 of data set *s16* (yellow) alongside the reflectance spectra of gold described in Aceto et al., 2014.

Figure (4.3.8.5.d) shows the spectra obtained from the three areas of the copper-containing paint/glaze. For a painting of this period, the potential copper-containing green pigments are typically either copper-based green mineral pigments, which often contain some copper carbonate; or synthesised copper green pigments which are in essence the salts of organic acid (acetic acid for verdigris, resins acids from pine resin for copper resinate etc). It should also be noted that many copper-based pigments are quite reactive, leading to colour change and/or reaction with the paint binding medium. For a mineral green, such reactions can result in materials that are chemically similar to synthesised copper green pigments.

As noted by Aceto et al., 2014, the reflectance maximum of green pigments can shift (in pigment mixtures or potentially if the pigment reacts with the medium or environment) and for unreacted pigments they suggest that the apparent absorption band and spectrum shape are more reliable means of identification.

Comparing the extracted spectral features of the greenest coloured region of the paint/glaze (region 4), to a reference spectrum obtained from the sample of copper resinate seen in Chapter (3.3.1) multiplied by the reflectance spectra of gold leaf [Figure 4.3.8.6], a fairly close match between the two spectra can be seen [Figure (4.3.8.7)]. However, while the copper resinate shows an absorption band centred at approximately 695 nm, the spectrum from region 4 shows an absorption band centred at a slightly higher wavelength of 705nm. It is possible that the glaze layer contains copper resinate or possibly verdigris (which Aceto et al suggest has an absorption band centred at 720 nm) which may have reacted with the binding medium resulting in slight spectral shifts [108]. However, given the difficulties of using reflectance spectra in the visible/NIR to distinguish green copper-based pigments and their known reactivity, the use of a green mineral pigment in the glaze (as employed in the landscape paint) by the artist cannot be excluded if the pigment has reacted with the paint medium and undergone degradation processes. It is likely that the entire layer contains the same pigment but that this is of a less degraded condition in regions 3 and 5.

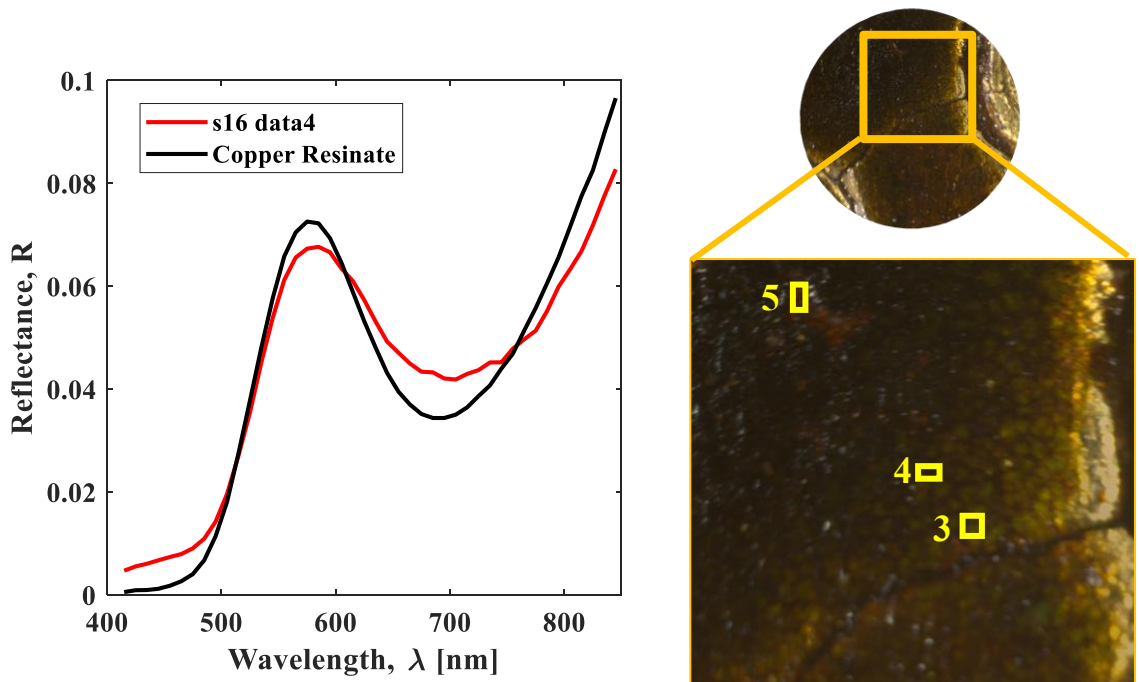


Figure 4.3.8.7. The mean reflectance spectra of region 4 of data set s16 (red) compared with the copper resinate sample simulated over gold (black) alongside the colour reconstruction of the spectral image

Although no conclusive identification of the original pigment can be made, the application of the microscopic spectral imaging provided by the hybrid system here, offers the ability to locally extract spectral measurements from such paints and glazes at differing stages of degradation. At present the chemistry of and the changes to spectra as these materials react and degrade is not well enough understood to be able to fully interpret the spectra. It is likely that a more comprehensive study on the spectral characteristics of the degradation products of copper-based pigments in various mixtures and under known conditions would be a great asset to sector for the interpretation of such scenarios.

4.4. Optical Coherence Tomography

4.4.1. OCT Design

The design of the OCT component of the combined instrument shares many of the same characteristics from the ultra-high resolution spectral domain OCT discussed in chapter 2, with modifications made to allow for the operation of the instrument in the near infrared region. In this case, the system is designed around a fibre-based Michelson interferometer utilising a Thorlabs TW1300R5A2 2×2 fibre coupler, centred at 1300nm with a 100nm bandwidth; and the coated fibre tip of a Thorlabs SMF28ER-50-1 fibre optic patch cable as a 50% reflective reference mirror.

Before coupling into the input arm of the interferometer, the broadband IR source is first conditioned to make it suitable for use in OCT. This entails the spectral shaping and attenuation of the beam, via a long pass dichroic filter (1180nm cut-on wavelength) and an absorption based neutral density filter (20% transmission), reducing the contribution of the prominent 1060nm laser pump within the spectrum and decreasing the incident power from the order of watts to milliwatts. In doing so, the power of the beam incident on the target sample is restricted to a non-destructive level of 1.0 mW.

The returning interferometric signal is collected via a spectrograph at the interferometer collection arm which consists of a reflective collimator and Watash Photonics 1145 lp.mm⁻¹ transmission grating (1310nm central wavelength) positioned such that the 1150nm-1350nm wavelength region of the interference spectra is collected. The spectrum of the continuum incident on the camera can be seen in Figure (4.4.3.1). Here the spectral shaping of the source by the optical components of the system, produces a continuum centred at 1260nm with a full width half maximum of 100nm.

To minimise the spot size of the beam incident on the detector, a wider collimated beam at the grating is desirable, thus a reflective collimator with a 22mm aperture is used to produce

a ~ 9 mm diameter beam incident on the grating. Collection is handled via a 1024 pixel ($25\mu\text{m}$ pixel size) 14-bit InGaAs linear array (SUI 1024-LDH camera connected through a camera link frame grabber NI PCIe 1433) preceded by a 50.2mm diameter achromatic doublet (75mm focal length), with an Thorlabs C anti-reflective coating (1050nm-1700nm) used to focus the light onto the detector.

The detector provides a maximum line rate of 47.348 kHz. For a typical OCT volume of 500 by 500 A-Scans with a $10\mu\text{m}$ transverse sampling resolution, and a collection of 180 A-scans for background subtraction per B-Scan, the minimum collection is therefore approximately 8 seconds excluding time required for data readout.

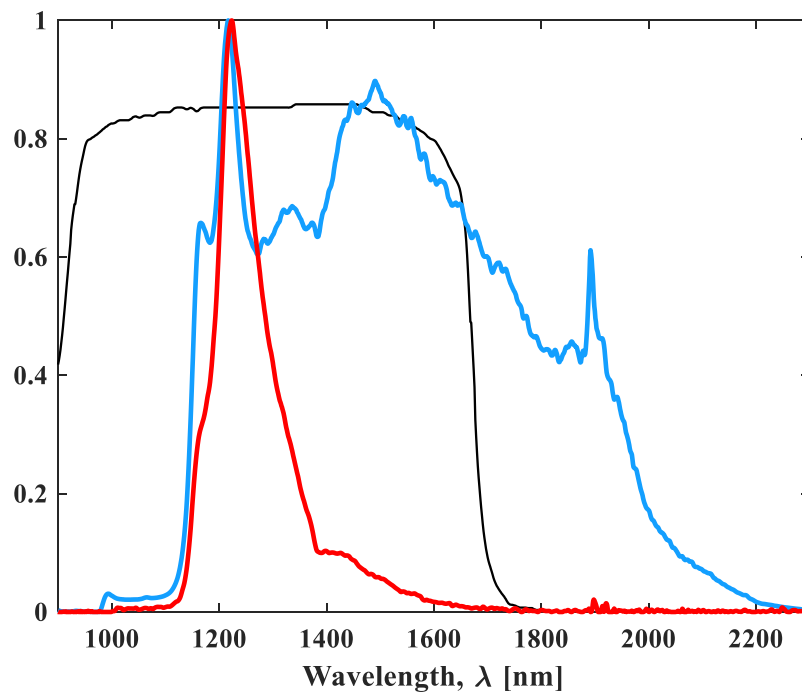


Figure 4.4.1.1. The quantum efficiency of the detector of the spectrometer (black), normalised spectra incident on the fiber coupler (blue) and normalised spectra incident on the grating of the spectrometer (red)

4.4.2. OCT Calibration

The associated response of the OCT spectrograph for returning signal from the reference arm is shown in Figure (4.4.2.1). It should be noted that the spectrograph used here for the demonstration of OCT is non ideal and serves only as a proof of concept. Imperfect 3D alignment between the detector focal plane and the focussed spectrum after the grating are to be expected alongside chromatic aberration due to the achromatic doublet used for refocussing.

To provide an approximate calibration for the spectrograph, an initial 6th order polynomial fitting to six known emission peaks of a Micropack Hpx-200 xenon arc lamp light source was carried out. This was in turn further refined via an optimisation of the polynomial fit in which the polynomial was varied iteratively to minimise the standard deviation in width of the axial point spread function at varying depths [22]. Here an air glass interface is positioned at the objective focus and the reference pathlength changed to produce a variation in depth.

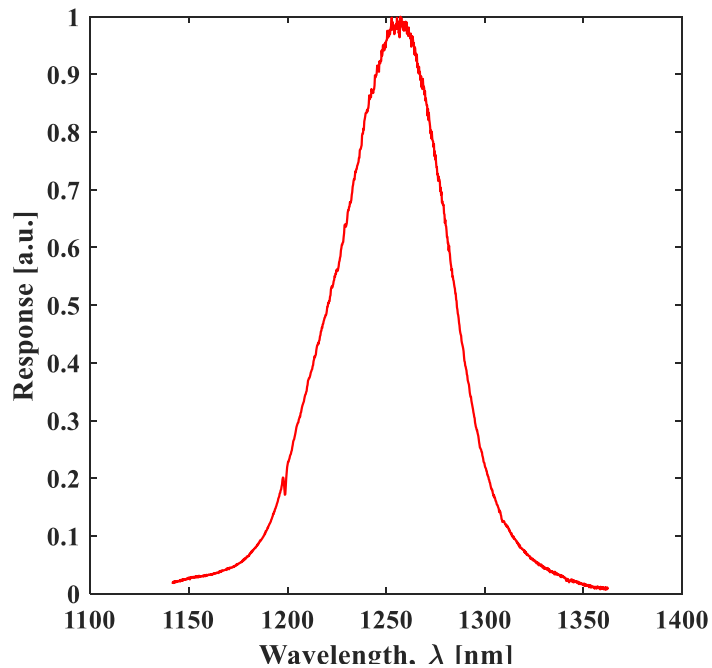


Figure 4.4.2.1. Normalised spectral response from the reference mirror by blocking the sample arm

To produce A-Scan depth profiles, the calibrated spectrum is background subtracted and then linearly resampled to the minimum k step via spline interpolation. This produces the maximum aliasing free imaging optical path length and a minimum axial sampling resolution of $1.185\mu\text{m}$. In this case, background measurements are collected with the sample arm blocked via the redirection of the galvanometer mirror away from the objective.

With this, the maximum aliasing free imaging optical path length over the spectral response can be calculated as seen in chapter (2.2.5) from the calculation reiterated here in Equation 4.4.1.1. In this case λ_0 is the wavelength and $\delta\lambda$ the sampling rate. to produce Figure (4.4.1.2.a). Here it can be seen that corruption of the A-scan due to aliasing will become present at approximately 1.8 mm at the central wavelength.

$$Z_{max}(\lambda) = \frac{\lambda_0^2}{4\delta\lambda}$$

Equation 4.4.2.1

Finally, before Fourier transform, apodization is applied to the resampled spectra via the Hann windowed function seen in Figure (4.4.1.2.b). This in turn reduces sidelobes within the axial point spread function of the interface below 40dB of the interface peak so that they can be treated as negligible in comparison to any successive interfaces in the depth profile.

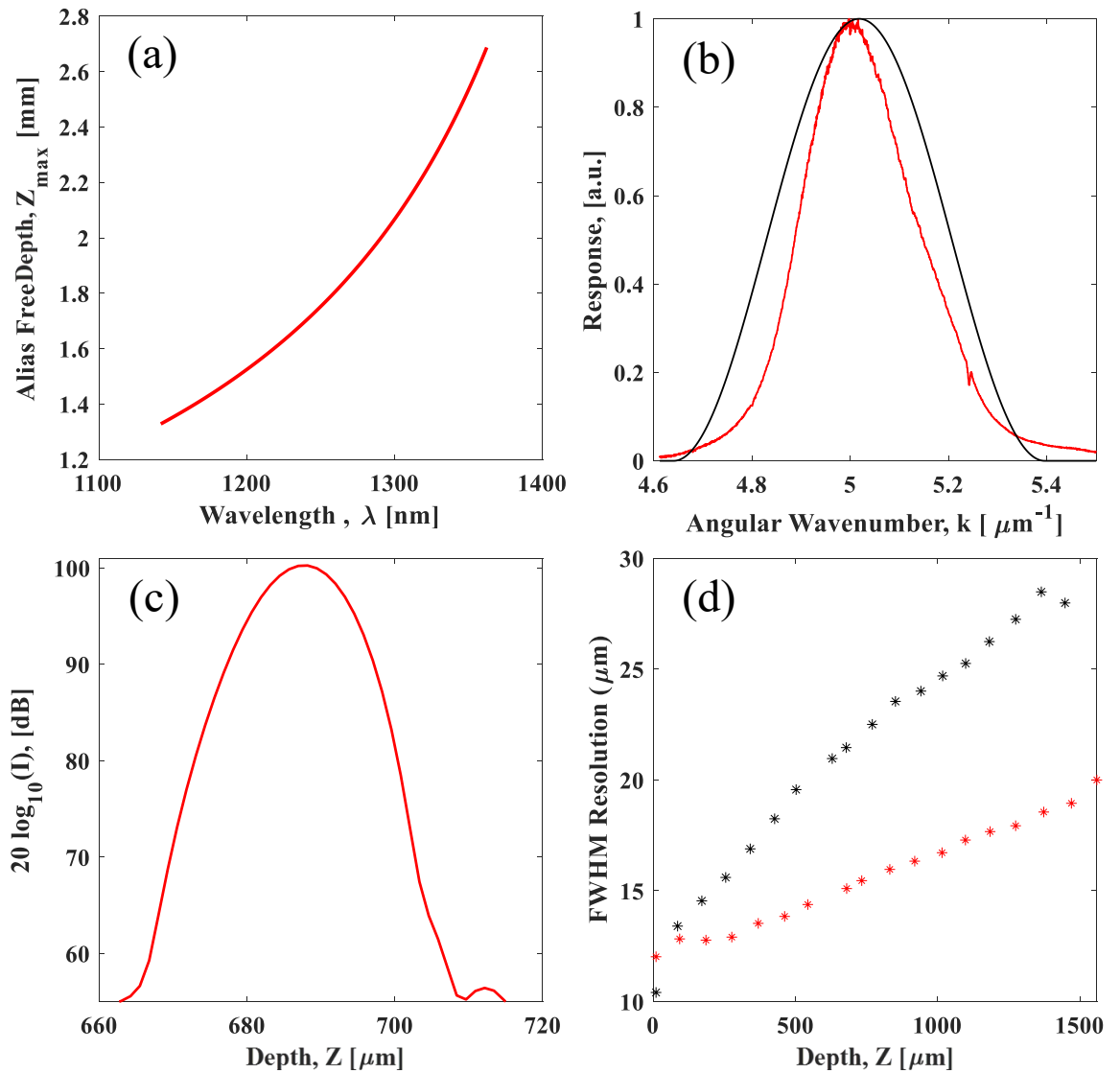


Figure 4.4.2.2. a) The theoretical alias free depth as a function of wavelength. b) The spectrum incident on the detector (red) alongside the Hann windowed function applied during processing as a function of angular wavenumber. c) the axial point spread function of an air-glass interface positioned at a depth of 685 μm . d) The FWHM axial resolution as a function of depth with (red) and without optimisation (black)

Figure (4.4.1.2.c) shows the resultant axial point spread function for an air-glass interface at depth of 685 μm alongside the associated FWHM resolution as a function of the imaging depth for both the initial and optimised wavelength calibration [Figure (4.4.1.2.c)]. Although a clear improvement can be seen from the optimised calibration, resolution is still seen to be degenerative with increasing depth but has since been amended through the

instrumentation alterations described in Chapter (4.4.6). For the purposes of demonstrating the functionality of the hybrid instrument, the calibration computed was deemed suitable for this work as the layer thickness in the proceeding examples are within the resolvable range of the instrument.

4.4.3. *A-scan Depth Profile Characterisation*

A typical A-scan depth profile of the air-glass interface of a glass block positioned at a depth of 600 μ m can be seen from the red line in Figure (4.4.1.3).

A distinctive depth dependence in the noise floor is clearly visible. This is characteristic of OCT under supercontinuum illumination [22,109–112] with its mechanisms discussed by Jensen et al [111]. Here, the variation in the noise floor is described as precipitating from the correlation of the excess photon noise over different scales when the sampling of the super continuum is at a great enough spectral resolution and sampling rate.

For this work, the noise floor is subtracted from the depth profile to remove the intensity variation in the background across the depth. This subtraction is provided via a 5th order polynomial fit to an A-scan of 250000 averages with the sample arm blocked for a given integration. To avoid overfitting, the DC peak contributions are excluded from the polynomial fitting with the extracted relationship interpolated to cover the entire depth range. As the contribution of the light on the spectrometer detector in most cases is expected to be dominated by the reference arm, this was found to be a relatively consistent approximation of the depth dependent trend in the noise floor.

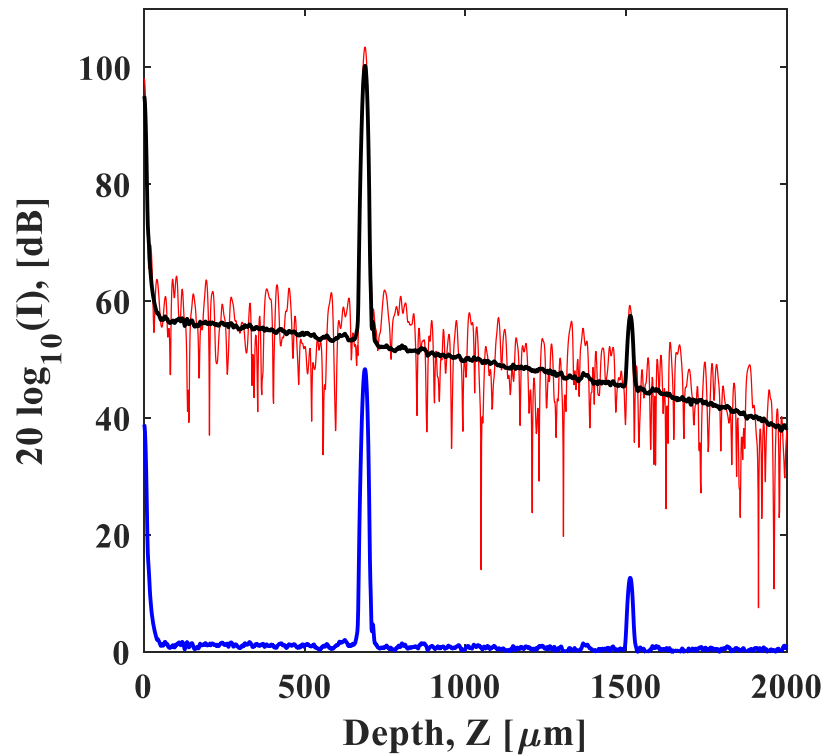


Figure 4.4.3.1 Single A-Scan of a glass block (red) compared with a 500 scan averaged A-Scan (black) and 500 scan averaged A-Scan after noise floor subtraction (blue)

With the removal of the noise floor, the system sensitivity can be characterised. Measurements of a single air-glass interface are collected at varying depths through the variation of the reference path length.

Here the peak can be approximated to the maximum intensity in the A-scan as seen in Equation 4.4.3.1. Here $I(z)$ is the A-scan intensity as a function of depth z , I_p is the interface peak intensity, z_p the peak depth and z_c a minimum depth as to avoid the inclusion of DC components in the calculation of the peak position.

$$I_p(z_p) = \max_{z \geq z_c} [I(z)] \quad , \quad z_p = \operatorname{argmax}_{z \geq z_c} [I(z)]$$

Equation 4.4.3.1

Equation (4.4.3.2) gives the ratio between the peak intensity $I_p(z)$ of an air/glass interface and $\sigma(z)$ the standard deviation in intensity calculated over $\#N$ scans as a function of depth estimated by the average of the noise floor intensity at $\pm 20\mu\text{m}$ from the peak position to avoid contributions from sidelobes to the calculation.

$$\text{SNR}(z_p) = \frac{I_p(z_p)}{\sigma(z_p)}$$

Equation 4.4.3.2

The resultant signal to noise (SNR) as a function of depth for an air-glass interface centred along the optical axis is visible in Figure (4.4.3.1.a). In this case the standard deviation of the noise was calculated for 500 depth profiles with an integration time of $21\mu\text{s}$ per A-Scan. Here roll-off in SNR produced is approximately 14dB over the first 1.3 mm, becoming significantly worse with increasing depth.

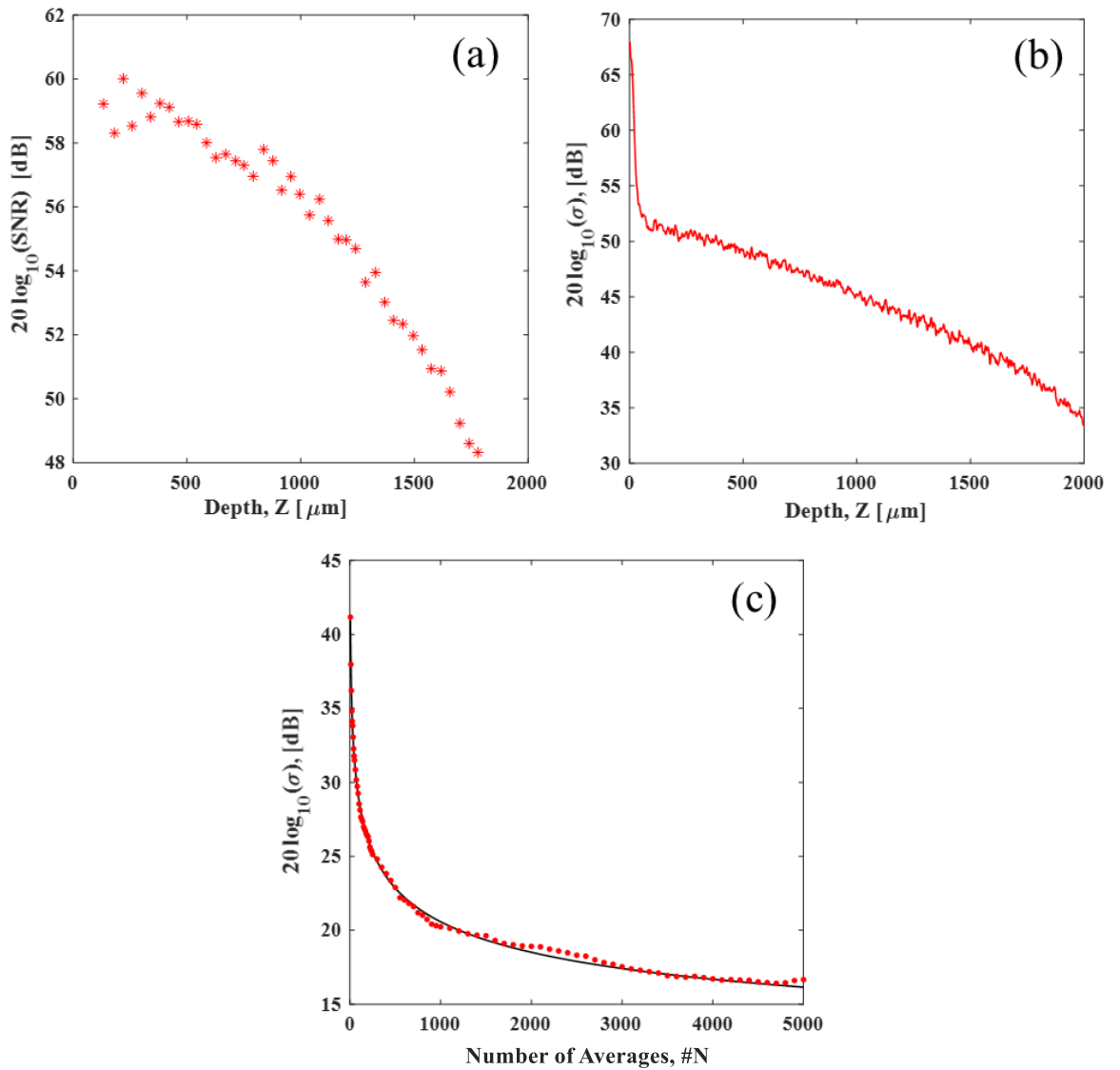


Figure 4.4.3.1 a) The signal to noise of an air glass interface at the objective focus with depth, b) the standard deviation in the noise floor with depth. c) The standard deviation in the noise floor with number of A-Scan averages (red) alongside $1/\sqrt{\#N}$ trend (black) fitted to the data.

Without a constraint in collection time, improvements in SNR can be made through the averaging of numerous scans. Figure (4.4.1.3.c) shows the variation in noise at depths ranging from $500\mu\text{m}$ to $600\mu\text{m}$ with growing number of averages, #N. This holds good agreement with expected behaviour for shot noise, following a reciprocal of $\sqrt{\#N}$ relationship. However, it should be expected that with the use of such super continuum sources, the system SNR will not eventually reach the shot noise limit because of high pulse-

to-pulse relative intensity noise (RIN) which scales with the incident illumination power [111]. The noise profile with depth z as seen in the reference only noise over 500 scans is seen in Figure (4.4.1.3.c) and demonstrates a reduction in the standard deviation with depth. With this, the reduction in the sensitivity resulting from the depth dependant noise floor will be in competition with the sensitivity roll off associated with the finite sampling of the spectra, producing an optimum depth range over which OCT can be collected.

The dynamic range of an OCT system is given by $DR = I_P/I_{bkg}$ at the focus of the objective for a 100% reflective surface. This is commonly referred to as the sensitivity of an OCT system. Assuming that the glass surface is positioned perpendicular to the probing beam, the reflectivity of the air-glass interface is expected to be $\sim 4\%$. This in turn would translate to a reduction of 14dB in the interface peak intensity for a perfect reflector. When including contributions from the objective lens depth of field, a reduction of 2dB is visible at optical pathlengths of $100\mu\text{m}$ from the objective focus and thus the objective lens focus has been centred around $500\mu\text{m}$ where the dynamic range is optimal. At this position the maximum dynamic range of this system at a depth of $500\mu\text{m}$, as determined by the ratio of the peak intensity of a perfect reflector and the sample free noise floor intensity, is 73dB. This again can be improved by averaging more scans until a RIN dictated limit is reached.

4.4.4. OCT Volume Characterisation

For this study, to maintain consistency with the ultra-high-resolution system described in previous chapters, OCT volumes and or cross-sectional B-Scans are collected with dimensions of 5mm by 5mm in the lateral plane x and y such that the lateral sampling resolution is equal to $10\mu\text{m}$. A typical example of such a B-Scan for an air-glass interface is visible in Figure (4.4.4.1.a). The objective lens used here produces a prominent Petzval field curvature [106], displacing the interface depth position depending on the lateral position [Figure (4.4.4.1.b)]. Here with an interface positioned at the objective focus, such that the surface is perpendicular to the optical axis, the maximum deviation in the interface depth position can be seen to be approximately $176\mu\text{m}$.

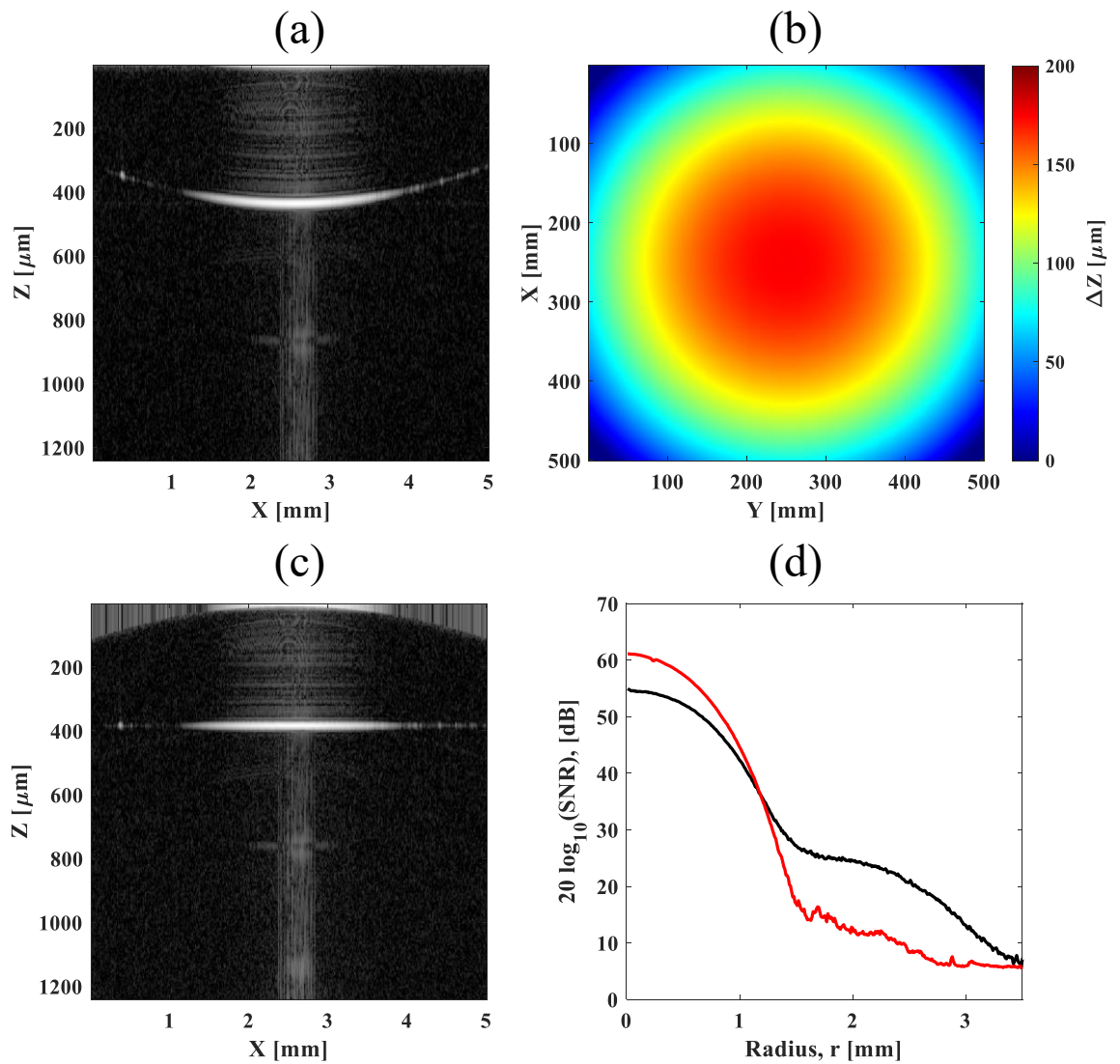


Figure 4.4.4.1 a) B-Scan of an air-glass interface along the centre of the volume b) The image field curvature across the collected OCT volume c) The field corrected B-Scan of an air-glass interface. d) The signal to noise of the interface as a function of radius from the image centre for a specularly reflective air-glass interface (red) and a scattering air-marterial interface for a British ceramics research 88% reflective white standard (black)

Such field curvature in the interface can simply be accounted for by the displacement of each component A-Scan within the volume. However, with the degradation in resolution with imaging depth present within the system; it can be inferred that the resolution along the optical axis for a flat interface is limited to a maximum of $12.8\mu\text{m}$ if the entire plane is to be imaged. To correct for field curvature [Figure (4.4.4.1.b)] each constituent A-Scan in the OCT volume is simply padded at the beginning of the A-Scan with intensity values equal to

the intensity in the first depth element as seen in Figure (4.4.1.2.c). The use of the first element is arbitrary and in this case aids to simplify segmentation processing by avoiding the introduction of artificial interfaces when calculating gradient images.

The SNR of an interface is also expected to decrease with increasing radius from the volumes centre similar to that seen for the spectral imaging in Chapter (4.3.6). The SNR as a function of radius across the lateral plane can be seen in Figure (4.4.1.2.d). As a qualitative assessment of the SNR across the lateral plane, a single specularly reflective air-glass interface and scattering Ceram (British Ceramics research Association) 88% white standard interface, both centred at a depth of approximately 400 μ m, have been collected. The resulting SNR calculations show an increased lateral field of view obtainable from the OCT volumes of scattering layers in comparison to specularly reflective layers in which the SNR decays to 15 dB at approximately 1.5mm from the image centre in comparison to the 25dB seen in the matt white standard.

4.4.5. Application of Hybrid OCT to Historical Painting

In this section, the hybrid OCT has been applied to the analysis of the painting NG6580 discussed in chapter (4.2.8). Here OCT has been applied in the exploration of the original decorative techniques being used by Francesco Pesellino in NG6580 ‘The Triumph of David’. In many regions of the painting, the burnished metal and silver leaf has been decorated with patterns of incised lines, tooling and ornamental punch marks with such marks providing additional decoration, helping to distinguish details (e.g. to mark haloes against a gilded background) and/or providing local variations in the path of specular reflections allowing the metal leaf to appear as if it was sparkling. A range of tools could be used including a stylus for linear details as well as pattern-ended punches for other types of decoration [113].

As each artist’s tools were hand-made, with tools possibly shared or handed down between artists working in the same workshop, characterising such tools can be important in studies of attribution and understanding artistic influences and workshop practice [114,115]. A

variety of approaches have been used to record and characterise punch marks and other tooling on metal leaf, including high resolution photography, 3D digital microscopy and OCT [25].

Figure (4.4.5.1.b) shows the colour reconstruction from the spectral imaging of a region of the tooled gold of the white horse's saddlecloth, with the corresponding OCT volume marked. The B-Scan cross section of the region [Figure (4.4.5.1.c)] reveals clear indentations on the order of 40 μm to 150 μm in depth into the gold surface with the presence of a semi-transparent scattering layer within some of the indentations. In this case such marks would have been created by tapping the shaped punch held vertically against the metal leaf with a hammer. By segmenting the air-gold interface, an axial depth map can be extracted corresponding to the interface, allowing the global measurement of the indentations across the volume as seen in Figure (4.4.5.1.c). Here the apparent vertical banding in the depth map corresponds to vibration artifacts rather than the tooling marks. From the map it can be seen that the punch produced indentations which were approximately triangular in shape with lateral major and minor axis lengths ranging from $\sim 25 \mu\text{m}$ to $\sim 70 \mu\text{m}$ and $\sim 15 \mu\text{m}$ to $45 \mu\text{m}$ respectively.

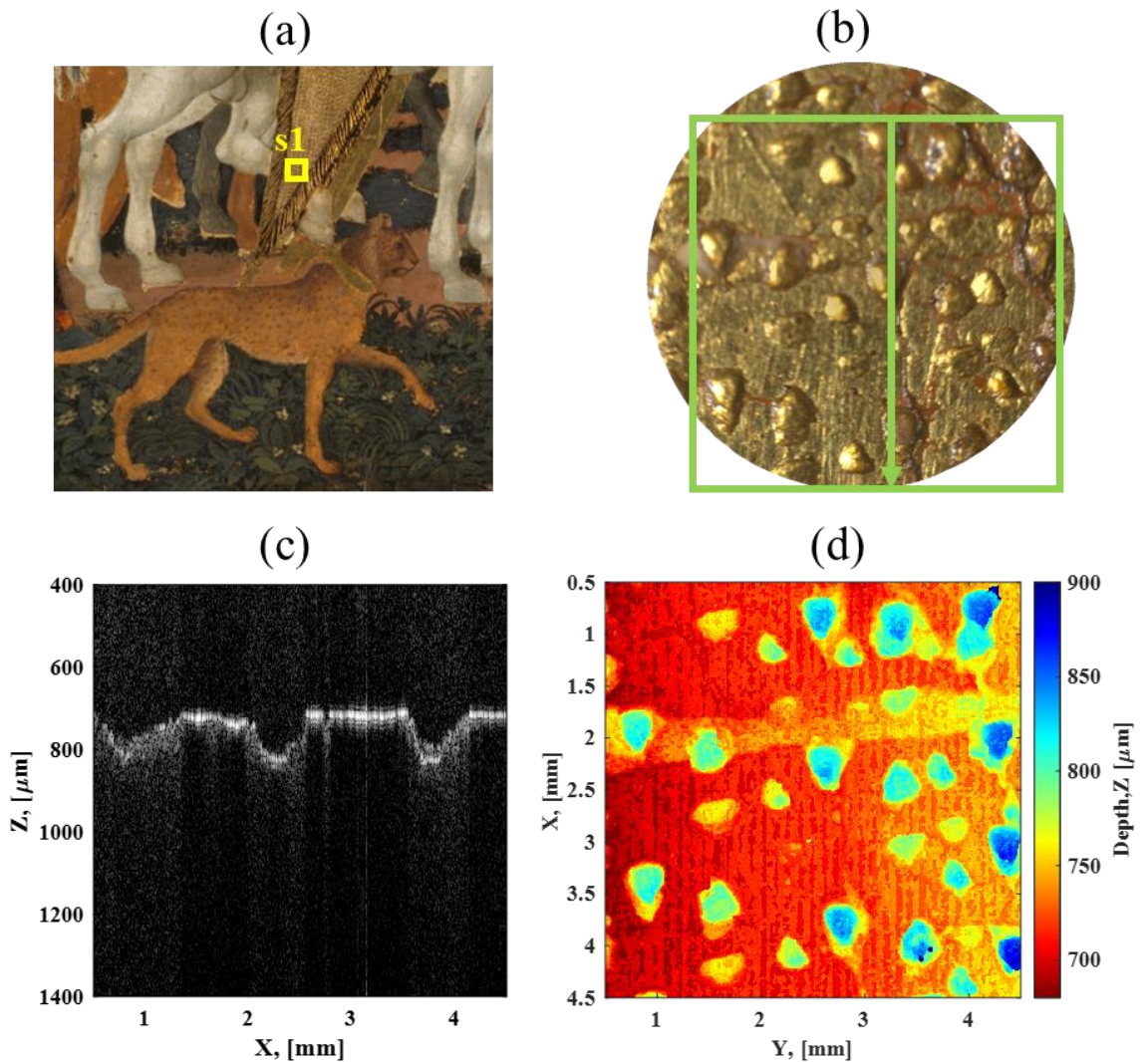


Figure 4.4.5.1. a) A section of NG6580 'The Triumph of David' by Francesco Pesellino © National Gallery London with the region of data set *s1* marked. b) Colour reconstruction of data set *s1* from the collected spectral image with OCT volume and constituent B-Scan location marked. c) B-Scan of *s1* showing tooling indentations in a gold gilded surface. Depth map of the air-gold interface in the OCT volume.

Tooling of the gold leaf can also be visualised even when they are seen to be covered with glaze layers via measurements with OCT. The region shown in Figure (4.4.5.2) is from the brocade dress of the woman in the group on the right (*s10*). Here the gold seems to have been tooled in the areas below the paint. The paint now appears dark but is likely to have originally been green in colour.



Figure 4.4.5.2 A section of NG6580 ‘The Triumph of David’ by Francesco Pesellino © National Gallery London (left) with the region of $3.25\text{ mm} \times 3.25\text{ mm}$ data set s10 marked (left). A zoom in of the region corresponding to s10 in which a degraded paint/glaze layer applied over a tooled gold is present (right)

Figure (4.4.5.3) shows, the segmentation results for such a region. Here, the depth map of the interface positions for the gold substrate must be corrected relative to the thickness of the glaze layer to account for the increase in optical path length from the layer medium via the method discussed in Chapter (3.2.6).

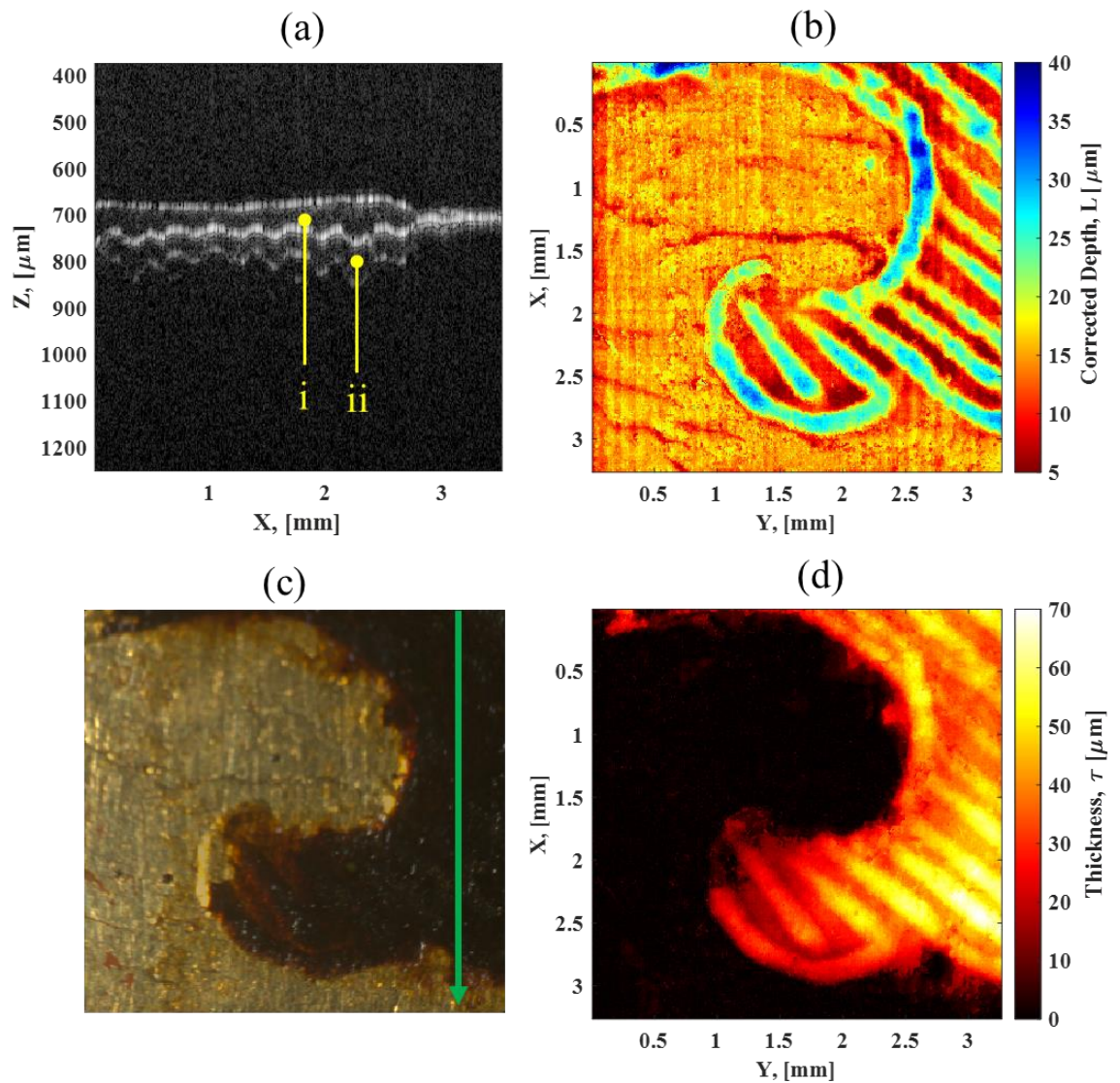


Figure 4.4.5.3. a) B-Scan of s_{10} displaying a degraded paint layer over tooled gold gilding with labels (i) and (ii) corresponding to the paint layer and multiple reflection artifact respectively. b) Depth map of the gold substrate interface corrected for the paint layer for a refractive index of 1.5. c) Colour reconstruction of the spectral image data with B-scan position marked. d) Thickness map of the paint layer.

The resultant layer thickness [Figure (4.4.5.3.b)] and gold interface depth maps [Figure (4.4.5.3.d)], show a glaze layer thickness varying from approximately $10\mu\text{m}$ to $70\mu\text{m}$ with corrugated indentations into the gold substrate (presumably created with a stylus) reaching a maximum $25\mu\text{m}$ relative to the substrate surface.

4.4.6. Optimisation of OCT Design & Performance Summary

It should be noted that for applications of the Hybrid System described in this thesis using the first version of the instrument, the major limiting factors, constraining the resolution of the OCT system, are issues with the alignment of the spectrometer and limited known spectral lines for accurate spectral calibration. These act to reduce axial resolution and SNR with depth. Additionally, the poor transmission of the fibre coupler interferometer was seen to significantly limit the bandwidth of the source spectrum and thus the axial resolution.

Such issues have since been amended with the later alterations to the system seen in Figure (4.4.6.1). Here the fibre coupler has been replaced with a free space interferometer consisting of four reflective collimators and a Thorlabs BS015 - 50:50 non-polarizing beam splitter (1100-1600 nm). Patch fibres of identical length connect the interferometer to the probe and reference arm with dispersion mismatch compensation being provided physically through additional glass within the reference arm.

In addition to alterations to the interferometer the spectrometer has been replaced with a Wasatch Cobra 1300-1300/400 spectrometer which is based on the 2048-pixel SUI GL2048 line scan camera. This in all allows for the collection of the much larger spectral band seen in Figure (4.4.6.2.a), thus providing increased axial resolution. Here, spectral measurements below 1150 nm are discarded due to the low signal resulting from the long pass dichroic used to remove the pump components of the spectrum. With better consideration of the optics used in the attenuation of the source, the spectral bandwidth may be further improved.

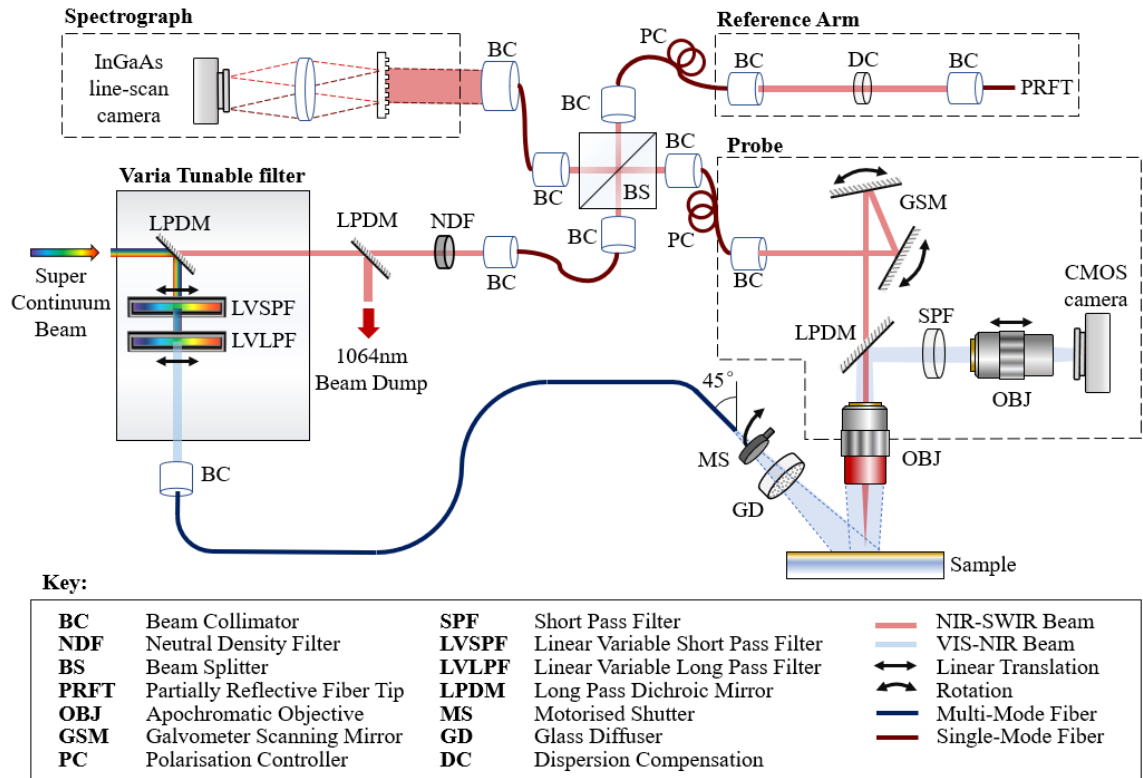


Figure 4.4.6.1. Schematic of the Hybrid Spectral Imaging and OCT system based on a freespace beam splitter and a super continuum light source

As the spectral response of the collected signal is asymmetric, additional steps in the processing of the signal are required to avoid prominent sidelobes within the data set. In this case, the collected interferometric signal is normalised by the source spectrum before apodization, to produce a more uniform amplitude in the modulation as a function of angular wavenumber.

This is by no means consistent in avoiding the precipitation of sidelobes into the axial point spread function as the spectral shape of the collected signal may vary with laser stability and sample reflectivity. Thus, an additional change to the apodization is introduced. Apodization is achieved via the multi-shaping technique described by Chen et al [116]. Here the interferometric signal is Fourier transformed for several window functions to produce a cluster of A-scan depth profiles with different apodizations for a single lateral position. Each A-Scan within the cluster is then normalised by its maximum intensity and a single A-scan is extracted through the minimisation of signal at each axial position. In this case 14 Hann

apodization windows were implemented, all centred on the central angular wave number $1/2(k_{max} + k_{min})$ and each with an equally stepped window length ranging from $1/2(k_{max} - k_{min})$ to $(k_{max} - k_{min})$ alongside an additional Dolph-Chebyshev window [117] to further constrain prominent side lobes to within $5\mu\text{m}$ of the interface peak. With such modifications an axial resolution of $5\mu\text{m}$ is achievable with a minimisation of the sidelobe intensity to approximately 30dB below the peak maximum as seen in the axial point spread function for an air-glass interface in Figure (4.4.5.6.b). In future work, the reduction in the side lobes intensity will be improved through the physical apodization of the spectrum via the use of band-pass filtering.

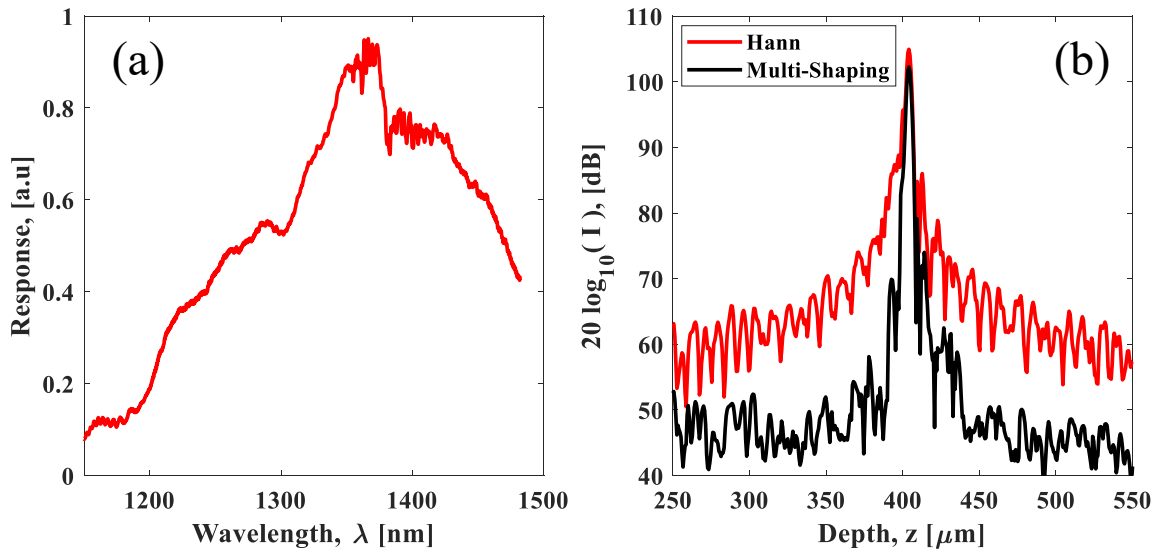


Figure 4.4.6.2. a) Spectral response of illumination incident on the OCT spectrometer. b) Comparison of the axial point spread function of a singular air-glass interface with a single Hann window apodization (red) and Multishaping apodization of a Dolph-Chebyshev window and 14 Hann windows

The equation for a Dolph-Chebyshev window function can be seen in Equation (4.4.6.1). Here the window function is defined over an arbitrary maximum and minimum angular wavenumber bounds k_{max} and k_{min} with $\#N$ equalling the number of samples within the bounding window. With the application of apodization, Δk will be reduced as a result of the multiplication of the spectral distribution $S(k)$ with the tapered window function thus apodization is seen to introduce a trade-off between the reduction of side lobe magnitude in

the axial PSF and preservation of axial resolution. For the Dolph-Chebyshev function an additional β term is introduced. Here β is defined via Equation (4.4.6.2). where α is arbitrary value allowing the scaling of the attenuation applied to the side lobes.

$$w_{DCh}(k) \triangleq \begin{cases} \frac{(-1)^{(k-k_{\min})} \cos \left[\#N \cos^{-1} \left[\beta \cos \left[\frac{\pi(k-k_{\min})}{\#N} \right] \right] \right]}{\cosh[\#N \cosh^{-1}[\beta]]}, & k_{\min} \leq k \leq k_{\max} \\ 0, & (k \leq k_{\min}) \vee (k \geq k_{\max}) \end{cases}$$

Equation 4.4.6.1

$$\beta = \cosh \left[\frac{1}{\#N} \cosh^{-1}[10^\alpha] \right]$$

Equation 4.4.6.2

The resulting averaged B-Scan for a region of the mock-up painting described in previous chapters of this thesis can be seen in Figure (4.4.6.3.a) as compared to a similar region under the ultra-high-resolution OCT utilised in Chapters 2 and 3 [Figure (4.4.6.3.b)]. Here both B-Scans are the result of 100 B-scan averages. It should be noted that image contrast is usually higher at shorter wavelength.

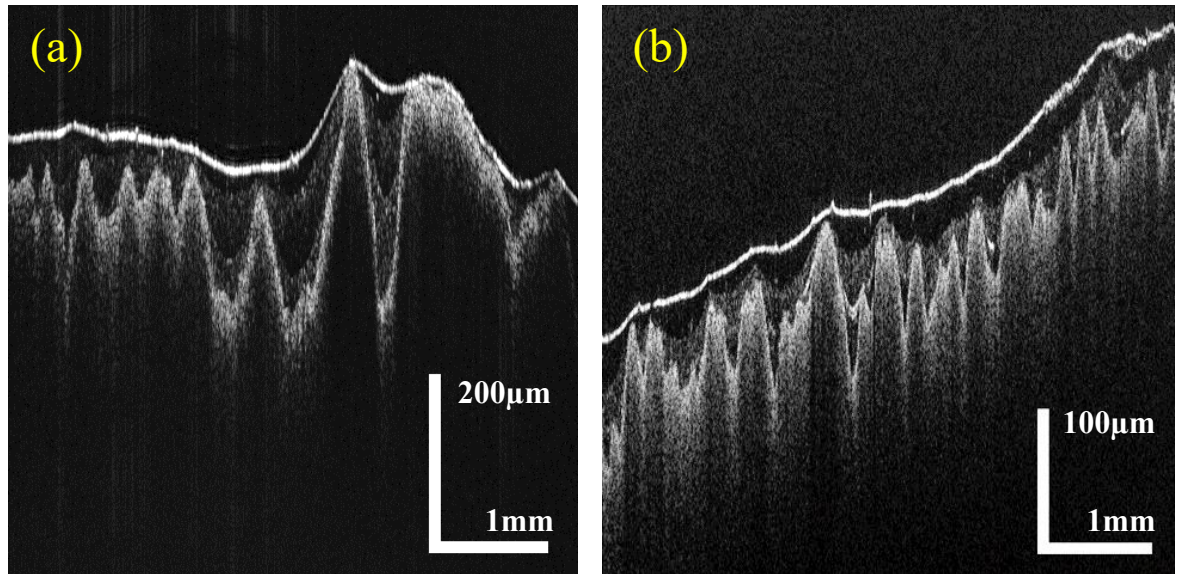


Figure 4.4.6.3. 100 scan time averaged B-Scan of similar regions of a varnished mock-up painting with a) the free space beam splitter based hybrid OCT system ($\sim 1350\text{nm}$ central wavelength) and b) the ultra-high-resolution OCT ($\sim 810\text{nm}$ central wavelength)

4.5. Extraction of Layer Spectral Features with a Multimodal Instrument

4.5.1. Data Alignment in the Hybrid System

With the collection of both modalities (OCT and spectral imaging), the segmentation of layer thickness maps and extraction of spectral features can again be applied. Here the processes of denoising OCT volumes, segmentation of the layer structure and the extraction of thickness-reflectance relationship are identical. However, some small changes are present.

Firstly, as a result of the limited SNR towards the lateral peripheries of the data sets resulting from the objective lens vignette, the lateral field of view is limited to an arbitrary region of interest. This acts to limit the inclusion of low SNR reflectance measurements and removes the inclusion of erroneous segmentation results where interfaces appear near to the noise floor.

Secondly, even with the collection of data through the same objective, the alignment of the data sets is still required in order to account for small angular and spatial variations between the two imaging regions and for deviations in the sampling resolution between the modalities. As in Chapter (3.3.8), an affine transformation based on manually selected tide points is used to co-register the datasets. Unlike the situation described in Chapter (3.3.8), the spectral image is instead down sampled owing to its greater lateral resolution in comparison the OCT volume. This in turn avoids interpolation and provides an additional increase in the reflectance SNR. As the system will have a consistent misalignment between data sets, common tide points for alignment can simply be obtained from a single scan and applied globally across data sets.

4.5.2. Extraction of Spectral Features within Prepared Samples

Here the segmentation and extraction of the spectral features for the experimental reconstruction panel prepared at the National Gallery in 1985, consisting of a green copper resinate glaze layer over opaque underpaints described in Chapter (3.4.1) is again assessed, this time with data collected via the multi-modal instrument. The resultant colour reconstruction of the spectral imaging region [Figure (4.5.2.1.a)] and accompanying extracted layer thickness maps [Figure (4.5.2.1.b)] can be seen for regions of copper resinate glaze applied over varying paint layers [Table (3.4.1.1)].

Thickness maps are largely consistent with the real layer stratigraphy, though regions of cracking where sudden changes in interface position occurs, are incorrect. Such areas are again ignored when extracting from the extinction relationship.

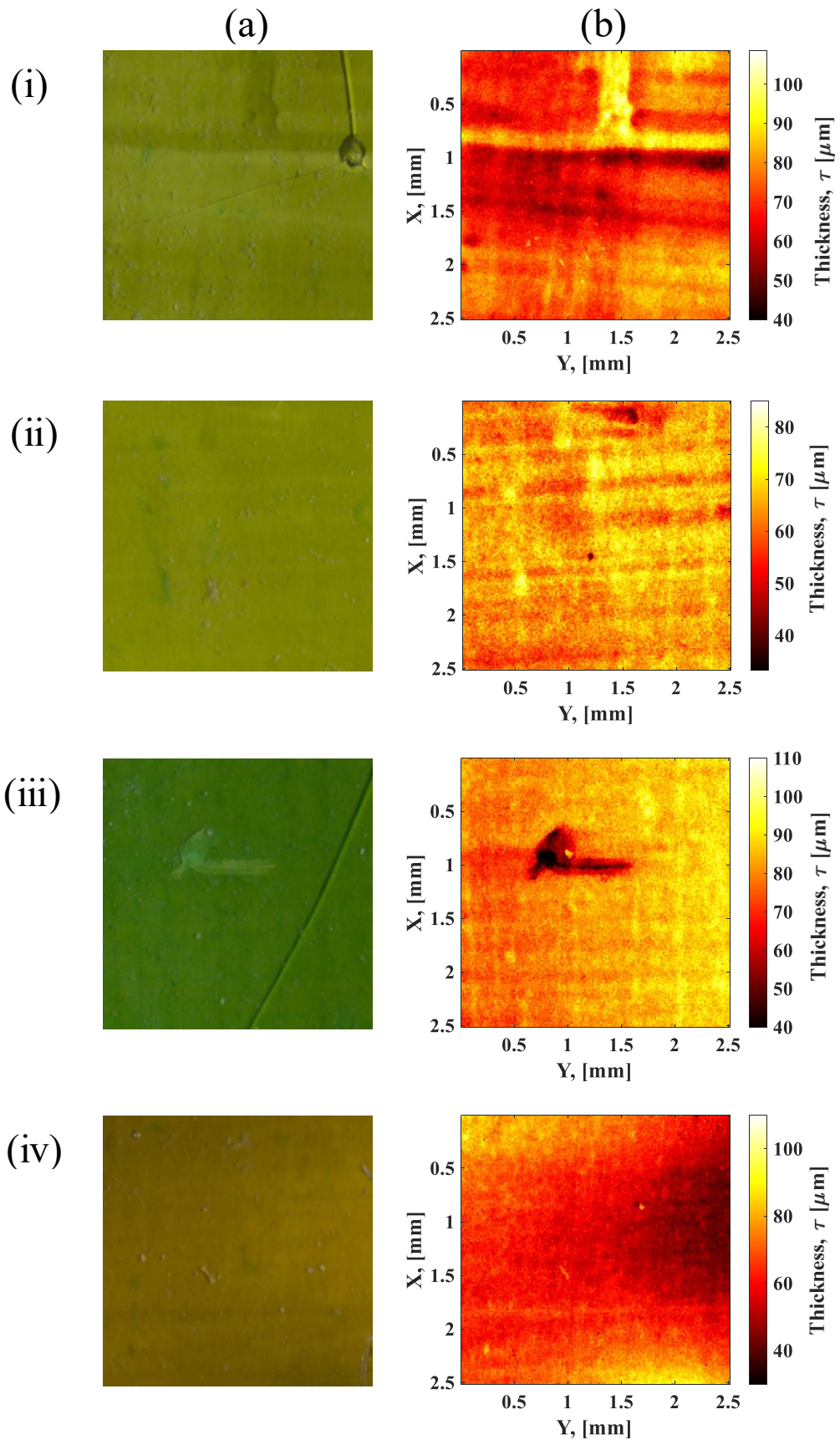


Figure 4.5.2.1. a) Colour reconstructions from spectral imaging for copper resinate over (i) white, (ii) yellow, (iii) green and (iv) yellow ochre. b) The corresponding thickness maps of the copper resinate layers

The extracted extinction relationship associated with the copper resinate sample over the varied paint layers can be seen in Figure (4.5.2.2.a) alongside the associated reflectance measurements of the region in Figure (4.5.2.2.b). The extracted spectral shapes of the extinction graphs again provide good correlation with each other in comparison to the extinction spectra extracted in Chapter (3.4.1), producing a peak at approximately 560nm which is consistent with the peak in reflectance measurements of copper resinate over titanium white. As previously mentioned, the expected absorption feature of copper resinate is expected to be positioned around 695nm. This is seen to be reflected in the extracted extinction coefficient for glaze layers over white, yellow and green which produce absorption features close to this value. For glaze over ochre, however, the absorption feature is seen to be slightly blue shifted. This is likely due to nonuniformity in the thickness of the underpaint.

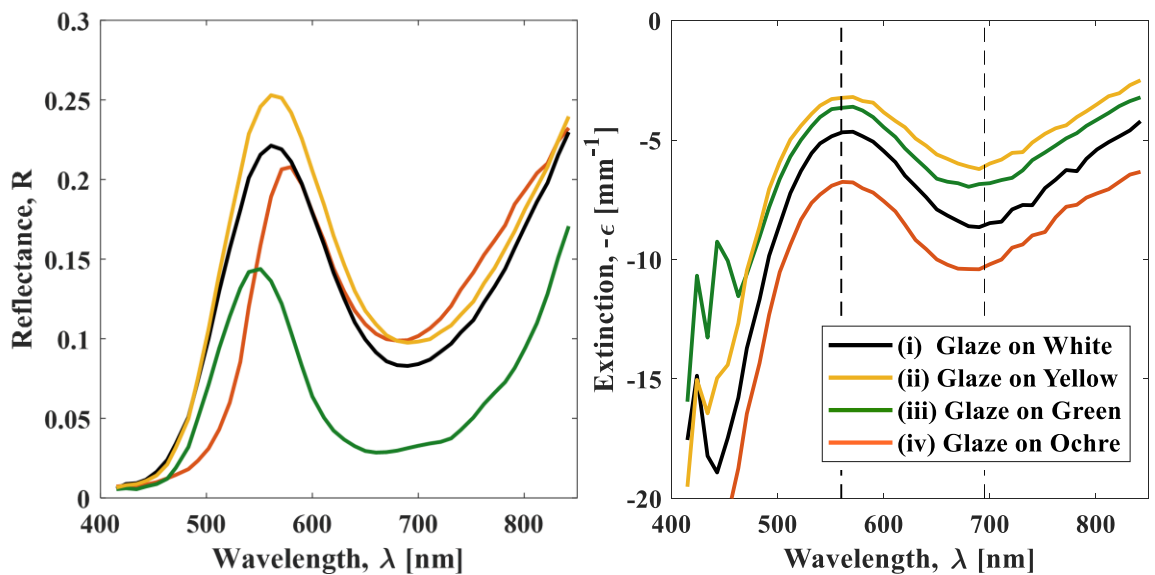


Figure 4.5.2.2. a) The reflectance and b) the extracted extinction coefficients of a copper resinate layer over (i) white, (ii) yellow, (iii) green and (iv) yellow ochre.

Following on from this, the extraction of extinction coefficients is applied to the Madder samples introduced in chapter (4.3.7). Figure (4.5.2.3a) and Figure (4.5.2.3b) again show the colour reconstruction and layer thickness maps for each madder sample with the extraction of the spectral features of the madder layer shown in Figure (4.5.2.4). Here it can be seen that the extracted extinction coefficients provide a much more prominent absorption feature in the region between 450nm and 550nm, in comparison to the reflectance image alone, enabling clear distinction and identification of the madder samples.

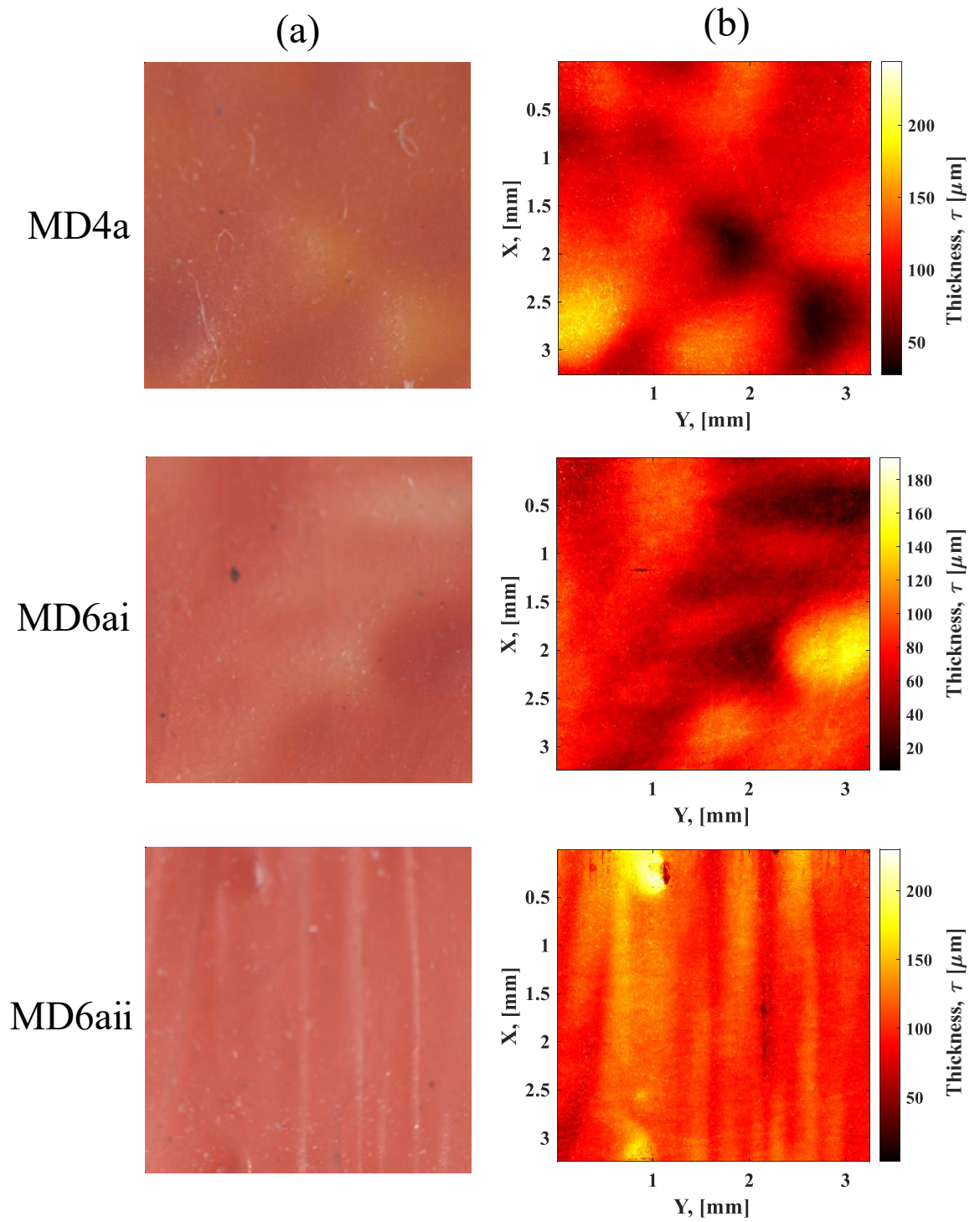


Figure 4.5.2.3 a) Colour reconstructions of spectral images collected for three madder lake samples MD4a, MD6ai and MD6aii alongside b) the extracted thickness maps of madder layers

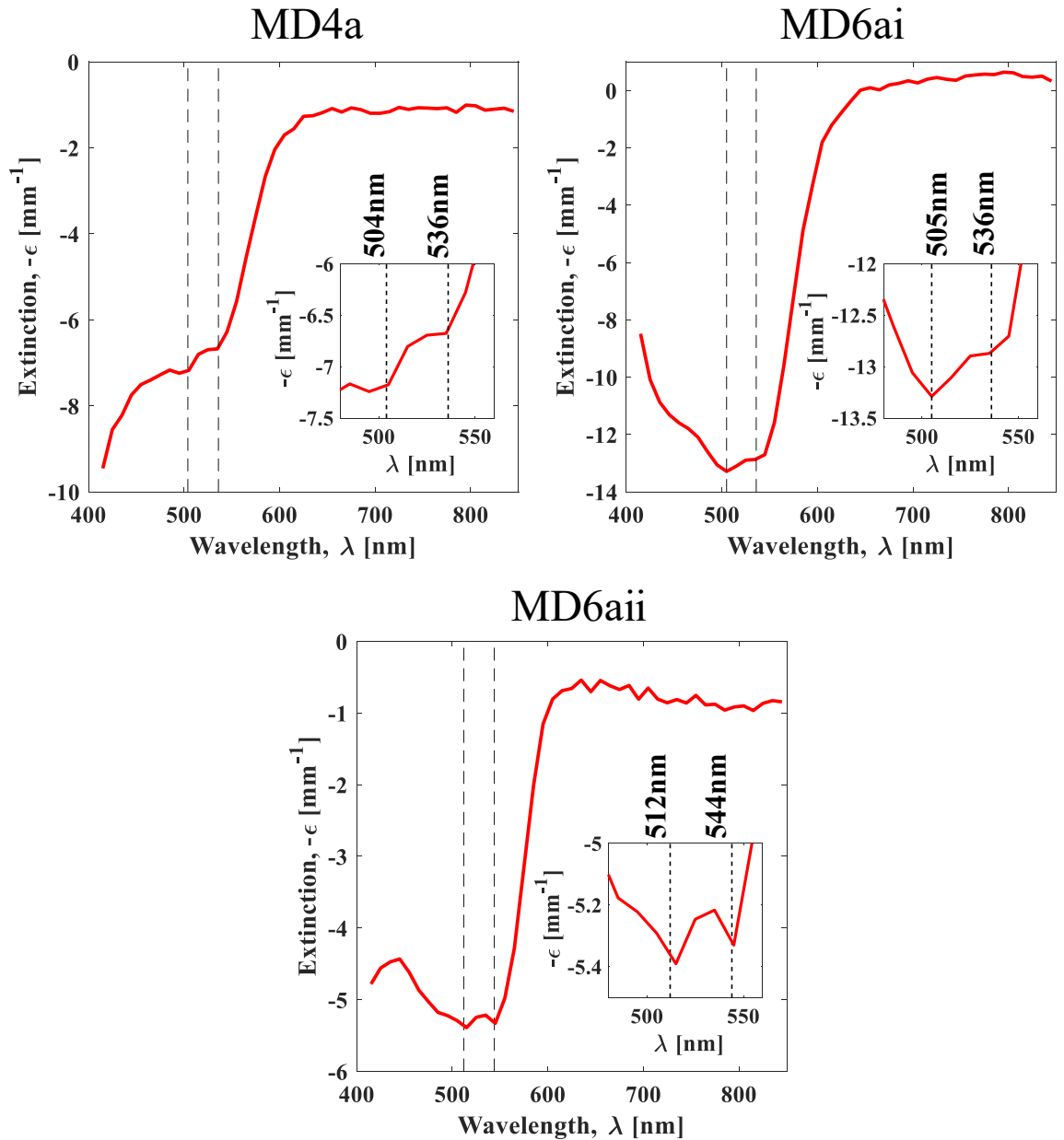


Figure 4.5.2.4. The extracted extinction coefficients of three madder lake samples MD4a, MD6ai and MD6aii. The extracted extinction coefficient amplify the madder absorption features in comparison to reflectance spectra seen in figure (4.3.7.2).

4.5.3. Extraction of Spectral Features from Historical Paintings via the Hybrid Instrument

In the following section the extraction of layer spectral features with the hybrid instrument is demonstrated on an Austrian School painting from the National Gallery in London, NG3662 'The Trinity with Christ Crucified', oil on wood, about 1410. The painting was undergoing conservation treatment at the time of examination (varnish layers had been removed) and there was interest in investigating the original materials used and how the paint and glazes were utilised in combination with metal leaf.

Here two regions from the robe of the angel on the right have been examined for the extraction of spectral features. These regions were of interest as there appeared to be the presence of a green glaze which was either applied directly over the metal leaf or over an opaque green paint (itself applied over the metal leaf). The regions s17 and s18 correspond to the glaze over the metal leaf and the green paint (without the glaze layer at the surface) over the metal leaf respectively [Figure 4.5.3.1].



Figure 4.5.3.1. NG3662 'The Trinity with Christ Crucified' by the Austrian school © National Gallery London with data sets s17 and s18 marked (top). Colour reconstructions of data sets s17 and s18 overlaid over the surrounding area. S17 covers an area of green glaze over tooled gold and s18 a green paint over tooled gold

Figure (4.5.3.2) and Figure (4.5.3.3) show the results for the extracted spectral features for the paint and glaze layers present in s17 and s18 respectively compared to the average reflectance measured within test regions described in Table (4.5.3.1). Looking at the peak, it can be seen that the paint peak position is approximately 545nm in comparison to that of the glaze which peaks at approximately 565nm. The absorption features for both the paint and the glaze are centred at around 720 nm [Figure (4.5.3.4)] which is consistent with verdigris according to Aceto et al., 2014. Verdigris is known to have been used within this painting from samples, but this is sometimes mixed with lead white or lead-tin yellow with other copper-based green pigments also possibly present in the mixture.

Data Set	Regions	Region Width \times Height [μm]	Descriptor
S17	1	500 \times 450	Gold Leaf
	2	400 \times 400	Thick Green Paint
	3	270 \times 300	Thin Green Paint on Gold
S18	1	138 \times 345	Gold Leaf
	2	315 \times 175	White Ground Layer
	3	350 \times 233	Glaze on Gold
	4	200 \times 280	Thin Glaze on Gold

Table 4.5.3.1

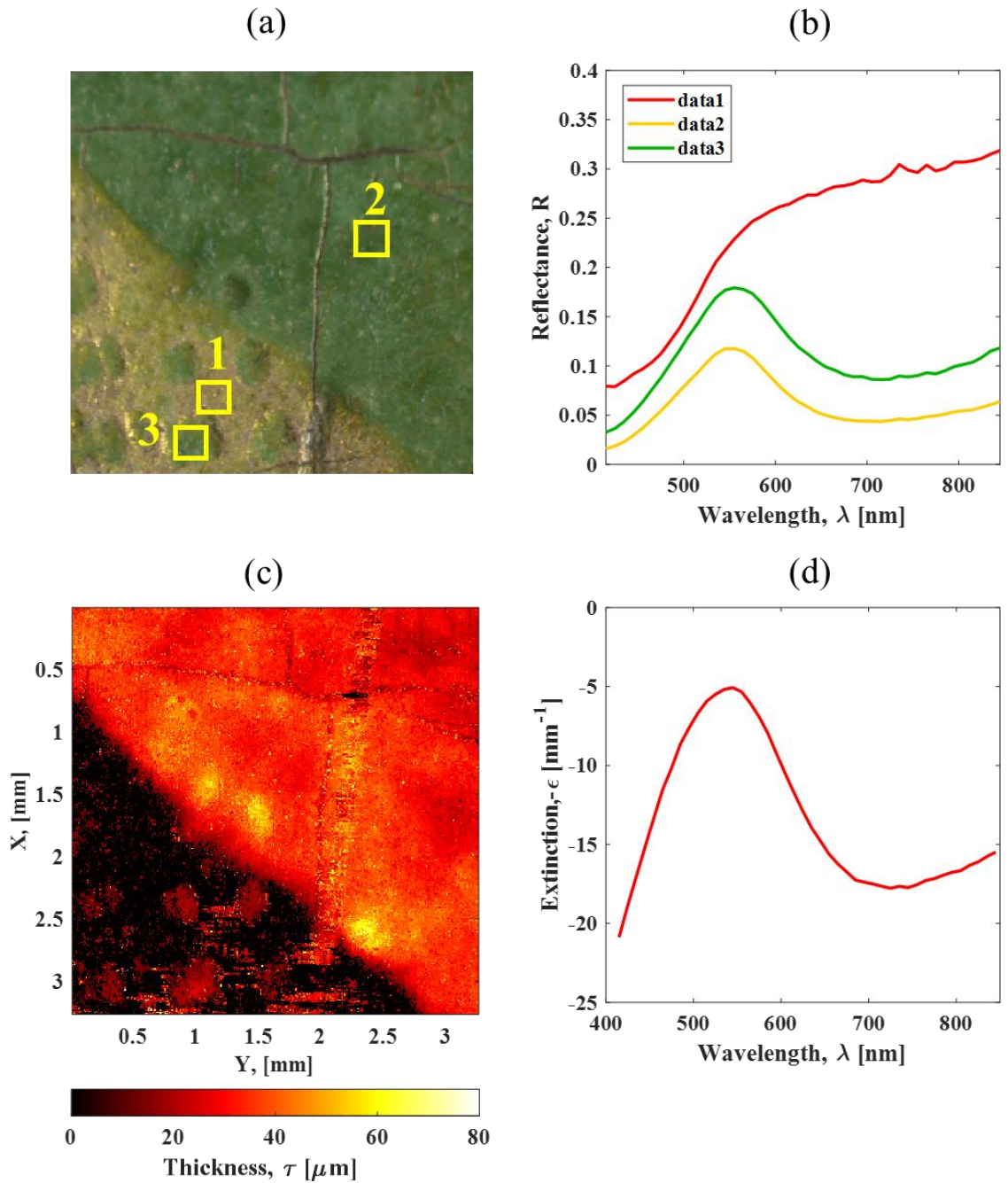


Figure 4.5.3.2. a) Colour reconstruction of data set s18 from the collected spectral image with regions of averaged spectra marked. b) The average spectra for regions of gold, thick paint and thin paint over gold. c) The extracted thickness map of the paint layer from s18. d) The extracted extinction coefficient from the paint layer.

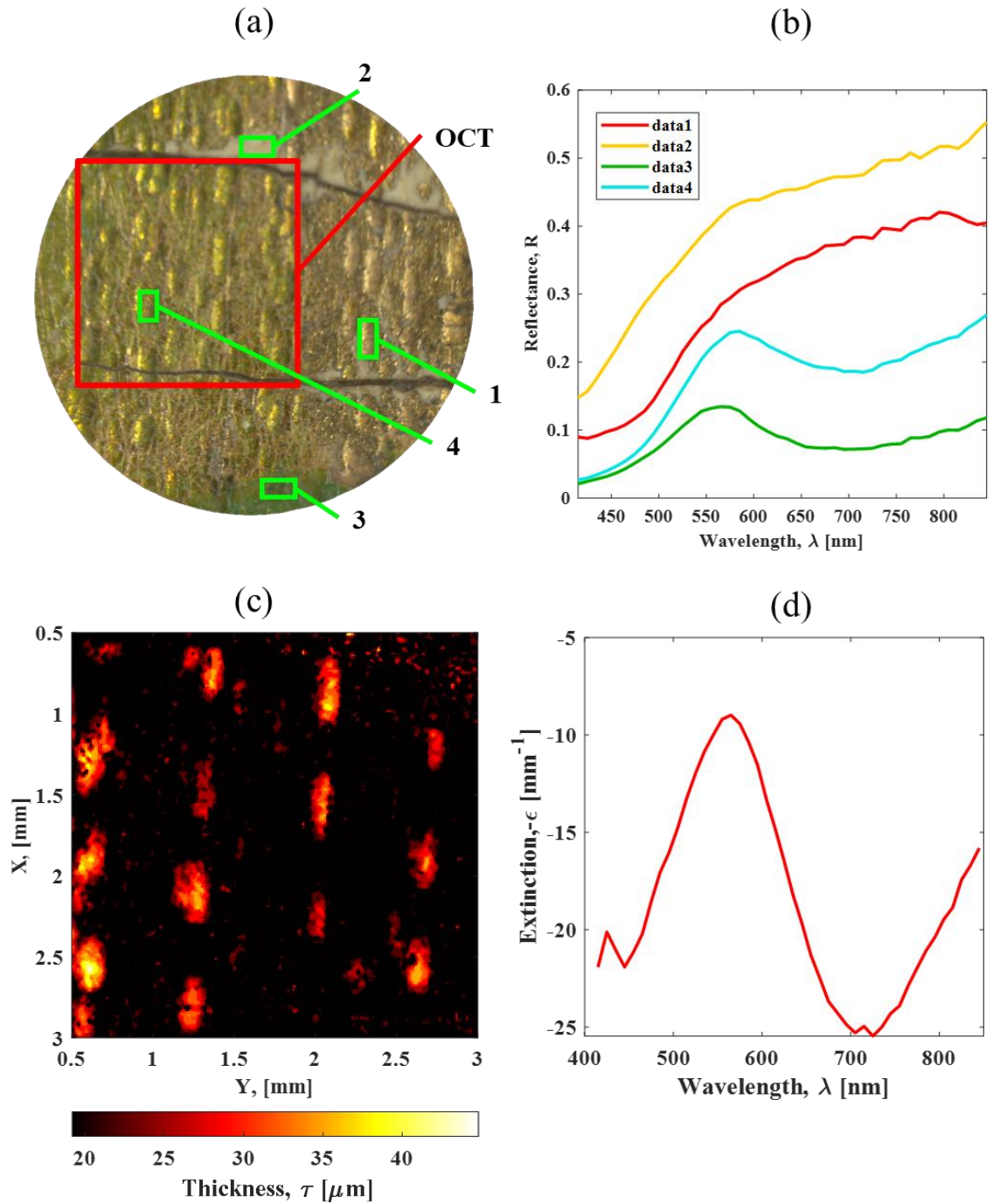


Figure 4.5.3.3. a) Colour reconstruction of data set s17 from the collected spectral image with regions of averaged spectra and OCT region marked. b) the average spectra for regions of white ground, gold, paint/glaze over gold and glaze over gold. c) The extracted thickness map of the glaze layer from s17. d) The extracted extinction coefficient from the glaze layer.

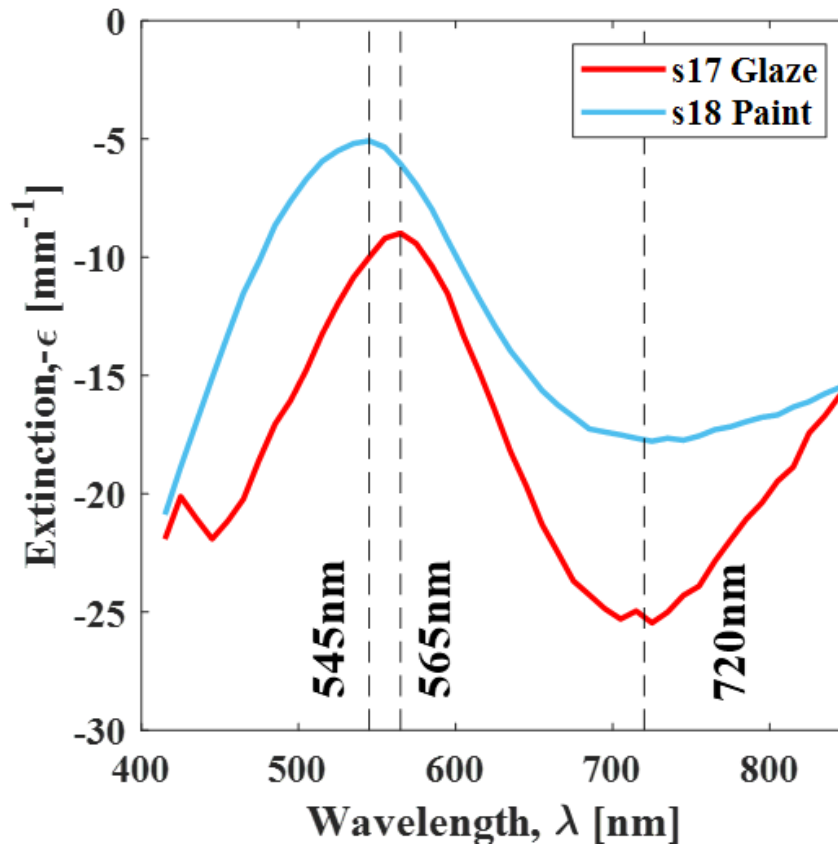


Figure 4.5.3.4. The extracted extinction coefficients for the glaze of s17 (red) and paint of s18 (blue) with the peak and trough positions marked. Both spectra produce an absorption feature centred at 720 nm indicating that both layers may likely correspond to verdigris, possibly at different stages of degradation

4.6. Conclusion

A combined multi-modal OCT and spectral imaging system has been demonstrated for applications in cultural heritage. The instrument takes advantage of a supercontinuum light source in which wavelengths below 850nm are used for a filtered illumination source (enabling spectral imaging) while wavelengths above 850nm provide a broadband illumination source for OCT.

The overall system performance for the optimised OCT system is stated in Table (4.6.1.1). To account for non-Gaussian spectral response of the OCT signal, the spectrum was normalised to produce a flat response with wavelength and a multi-windowed apodization routine was applied to maintain resolution while reducing sidelobe magnitude in the axial point spread function.

Feature	Performance
Central Wavelength	~1350nm
Axial Resolution (air /polymer)	~5 μ m/~3 μ m
Lateral Resolution	~5.5 μ m
Theoretical Image Depth (air/polymer)	~2mm/~1.3mm
Maximum A-Scan Rate	76 kHz
Maximum System Dynamic Range	77 dB

Table 4.6.1.1

The OCT system has been applied to the historical painting NG6580 ‘The Triumph of David’ by Francesco Pesellino for the characterisation of tooling indentations within regions of gold. To do so, the interface positions were extracted to produce depth maps of the metallic interfaces, revealing triangular punch marks within a region corresponding to the white horse’s saddlecloth. The application of OCT in this region also enabled the characterisation of tooling below the paint layer, in which indentations beneath a degraded paint layer can be measured through the refractive index correction of the interface position.

The performance of the microscopic spectral imaging through filtered supercontinuum illumination has been summarised in Table (4.6.1.2).

Feature	Performance
Spectral Resolution	10nm
Wavelength Range	415nm-845nm
Lateral resolution	~5.3 μ m
Field of View Diameter	~5 mm

Table 4.6.1.2

Out of band spectral components contributing to the filtered illumination for spectral imaging were suppressed to below 2% of total irradiance. The stability of the spectral imaging illumination was seen to vary by $\pm 5\%$ after being left to stabilise for approximately 70 minutes. To account for the poor stability of the light source future modifications to the system will monitor the spectral band intensity. Spatial variation in the illumination field resulting from modal interference was suppressed through the use of a glass diffuser providing a uniform illumination field.

The shared objective between the two modalities provided co-registration of their respective data sets. However, this also introduced some limitations on the optics limiting the lateral field of view such and introducing vignetting into the image circle. As vignetting is systematic for all datasets, the radial variations in reflectance can be addressed through flat field correction. The vignetting however does result in a radial reduction in signal to noise for both modalities.

The collection of microscopic spectral imaging was demonstrated on the historical painting NG6580 'The Triumph of David' by Francesco Pesellino, enabling the extraction of reflectance spectra from individual pigment particles and confirming the presence of azurite and ultramarine within the paint layer. Similarly, microscopic spectral imaging was demonstrated on a region of degraded copper based green, allowing the localised extraction of reflectance spectra from regions of unreacted/less degraded pigment.

Combining the segmented layer thickness with the accompanying reflectance value in the extraction of extinction coefficients has been shown to reduce the influence of the ground paint layer and accentuate weak absorption features such as those seen in natural dyes and lakes like madder.

Applying this technique to the painting NG3662 'The Trinity with Christ Crucified' has allowed the spectral characterisation of layers within regions of green paint and green glaze

applied over gold. The extracted extinction coefficient found that both layers produced absorption features around 720nm, likely identifying them as verdigris.

Chapter 5: Conclusion

In conclusion, this work has demonstrated the application of a hybrid instrument combining spectral domain optical coherence tomography in the Short-Wave Infrared (SWIR: 1000-2500 nm) spectral region with a filtered illumination based spectral imaging system in the VIS-NIR based on a single super continuum illumination source. By collecting OCT in the SWIR spectral range (1350nm central wavelength), depth penetration is maximised while maintaining a high axial resolution, since scattering is reduced as wavelength increases in the SWIR regime, but axial resolution improves with the inverse of central wavelength squared. Likewise, the collection of spectral imaging in the VIS-NIR between 415 and 845nm is beneficial as it is rich in spectral features relevant for pigment identification in historical paintings.

The system produces OCT volumetric data sets, with axial and transverse resolutions of approximately 3 μ m (in varnish/glaze) and 5.5 μ m respectively, which are co-registered with spectral image cubes with lateral and spectral resolutions of 5.3 μ m and 10nm respectively. The lateral resolution of the spectral images enables the targeted collection of reflectance spectra from individual particles above 11 μ m in diameter, enabling the identification of paint mixtures.

Co-registration of the data at similar spatial resolution is demonstrated to be beneficial in the interpretation of data from the complementary modalities. The ability to cross reference the reflectance spectra, with the stratigraphy of a region, allows more detailed understanding of the stratigraphy. The precise co-registration only needs to be performed once after the instrument has been setup. Thus, improving the efficiency of data interpretation.

This is particularly useful when applied to cases of varnish and glazing layers. Under the conditions that scattering within the layer is negligible, segmentation of the layer thickness, and relation of thickness to reflectance enables the extraction of the layer extinction coefficient per wavelength channel, in turn isolating the spectral characteristics of the layer. The extraction of extinction spectrum has also been shown to accentuate weak spectral features providing clearer identification of the material. It is hoped that such a technique will be ideal for on-line monitoring of conservation treatments of artwork.

The segmentation of OCT volume and the extraction of interface depth maps and layer thickness maps also prove useful in the analysis of stratigraphy and offer further opportunities for analysis and interpretation on a global scale over the whole painting. The refractive index corrections, in particular, enables OCT B-Scans to reflect the true physical cross section, simplifying interpretation and thus will become routine in the analysis of future data sets.

Even without the combination of both modalities, the instrument has been shown to be a versatile tool. The attainment of RGB true colour images which are co-registered with OCT data sets has been seen to be particularly beneficial for identifying the exact position from which OCT data has been collected. This offers also the opportunity to simplify the alignment of OCT data sets with data sets collected from other modalities which often use the colour image as a reference to align to, offering more avenues for the characterisation of a region.

As of this date, the instrument has already seen wide applications with its use in analysing a range of cultural heritage objects:

- The investigation of stratigraphy of superficial layers in 19th century paintings by James Ensor at Royal Museum of Fine Arts, Antwerp.
- The investigation of surface coatings to inform conservation strategy for abstract and minimalist paintings by prominent Norwegian artists from 1966-1982 in the National Museum of Norway collection.

- The assessment of conservation treatment of archaeological metal in World War II fighter planes in the collection of Laboratoire Arc'antique, Nantes
- The extraction of adaptive windowed enface projections to reveal writings in charred papyri (Herculean papyri from the National Library of Naples) and missing writings in one of the oldest records of the Ten Commandments (Nash papyri from the Cambridge University Library)
- The monitoring of conservation treatments in wall paintings from the Benedictine Convent of St John in Müstair Switzerland
- The examination of stratigraphy of enamels at the British Museum for the monitoring of degradation and investigation of manufacturing techniques

In future work, the instrument will be modified in a number of ways to further improve the data collected. Firstly, the monitoring of the spectral imaging illumination source will be implemented to allow for better calibration of reflectance spectra and remove the artifacts associated with the illumination stability. Secondly, the systems optics will be redesigned to provide higher lateral resolution, lower lateral field of view data sets in order to enable the collection of reflectance spectra from smaller pigment particles. This should in turn drastically reduce the strong vignetting visible, improving signal to noise at the peripheries of the scans. Finally, physical apodization of the OCT illumination spectra will be added to reduce the magnitude of side lobes in the axial point spread function.

Additional future work in data processing is in development to improve the accuracy of the segmentation of complex layers through a new deep learning-based segmentation routine. It is hoped that such techniques will also expediate processing of large numbers of data sets.

References

1. E. R. de la Rie, "The Influence of Varnishes on the Appearance of Paintings," *Stud. Conserv.* **32**(1), 1 (1987).
2. J. K. Delaney, E. R. de la Rie, M. Elias, L. Sung, and K. M. Morales, "The Role of Varnishes in Modifying Light Reflection from Rough Surfaces - A Study of Changes in Light Scattering Caused by Variations in Varnish Topography and Development of a Drying Model," *Stud. Conserv.* **53**(3), 170–186 (2008).
3. M. Elias, E. René de la Rie, J. K. Delaney, E. Charron, and K. M. Morales, "Modification of the surface state of rough substrates by two different varnishes and influence on the reflected light," *Opt. Commun.* (2006).
4. E. R. de la Rie, J. K. Delaney, K. M. Morales, C. A. Maines, and L.-P. Sung, "Modification of Surface Roughness by Various Varnishes and Effect on Light Reflection," *Stud. Conserv.* **55**(2), 134–143 (2010).
5. J. Dunkerton, J. Kirby, and R. White, "VARNISH AND EARLY ITALIAN TEMPERA PAINTINGS," *Stud. Conserv.* **35**(sup1), 63–69 (1990).
6. J. van Eyck, J. Dunkerton, M. Spring, D. Peggie, and S. Stelzig, "Original or Early Surface Coatings on Portraits," in *National Gallery Technical Bulletin Vol 41* (2021), pp. 4–17.
7. J. Kirby and W. Raymond, "A Survey of Nineteenth- and Early Twentieth-Century Varnish Compositions Found on a Selection of Paintings in the National Gallery Collection," in *National Gallery Technical Bulletin Vol 22* (2001), pp. 64–84.
8. E. R. de la Rie, "Photochemical and Thermal Degradation of Films of Dammar Resin," *Stud. Conserv.* **33**(2), 53 (1988).
9. R. L. Feller, N. Stolow, and E. H. Jones, *On Picture Varnishes and Their Solvents* (National Gallery of Art, Washington, 1985).
10. J. Mills and R. White, *Organic Chemistry of Museum Objects*, 2nd ed. (Routledge, 1999).

11. C. Higgitt, "Memling's God the Father with Singing and Music-Making Angels: Oxalate Formation in Old Master Paintings," in *Harmony in Bright Colors. Memling's God the Father with Singing and Music-Making Angels Restored*, L. Klaassen and D. Lampens, eds. (BREPOLs, 2021, 2021), pp. 192–209.
12. E. Geddes da Filicaia, R. P. Evershed, and D. A. Peggie, "Review of recent advances on the use of mass spectrometry techniques for the study of organic materials in painted artworks," *Anal. Chim. Acta* **1246**(October 2022), 340575 (2023).
13. J. Plesters, "Cross-sections and Chemical Analysis of Paint Samples," *Stud. Conserv.* **2**(3), 110–157 (1956).
14. J. sun Tsang, E. Friedberg, and T. Lam, "An easy-to-use method for preparing paint cross sections," *J. Am. Inst. Conserv.* **58**(3), 123–131 (2019).
15. D. Pinna, M. Galeotti, and R. Mazzeo, *Scientific Examination for the Investigation of Paintings: A Handbook for Conservators-Restorers* (Centro Di, 2009).
16. M. Spring, C. Ricci, D. A. Peggie, and S. G. Kazarian, "ATR-FTIR imaging for the analysis of organic materials in paint cross sections: Case studies on paint samples from the National Gallery, London," *Anal. Bioanal. Chem.* **392**(1–2), 37–45 (2008).
17. L. Oakley, S. Zaleski, B. Males, O. Cossairt, and M. Walton, "Improved spectral imaging microscopy for cultural heritage through oblique illumination," *Herit. Sci.* **8**(1), 1–11 (2020).
18. E. Pouyet, B. Fayard, M. Salomé, Y. Taniguchi, F. Sette, and M. Cotte, "Thin-sections of painting fragments: opportunities for combined synchrotron-based micro-spectroscopic techniques," *Herit. Sci.* **3**(1), 3 (2015).
19. C. Chillè, V. M. Papadakis, and C. Theodorakopoulos, "An analytical evaluation of Er:YAG laser cleaning tests on a nineteenth century varnished painting," *Microchem. J.* **158**, 105086 (2020).
20. P. Moretti, M. Iwanicka, K. Melessanaki, E. Dimitroulaki, O. Kokkinaki, M. Daugherty, M. Sylwestrzak, P. Pouli, P. Targowski, K. J. van den Berg, L. Cartechini, and C. Miliani, "Laser cleaning of paintings: in situ optimization of operative parameters through non-invasive assessment by optical coherence

tomography (OCT), reflection FT-IR spectroscopy and laser induced fluorescence spectroscopy (LIF)," *Herit. Sci.* **7**(1), 44 (2019).

21. M. Iwanicka, P. Moretti, S. Van Oudheusden, M. Sylwestrzak, L. Cartechini, K. Jan, V. Den Berg, P. Targowski, and C. Miliani, "Complementary use of Optical Coherence Tomography (OCT) and Reflection FTIR spectroscopy for in-situ non-invasive monitoring of varnish removal from easel paintings," *Microchem. J.* **138**, 7–18 (2018).
22. C. S. Cheung, M. Spring, and H. Liang, "Ultra-high resolution Fourier domain optical coherence tomography for old master paintings," *Opt. Express* **23**(8), 10145 (2015).
23. P. Targowski and M. Iwanicka, "Optical Coherence Tomography: its role in the non-invasive structural examination and conservation of cultural heritage objects—a review," *Appl. Phys. A* **106**(2), 265–277 (2012).
24. H. Liang, B. Peric, M. Hughes, A. G. Podoleanu, M. Spring, and S. Roehrs, "Optical Coherence Tomography in archaeological and conservation science - a new emerging field," (2008), **7139**, p. 713915.
25. D. C. Adler, J. Stenger, I. Gorczynska, H. Lie, T. Hensick, R. Spronk, S. Wolohojian, N. Khandekar, J. Y. Jiang, S. Barry, A. E. Cable, R. Huber, and J. G. Fujimoto, "Comparison of three-dimensional optical coherence tomography and high resolution photography for art conservation studies," *Opt. Express* **15**(24), 15972 (2007).
26. H. Liang, M. G. Cid, R. G. Cucu, G. M. Dobre, A. G. Podoleanu, J. Pedro, and D. Saunders, "En-face optical coherence tomography - a novel application of non-invasive imaging to art conservation," *Opt. Express* **13**(16), 6133 (2005).
27. S. Lawman and H. Liang, "High precision dynamic multi-interface profilometry with optical coherence tomography," *Appl. Opt.* **50**(32), 6039 (2011).
28. C. L. Koch Dandolo, V. Detalle, J.-B. Bodiguel, M. Lopez, X. Bai, D. Martos-Levif, A. Genty-Vincent, C. Pasquali, and M. Menu, "Insights into the Blanching of Water-Damaged Varnish by Means of Spectral-Domain Optical Coherence Tomography," *Stud. Conserv.* **67**(3), 151–160 (2022).

29. P. Targowski, R. Ostrowski, J. Marczak, M. Sylwestrzak, and E. A. Kwiatkowska, "Picosecond laser ablation system with process control by optical coherence tomography," in L. Pezzati and R. Salimbeni, eds. (2009), p. 73910G.
30. J. Striova, B. Salvadori, R. Fontana, A. Sansonetti, M. Barucci, E. Pampaloni, E. Marconi, L. Pezzati, and M. P. Colombini, "Optical and spectroscopic tools for evaluating Er:YAG laser removal of shellac varnish," *Stud. Conserv.* **60**(sup1), S91–S96 (2015).
31. D. Huang, E. A. Swanson, C. P. Lin, J. S. Schuman, W. G. Stinson, W. Chang, M. R. Hee, T. Flotte, K. Gregory, C. A. Puliafito, and J. G. Fujimoto, "Optical Coherence Tomography," *Science* (80-.). **254**(5035), 1178–1181 (1991).
32. M. E. Brezinski, *Optical Coherence Tomography: Principles and Applications* (Elsevier, 2006).
33. W. Drexler and J. G. Fujimoto, *Optical Coherence Tomography : Technology and Applications* (Springer Berlin / Heidelberg, 2008).
34. S. Lawman, Z. Zhang, Y.-C. Shen, and Y. Zheng, "Line Field Optical Coherence Tomography," *Photonics* **9**(12), 946 (2022).
35. L. Wang, R. Fu, C. Xu, and M. Xu, "Methods and applications of full-field optical coherence tomography: a review," *J. Biomed. Opt.* **27**(05), (2022).
36. R. F. Spaide, T. Otto, S. Caujolle, J. Kübler, S. Aumann, J. Fischer, C. Reisman, H. Spahr, and A. Lessmann, "Lateral Resolution of a Commercial Optical Coherence Tomography Instrument," *Transl. Vis. Sci. Technol.* **11**(1), 3–9 (2022).
37. C. K. Hitzenberger, A. Baumgartner, W. Drexler, and A. F. Fercher, "Dispersion Effects in Partial Coherence Interferometry: Implications for Intraocular Ranging," *J. Biomed. Opt.* **4**(1), 144 (1999).
38. C. K. Hitzenberger, A. Baumgartner, and A. F. Fercher, "Dispersion induced multiple signal peak splitting in partial coherence interferometry," *Opt. Commun.* **154**(4), 179–185 (1998).
39. R. Leitgeb, C. Hitzenberger, and A. Fercher, "Performance of fourier domain vs time domain optical coherence tomography," *Opt. Express* **11**(8), 889 (2003).

40. Y. Ling, M. Wang, X. Yao, Y. Gan, L. Schmetterer, C. Zhou, and Y. Su, "Effect of spectral leakage on the image formation of Fourier-domain optical coherence tomography," *Opt. Lett.* **45**(23), 6394 (2020).
41. R. Tripathi, N. Nassif, J. S. Nelson, B. H. Park, and J. F. de Boer, "Spectral shaping for non-Gaussian source spectra in optical coherence tomography," *Opt. Lett.* **27**(6), 406 (2002).
42. J. M. Schmitt, S. H. Xiang, and K. M. Yung, "Speckle in Optical Coherence Tomography," *J. Biomed. Opt.* **4**(1), 95 (1999).
43. H. Liang, B. Peric, M. Hughes, A. Podoleanu, M. Spring, and D. Saunders, "Optical coherence tomography for art conservation and archaeology," in C. Fotakis, L. Pezzati, and R. Salimbeni, eds. (2007), p. 661805.
44. K. Stonor and R. Morrison, "Adolphe Monticelli: The Materials and Techniques of an Unfashionable Artist," in *National Gallery Technical Bulletin Volume 33* (2012), pp. 50–72.
45. H. Liang, "Advances in multispectral and hyperspectral imaging for archaeology and art conservation," *Appl. Phys. A* **106**(2), 309–323 (2012).
46. M. Picollo, C. Cucci, A. Casini, and L. Stefani, "Hyper-Spectral Imaging Technique in the Cultural Heritage Field: New Possible Scenarios," *Sensors* **20**(10), 2843 (2020).
47. C. Cucci, J. K. Delaney, and M. Picollo, "Reflectance Hyperspectral Imaging for Investigation of Works of Art: Old Master Paintings and Illuminated Manuscripts," *Acc. Chem. Res.* **49**(10), 2070–2079 (2016).
48. J. Striova, A. Dal Fovo, and R. Fontana, "Reflectance imaging spectroscopy in heritage science," *La Riv. del Nuovo Cim.* **43**(10), 515–566 (2020).
49. H. Liang, A. Lucian, R. Lange, C. Cheung, and B. Su, "Remote spectral imaging with simultaneous extraction of 3D topography for historical wall paintings," *ISPRS J. Photogramm. Remote Sens.* **95**, 13–22 (2014).
50. H. Liang, K. Keita, and T. Vajzovic, "PRISMS: a portable multispectral imaging system for remote in situ examination of wall paintings," in C. Fotakis, L. Pezzati, and R. Salimbeni, eds. (2007), **6618**, p. 661815.

51. N. Ohta and A. R. Robertson, "CIE Standard Colorimetric System," in *Colorimetry: Fundamentals and Applications* (Wiley, 2005), pp. 63–114.
52. L. M. Dingemans, V. M. Papadakis, P. Liu, A. J. L. Adam, and R. M. Groves, "Optical coherence tomography complemented by hyperspectral imaging for the study of protective wood coatings," in L. Pezzati and P. Targowski, eds. (2015), p. 952708.
53. A. Dal Fovo and R. Fontana, "Stratigraphic mapping of paintings by multispectral reflectography," *Eur. Phys. J. Plus* **138**(12), 1112 (2023).
54. A. Dal Fovo, M. Martínez-Weinbaum, M. Oujja, M. Castillejo, and R. Fontana, "Reflectance Spectroscopy as a Novel Tool for Thickness Measurements of Paint Layers," *Molecules* **28**(12), 4683 (2023).
55. Z. Gao, J. Wang, X. Wang, X. Dong, and Y. Li, "A Review of Segmentation and Classification for Retinal Optical Coherence Tomography Images," 2021 IEEE 2nd Int. Conf. Pattern Recognit. Mach. Learn. PRML 2021 129–135 (2021).
56. R. Kafieh, H. Rabbani, and S. Kermani, "A review of algorithms for segmentation of optical coherence tomography from retina.," *J. Med. Signals Sens.* **3**(1), 45–60 (2013).
57. Kang Li, Xiaodong Wu, D. Z. Chen, and M. Sonka, "Optimal Surface Segmentation in Volumetric Images-A Graph-Theoretic Approach," *IEEE Trans. Pattern Anal. Mach. Intell.* **28**(1), 119–134 (2006).
58. S. J. Chiu, X. T. Li, P. Nicholas, C. A. Toth, J. A. Izatt, and S. Farsiu, "Automatic segmentation of seven retinal layers in SDOCT images congruent with expert manual segmentation," *Opt. Express* **18**(18), 19413 (2010).
59. C. Cuartas-Vélez, R. Restrepo, B. E. Bouma, and N. Uribe-Patarroyo, "Volumetric non-local-means based speckle reduction for optical coherence tomography," *Biomed. Opt. Express* **9**(7), 3354 (2018).
60. Y. Wu, B. Tracey, P. Natarajan, and J. P. Noonan, "Probabilistic non-local means," *IEEE Signal Process. Lett.* **20**(8), 763–766 (2013).
61. E. W. Dijkstra, "A note on two problems in connexion with graphs," *Numer. Math.* **1**(1), 269–271 (1959).

62. T. O. M. C. Allewaert, J. O. D. Ik, and J. E. K. Alkman, "Segmentation of thin corrugated layers in high-resolution OCT images Segmentation of thin corrugated layers in high-resolution OCT images," (2017).
63. T. Callewaert, J. Guo, G. Harteveld, A. Vandivere, E. Eisemann, J. Dik, and J. Kalkman, "Multi-scale optical coherence tomography imaging and visualization of Vermeer's Girl with a Pearl Earring," *Opt. Express* **28**(18), 26239 (2020).
64. S. R. Robertson, "The refractive index of a solid film of linseed oil rise in refractive index with age," *Proc. R. Soc. London. Ser. A - Math. Phys. Sci.* **159**(896), 123–133 (1937).
65. R. S. Berns and E. R. de la Rie, "The Effect of the Refractive Index of a Varnish on the Appearance of Oil Paintings," *Stud. Conserv.* **48**(4), 251–262 (2003).
66. V. Westphal, A. Rollins, S. Radhakrishnan, and J. Izatt, "Correction of geometric and refractive image distortions in optical coherence tomography applying Fermat's principle," *Opt. Express* **10**(9), 397 (2002).
67. R. A. Leitgeb, "En face optical coherence tomography: a technology review [Invited]," *Biomed. Opt. Express* **10**(5), 2177 (2019).
68. H. Liang, M. G. Cid, R. G. Cucu, G. M. Dobre, A. G. Podoleanu, J. Pedro, and D. Saunders, "En-face optical coherence tomography - a novel application of non-invasive imaging to art conservation," *Opt. Express* **13**(16), 6133 (2005).
69. M. Aceto, A. Agostino, G. Fenoglio, A. Idone, M. Gulmini, M. Picollo, P. Ricciardi, and J. K. Delaney, "Characterisation of colourants on illuminated manuscripts by portable fibre optic UV-visible-NIR reflectance spectrophotometry," *Anal. Methods* **6**(5), 1488–1500 (2014).
70. M. Pappas and I. Pitas, "Digital color restoration of old paintings," *IEEE Trans. Image Process.* **9**(2), 291–294 (2000).
71. G. Trumpy, D. Conover, L. Simonot, M. Thoury, M. Picollo, and J. K. Delaney, "Experimental study on merits of virtual cleaning of paintings with aged varnish," *Opt. Express* **23**(26), 33836 (2015).
72. M. Elias and P. Cotte, "Multispectral camera and radiative transfer equation used to depict Leonardo's sfumato in Mona Lisa," *Appl. Opt.* **47**(12), 2146–2154 (2008).

73. M. Barni, F. Bartolini, and V. Cappellini, "Image processing for virtual restoration of artworks," *IEEE Multimed.* **7**(2), 34–37 (2000).
74. M. Maali Amiri and D. W. Messinger, "Virtual cleaning of works of art using deep convolutional neural networks," *Herit. Sci.* **9**(1), 1–19 (2021).
75. J. Linhares, L. Cardeira, A. Bailão, R. Pastilha, and S. Nascimento, "Chromatic changes in paintings of Adriano de Sousa Lopes after the removal of aged varnish," *Conserv. Patrim.* **2020**(34), 50–64 (2020).
76. C. M. T. Palomero and M. N. Soriano, "Digital cleaning and “dirt” layer visualization of an oil painting," *Opt. Express* **19**(21), 21011 (2011).
77. E. Kirchner, I. van der Lans, F. Ligterink, E. Hendriks, and J. Delaney, "Digitally reconstructing Van Gogh’s Field with Irises near Arles. Part 1: Varnish," *Color Res. Appl.* **43**(2), 150–157 (2018).
78. H. S. Nam and H. Yoo, "Spectroscopic optical coherence tomography: A review of concepts and biomedical applications," *Appl. Spectrosc. Rev.* **53**(2–4), 91–111 (2018).
79. N. Bosschaart, T. G. van Leeuwen, M. C. G. Aalders, and D. J. Faber, "Quantitative comparison of analysis methods for spectroscopic optical coherence tomography," *Biomed. Opt. Express* **4**(11), 2570 (2013).
80. F. E. Robles, C. Wilson, G. Grant, and A. Wax, "Molecular imaging true-colour spectroscopic optical coherence tomography," *Nat. Photonics* **5**(12), 744–747 (2011).
81. S. Fitzgerald, J. Akhtar, E. Schartner, H. Ebendorff-Heidepriem, A. Mahadevan-Jansen, and J. Li, "Multimodal Raman spectroscopy and optical coherence tomography for biomedical analysis," *J. Biophotonics* **16**(3), (2023).
82. C. A. Patil, H. Kirshnamoorthi, D. L. Ellis, T. G. van Leeuwen, and A. Mahadevan-Jansen, "A clinical instrument for combined raman spectroscopy-optical coherence tomography of skin cancers," *Lasers Surg. Med.* **43**(2), 143–151 (2011).
83. C. A. Patil, N. Bosschaart, M. D. Keller, T. G. van Leeuwen, and A. Mahadevan-Jansen, "Combined Raman spectroscopy and optical coherence tomography device for tissue characterization," *Opt. Lett.* **33**(10), 1135 (2008).

84. C. A. Patil, J. Kalkman, D. J. Faber, J. S. Nyman, T. G. van Leeuwen, and A. Mahadevan-Jansen, "Integrated system for combined Raman spectroscopy–spectral domain optical coherence tomography," *J. Biomed. Opt.* **16**(1), 011007 (2011).
85. J. Klemes, A. Kotzianova, M. Pokorny, P. Mojzes, J. Novak, L. Sukova, J. Demuth, J. Vesely, L. Sasek, and V. Velebny, "Non-invasive diagnostic system and its opto-mechanical probe for combining confocal Raman spectroscopy and optical coherence tomography," *J. Biophotonics* **10**(11), 1442–1449 (2017).
86. X. Ren, K. Lin, C.-M. Hsieh, L. Liu, X. Ge, and Q. Liu, "Optical coherence tomography-guided confocal Raman microspectroscopy for rapid measurements in tissues," *Biomed. Opt. Express* **13**(1), 344 (2022).
87. A. Varkentin, M. Mazurenka, E. Blumenröther, L. Behrendt, S. Emmert, U. Morgner, M. Meinhardt-Wollweber, M. Rahlves, and B. Roth, "Trimodal system for in vivo skin cancer screening with combined optical coherence tomography-Raman and colocalized optoacoustic measurements," *J. Biophotonics* **11**(6), 1–12 (2018).
88. K. M. Khan, H. Krishna, S. K. Majumder, K. D. Rao, and P. K. Gupta, "Depth-sensitive Raman spectroscopy combined with optical coherence tomography for layered tissue analysis," **85**(1), 77–85 (2014).
89. H. Pan, Z. Yang, J. Zhao, Y. Yu, and Y. Liang, "Multimodal imaging with integrated auto-fluorescence and optical coherence tomography for identification of neck tissues," *Lasers Med. Sci.* (2020).
90. H. S. Nam, W. J. Kang, M. W. Lee, J. W. Song, J. W. Kim, W.-Y. Oh, and H. Yoo, "Multispectral analog-mean-delay fluorescence lifetime imaging combined with optical coherence tomography," *Biomed. Opt. Express* **9**(4), 1930 (2018).
91. B. E. Sherlock, X. Zhou, J. Bec, and L. Marcu, "Synchronous fluorescence lifetime imaging and optical coherence tomography using a double clad fiber," *2016 IEEE Photonics Conf. IPC 2016* **42**(19), 3753–3756 (2017).
92. X. Li, W. Zhang, W. Y. Wang, X. Wu, Y. Li, X. Tan, D. L. Matera, B. M. Baker, Y. M. Paulus, X. Fan, and X. Wang, "Optical coherence tomography and fluorescence microscopy dual-modality imaging for in vivo single-cell tracking with nanowire lasers," *Biomed. Opt. Express* **11**(7), 3659 (2020).

93. W. Zhang, Y. Li, V. P. Nguyen, Z. Huang, Z. Liu, X. Wang, and Y. M. Paulus, "High-resolution, in vivo multimodal photoacoustic microscopy, optical coherence tomography, and fluorescence microscopy imaging of rabbit retinal neovascularization," *Light Sci. Appl.* **7**(1), 103 (2018).
94. J. Mavadia, J. Xi, Y. Chen, and X. Li, "An all-fiber-optic endoscopy platform for simultaneous OCT and fluorescence imaging," *Biomed. Opt. Express* **3**(11), 2851 (2012).
95. S. Yuan, C. A. Roney, J. Wierwille, C.-W. Chen, B. Xu, G. Griffiths, J. Jiang, H. Ma, A. Cable, R. M. Summers, and Y. Chen, "Co-registered optical coherence tomography and fluorescence molecular imaging for simultaneous morphological and molecular imaging," *Phys. Med. Biol.* **55**(1), 191–206 (2010).
96. S. Lee, M. W. Lee, H. S. Cho, J. W. Song, H. S. Nam, D. J. Oh, K. Park, W.-Y. Oh, H. Yoo, and J. W. Kim, "Fully Integrated High-Speed Intravascular Optical Coherence Tomography/Near-Infrared Fluorescence Structural/Molecular Imaging In Vivo Using a Clinically Available Near-Infrared Fluorescence-Emitting Indocyanine Green to Detect Inflamed Lipid-Rich Atherom," *Circ. Cardiovasc. Interv.* **7**(4), 560–569 (2014).
97. J. Scholler, K. Groux, O. Goureau, J.-A. Sahel, M. Fink, S. Reichman, C. Boccara, and K. Grieve, "Dynamic full-field optical coherence tomography: 3D live-imaging of retinal organoids," *Light Sci. Appl.* **9**(1), 140 (2020).
98. R. Guay-Lord, X. Attendu, K. L. Lurie, L. Majeau, N. Godbout, A. K. E. Bowden, M. Strupler, and C. Boudoux, "Combined optical coherence tomography and hyperspectral imaging using a double-clad fiber coupler," *J. Biomed. Opt.* **21**(11), 116008 (2016).
99. X. Attendu, M.-H. Bourget, M. P. de Sivry-Houle, and C. Boudoux, "Coregistered optical coherence tomography and frequency-encoded multispectral imaging for spectrally sparse color imaging," *J. Biomed. Opt.* **25**(03), 1 (2019).
100. S. Dontu, S. Miclos, D. Savastru, and M. Tautan, "Combined spectral-domain optical coherence tomography and hyperspectral imaging applied for tissue analysis: Preliminary results," *Appl. Surf. Sci.* **417**, 119–123 (2017).

101. D. Savastru, S. Miclos, N. Iftimia, M. A. Calin, R. Savastru, D. Manea, and S. Dontu, "Dual mode SDOCT-HSI approach for cancer surgery guidance," *J. Optoelectron. Adv. Mater.* **18**(11–12), 993–999 (2016).
102. M. Göb, T. Pfeiffer, and R. Huber, "Towards combined optical coherence tomography and multi-spectral imaging with MHz a-scan rates for endoscopy," *Opt. InfoBase Conf. Pap. Part F142-*, 4–6 (2019).
103. S. L. Pugh and J. T. Guthrie, "The development of light fastness testing and light fastness standards," *Rev. Prog. Color. Relat. Top.* **31**(1), 42–56 (2001).
104. B. Ford and C. Korenberg, "Manufacturing Variations in ISO Blue Wool Fading Standards under Microfading Exposure Conditions," *Stud. Conserv.* **0**(0), 1–12 (2023).
105. L. Rodriguez-Cobo, M. Lomer, C. Galindez, and J. M. Lopez-Higuera, "Speckle characterization in multimode fibers for sensing applications," *Speckle 2012 V Int. Conf. Speckle Metrol.* **8413**, 84131R (2012).
106. E. Hecht, "Geometrical Optics," in *Optics*, 3rd ed. (Addison Wesley, 1998), pp. 148–246.
107. J. Kirby, C. Higgitt, and M. Spring, "Madder Lakes of the 15th - 17th Centuries: Variability of Dyestuff Content," in *The Diversity of Dyes in History and Archaeology*, J. Kirby, ed. (Archetype Publications, 2017), pp. 148–161.
108. M. Alter, L. Binet, N. Touati, N. Lubin-Germain, A. S. Le Hô, F. Mirambet, and D. Gourier, "Photochemical origin of the darkening of copper acetate and resinate pigments in historical paintings," *Inorg. Chem.* (September), (2019).
109. L. Bernstein, A. Ramier, J. Wu, V. D. Aiello, M. J. Béland, C. P. Lin, and S.-H. Yun, "Ultrahigh resolution spectral-domain optical coherence tomography using the 1000–1600 nm spectral band," *Biomed. Opt. Express* **13**(4), 1939 (2022).
110. M. I. M. Aria, I. V. A. N. B. R. G. Onzalo, T. H. F. Euchter, M. A. R. K. D. Enninger, P. E. M. M. Oselund, L. A. L. Eick, O. L. E. B. Ang, and A. D. P. Odoleanu, "Q-switch-pumped supercontinuum for ultra-high resolution optical coherence tomography," **42**(22), 4744–4747 (2017).
111. M. Jensen, I. B. Gonzalo, R. D. Engelsholm, M. Maria, N. M. Israelsen, A.

- Podoleanu, and O. Bang, "Noise of supercontinuum sources in spectral domain optical coherence tomography," *J. Opt. Soc. Am. B* **36**(2), A154 (2019).
112. W. J. Brown, S. Kim, and A. Wax, "Noise characterization of supercontinuum sources for low-coherence interferometry applications," *J. Opt. Soc. Am. A* **31**(12), 2703 (2014).
113. D. Bomford, J. Dunkerton, D. Gordon, and R. Ashok, *Art in the Making: Italian Painting before 1400* (National Gallery Company Ltd, 1989).
114. E. S. Skaug, *Punch Marks from Giotto to Fra Angelico : Attribution, Chronology, and Workshop Relationships in Tuscan Panel Painting : With Particular Consideration to Florence, c.1330-1430* (IIC, Nordic Group, the Norwegian section Oslo, 1994).
115. M. S. Frinta and P. M. Lukehart, "Observations on the Trecento and early Quattrocento workshop," in *The Artist's Workshop* (National Gallery of Art, 1993), pp. 18–34.
116. Y. Chen, J. Fingler, and S. E. Fraser, "Multi-shaping technique reduces sidelobe magnitude in optical coherence tomography," *Biomed. Opt. Express* **8**(11), 5267 (2017).
117. F. J. Harris, "On the Use of Windows for Harmonic Analysis with the Discrete Fourier Transform," *Proc. IEEE* **66**(1), 51–83 (1978).